Quantifying South African Uplift:

Using apatite fission track thermochronology and offshore sediment volumes to test the balance between denudation (onshore) and deposition (offshore) since Gondwana break-up

Justine Tinker

Thesis submitted in fulfilment of the requirements for the degree of Doctor of Philosophy

Department of Geological Sciences
University of Cape Town
October, 2005

UNIVERSITY OF CAPE TOWN

Abstract

Southern Africa's hypsometry is distinctive. First, its topography is anomalously high relative to other continents, given that it is surrounded by extensional passive margins. Second, it is divided by the steeply dipping 'Great Escarpment' into two distinct regions: an interior plateau of low relief and high average elevation, separated from a coastal region of high relief and low average elevation. How this topography has evolved is part of ongoing discourse. In particular, the origin of the Great Escarpment is in contention: did it form close to its present position, or has it retreated from an initial location near the coast? Since the break-up of Gondwana, several hundred thousand km^3 of rock has been eroded from the continent and the products of this erosion are preserved as accumulated sediments offshore. This thesis focuses on the southern Cape and relates onshore denudation to offshore accumulation in an attempt to unravel the mechanisms driving denudation over the last ~140 Myrs and resolving some of the issues concerning its topography.

Onshore denudation is quantified using apatite fission track analysis (AFTA). Twenty-five outcrop samples were taken from a ~600 km, north-south transect extending across the Cape Fold Belt Mountains, the Great Escarpment and into the Karoo interior, from George on the south coast to Marydale inland. Fission track ages are Cretaceous, ranging from 89 ± 6 Ma to 157 ± 14 Ma, and the oldest ages are from the top of the Great Escarpment. These apatite fission track ages are significantly younger than the stratigraphic ages of their host rocks, indicating that the samples have experienced elevated paleotemperatures since their formation. Mean track lengths vary from 11.86 to 14.23 μm and their length distributions are negatively skewed with tails of shorter tracks, indicating partial annealing. The lack of Cenozoic apatite ages indicates that major cooling (and denudation) was over by the end of the Cretaceous. FT ages are not correlated to distance from the rift margin. The AFTA (supported by published cosmogenic isotopic dating) suggests that if the escarpment did retreat, it must have done so rapidly in the Cretaceous (~250 km in <~75 Myrs along the south coast, at a rate of >3.3 km/Ma).

Three boreholes situated south of the escarpment, were sampled at a depth interval of ~300 m (31 samples). Plots of fission track age versus depth show an episode of increased denudation in the mid Cretaceous (100-80 Ma) and an earlier episode of increased denudation (140-120 Ma) is identified from a borehole north of the escarpment. Thermal

modelling supports an exhumation history involving denudation of 1 to 2.6 km in the early Cretaceous (140-120 Ma). Denudation of 2.1 to 3.5 km took place in the mid Cretaceous (100-80 Ma), mostly south of the escarpment, which increased the escarpment's relief and exhumed the Cape Fold Belt Mountains. The escarpment was 'pinned' and its rate of retreat reduced by intersection with the Karoo dolerites. Less than 1.1 km has been eroded since the late Cretaceous (<80 Ma).

A total sediment volume of $2.7*10^5$ km^3 accumulated offshore since ~136 Ma in the Outeniqua and Southern Outeniqua Basins (as calculated from 173 wells and seismic reflection profiles). Accumulation volumes and rates were highest in the early Cretaceous ($4.9*10^4$ km^3 at 8134 km^3/Ma from ~136-130 Ma, and $5.8*10^4$ km^3 at 5750 km^3/Ma from ~130-120 Ma) and mid-late Cretaceous ($8.4*10^4$ km^3 at 3219 km^3/Ma from ~93-67 Ma). Volumes and accumulation rates were lowest for the early-mid Cretaceous ($4.7*10^4$ km^3 at 1752 km^3/Ma from ~120-93 Ma) and the Cenozoic ($3.1*10^4$ km^3 at 465 km^3/Ma from ~67-0 Ma).

Onshore denudation exceeds offshore accumulation by ~300-400 %, yet the timing of changes in denudation closely matches the timing of changes in offshore accumulation. Episodes of increased denudation and accumulation in the early and mid-late Cretaceous are regionally widespread, since they have been identified as far as, for example, Namibia and Mozambique. Regionally, there appears to be a close temporal relationship between increased denudation and kimberlite emplacement. At ~120 Ma, 20 Myrs after the initiation of increased denudation, ~200 Group-2 kimberlites intruded across southern Africa. Early Cretaceous denudation, however, overlaps with continental rifting (at ~136 Ma) and that is more likely to be its cause. From ~120 to 100 Ma low denudation/ accumulation coincides with a period of subdued kimberlite activity. Increased denudation in the mid Cretaceous is synchronous with the emplacement of ~450 Group-1 kimberlites (at ~90 Ma). Thus mid Cretaceous uplift, denudation and perhaps tectonic exhumation (e.g. of the Cango Inlier at ~90 Ma) may be linked more directly to deep-seated mantle processes that generated the Group-1 kimberlites.

Climate and lithology have likely also influenced denudation and subsequent sediment accumulation offshore. A greater density of thermochronologic data is needed to unravel this further.

Table of Contents

List of Figures

List of Tables

* This assumption is invalid. However, since correlation between t0 and t1 is unknown, the correct formula for the subtraction of errors cannot be applied [var(X±Y)= var(X) + var(Y) ± 2cos(X,Y)]. The application of the correct formula results in an error that is ± 2 units (or ± 2 Ma in the case of t0-t1) different to that calculated assuming independence.

Acknowledgements

Maarten de Wit has been my supervisor, motivator and mentor for the last 8 years. He has provided encouragement when needed and criticism when needed and managed to get the level between the two just right. He has inspired me to produce nothing less than my best, which was often more than I thought I could do. I owe him a huge debt of gratitude for all he has done for me over the years. All the support, last minute marking, patience and humour have been much appreciated.

This research began with data collection ably assisted by my fiancé, Dave, who wielded a 14 pound hammer through the Karoo without (much) complaint. Martin Kohler from Council for Geoscience located and organized the core I needed. David Motloi, from the Council for Geoscience sent additional borehole information I found I suddenly needed. Thank you to Ian McLachlan and Jacques Roux from the Petroleum Agency SA, for facilitating access to the offshore data I required.

The bulk of the fission track analysis was carried out in Melbourne, Australia where I was lucky enough to be surrounded by all the expert help and friendship I could ask for. Rod and Sue Brown generously accommodated me when I was new to the continent and did not know a sole. Their warmth and hospitality throughout my 8 month stint was hugely appreciated. Thanks to Rod for all the scientific support and discussions. Your input has greatly improved my thesis. Thank you to Asaf Raza for expertly teaching me the fission track technique with unending patience and encouragement. I thank the rest of the Melbourne crew, Andy Gleadow, Barry Kohn and my fellow students for all the fruitful discussions and for making me feel welcome. Thanks to Vicki-Ann especially, my first friend in Aus!

Back at UCT, Giulio Viola and Alex Kounov are thanked for sharing their expertise which has greatly improved my work. It has been good to have had the knowledge of fellow 'fission trackers' on hand to draw on. Thanks too to Moctar Doucouré for his help (via a multitude of emails) in getting me started on Oasis Montaj; to Jacek Stankiewicz for his Matlab expertise; John Decker for his Karoo expertise and Christien Thiart for her statistical help.

Other scientists whose specialist knowledge has been a great help are Mike Jones, from Wits (geothermal gradients), Mike de Wit from de Beers (southern African geomorphology), Hielke Jelsma from de Beers (kimberlites) and Doug Cole, from Council for Geoscience (the Karoo Supergroup).

Thanks to Marek Ranoszek and Pioneer Natural Resources for providing personal funding and support as well as for helping to get me to the 10th International Fission Track Conference in Amsterdam. Thanks also to the Upstream Training Trust for paying for the bulk of my Australian experience and to the N.R.F. for funding whilst at CIGCES.

Lastly, a huge thanks to my parents, family and friends for their encouragement and love, and to Dave for always being so supportive, even from afar while I was in Australia.

Justine Tinker
February 2005.

Acronyms used in this thesis

(A)FTA: (Apatite) Fission Track Analysis

PAZ: Partial Annealing Zone

PPAZ: Paleo-partial Annealing Zone

SPT: Sodium Polytungstate

Sequence Stratigraphy and Chronostratigraphy

This thesis uses the offshore sequence stratigraphic nomenclature outlined in Brown *et al.* (1995) with ages of regional unconformities readjusted according to the timescale of Gradstein *et al.* (2004).

Onshore

The early Cretaceous is defined as 140-120 Ma,

Early-mid Cretaceous= 120-100 Ma

Mid Cretaceous= 100-80 Ma

Late Cretaceous= 80-65 Ma

Offshore

The early Cretaceous is defined as 136-120 Ma,

Early-mid Cretaceous= 120-93 Ma

Mid-late Cretaceous= 93-67 Ma

(Throughout text age ranges are given with oldest age first e.g. 136-120 Ma)

Tectonic Definitions

Rift

The term 'rift' is commonly used to denote those sequences deposited along passive continental margins during extensional deformation (normal faulting), resulting in well-defined crustal graben structures, infilled with coarse siliclastics and volcanics. The latter often are detected seismically along continental margins as seaward dipping reflectors.

Drift

The 'drift' succession is composed of sediments that are deposited during subsequent thermal subsidence.

Rift-drift transition

Here defined as the period (~136-120 Ma) preceding thermal subsidence when minor movement along normal faults continues although most deformation has ended.

Rift-drift unconformity

Separates the older rift succession from younger sediments deposited during the rift-drift transition. Along the south coast this is the 1At1 unconformity (~136 Ma).

5At1/6At1

The prominent unconformity offshore at ~130 Ma is called the 6At1 unconformity in the Pletmos, Gamtoos and Algoa Basins and 5At1 in the Bredasdorp Basin. To avoid confusion, it has been named the 6At1 throughout this thesis.

Chapter 1: Introduction

Africa can be divided into two extensive regions of different mean elevation. Central-west and West Africa have low average elevation of ~450 m. Eastern and southern Africa has a high average elevation of ~1015 m (Doucouré and de Wit, 2003). The origin and timing of southern Africa's anomalously high elevation is poorly understood, with a variety of causes rooted in mantle dynamics suggested by Nyblade and Robinson (1994), Burke (1996), Lithgow-Bertelloni and Silver (1998), Ebinger and Sleep (1998), Gurnis *et al.* (2000) and Doucouré and de Wit (2003).

The uplift history and geomorphological evolution of Southern Africa has, in fact, been widely debated since the early days of Du Toit (1937, 1954) and King (1951). Since the break-out of southern Africa from Gondwana between ~180-130 Ma, several hundred thousand km^3 of rock has been eroded, episodically, from the continent and most is now presumably preserved as sediments offshore. There is little consensus as to the precise timing, duration and magnitude of the uplift and erosion. Geomorphological studies have hinged on the identification of erosional surfaces to which ages have been assigned, a practice criticised by Summerfield (1996) and Brown *et al.* (2000), for example. Good quantitative chronological control is lacking to evaluate the major tectonic events that have played pivotal roles in processes that include redistribution of erosional products and the formation of diamond placers and oil/gas reserves offshore. At least as a first order assumption, what is lost from the continent should be gained on the continental shelf, rise and ocean floor.

This thesis tests the balance between the amount of erosion of the southern Cape, against the volume of sediment along its southern margin since the break-up of Gondwana, with the aim of enhancing understanding of the geomorphological and topographic evolution of South Africa. The question to be probed is whether we can we link sediment accumulation offshore with denudation (perhaps due to variable tectonic uplift) of the onshore. South Africa's south coast, offshore and inland, is a particularly good place to test this onshore-offshore balance because hydrocarbon exploration has resulted in a wealth of data.

The thesis begins with a summary of the geological and geomorphological setting of the study area (chapter 2 and 3, respectively). Apatite fission track analysis (AFTA) is used in chapter 4 to quantify onshore denudation of the southern Cape region since Gondwana break-up. The low closure temperature of apatite (110 ± 10°C) makes AFTA particularly useful in timing and quantifying shallow crustal thermal changes related to denudation, often coupled with uplift and has been applied to a wide variety of geological and geomorphological problems, summarized in Gallagher *et al.* (1998). After a short introduction to the method (4.1) the sampling technique is described (4.2). Twenty-five outcrop samples yielded sufficient apatite to calculate a fission track age. These were collected along a N-S transect from Victoria Bay on the south coast, across the Cape Fold Belt, Cango Inlier and younger Uitenhage Group Basins, into the Karoo Basin and ending in Marydale, at the edge of the Kaapvaal Craton (Figure 1.1). The transect crosses the Great Escarpment, as well as numerous E-W trending faults (both reverse and normal) associated with the assembly and break-up of Gondwana, respectively. Three deep boreholes SA1/66 (4110 m), KW1/67 (5219 m) and CR1/68 (3498 m) (from west to east, Figure 1.1), situated south of the escarpment, were sampled at a depth interval of ~300 m (31 samples). All samples were separated, prepared and counted at the University of Melbourne's fission track laboratory. Selected samples were recounted at the fission track laboratory of the University of Cape Town. The AFTA results are given in section 4.3 (and Appendix C), interpreted in 4.4, and modelled in 4.5. A model for the timing and degree of denudation across the southern Cape is proposed in chapter 5.

In chapter 6, offshore seismic and borehole data, acquired due to hydrocarbon exploration and supplied by PetroSA (then SOEKOR), are used to quantify sediment volumes for various time intervals since the break-up of Gondwana. Rifting during Gondwana break-up saw the formation of several offshore Mesozoic basins that were the depositories for sediments derived from onshore southern Africa since the early Cretaceous. Along the south coast the four basins, collectively called the Outeniqua Basin here, are (from east to west) the Algoa, Gamtoos, Pletmos and Bredasdorp Basins. To the south, lying deeper offshore, is the Southern Outeniqua Basin (Figure 1.1).

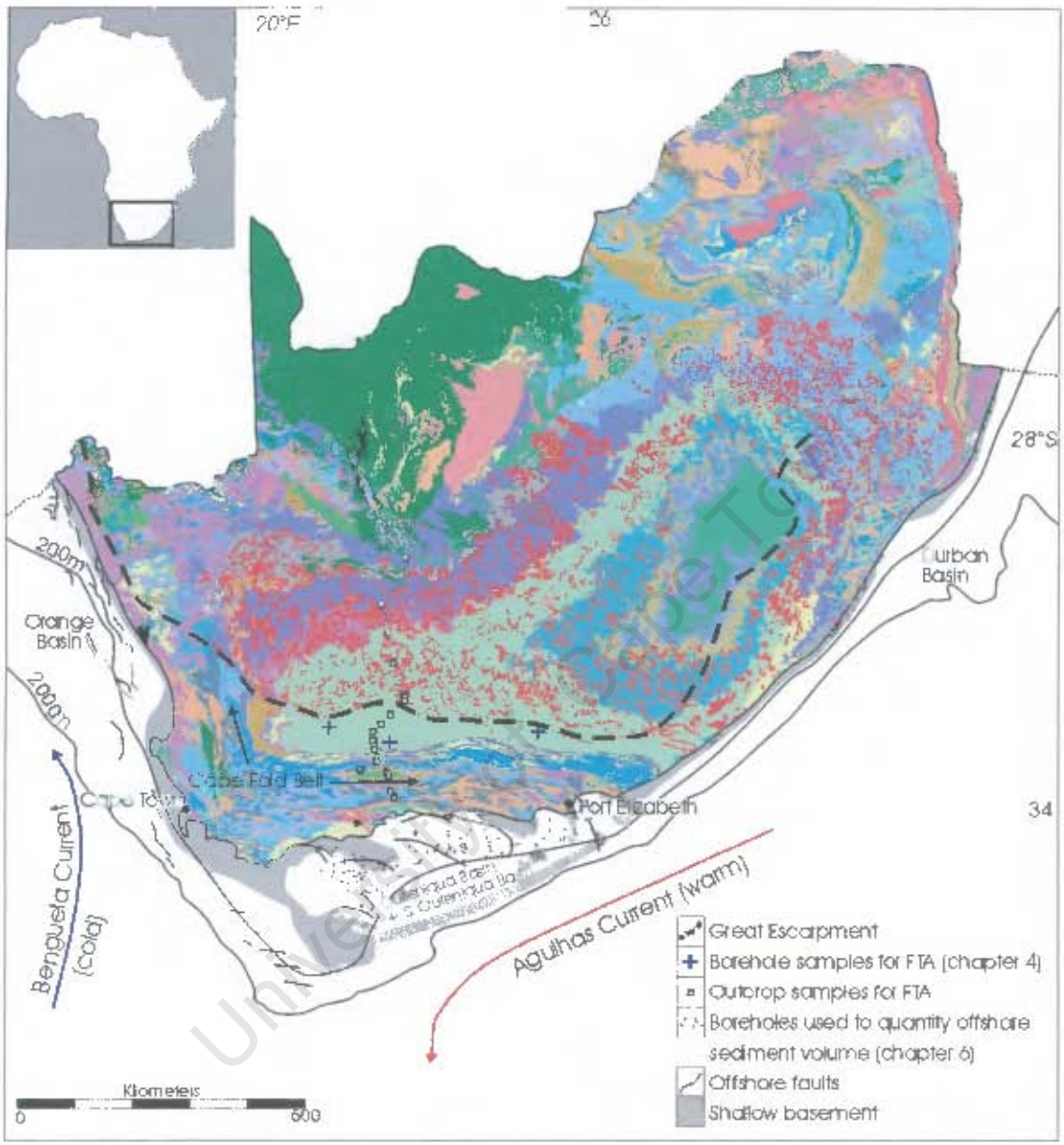

Figure 1.1: Onshore geology and offshore basins of South Africa. Boreholes used in fission track analysis are marked with blue crosses, outcrop samples as white squares (Chapter 4). The escarpment is delineated with a heavy dashed line. Offshore boreholes used to determine sediment volume off the south coast (Chapter 6) are shown as small black dots. Geological map from Martini *et al.* (2001). Legend in appendix A.

Borehole data from 173 wells acquired from SOEKOR well reports are used to contour depths to 5 major unconformities (using Oasis Montaj 6.0, Geosoft inc.), chosen because they extend across the southern offshore basins. These are, using the sequence stratigraphic nomenclature of Brown *et al.* (1995) and time scale of Gradstein *et al.* (2004), 1At1 (~136 Ma), 6At1 (~130 Ma), 13At1 (~120 Ma), 15At1 (~93 Ma) and 22At1 (~67 Ma). From these data, 5 isopach maps of accumulated sediment in the time intervals of ~136-130 Ma; ~130-120 Ma; ~120-93 Ma; ~93-67 Ma and ~67-0 Ma are derived and in turn the volume of sediment estimated (section 6.3 and 6.4).

Chapter 7 compares the results of the fission track estimate of denudation (Chapter 5) to estimates of offshore accumulation from borehole and seismic data (Chapter 6) for 5 time intervals. These are the early Cretaceous (140-120 Ma), the early-mid Cretaceous (120-100 Ma), the mid Cretaceous (100-80 Ma), the late Cretaceous (80-65 Ma) and the Cenozoic (65-0 Ma). This comparison leads to an assessment of the denudation (and uplift) history of southern Africa and its geomorphological evolution since Gondwana break-up, followed by an evaluation of possible driving mechanisms of this uplift. The thesis ends with the intriguing overlap of peak kimberlite emplacement and peak rates of denudation/ accumulation, and therefore a proposal of a link between episodic uplift, denudation, kimberlite intrusion and mantle upwelling. Following in chapter 8 are concluding remarks on the role of climate in denudation and how future efforts in quantifying geomorphology may enhance our understanding of the evolution of the southern African landscape.

Chapter 2: Geological Setting

2.1 Introduction

The southern Cape geologic history spans ~650 Myrs from the Neoproterozoic Malmesbury Group to raised paleo-beaches from the last Pleistocene interglacial (Figure 2.1). Here, this history is described in 6 sections: 1. The 'basement' units: the Malmesbury, Kaaimans and Cango Groups and Cape Granite Suite, 2. The Cape Supergroup, 3. The Karoo Supergroup, 4. Gondwana break-up, 5. The deposition of the Uitenhage Group, preserved in extensional basins (half grabens) within the Cape Fold Belt, and the Cenozoic deposits around South Africa. Most Cretaceous rock has been eroded from the continent and is now preserved in several offshore basins. These are described in Chapter 6.

Figure 2.1 (over the page): Composite stratigraphic column with summary of the changing tectonic environments and climate since the Neoproterozoic. The first order eustatic sea level curve (red line) is from Haq *et al.* (1987). Increase in eustatic sea level relative to its present-day level is shown by excursions to the left. ?'s denote times where the onshore stratigraphic record is scarce. §: Age range of Cango Group except the older Nooidtgedacht Member. LIP: Large igneous province, LIP1= Karoo (182 ± 1 Ma, ^{40}Ar-^{39}Ar, Duncan *et al.*, 1997); LIP2= Paraná (132 ± 1 Ma, ^{40}Ar/^{39}Ar, Renne *et al.*, 1996). Ages are assigned to biostratigraphic intervals based on the timescale of Gradstein *et al.*, 2004. Numbers in the age column are links to references that follow below.

1. Based on seismic stratigraphic evidence (Weigelt and Uenzelmann-Neben, 2004).
2. Sundays River Formation, Uitenhage Group, paleontological evidence (McLachlan and McMillan, 1976).
3. ^{40}Ar-^{39}Ar on feldspars and whole rocks (Duncan *et al.*, 1997).
4. Elliot Formation, Norian to early Jurassic, paleontological evidence (Gauffre, 1993).
5. (a) Tarkastad Subgroup, upper Beaufort Group, (b) Adelaide Subgroup, lower Beaufort Group, Paleontological evidence, (Groenewald and Kitching, 1995; Kitching, 1995).
6. U-Pb SHRIMP (Armstrong *et al.*, 1998).

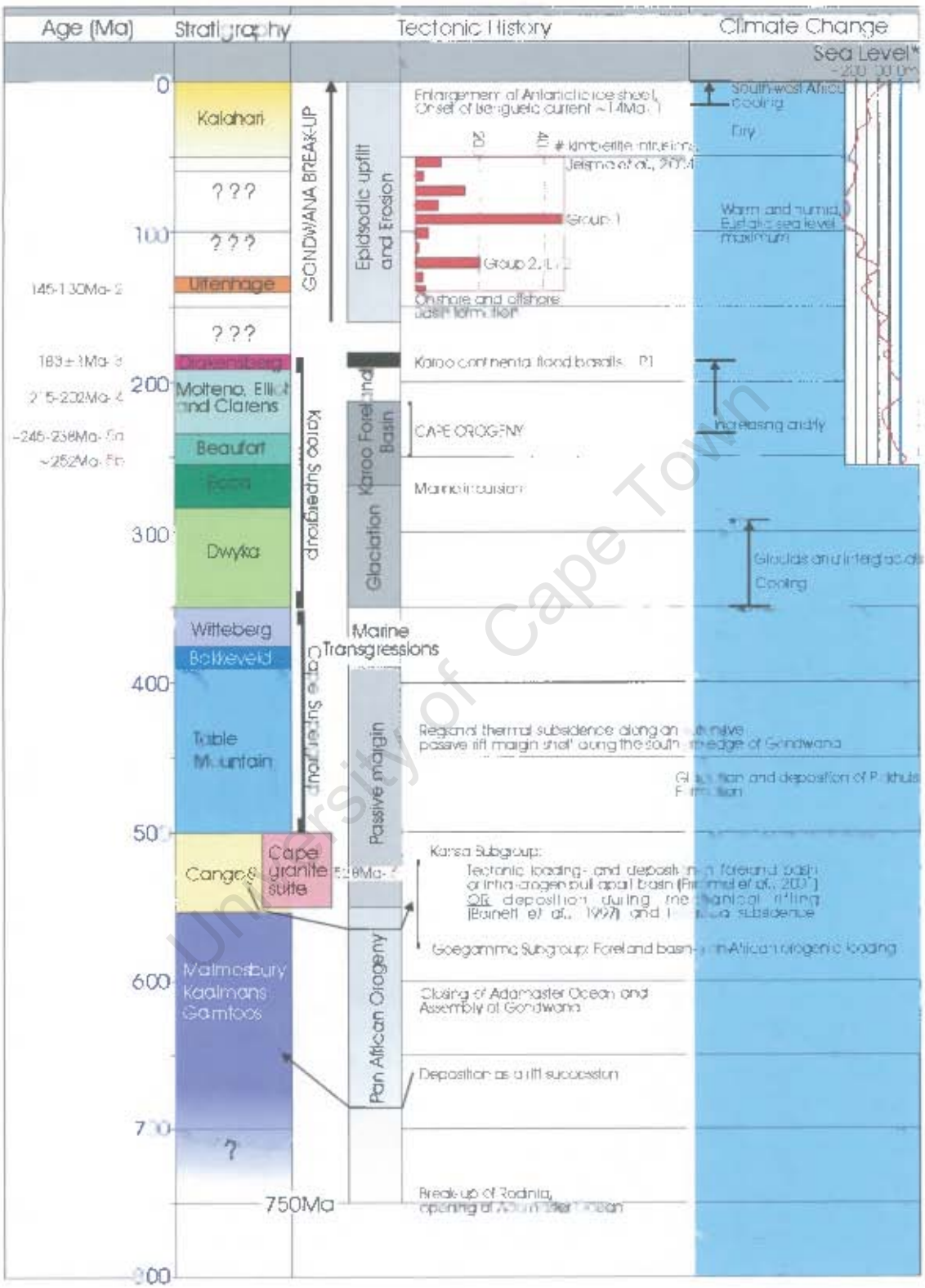

2.2 The Malmesbury, Kaaimans and Cango Groups and Cape Granite Suite (~650-500 Ma) (Figure 2.2)

The Malmesbury, Gamtoos and lower Cango Groups are interpreted to be the distal facies of rift successions deposited in pull-apart basins that formed during the break-up of Rodinia and the opening of the Adamaster Ocean (Rozendaal *et al.*, 1999). Reversal of this spreading and the closing of the Adamaster Ocean led to the deformation of these units during the Pan-African orogeny (~650±100 Ma, de Wit and Ransome, 1992). The Saldanian Belt (~650-550 Ma, Barnett *et al.*, 1997) is one of several Neo-Proterozoic mobile belts associated with the formation of Gondwana. The Malmesbury, Gamtoos, Kaaimans and Cango Groups outcrop as inlier remnants of the belt and are preserved in anticlinal hinges within the Cape Fold Belt. These inliers are now exposed due to subsequent denudation (Figure 2.2).

The *Malmesbury Group* is composed of tectonically and stratigraphically different terranes. The maximum age for one part of the Malmesbury Group (Tygerberg Subgroup of the Tygerberg Terrane, Figure 2.2) is 560 Ma, established from U-Pb zircon dating of detrital zircons (Armstrong *et al.*, 1998). Other detrital zircons of this Group have ages from 900-1050 Ma (sourced from the Namaqua-Natal Mobile Belt) and 575-700 Ma (sourced from Pan-African rocks) and the oldest measured age is Archean, 2960 Ma (Armstrong *et al.*, 1998). The minimum age for the Malmesbury, Gamtoos and Kaaimans Groups is given by the age of the intruding Cape Granite Suite (550-510 Ma, Rozendaal *et al.*, 1999). The Cape Granite Suite sampled at Seapoint is dated at 540 ± 4 Ma (95% confidence limit, U-Pb zircon, Armstrong *et al.*, 1998). The Malmesbury Group is composed of a deformed and metamorphosed succession of predominately marine shales (Rozendaal *et al.*, 1999). The *Kaaimans Group*, which outcrops in the George-Knysna area (Figure 2.2), is composed of massive quartzite, quartz schist and phyllite and impure limestone (Rozendaal *et al.*, 1999). The *Gamtoos Group* outcrops in the core of an anticline near Port Elizabeth (Figure 2.2) and is composed of phyllite, greywacke, limestone with subordinate grit and arkose overlain by limestone, dolomite and arkose and conglomeritic subarkose (Rozendaal *et al.*, 1999).

The *Cango Group* is divided into the Geogamma (older) and Kansa Subgroups (younger), separated by an unconformity. SHRIMP dating of detrital zircons from the Goegamma Subgroup indicates that these sediments were probably derived from the

~1000-1100 Ma Namaqua-Natal Province (Barnett *et al.*, 1997). Cambrian as well as Meso-Proterozoic detrital zircon ages for the Kansa Subgroup above suggest that these sediments are sourced from both the Namaqua-Natal province and the Cape Granite Suite (Barnett *et al.*, 1997). Barnett *et al.* (1997) propose a mid-Cambrian or younger age for the Kansa Subgroup (<518 ± 9 Ma) and suggest it was deposited as a mechanical rift sequence with subsequent thermal subsidence resulting in the deposition of the Table Mountain Group (Cape Supergroup) along a passive margin (Barnett *et al.*, 1997). Frimmel *et al.* (2001) relate the development of the Goegamma Subgroup to tectonic loading in the Gariep and Damara orogenic belts (570-540 Ma). They suggest that the Kansa Subgroup was deposited either in a second foreland basin, or in a pull-apart basin associated with tectonic loading between 510 Ma and the maximum age of the overlying Cape Supergroup.

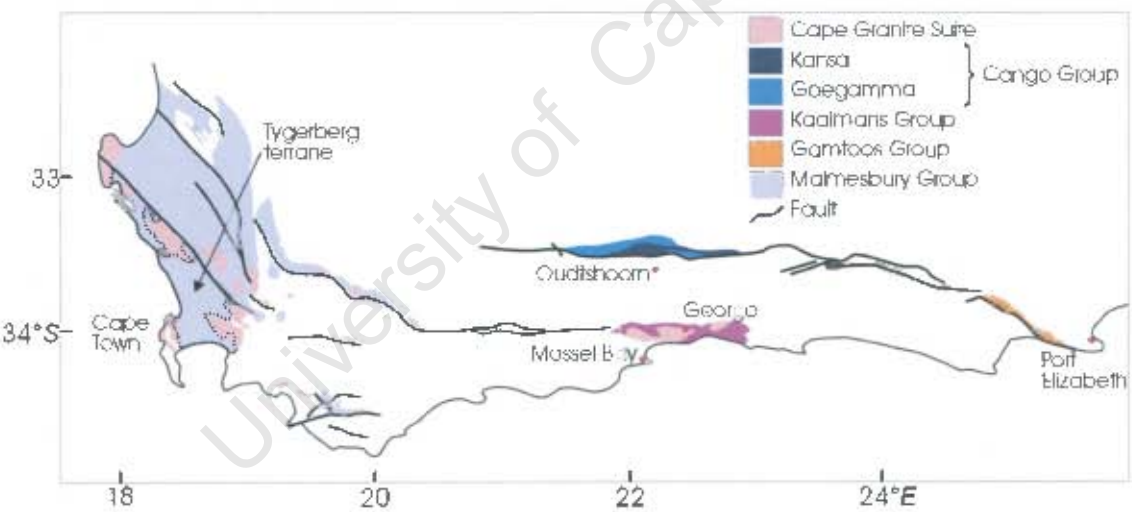

Figure 2.2: Location of inliers and basement to the Cape Supergroup within the Cape Fold Belt (~650-500 Ma) adapted from Rozendaal *et al.* (1999).

2.3 The Cape Supergroup (~500-330 Ma)

The Cape Supergroup is a 6-10 km thick siliciclastic sequence (Broquet, 1992) and is divided into the Table Mountain, Bokkeveld and Witteberg Groups (Figure 2.3). The thick sandstones of the Table Mountain Group were initially deposited along a regionally subsiding shelf (from ~500 Ma) and are either fluvial or marine in origin (Broquet, 1992). The lower Table Mountain Group consists of the Piekenierskloof, Graafwater and Peninsula Formations. The middle Table Mountain Group consists of the glaciogenic Pakhuis tillite and glacial outwash sediments of the Cedarberg Formation (~2-150 m) and is overlain by the Nardouw Formation (1300 m) (Cocks and Fortey, 1986). Lithologies within the Table Mountain Group range from conglomerates and sandstone of the Piekenierskloof Formation to mudstones of the Graafwater Formation, mature quartz arenites of the Peninsula Formation, Pakhuis tillites, Cedarberg shales and the Nardouw quartz arenites. Early Paleozoic plant fossils and trilobites found in the Soom Shale member of the Cedarberg Formation (famous for its giant conodonts, Theron *et al.*, 1990) dates it as late Ordovician to early Silurian in age (Gray *et al.*, 1986, Cocks and Fortey, 1986). The Nardouw Subgroup, based on palcontological evidence is 438-410 Ma (Broquet, 1992).

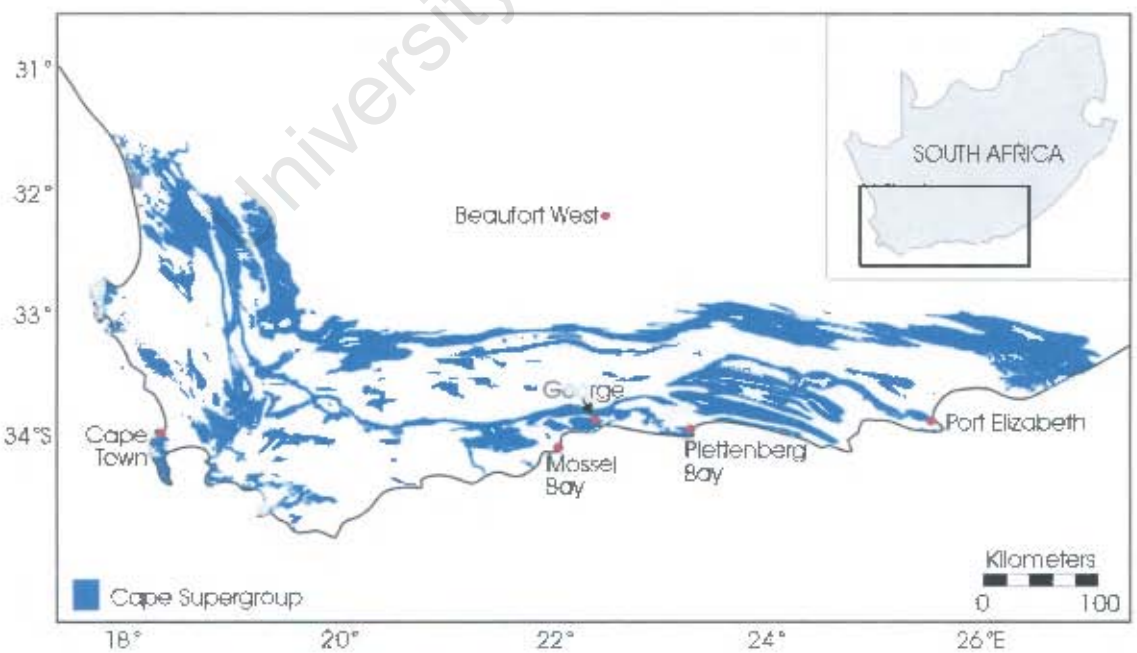

Figure 2.3: Outcrop of the Cape Supergroup (from GIS database of Martini *et al.*, 2001).

The transition from the Table Mountain Group to the Bokkeveld Group (up to 4000 m thick, Broquet, 1992) occurred during a marine transgression assumed to be related to an increase in subsidence rate and/ or an increase in eustatic sea level (Broquet, 1992). The Devonian-aged argillaceous, fossiliferous (~390-375 Ma, Broquet, 1992) Bokkeveld Group was deposited in two marine sub-basins of varying rate of subsidence, resulting in inter-basin thickness difference (Cloetingh *et al.*, 1992). The overlying Witteberg Group (1100-2200 m thick) is composed of equal proportions of sandstone and mudstone and records the last shelf sedimentation, prior to the onset of the Dwyka glaciation, the Cape Fold Belt orogeny and associated Karoo foreland basin (Broquet, 1992).

2.4 The Karoo Supergroup (~310-183 Ma)

The Karoo Supergroup spans 130 Myrs, from the glacial Dwyka tillite deposited in the late Carboniferous to the Drakensberg basalts which extruded in the Jurassic. The outcrop of the Karoo Supergroup dominates the geological map of South Africa (Figure 2.4) and Karoo rocks are preserved in the main Karoo Basin as well as several smaller basins.

The main Karoo basin has been modeled as a retro-arc foreland basin formed in response to orogenic loading and unloading in the Cape Fold Belt to the south (Johnson *et al.*, 1996, 1997, Cole and Wipplinger, 2001; Catuneanu *et al.*, 1998, 2002). Turner (1999), however, asserts that a foreland model for the upper Karoo Basin does not fit the stratigraphy, stacking patterns and succession ages of the Karoo. His model requires extension in this latter time interval and proposes that extension may have been caused by plume-related uplift preceding the Karoo basalt extrusion at 183 Ma by up to 40 Myrs (Turner, 1999).

The Cape Fold Belt formed during crustal shortening associated with the subduction and accretion of the paleo-Pacific plate beneath the Gondwana plate (de Wit and Ransome, 1992). Hälbich *et al.* (1983) proposes 4 phases of deformation associated with Cape Fold Belt orogeny between ~280 Ma and 215 Ma. Gresse *et al.* (1992) identify 5 pulses of deformation between 294 Ma and 223 Ma. These are, however, based on whole rock K-Ar and ^{40}Ar-^{39}Ar ages.

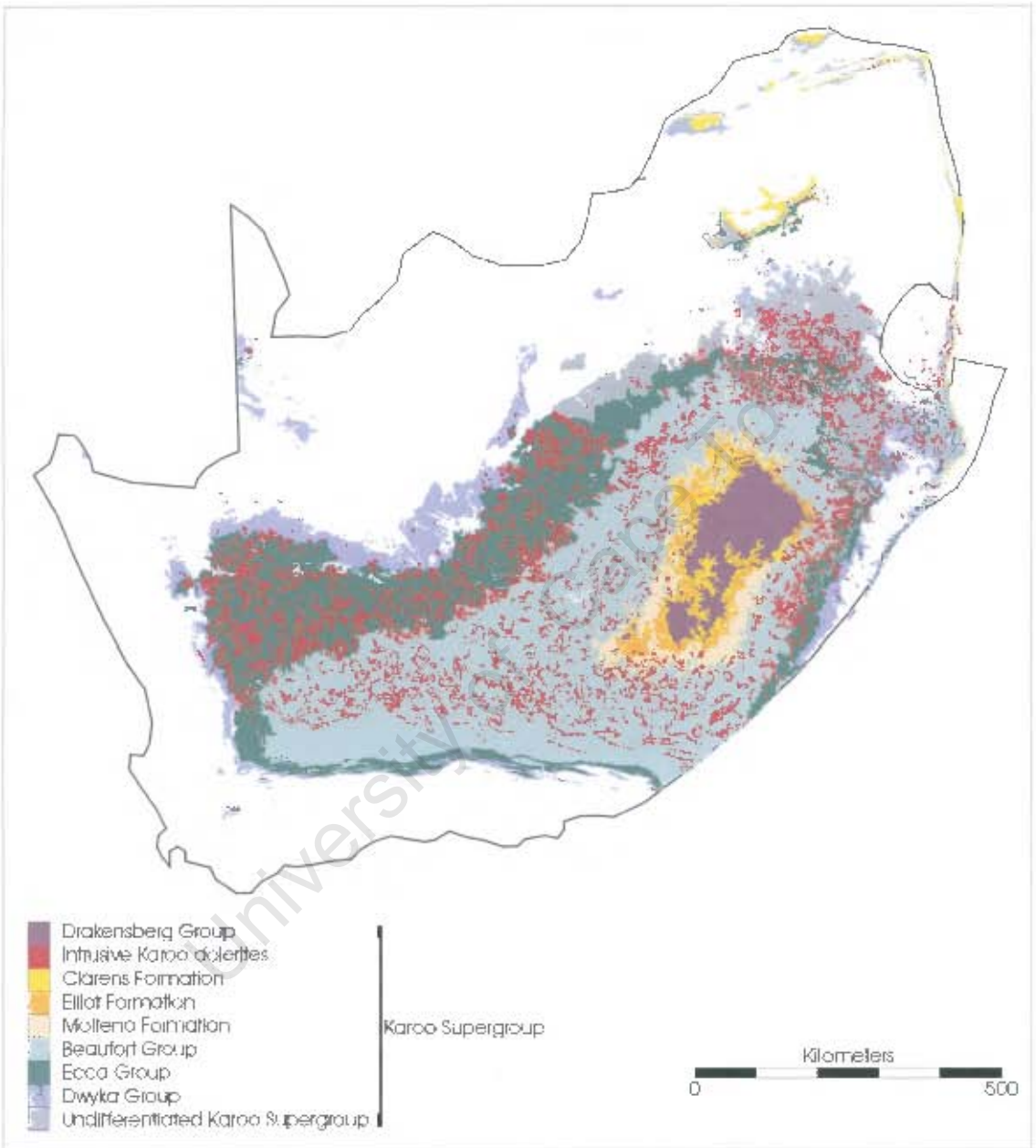

Figure 2.4: Outcrop of the Karoo Supergroup (from GIS database of Martini *et al.*, 2001).

The daughter isotope of this decay scheme, Ar, is highly volatile and is therefore easily lost, particularly when low temperature alteration has occurred. The Ar-Ar technique is also hampered by heterogeneity of the standard used. Renne (1998) performed a high precision intercallibration of the Ar-Ar standards to partially solve this problem. However, since the ages of Halbich *et al.* (1983) are more 20 years old, they should be treated with caution. The Karoo Supergroup in the Main Karoo Basin (excepting the Drakensberg basalts) thickens to the south into the Cape Fold Belt but differs stratigraphically in terms of facies, age, provenance and transport direction from region to region (Catuneanu *et al.*, 1998). Ages of the Karoo sedimentary succession are based on vertebrate paleontology, therefore must be treated with caution. In most of the literature the age-range of stratigraphic groups or subgroups is given as chronostratigraphic stages (e.g. Scythian to early Anisian). Here these stages have been converted to approximate ages based on the timescale of Gradstein *et al.* (2004).

During the early to mid-Carboniferous, southwestern Gondwana was bordered by a broad, relatively stable continental shelf within a passive margin environment (Visser, 1992). Visser (1992) proposed an hiatus in sedimentation of ~30 Ma during which time mountain ice caps expanded to form ice flows and spread from provenances in the north, south and east (Visser, 1989). New paleontological and sedimentological data, however, suggests that the onset of glaciation co-incided with the deposition of the upper Witteberg Group, ~350 Ma (Streel and Theron, 1999). Glacial sedimentation continued (up to 800 m thick) until the early Permian (Visser, 1992). The Dwyka Group is conformably overlain by the black shales of the Prince Albert and Whitehill Formations of the Ecca Group that resulted from the slow suspension settling of mud (Cole, 1992). The Ecca Group and lower Beaufort Group (up to 3000 m thick in the south) are characterised by shales, interbedded with siltstones, sandstones and occasional coal seams, which were deposited in reducing conditions in marine, lacustrine, deltaic and fluvial environments (Johnson *et al.*, 1996). By the time of lower Beaufort Group deposition (Adelaide Subgroup, lower Beaufort Group, ~252 Ma, Groenewald and Kitching, 1995; Kitching, 1995) non-marine conditions extended across the Main Karoo Basin (Catuneanu *et al.*, 1998).

The upper Karoo Group (Tarkastad Subgroup, upper Beaufort Group, Scythian to early Anisian in age, ~245-238 Ma, Groenewald and Kitching, 1995; Kitching, 1995) is

divided into 2 facies, proximal deposition in the southern Karoo Basin and distal deposition in the northern Karoo Basin (Catuneanu *et al.*, 1998). Lithologically, the lower Tarkastad Subgroup ranges from coarse grained sandstones, with minor mudstones in the south to medium-fine grained sandstones in the distal north. The upper Tarkastad Subgroup is composed of upward fining sequences of medium-fine grained sandstone in the south and again, finer grained sandstones, siltstones and mudstones in the north (Catuneanu *et al.*, 1998).

The mid-Triassic to Early Jurassic (Cole, 1992) upper Karoo, Molteno, Elliot and Clarens Formations (here referred to as the Stormberg Group), are characterised by mudrocks, sandstones and conglomerates which were deposited in sub-aerial, fluvial conditions (Johnson *et al.*, 1996). These units together with the upper Beaufort Group are up to 7000 m thick, though significantly thinner relative to the pre-Cape Fold Belt units in the west (Johnson *et al.*, 1996). The Molteno Formation unconformably overlies the Beaufort Group and, according to Catuneanu *et al.* (1998), was deposited as 2 coarsening upward sequences composed of reworked older Dwyka, Ecca and Beaufort sediment (see Chapter 5.1.2 for further discussion). The Elliot Formation (Norian to early Jurassic, Gauffre, 1993, ~215-202 Ma) was deposited distally and is composed of mudstones with an increasing aeolian component as one goes up in the stratigraphy (Catuneanu *et al.*, 1998). Bordy *et al.* (2004) identify a break in sedimentation within the Elliot Formation that is associated with a change in sediment supply and paleocurrent direction (from north to east and northeast). The Elliot Formation is overlain by the Clarens Formation that was deposited in a progressively arid environment (Cole, 1992).

2.5 Gondwana break-up and the Drakensberg Group basalts

It was the recognition of how well the coastlines of eastern South America and western Africa fit together that first stimulated thought on continental drift. The identification of magnetic anomaly patterns preserved in ocean crust helped to prove the concept of sea floor spreading. Aeromagnetic and gravity surveys (c.f. Reeves, 1999) as well as paleomagnetic studies have since improved our understanding of how the continents once fitted together as the supercontinent Gondwana and how, when and in what order Gondwana split apart. What is still not certain is the role of mantle plumes in this supercontinental break-up.

According to Hawkesworth *et al.* (1999) the break-up of Gondwana occurred in 3 stages. The first (~180-156 Ma) resulted in the separation of west Gondwana (Africa and South America) from east Gondwana (Australia, Antarctica, India and New Zealand). This corresponds to regime 1 of Reeves and de Wit (2000) though they propose a later termination of this first stage at 136 Ma. The first oceanic crust formed between Africa and Antarctica at 155 Ma (Jokat *et al.*, 2003) or 156 Ma (Hawkesworth *et al.*, 1999) (Figure 2.5a). ~27 Myrs prior to this at 183 ± 1 Ma ($^{40}Ar/^{39}Ar$ age, Duncan *et al.*, 1997) was the extrusion of a thick (>1650 m, Duncan and Marsh, in press) pile of basalts of the Drakensberg Group, Karoo Supergroup and emplacement of numerous dolerite sills (Figure 2.4; 2.6). The extremely voluminous (~2.5 * 10^6 km^3) Karoo basalts were emplaced rapidly (over 3-5 Myrs) with an average eruption rate of 0.5-1 km^3/yr (Riley and Knight, 2001) over a possible area of ~2 million km^2 (Cox, 1978) (Figure 2.7). The large igneous province extends into Antarctica, therefore may be considerably larger (Encarnación *et al.*, 1996). It has also been suggested that their extrusion is linked to the break-up of Gondwana (Cox, 1992, Duncan *et al.*, 1997; Hawkesworth *et al.*, 1999).

According to Jokat *et al.* (2003), the ~27 Myr separation between Karoo magmatism and the onset of sea floor spreading suggests that the mantle plume responsible for the former was not a trigger for the break-up of Gondwana. However, in the model of Hawkesworth *et al.* (1999) supercontinents 'self destruct' in response to a long term (~120 Myr) build up of heat and magmatism that weakens the lithosphere. According to Hawkesworth *et al.* (1999) the build up of heat makes supercontinents more likely to break-up in response to other regional tectonic forces.

The second stage of Gondwana break-up described by Hawkesworth *et al.* (1999) is the separation of South America from Africa and the Africa+India Plate from Antarctica in the Early Cretaceous (~130 Ma). Their third stage of break-up involves the separation of Australia and New Zealand from Antarctica and the separation of Madagascar+Seychelles from India in the late Cretaceous (~90 to 100 Ma).

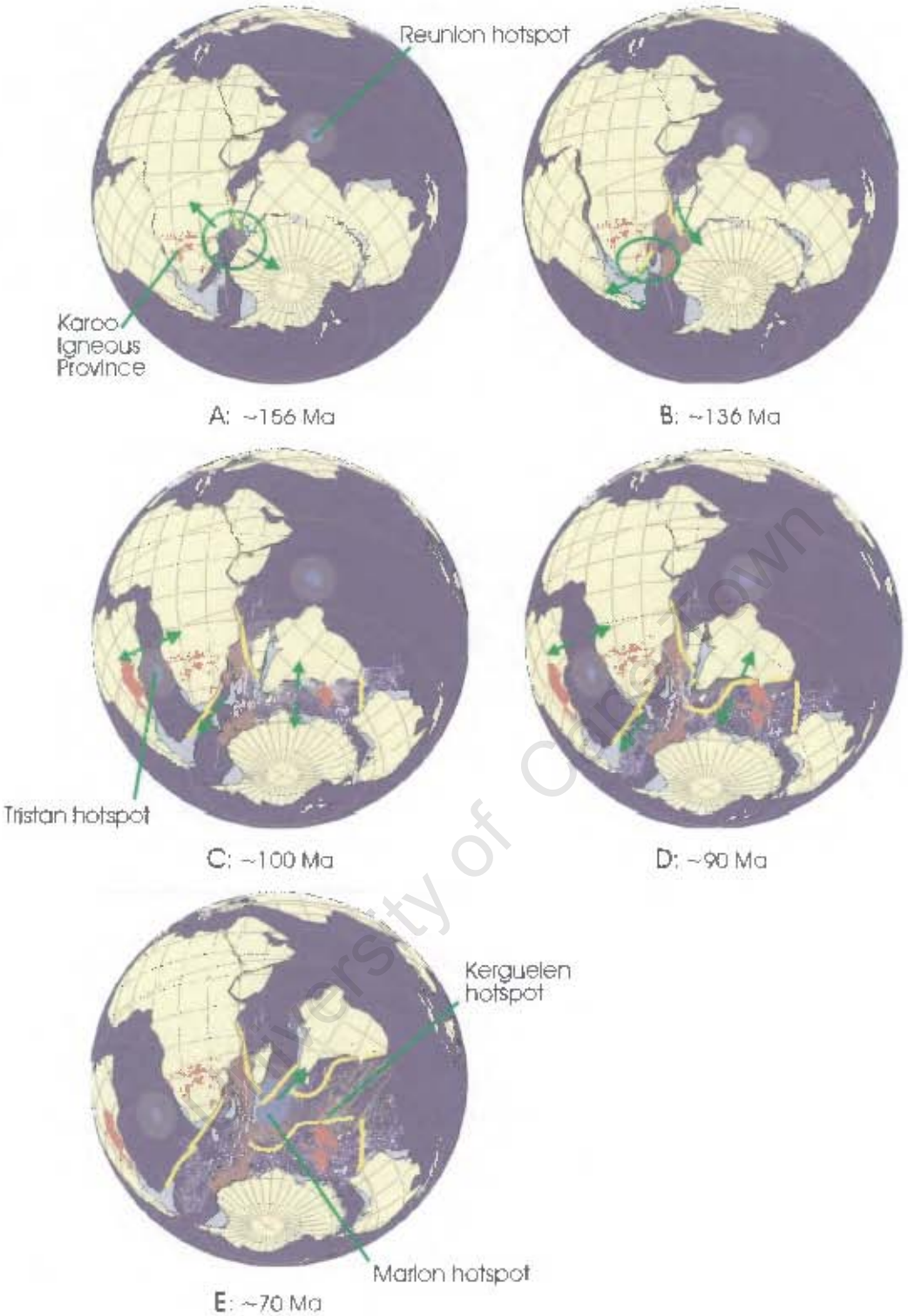

Figure 2.5: Break-up of Gondwana. 'Freeze-frames' taken from a computer animation created by C. V. Reeves (http://kartoweb.itc.nl/gondwana/index.asp) The position of the plates (with specific areas of interest circled in green) at (a) ~156 Ma, when the first ocean crust formed between Africa and Antarctica, (b) ~136 Ma, the initiation of the South Atlantic and beginning of movement of South America westwards along the Falkland Agulhas Fracture Zone. (c) ~100 Ma, (d) ~90 Ma, (e) ~70 Ma (note, India's rapid movement northward).

Reeves and de Wit (2000) consider the break-up of Gondwana from the early (136 Ma) to late Cretaceous (89 Ma) as their regime 2. The position of the plates at ~136 Ma is shown in figure 2.5b. According to their model, the initiation of the South Atlantic begins at 136 Ma as South America began to slide westward along the Falkland Agulhas Fracture Zone. The Paraná-Etendeka lavas are dated at 132 ± 1 Ma ($^{40}Ar/^{39}Ar$ on mineral separates, Renne *et al.*, 1996) and are likely related to the opening of the South Atlantic (Figure 2.7) (Lawver *et al.*, 1999; Hawkesworth *et al.*, 1999).

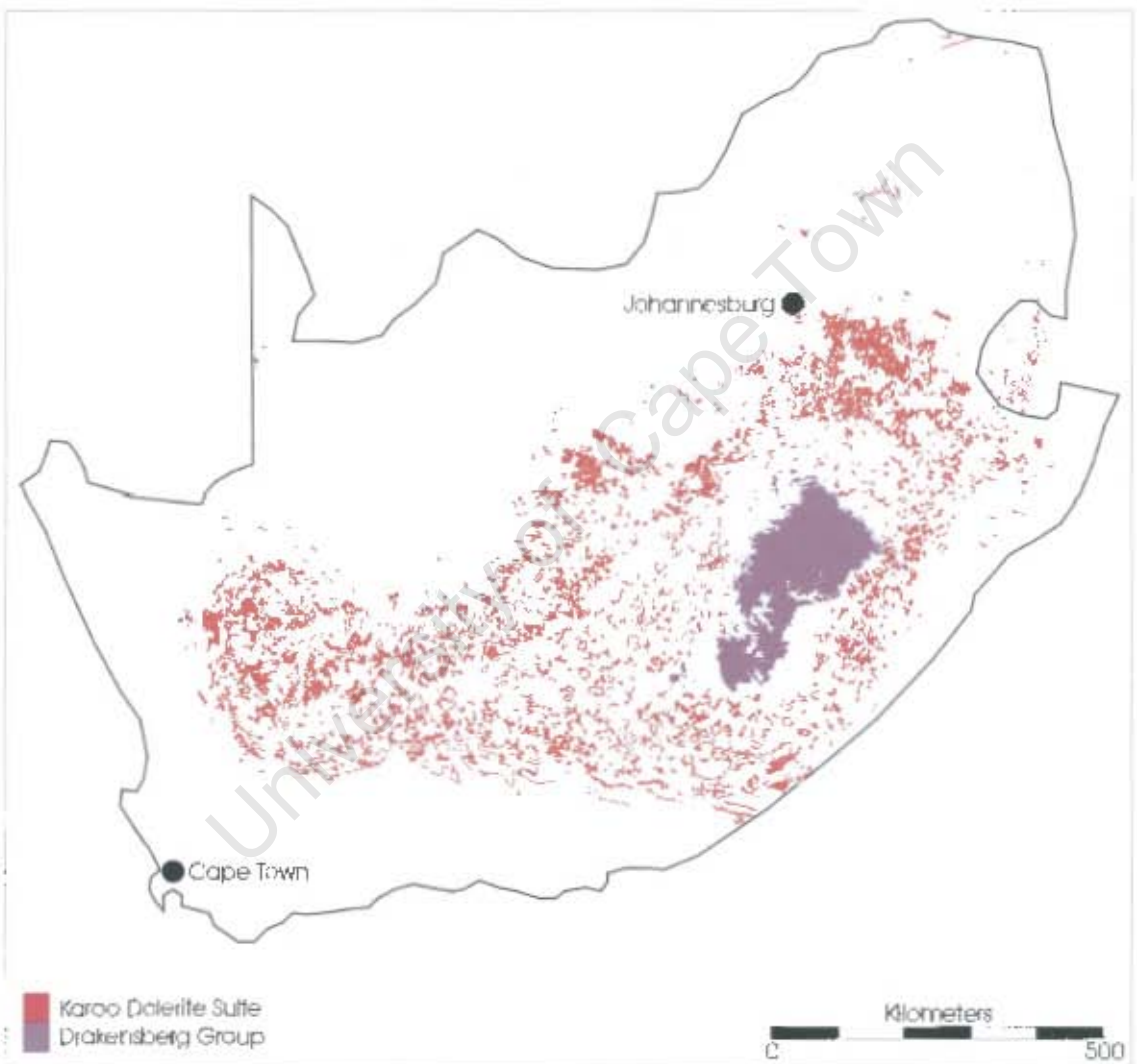

Figure 2.6: Outcrop of Drakensberg Group basalts and Karoo dolerite sills (from GIS database of Martini *et al.*, 2001).

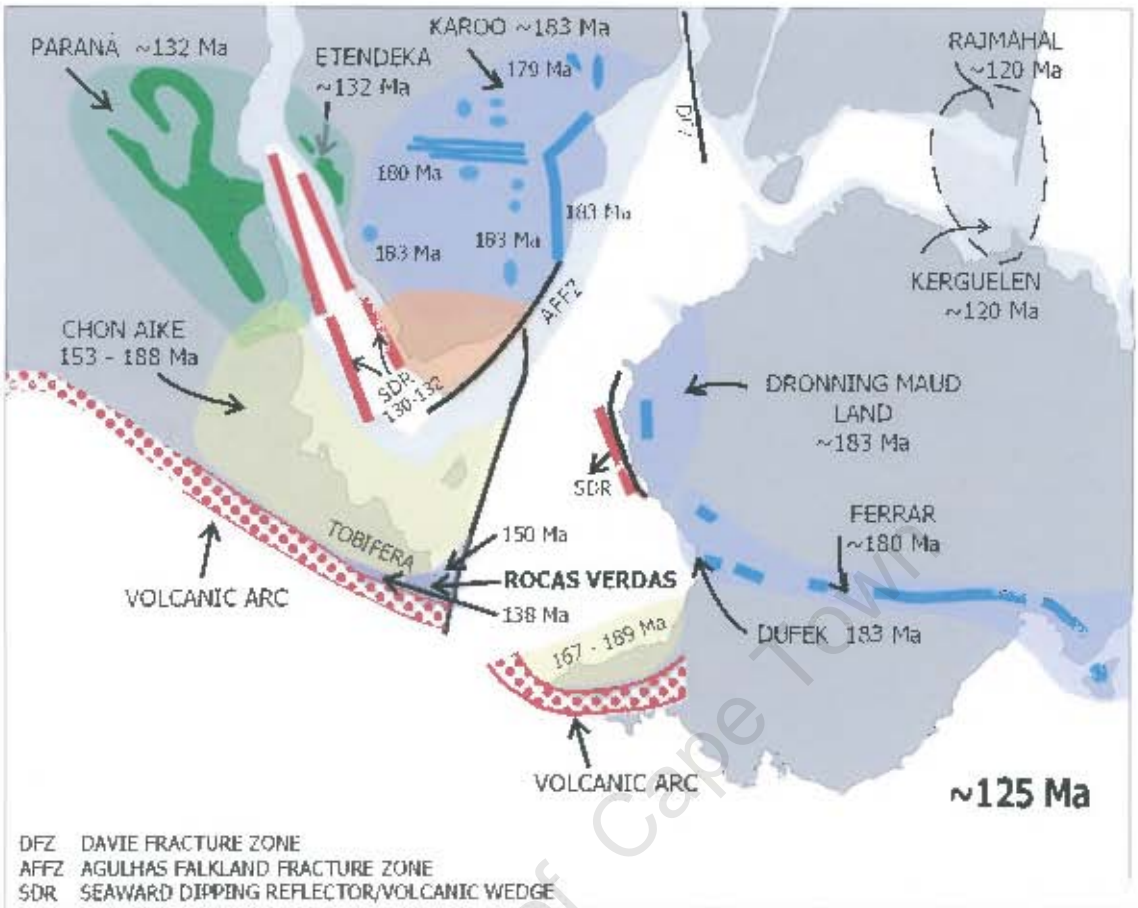

Figure 2.7: Location and spatial distribution of the large igneous provinces. Green= Paraná-Etendeka Province; Blue= Karoo-Ferrar Province; Yellow= Tobifera Province. Red lines= Seaward dipping reflectors. Orange= the southern Cape area of interest (from Stern and de Wit, 2003).

In the mid-Cretaceous, Antarctica continued to move away from Africa, and South America from Africa. Figure 2.5c shows the plate positions at 100 Ma. From the late Cretaceous (~89 Ma) India began to move rapidly north (Reeves and de Wit, 2000). Figure 2.5d and e show the plate's positions at the start and during India's move northwards at 90 Ma and 70 Ma, respectively. Although not shown on figure 2.5e the Madagascar flood basalts are dated at 88 ± 1 Ma (^{40}Ar-^{39}Ar, Storey *et al.*, 1995) and are possibly related to the Marion plume which may have played a role in the break-up of Madagascar and India (Storey, 1995).

The Deccan traps of India are dated at 65.6 ± 0.3 Ma (Re-Os, Allègre *et al.*, 1999) and also may be related to continental break-up, this time between the Seychelles and India (Hawkesworth *et al.*, 1999).

Reeves and de Wit (1998, 2000)'s fourth phase of Gondwana break-up starts at ~43 Ma when a triple junction developed in the South Indian Ocean separating the African, Antarctica and Australia+India plates.

2.6 Onshore Mesozoic Basins: The Uitenhage Group (~145-130 Ma)

Rifting associated with continental break-up may be controlled by prior orogenic structures that were reactivated in successive periods of extension (de Wit, 1992). Crustal extension during Gondwana break-up resulted in the inversion of several east-west trending, formerly compressional faults (associated with the Cape Fold Belt orogeny) creating several onshore and offshore, extensional basins (de Wit, 1992).

The Heidelberg/Riversdale basin is one example of a taphrogenic basin along the discontinuous Worcester/Pletmos basin line of half grabens which extends E-W over ~400 km (Dingle *et al.*, 1983; Viljoen, 1992) (Figure 2.8). These basins are bounded to the north by normal faults (e.g. the Worcester Fault, Figure 2.8) that are down faulted to the south (Viljoen, 1992). These faults are likely to be listric faults. Seismic reflection profiling has imaged the offshore extensions of faults of similar age and trend (e.g. the St Croix Fault and the Gamtoos Fault, see Figure 6.8) and clearly shows their listric geometry. Onshore, to the north of the Worcester/Pletmos line of basins is the Cango Fault that bounds the Oudtshoorn Basin. Episodic movement along this bounding listric, growth fault created accommodation space that was continuously filled by the poorly sorted Enon Formation (Uitenhage Group) to form the Cretaceous Oudtshoorn Basin (Figure 2.8). The onshore Mesozoic sediments of the Uitenhage Group are confined to these fault-bounded basins along the Cape Fold Belt (Figure 2.8) (McLachlan and McMillan, 1976).

According to paleontological evidence (ammonites), the marine Sundays River Formation of the Uitenhage Group (Figure 2.8) is Upper Valanginian to Hauterivian in age (McLachlan and McMillan, 1976, ~140-130 Ma). McLachlan and McMillan (1976) propose a Lower Valanginian to Berriasian age for the Enon and Kirkwood Formations (~144-137 Ma). McLachlan and McMillan (1976) claim that no Uitenhage Group sediments of Jurassic age have yet been dated. The only available radiometric age is 162 ± 7 Ma for the underlying Suurberg Group, which is a K-Ar whole rock age from a single basalt sample that is unpublished and therefore unreliable (radiometric

age mentioned in McLachlan and McMillan, 1976). Apart from the uncertainty inherent in K-Ar whole rock analysis, McLachlan and McMillan (1976) emphasize caution in using this age as a maximum for the Uitenhage Group as there may have been an erosional or non-depositional break between the two groups.

Detailed discussion of the formation of the *offshore* basins resulting from Gondwana break-up is included in Chapter 6.

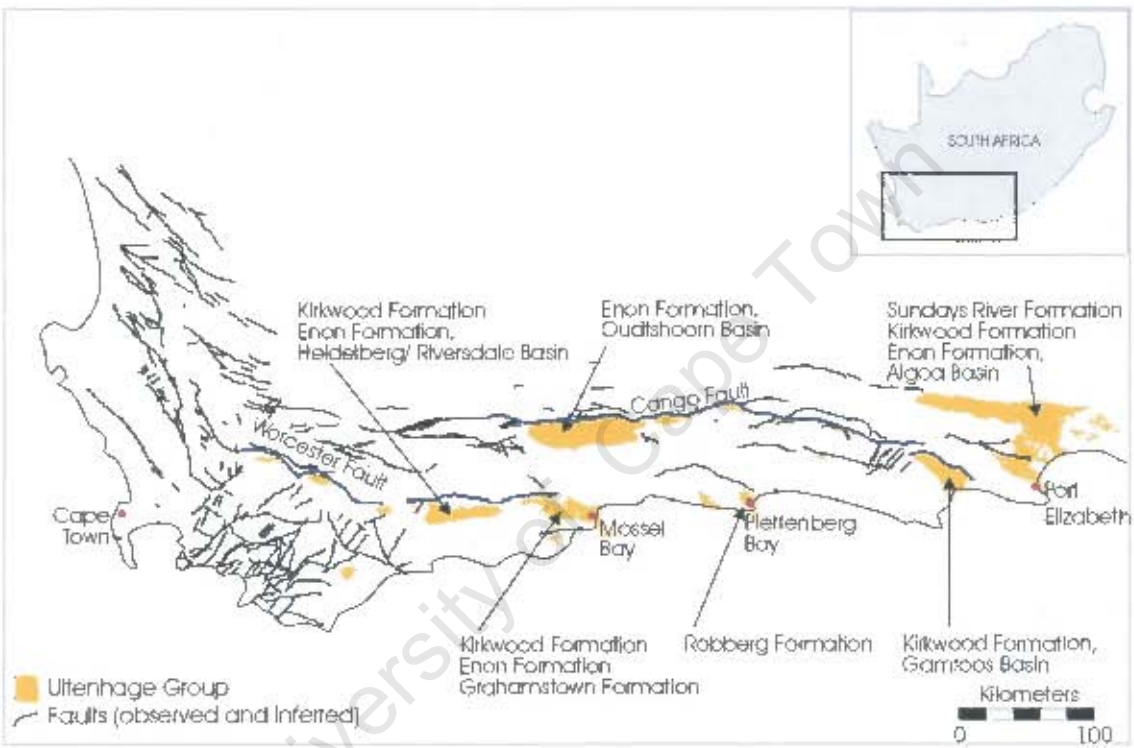

Figure 2.8: Southern Cape Mesozoic outcrop, Uitenhage Group and faults (from GIS database of Martini *et al.*, 2001 and McLachlan and McMillan, 1976).

2.7 Cenozoic Geology

The Cenozoic paleo-climate of southern Africa was dry and cool relative to the warm, humid Cretaceous (Dingle *et al.*, 1983; Partridge and Maud, 2000). Onshore the Cenozoic rock record is sparse (Figure 2.9a). Cenozoic outcrop includes the Kalahari Basin in the north, Mio-Pliocene beach terraces along the west coast and limestones along the south coast and carbonates, shales, sandstones and evaporates in northern Kwazulu-Natal, southern Mozambique. Cenozoic-aged silcretes are widespread around South Africa (Figure 2.9a). In the southern and south western Cape remnants of

ubiquitous silcrete-capped terraces can be seen capping broad Tertiary paleo-river valleys linking adjacent quartzite ridges of the Cape Fold Belt (Figure 2.9b).

The Kalahari Basin is a large (>2.5 million km^2, Haddon, 2000), flat intracontinental depression of internal drainage, fed mainly from the Okavango River and tributaries (Stankiewicz and de Wit, 2005a,b,c). The Kalahari Group is >300 m thick (Haddon, 2000). A seismic line, extending ~NE-SW across the Northern Cape to the South African-Botswana border (Figure 2.9a), images a fluvial channel at the base of the Kalahari Group (Tinker, 2001; Tinker *et al.*, 2002). Partridge and Maud (1987) propose that Kalahari sedimentation began in the end Cretaceous. This is supported by the presence of fluvial channels which suggests that the climate in this region was wet at the onset of Kalahari sedimentation, as it was in the end Cretaceous (Wilson and Norris, 2001, Poulsen, 2004, Jenkyns *et al.*, 2004). Alternatively, fluvial channels at the base of the Kalahari Group may have been produced by a river that originated in a wetter area upstream and then flowed through a more arid area downstream, like today's Orange River (Haddon, 2000).

Along the west coast, relative sea level oscillations, fluvial activity and climatic fluctuations have aided in the creation of a wide bevelled surface that stretches up to 80 km inland (Pether *et al.*, 2000). Oligocene marine regressions have eroded most evidence of Paleogene sea level highs (Pether *et al.*, 2000). The highest preserved evidence of maximum sea level (~90 m) is a product of Miocene-Pliocene transgression (Rogers, 1980). Cenozoic deposition along the southern and south eastern coasts ranges from littoral marine, estuarine, lacustrine to eolian in origin and, like the west coast, is characterised by marine transgressions and regressions (Maud and Botha, 2000). Along the south coast Miocene to Pliocene-aged limestones of variable thickness (up to 150 m) outcrop along a narrow strip, ~10km wide (Dingle *et al.*, 1983).

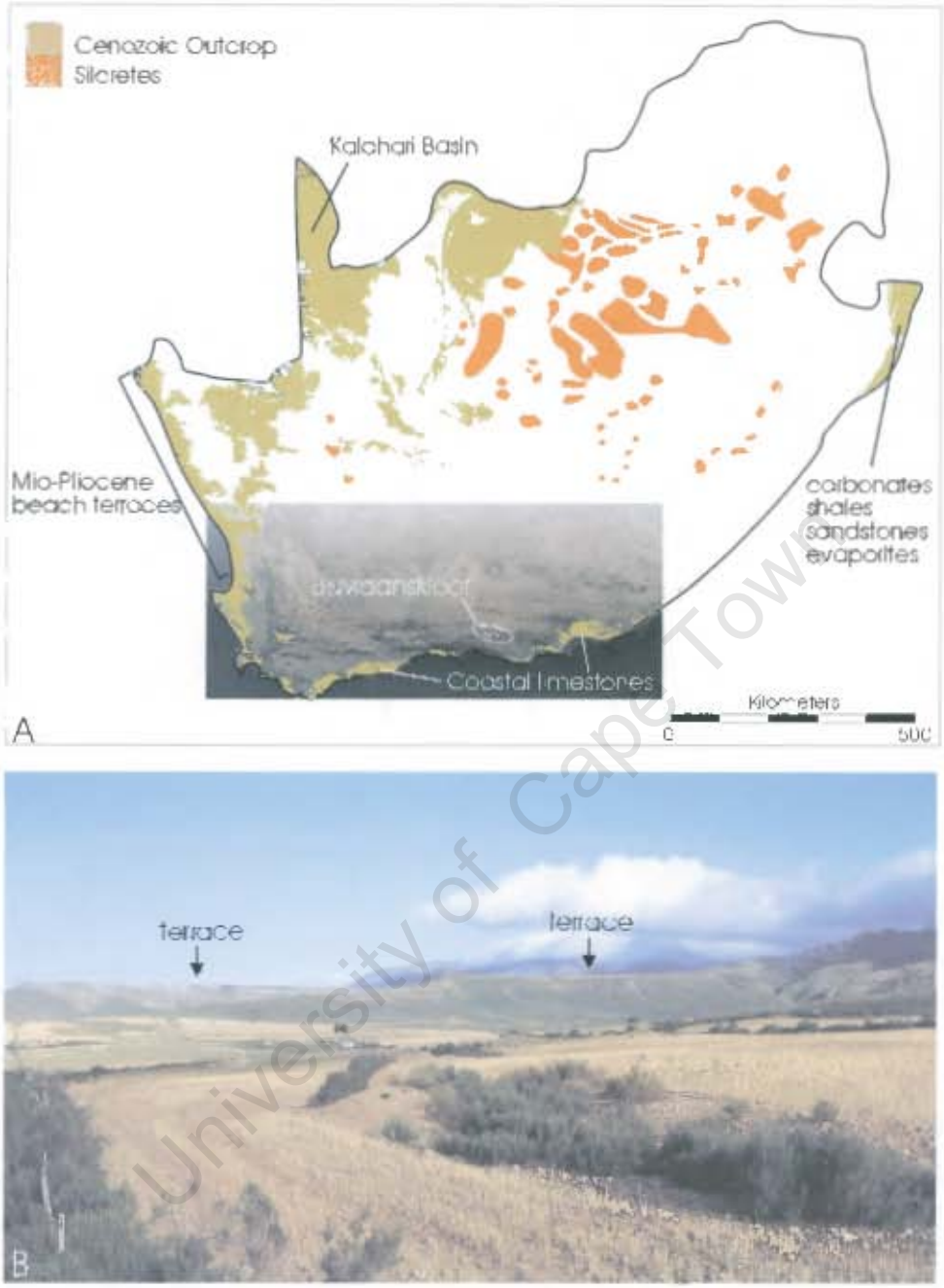

Figure 2.9: (A) The distribution of Cenozoic outcrop (from GIS database of Martini *et al.*, 2001) and silcretes (from CIGCES data base, University of Cape Town). (B) One of many silcrete-capped terraces capping Tertiary paleo-river valleys within the Cape Fold Belt (from Baviaanskloof, location marked in A).

Chapter 3: Southern Africa's Regional Geomorphology

3.1 Introduction

The southern African landscape is characterised by two regional terrains separated by the steeply dipping Great Escarpment. The escarpment is an erosional scarp cutting a variety of rocks types along its considerable length (~1400 km in South Africa). To the south of the escarpment is the coastal terrain, with a relatively high relief (~500 m) and low average elevation. This terrain is drained by short, parallel (occasionally meandering) rivers oriented ~perpendicular to the coastline or in the case of the south coast, occasionally parallel to it and parallel to prominent Cape Fold Belt ridges. The inland terrain of high average elevation comprises a peneplain of relatively low relief (~250 m) with dendritic rivers that connect with the coastal rivers (Gilchrist *et al.*, 1994). The origin of the Great Escarpment and South Africa's form as a whole has been debated since the 1940's and several models have been suggested for its geomorphological development. Early studies are reviewed in Partridge and Maud (1987 and 1988). This chapter reviews various models for landscape evolution, paying particularly attention to the formation and evolution of the Great Escarpment. Numerical models of passive margin evolution are also briefly discussed along with the evidence with which these models are tested.

3.2 The classical polycyclic model for landscape and escarpment evolution

In the 1950's Lester C. King evolved his classical concept of 'erosional cycles' to explain southern Africa's geomorphological evolution. In this model, topography evolves in response to rapid uplift followed by long periods of backwearing, leading to the development of planation surfaces. In King's view, the South African margin, the Great Escarpment, is created by the downflexing of the lithosphere creating a broad monocline that is subsequently eroded by backwearing (King, 1963) (Figure 3.1A). King (1953, 1962 and 1963) proposed that the southern African landscape is characterized by pediplanation (backwearing) formed by parallel retreat of the escarpment following relative base-level falls.

King recognised several regional surfaces across Africa that, in his view, are the product of various cycles of erosion. The oldest and second oldest of these surfaces he

named the 'sub-Karoo Surface' and 'Gondwana Land Surface', respectively. The latter, he claimed, is a product of Gondwana-wide erosion to base level in the Jurassic. Partridge and Maud (1988) who have retained King's framework of erosional cycles in their geomorphological analysis (see below), claim that they cannot find any evidence for the preservation of erosional surfaces dating from before Gondwana break-up.

King recognised a third continent-wide planation surface that he termed the 'African surface'. This surface, he claimed, was formed during a phase of crustal quiescence in the late Cretaceous to mid Tertiary (King, 1963). King argued that his African Surface had been deeply weathered resulting in the development of silcretes, laterites and calcretes. He proposed uneven late-Cenozoic uplift that caused erosion in some areas and deposition in the Kalahari basin. King (1963) also called for a doming movement in the late Tertiary (Plio-Pleistocene) that produced central uplift and the outward tilting of marginal regions causing deep river incision responsible for South Africa's present form.

King (1963, 207) claimed that during the African peneplanation: "rocks as different as friable schists, hard ironstones, readily-weathered granites, tough epidiorites and weak Karroo strata were bevelled alike". In fact, lithology plays an important control on landscape morphology (Wellington, 1955). The flat topped 'koppies' (hills) of the Great Karoo region of South Africa are one example of how competent, hard dolerite sills 'protect' the softer Karoo sediment beneath from erosion. As Burke (1996) cautions: "An inherent and unavoidable weakness is that the development and preservation of a weathered rock surface depends on many variables besides the timing of a particular weathering episode" (Burke, 1996, 366).

The concept of a single long-lived erosion surface itself is not without criticism. Newly available cosmogenic data (obviously not available to King in the 1950's) from the low relief Drakensberg summit show that while denudation rates are low, they are sufficient to prevent the intact preservation of even this, hard, erosion-resistant surface over geological time (Fleming *et al.*, 1999).

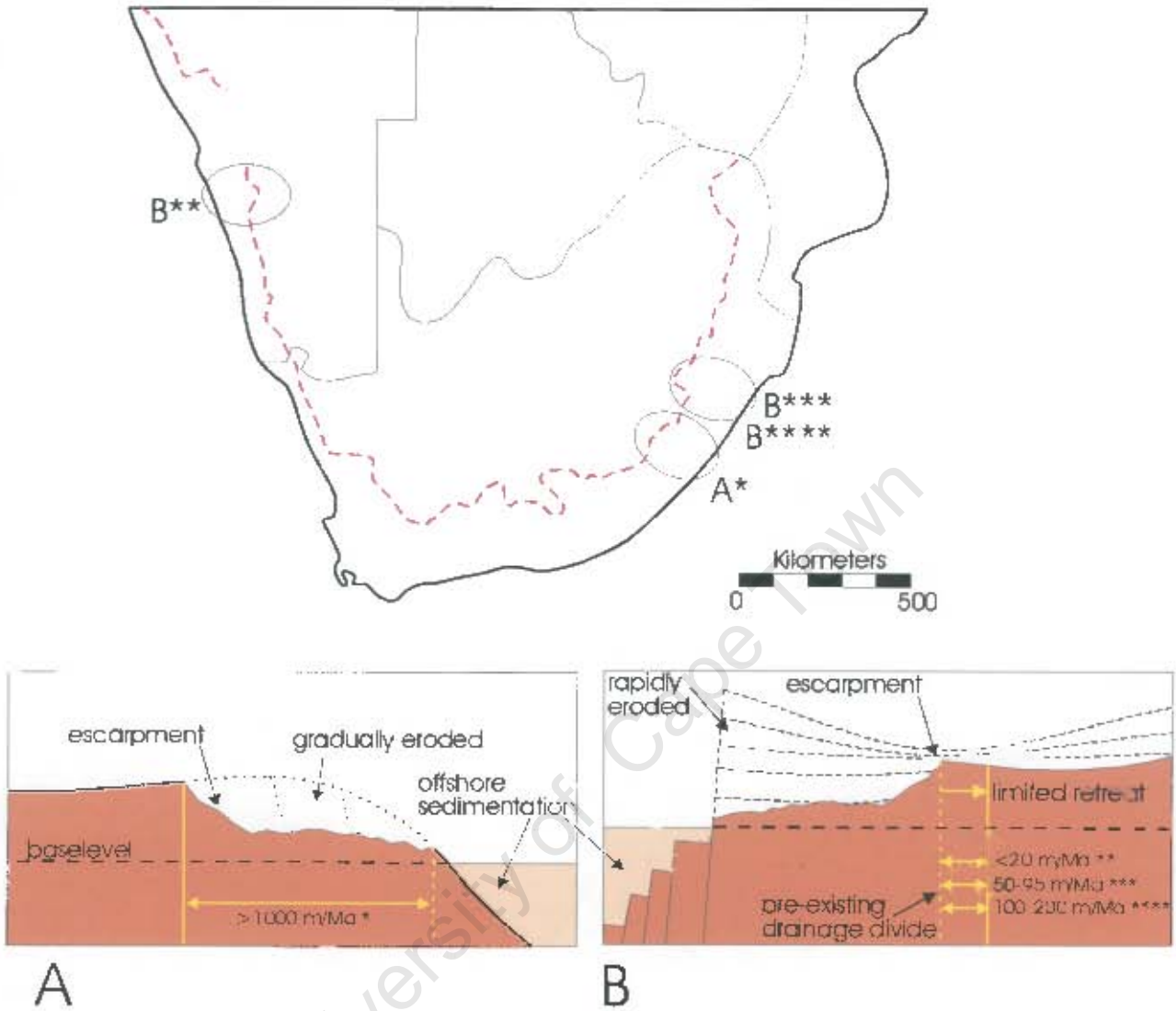

Figure 3.1: Models for escarpment formation based on the work of King, and on fission track thermochronology and cosmogenic isotope analysis. (A*) Downwarp model of escarpment formation, as proposed by King (1962). Escarpment forms by 'backwearing' during relative base level falls; (B) Pinned divide model. Here the escarpment, originally formed at the coast, is rapidly destroyed by fluvial incision to reform at a preexisting (i.e. pre-rift) drainage divide. The Namibian escarpment has retreated at <20 m/Ma since the end of the Eocene (** Cockburn *et al.*, 2000). The Drakensberg escarpment has retreated at 50-95 m/Ma over the last 1 Ma (*** Fleming *et al.*, 1999) to 100-200 m/Ma from when it became pinned at the drainage divide, shortly after rifting (**** Brown *et al.*, 2002). Model figures adapted from Gallagher and Brown (1999a).

King's framework of erosional cycles was retained by Partridge and Maud (1987). However they disagree with the correlation of single surfaces across the entire continent width, as King suggested. Partridge and Maud (1987) identify three erosional surfaces: King's African surface (Late Jurassic/ early Cretaceous to end of early Miocene, ~18 Ma) and post-African surfaces I (Early mid-Miocene, ~18 Ma to late Pliocene, ~2.5 Ma) and II (late Pliocene, ~2.5 Ma to Holocene).

Partridge and Maud (1987) correlate the African surface above and below the escarpment. In the southern Cape, south of the escarpment they claim (based on field evidence), that the African surface cuts across the Enon conglomerate. The identification and correlation of surfaces based on morphological or sedimentological characteristics has been criticized (Summerfield, 1996, Brown *et al.*, 2000, van der Beek *et al.*, 2002) and in this particular example even the age of the underlying Enon Formation is still uncertain (McLachlan and McMillan, 1976). Without absolute ages on these surfaces their designation as part of the "African surface" is unconvincing.

Like King, Partridge and Maud (1987) argue that the escarpment formed after continental rifting where a pre-existing upwarped hinterland was subject to new oceanic base levels. These new base levels created an erosional face that then receded rapidly mostly parallel to the continental margin in the Cretaceous. Thus, erosion that produced the 'African surface' continued until the Miocene, but was at a maximum in the late Jurassic to Cretaceous (Partridge and Maud, 1987). Partridge (1998) uses river-pebble evidence from Matthews (1978) to suggest that the escarpment was <20 km from its present position by the end of the Cretaceous. Major Cretaceous erosion was assisted by a warm, humid climate (Partridge, 1998, de Wit, 1999) and led to a large terrigenous, organic component in marine sequences, eventually creating oil/ gas reserves offshore. By the end of the Cretaceous almost all the terrestrial Cretaceous rock had been eroded from the southern continent.

3.3 Numerical modelling to evaluate escarpment formation

The acceptance of plate tectonic theory in the 1960's resulted in the proposal of alternative tectonic controls on the development of continental margins and escarpment formation.

Gilchrist *et al.* (1994) offer a model of landscape development that has abandoned the concept of landscape cycles, concentrating rather on marginal tectonics during rifting and the evolution of the drainage systems. This hinges on Gilchrist and Summerfield's (1990) model of the development of a marginal topographic upwarp by flexural isostatic uplift due to differential denudation. According to Gilchrist *et al.* (1994), extension associated with rifting causes initial localised subsidence and sedimentary basin formation which lowers the base level of fluvial systems draining into the rift. Rift flank uplift may deflect the existing drainage pattern, reorienting it into two new fluvial systems, one draining into the rift (exterior catchment) and the other deflected away from the rift, inland (interior catchment). Along the rift margin, base level is dramatically lowered, causing fluvial incision and catchment growth by retreat of headwaters, thereby forming a terrain of high relief. Inland, base level is not significantly lowered, therefore relief is low (Gilchrist *et al.*, 1994).

Denudation of the exterior catchment areas results in isostatic uplift of those areas, thus in turn reducing the lowering effect of denudation and maintaining the elevation of the exterior catchments. Interior drainage systems feed the inland basins (eg. Kalahari Basin) where relatively small volumes of sediment are deposited relative to that which accumulates in the coastal rift basins (Gilchrist *et al.*, 1994).

According to the model of Gilchrist *et al.* (1994), as the catchment divide retreats inland, the exterior rivers compete to capture upland regions of adjacent catchments. The largest drainage areas grow fastest head ward, towards the interior. At a point these large rivers may breach the marginal divide and capture the interior drainage. In their model, the further development of these drainage systems depends on the occurrence of renewed tectonic activity, intrinsic strength of the rocks (presence of joint fractures, faults) and climate (Gilchrist *et al.*, 1994).

Several authors have developed numerical models to uncover the controlling factors in the evolution of rift margins (e.g. Gilchrist *et al.*, 1994; Kooi and Beaumont, 1994; Van der Beek *et al.*, 2002).

Gilchrist *et al.* (1994) numerically model scenarios depicting how an escarpment may form under varying climate, lithology, antecedent topography and lowered baselevel of

the interior catchment. They conclude that several styles of landscape evolution fit their observations including regular escarpment retreat (as King suggested). Kooi and Beaumont (1994) likewise model the evolution of an escarpment associated with a rift margin and find that antecedent topography (or the pre-break-up topography of the margin) is a principal controlling factor. Other principal controls include the timescale of fluvial entrainment, the flexural response of the lithosphere to denudation and the efficiency of sediment transport processes (Kooi and Beaumont, 1994). A further conclusion drawn from their model is that erosion resistant cap rock is not an *essential requirement* for an escarpment to form/retreat (Kooi and Beaumont, 1994).

Van der Beek *et al.* (2002) use fission track (Brown *et al.*, 2002) and cosmogenic exposure data (Fleming *et al.*, 1999) in their numerical model for landscape development across the southeastern African margin. Like Gilchrist *et al.* (1994), Van der Beek *et al.* (2002) find that antecedent (prebreak-up) topography is a fundamental controlling factor on the evolution of a rift margin. Secondary controls include lithospheric rheology, crustal lithological variations and baselevel falls in the interior (Van der Beek *et al.*, 2002). In their model a pre-existing high elevation inland plateau is rapidly eroded by rivers flowing seaward from a drainage divide only ~20-30 km seaward of its present position. In this model the escarpment is formed close to its current position experiences limited retreat since rifting (Van der Beek *et al.*, 2002).

3.4 Pre-rift topography

Little is known of the paleo-topography of southern Africa pre-break-up. Gilchrist and Summerfield (1990) calculate a high pre-rifting elevation of the Atlantic draining catchment area of South Africa of ~1200 m. This is based on reloading the calculated volume of sediment preserved off the west coast (Gilchrist and Summerfield, 1990) onto the present-day mean elevation of Atlantic-draining catchments and allowing for adjustment by Airy isostasy (Gilchrist and Summerfield, 1990).

Present-day African topography is bi-modal, i.e. the southern and eastern regions have high average elevation (>1000 m) and the central and western regions have low average elevation (<500 m). The south-east region of the African plate (including oceanic lithosphere) of anomalously high elevation (and shallow bathymetry, respectively) has been termed the termed the 'African Superswell' (Nyblade and

Robinson, 1994). The cause of the African Superswell is poorly understood and theories, summarised in Doucouré and de Wit (2003), include uplift due to a thermal perturbation of the lithosphere (Nyblade and Robinson, 1994), upwelling from the core-mantle boundary (Lithgow-Bertelloni and Silver, 1998), the presence of a large-scale positively buoyant structure within the mid-lower mantle (Gurnis *et al.*, 2000), a plume (Ebinger and Sleep, 1998) or numerous plumes (~40, Burke, 1996). Burke's explanation requires the African plate to have come to a standstill relative to mantle circulation (Burke, 1996).

The age and evolution of the African Superswell is still debated. The prebreak-up topography of Africa as a whole is investigated by Doucouré and de Wit (2003). From the poor correlation of African free-air gravity and surface topographic maps, they claim that the broad African uplifts, described above, are not crustal features. Doucouré and de Wit (2003) produce a normalised pre-Cretaceous topography of Africa (maximum elevation of ~750 m) by calculating a trend surface of its present-day topography and then removing the topographic effects of surface features younger than the Cretaceous, also taking eustatic sea level changes and erosion into account. Doucouré and de Wit (2003) find that at least some of the bimodality of Africa's topography was already in existence in the late Mesozoic.

Significant denudation of the southern African land surface in the Cretaceous, described in this section, may be indicative of the onset of the African Superswell. More detailed discussion based on new data follows in chapter 7.

Whether the escarpment first formed at the margin and rapidly retreated (Partridge and Maud, 1987), or whether it formed close to its current position and has retreated only ~20-30 km since then (Van der Beek *et al.*, 2002) the commonly held view (excepting Burke, 1996, section 3.9) is that major erosion and denudation across southern Africa was over by the end Cretaceous. This is supported by a wide range of evidence including calculation of offshore sediment volume (boreholes and seismic stratigraphy), apatite fission track thermochronology, cosmogenic isotope analysis and the differential erosion of Kimberlite pipes.

3.5 Calculating erosion rates using offshore sediment volumes

In-depth studies of the offshore basins of the south and east coast of South Africa, using paleontological and seismic evidence, points to very thin deposition of Tertiary and Quaternary sediment (65-0 Ma) mostly consisting of claystones (Brown *et al.*, 1995, McMillan *et al.*, 1997, McMillan, 2003). For example, sediment accumulation estimates from the west coast suggest a decrease in source area erosion rate for the Atlantic-draining catchment areas for the latter Cenozoic, from 41-82 m/Ma (~152-113 Ma) to 7-9 m/Ma (~37-0 Ma) (Rust and Summerfield, 1990). The west coast offshore sedimentary record suggests an average denudation of ~1.8 km across the Atlantic draining catchments of southern Africa since rifting (Rust and Summerfield, 1990). Similar decreases in sediment accumulation from the Cretaceous to the present for South Africa's west coast have been calculated by Brown *et al.*, (1990) and for offshore Namibia (Gallagher and Brown, 1999b) (see chapter 6.4).

The reduction in offshore sediment accumulation in the Tertiary on South Africa's continental shelves implies a reduction in onshore denudation. The distribution of sediment along the south coast is discussed in detail in Chapter 6.

3.6 Calculating erosion rates using apatite fission track thermochronology

Apatite fission track thermochronology has the potential to solve geomorphological problems relating to shallow crustal movements due to the low temperature at which the fission tracks begin to accumulate (Chapter 4.1). Fission track studies involving borehole and outcrop samples have been undertaken for the southeastern margin (Brown, 1992, Brown *et al.*, 2002), southwestern margin (Brown *et al.*, 1990, Brown, 1992, Gallagher and Brown, 1999a, Brown *et al.*, 2000) and across the Kaapvaal Craton (Brown, 1992). Based on apatite fission track analysis of borehole and outcrop samples from south-western Africa, Brown *et al.* (1990) propose rapid cooling related to accelerated denudation in the early Cretaceous for this region. Thermal modelling of borehole QU1/65, north of the escarpment (see Figure 4.23 for location), using an estimated paleogeothermal gradient of 30°C/km (measured in a borehole, ~200 km to the east) gives a total denudation of ~3 km (Brown *et al.*, 1990). Uncertainty in the paleogeothermal gradient is acknowledged by Brown *et al.* (1990) who quote a second estimate of ~20°C/km, measured from an area between Upington and the Atlantic coast. Required denudation using this latter paleogeothermal gradient is ~5km (Brown

et al., 1990).

Gallagher and Brown (1999b) take these data further and propose that as well as accelerated denudation around the time of Gondwana rifting, a further period of accelerated denudation occurred around 90-70 Ma, which is unlikely to be related to rifting (Gallagher and Brown, 1999b). Brown *et al.*, (2002) propose that the south-eastern margin has undergone a minimum of 4.5 km denudation since rifting at ~130 Ma. Like the south-western margin, thermal modelling of boreholes indicates that accelerated denudation occurred in the early Cretaceous. This was followed by accelerated denudation between 91 and 69 Ma (seaward of the escarpment) and between 78 and 64 Ma (landward of the escarpment). Fission track data for the south-western margin suggests that denudation rates decreased significantly in the Tertiary to ~10 m/Ma. Brown *et al.* (2002) claim that the fission track data are inconsistent with the formation of the escarpment near the coastline. They prefer a model where the escarpment is formed by rapid post-break-up incision seaward of a pre-existing drainage divide. The escarpment became pinned at this divide and has since retreated slowly (Figure 3.1, Brown *et al.*, 2002).

3.7 Evaluating erosion rates using cosmogenic isotope analysis

Cosmogenic isotope dating has been undertaken in the southern Drakensberg (Fleming *et al.*, 1999) and Namib Desert (Cockburn *et al.*, 1999, Cockburn *et al.*, 2000, Van der Wateren and Dunai, 2001) to calculate exposure ages, and, in turn, erosion rates. From in-situ-produced cosmogenic ^{36}Cl measurements, Fleming *et al.* (1999) calculate that the southern Drakensberg escarpment has retreated at 50-95 m/Ma over the last million years (Figure 3.1b). In contrast, the flatter inland summit surface has been denuded over this time span at a rate of 6 m/Ma. These rates are an order of magnitude lower than what would be expected if the escarpment had formed at the continental margin at rifting, and retreated at a constant rate since then (=1-1.5 km/Ma) (Fleming *et al.*, 1999).

Cockburn *et al.* (2000) has produced cosmogenic data ($^{10}Be/^{26}Al$) that support an escarpment retreat rate of ~10 m/Ma since the end of the Eocene in Namibia (~5 to 10 times less than the Drakensberg escarpment) and denudation rate seaward of the escarpment of <20 m/Ma. According to Cockburn *et al.* (2000) these data support a

landscape evolution model where the escarpment is pinned at an inland drainage divide (Figure 3.1b). The Namibian escarpment, where sampled by Cockburn *et al.* (2000), is composed of granite capped by a 25 m quartzite layer (Nama in age, ~500-600 Ma). The climate here has been arid to semi-arid since the enlargement of the Antarctic ice sheet and the onset of the Benguela current in the middle Miocene (~14 Ma, Weigelt and Uenzelmann-Neben, 2004). The Drakensberg escarpment is capped by Karoo basalt and is situated in a high rainfall area. Thus it may be that the Drakensberg escarpment is retreating ~5 to 10 times faster than its counterpart in Namibia because of climatic and physical (lithological) differences.

Van der Wateren and Dunai (2001) present cosmogenic isotope measurements (^{21}Ne) from the central Namib Desert. Denudation rates for the central Namib since at least 5 Ma are ~0.5-1 m/Ma (Van der Wateren and Dunai, 2001). Accelerated denudation from around 2.81 ± 0.11 Ma is interpreted to be a response to climatic changes, specifically Plio/Pleistocene global cooling (Van der Wateren and Dunai, 2001). They claim that the pediment surface seaward of the escarpment has experienced <10 m of denudation since the mid Miocene. Their calculated low denudation rate fits with escarpment evolution models that involve rapid denudation, post break-up followed by long-term slow denudation (Van der Wateren and Dunai. 2001).

3.8 Differential kimberlite erosion

Hawthorne (1975) pioneered the use of kimberlite pipes to quantify landscape denudation across southern Africa. Subsequent authors have taken this analysis further (Gilchrist *et al.*, 1994 and de Wit, 1999). Evaluating the outcropping kimberlite facies against Hawthorne's (1975) model of a kimberlite pipe has allowed researchers to assess the extent of differential erosion since the pipe's emplacement. The presence of crater facies kimberlite indicates little erosion since emplacement. From the distribution of these kimberlites (see Figure 3.2), Hawthorne (1975) concludes that the southern and eastern parts of southern Africa have been more highly eroded than those in the northern and western parts and that at Kimberley, 1400 m of Karoo rock has been eroded since kimberlite emplacement, at ~90 Ma (age from Jelsma *et al.*, 2004). Along South Africa's west coast, kimberlites retain their crater facies therefore the landscape in this area *has not been significantly denuded since kimberlite intrusion at the beginning of the Tertiary* (Gilchrist *et al.*, 1994).

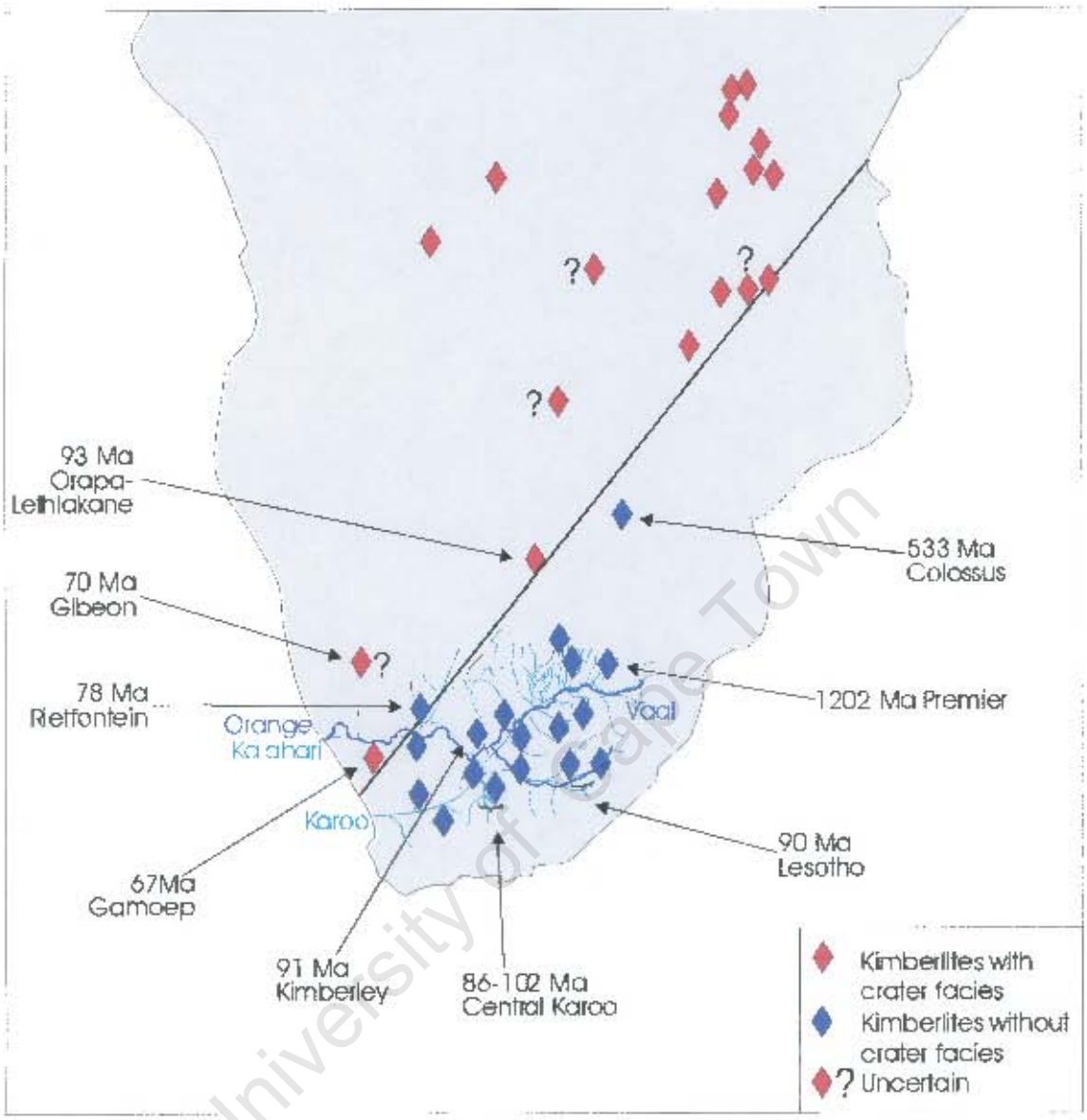

Figure 3.2: Distribution of kimberlites with and without their crater facies (after Hawthorne, 1975 and using kimberlite ages from Jelsma *et al.*, 2004). Average crater facies depth is <150 m though some extend to depths of over 300 m (Hawthorne, 1975). Hawthorne noted that north-west of a line drawn across Africa, kimberlite pipes retain their crater facies and therefore suggests that *there has been less erosion in this north-west region* since kimberlite emplacement (youngest at ~67 Ma). South-east of this line, the kimberlites crater facies have been eroded. The youngest pipes here are 86 Ma, giving a maximum age of erosion. Uncertain?: Kimberlite clusters which may or may not contain epiclastic kimberlite. Position of the mid-Cretaceous Karoo and Kalahari rivers (light blue) from Partridge (1998).

de Wit (1999) reconstructs the development of Cenozoic drainage in western South Africa using (amongst other lines of evidence) the differential erosion of kimberlites. He proposes erosion in three time intervals: continental break up to the end-Cretaceous; early-middle Cenozoic and the late Cenozoic. The humid Cretaceous was a period of high denudation, the highest occurring in the central interior (de Wit, 1999). Cretaceous-aged kimberlites were eroded and their diamonds transported to the coast via two main river systems, the Karoo and Kalahari rivers (de Wit, 1999). Accelerated uplift of the southern and eastern subcontinental margins (100-80 Ma) led to the capture of the upper Karoo River by the Kalahari River to become the more northerly Orange River network in the late Cretaceous to early Tertiary (de Wit, 1999). The onset of aridity in the early to middle Cenozoic resulted in a reduction of erosion rates and the presence of Late Cretaceous crater facies in South Africa's Northern Province indicates that there has been *only little erosion there since that time* (de Wit, 1999).

3.9 Cenozoic uplift?

The evidence above supports a dramatic decrease in denudation rate but does not preclude Cenozoic uplift. Partridge and Maud (1987) propose 150 to 300 m of uplift in the Miocene to late Pliocene (~18-~2.5 Ma) that they say caused a slight tilting of Southern Africa to the west to produce the post-African I surface. This Miocene uplift was localised in discrete zones and resulted in the elevation of eastern coastal areas. According to Partridge (1998), a further 900 m of late Pliocene (~2.5 Ma) uplift resulted in river incision along the east coast, downcutting of rivers in the interior and amplification of relief along the escarpment due to downcutting of river headwaters. Evidence given in Partridge (1997) for Pliocene uplift in the east includes convex up profiles of southeast coast rivers and late Miocene and early Pliocene marine sediments now 330 m above sea level near Port Elizabeth. Maximum sea level at during the Pliocene was 35 m above its present day level (Partridge, 1998). The main line of evidence, however, given to support significant Neogene uplift is the deformation or 'warping' of remnants of the 'African' surface and 'Post-African I' surface. Partridge (1997) describes the increase in gradient of both surfaces from 1 m/km for undisturbed surface remnants to 30 m/km (for the African surface) in the coastal hinterland of Natal, where uplift has apparently occurred. Again, though this line of evidence hinges on the correct identification, correlation and prescribing of ages to these surfaces, a procedure which has been repeatedly criticised (Summerfield, 1996; Brown *et al.*,

2000).

Several workers agree, based on field evidence (Partridge and Maud, 1987, Partridge, 1997, 1998), fission track thermochronology (Brown, 1992, Brown *et al.*, 2002), cosmogenic isotope analysis (Fleming *et al.*, 1999; Cockburn *et al.*, 2000; Van der Wateren and Dunai, 2001), geophysical models (Gilchrist *et al.*, 1994; van der Beek *et al.*, 2002) and kimberlite evidence that the major erosion that led to escarpment formation occurred (and was mostly over) in the Cretaceous. In spite of this overwhelming evidence of a reduction in Cenozoic denudation, Burke (1996) proposes that the erosion that has given rise to present day topography has occurred in the last 30Myrs. He characterises the early Cenozoic (65-30 Ma) as a relatively quite interval of a low-lying African Plate in terms of its igneous activity, topographic and tectonic history. Between 65 and 30 Ma he describes widespread deep weathering producing laterites and bauxites. His central hypothesis is that the African Plate has developed as it has over the last 30 Myr because it has come to rest with respect to the underlying mantle. He further suggests that South Africa may have been covered in marine sediments during the Cretaceous that have been subsequently eroded following uplift since 30 Ma. The crater facies of Cretaceous epiclastic kimberlites, however, are composed of sediments of lacustrine, not marine origin (Hawthorne, 1975), as indicated by the preservation of frog fossils for example (Smith, 1986).

Burke's (1996) Cenozoic period of uplift begins at 30 Ma when, he proposes, the escarpment developed and continued to retreat until the present. Extensive sedimentological and palaeontological work on the west, south and east coasts over several decades by McLachlan and McMillan (1976), McMillan *et al.* (1997) and McMillan (2003) amongst others negates Burke's claim. Significant denudation in the Late Cenozoic is also contrary to onshore evidence from fission track thermochronology and cosmogenic isotope analysis.

3.10 Conclusion

Classical models of landscape evolution through erosional cycles have traditionally been hampered by difficulties in dating and correlating erosion surfaces. New models that take additional factors such as antecedent (or pre-existing) topography, flexural isostatic uplift, climate/ lithological variations and baselevel changes into account are

improving our understanding of the controls on rift margin evolution.

There is a broad consensus, based on offshore evidence, fission track thermochronology, cosmogenic isotope analysis and kimberlite erosion, that major denudation was initiated by Gondwana break-up, occurred at highest rates in the Cretaceous and was mostly over by the Cenozoic. The cause of this Cretaceous uplift is not known, but may be related to the development of the African Superswell (see Chapter 7).

There is little agreement on the mechanisms for the formation and evolution of the escarpment. We do not know where the escarpment initially formed, i.e. whether it formed at the continental margin, or at/near a pre-existing drainage divide. However, from fission track and cosmogenic dating we do know that current rates of escarpment retreat are too low to explain a gradual retreat over the 140 Myrs since Gondwana break-up. Numerical models have attempted to solve this problem. However, the south coast is a strike-slip margin, not a simple, extensional, passive rift margin therefore its evolution may differ from numerical models developed from observations of extensional rift margins.

The decrease in denudation in the Tertiary is reflected by the decrease in sediment volume along the south and east coasts, and by the cosmogenic and fission track data. The reason for this decrease may reflect a decrease in uplift and/or an increasingly arid climate. Uplift younger than 2 Ma is still debated. The asymmetric uplift <2 Ma (~900 m) of southeast Africa described by Partridge and Maud (1987), Partridge (1997, 1998) and Hartnady and Partridge, (1995) is challenged by Brown *et al.* (2002) and Van der Beek *et al.* (2002). Possible mechanisms for this and earlier periods of uplift are poorly understood. Thus, there are many unanswered questions that a more detailed and thorough quantitative dataset may help to constrain.

Chapter 4: Fission Track Thermochronology

4.1. Introduction

Fission tracks are "scars" or damage to the crystal lattice of minerals such as apatite and zircon resulting from radiation damage during spontaneous fission of trace amounts of ^{238}U (1- 1000 ppm) (Figure 4.1). They are microscopic (initially ~16 microns in length when enlarged by chemical etching) and measured using a high power optical microscope. Chemical etching was first used by Price and Walker (1963) who also suggested that the accumulation of radiation damage produced by the spontaneous decay of ^{238}U may be used in geological dating. Basic procedures for this dating technique were first established by Price and Walker (1963); Naeser (1967) and Wagner (1968), and work by many authors since (Naeser and Faul, 1969, Fleischer *et al.*, 1965a,b, 1974; Green *et al.*, 1986; Gleadow *et al.*, 1983, 1986 etc.) has improved the procedures of the technique.

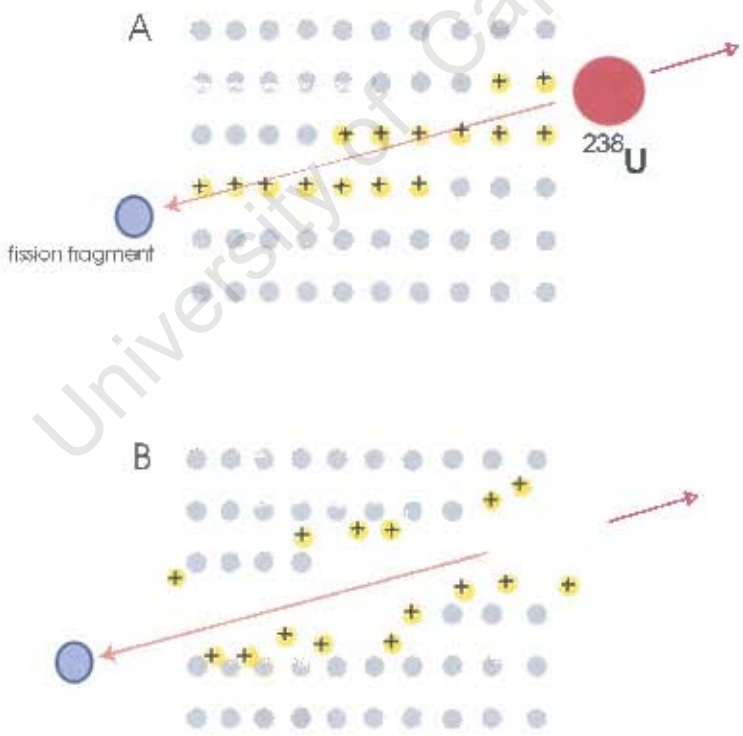

Figure 4.1: Track Formation (after Fleischer *et al.*, 1975). A. The fission fragment ionizes atoms of the crystal lattice along its trajectory. B. Along this trajectory atoms are displaced due to electrostatic repulsion, forming a 'track'.

The number of fission tracks depends on the uranium concentration in the crystal and the length of time over which the tracks have been accumulating (Gallagher and Brown, 1999a). The uranium concentration can be determined experimentally (by calculating ^{235}U, knowing that the isotopic ratio to ^{238}U is constant), and the number of tracks in a mineral can be counted. From this how much time has elapsed since the tracks began to accumulate can be calculated. This establishes its fission track age.

Fission tracks remain "frozen" in the system when the mineral cools below a certain temperature, known as the annealing (or closure) temperature. Above this temperature the mineral lattice adjusts, healing the tracks as they form. Below the annealing temperature, but above 60°C (in apatite), partial 'healing' occurs. This temperature zone is called the Partial Annealing Zone (PAZ) (Gleadow and Fitzgerald, 1987). Minerals used for fission track analysis include apatite and zircon which have annealing or closure temperatures of ~110 ± 10°C and 250 ± 25°C, respectively (Gleadow and Duddy, 1981, Gallagher *et al.*, 1998).

4.1.1 Track Lengths

Track lengths supply information regarding the cooling history of the mineral. The length of a track depends on the maximum temperature to which it was exposed since it was formed (Gleadow *et al.*, 1986). New tracks continually form below the closure temperature. Each new track, therefore, will have experienced a different fraction of the total thermal history (Gleadow *et al.*, 1986; 2002). Track length decreases as ambient temperature increases. If cooling is rapid, we expect all tracks to be of equal length. More than one cooling stage will be reflected by a greater spread of track lengths. For example, tracks accumulating in a mineral that cools slowly through the PAZ will shorten as the crystal lattice adjusts. If this mineral then rapidly cools beyond the PAZ, subsequent tracks will be longer, giving a range in track lengths.

Track length data provides information on the temperature variations that a mineral has experienced, whereas the fission track age (calculated from the number of tracks) allows determination of the duration of these variations (Gallagher and Brown, 1999a).

4.1.2 The Fission Track Method (for apatite)

4.1.2.1 Mineral Separation

The analytical procedure for the preparation of fission track slides is outlined in figure 4.2. Mineral separation is the separation of apatite grains from whole rocks. The rocks are crushed in a jaw crusher to 1-2 cm pieces and milled to sand sized particles (~60-300 μm) using a disk mill. A Wilfley table gravimetrically separates the light minerals (quartz, feldspar etc.) from the heavier minerals. After drying, the heavier fraction is run through a vertical Frantz magnetic separation where the ferromagnetic minerals are removed quickly. Sodium Polytungstate (SPT) is a heavy liquid made up to a specific gravity of 2.85 $g.cm^{-3}$ that removes the lighter minerals that may have slipped through the Wilfley table process. The sample is run through a horizontal Frantz electromagnetic separator at ~0.5 and ~1.0A, to remove the paramagnetic minerals. Lastly, methylene iodide (DIM), a second heavy liquid of 3.32 $g.cm^{-3}$, is used to separate zircon from apatite. If, when checked optically, separation is not complete, centrifuging in SPT may remove remaining unwanted mineral grains.

4.1.2.2 Mount Preparation

Apatite grains are mounted in epoxy on glass slides at a temperature of ~100°C (Figure 4.3A). The grain mounts are ground down so that the internal surfaces of a single layer of grains are exposed (B, C). The mounts are then polished to remove any grinding scratches. Etching of each sample in dilute nitric acid (5M HNO_3) for seventeen seconds at room temperature reveals the spontaneous tracks in the apatite grains (D). Every batch of samples was checked carefully to ensure adequate etching. An external detector, mica (with low uranium content), is fixed to each sample (E) with heat-shrink plastic, and 12 to 13 samples are loaded per irradiation can between two standard glasses of known uranium concentration. The cans are subjected to thermal neutron radiation at the Lucas Heights reactor in New South Wales, Australia, and then left to cool for several weeks. Standard glasses are used to detect the flux and measure the flux gradient between the first and last sample in the irradiated can.

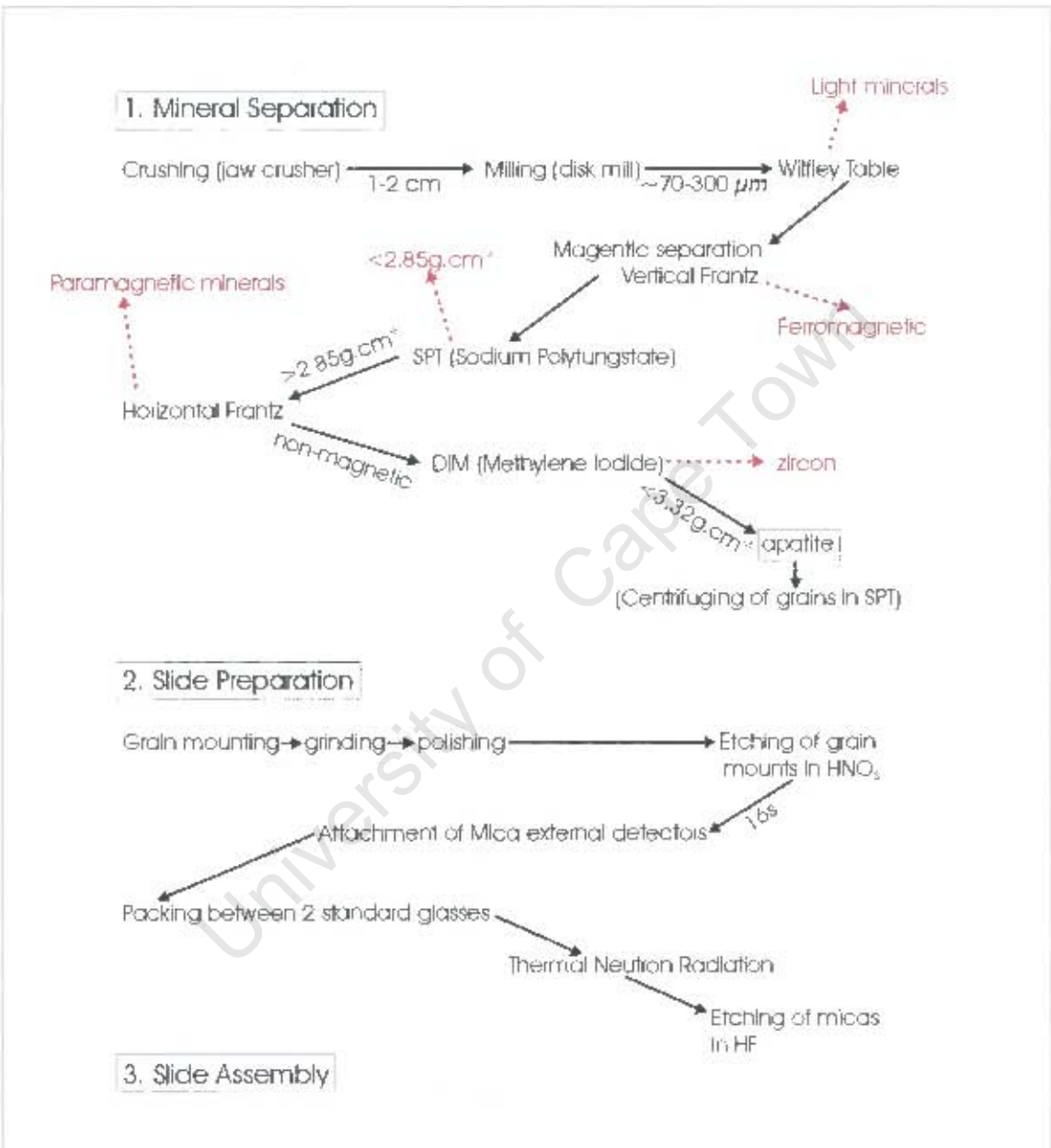

Figure 4.2: Flow chart of mineral separation and apatite mount preparation procedure.

Grains mounts returned from the reactor are marked with pinpricks through the mount and mica that allow for microscope stage alignment before counting begins. The mica external detectors once removed from the grain mounts are etched in hydrofluoric acid (48% HF) for an hour to reveal the newly formed induced fission tracks. ^{235}U fission produces induced tracks in the mica detector attached to each sample. From this induced track density, and known neutron fluence during irradiation (from the standard glasses at each end of the can), the ^{235}U concentration is determined, and thus the ^{238}U concentration for each grain mount ($^{235}U/^{238}U$ is constant in nature). The use of mica to quantify ^{238}U concentration for each mount is called the *external detector method* (Gleadow, 1981). The final step is the assembly of the fission track slides that compose of the grain mount and external mica detector at similar height and a reference point for slide alignment (F).

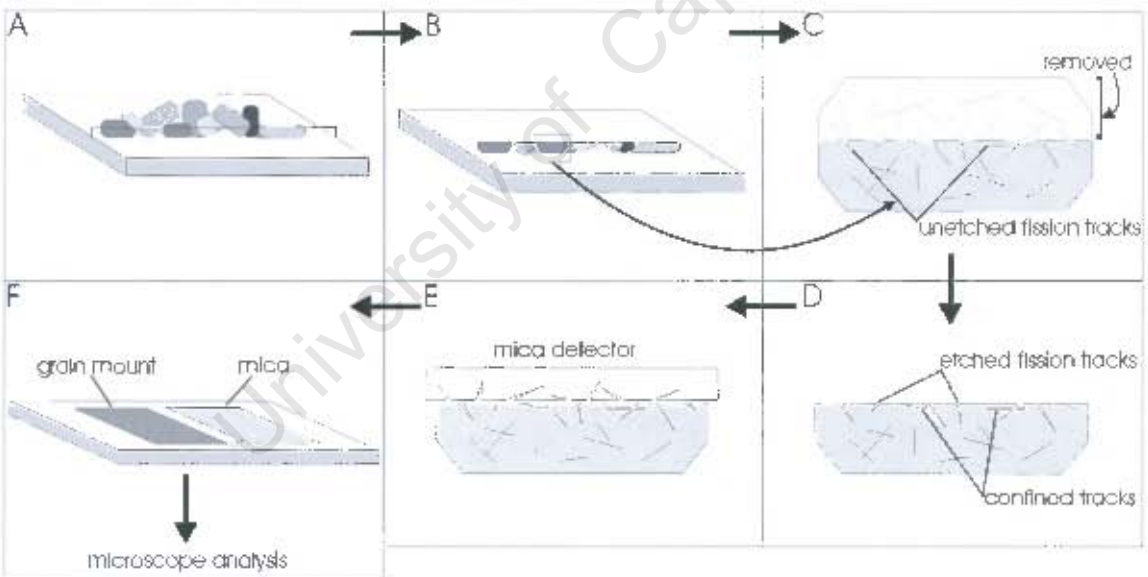

Figure 4.3: Schematic of the fission track mount preparation process. See text for details.

4.1.2.3 Counting the tracks

Counting of fission tracks is made possible by acid etching and a high-powered microscope (1600X magnification). Selection of grains is made following strict criteria. The annealing process is anisotropic: rates of annealing and etching depend on the orientation of the track within the crystal (Laslett *et al.*, 1984; Gleadow *et al.*, 1986). Tracks parallel to the C-axis anneal at a slower rate than those perpendicular to the C-axis (Gleadow *et al.*, 1986). Due to this anisotropic response only grain surfaces that are parallel to the C-axis are counted. Grains with visible dislocations, uneven uranium distribution and large inclusions are avoided. To eliminate bias in grain selection, slides are scanned methodically from one end to the other and every grain that fits the above criteria is counted (up to 30 grains per sample).

4.1.2.4 Calculating the Fission Track Age

The spontaneous and induced tracks are counted consecutively. For each grain the same area is counted on the mica print as on the grain to determine the induced track count. A motorized microscope and dedicated computer program speed up the counting process and allow for greater statistical accuracy. The ratio of spontaneous (from the grain mount) to induced tracks (from the mica print) for a given area is used to calculate its age. The 'age' when the sample cooled through its closure temperature is calculated from these single grain ages.

A fission track age is calculated using the fundamental equation for fission track analysis (after Price and Walker, 1963; Fleischer *et al.*, 1965b; Naeser, 1967 and Hurford and Green, 1982, 1983):

$$t = 1/\lambda_D \ln [1 + (\lambda_D I\sigma\phi / \lambda_f)(\rho_s/\rho_i)] \quad [1]$$

t = Fission track age; λ_D and λ_f = Decay constants for α emission and spontaneous fission, respectively; ρ_s = Density of spontaneous tracks; ρ_i = Density of tracks induced by irradiating the sample in a nuclear reactor with a fluence (ϕ) of thermal neutrons; $I = {}^{235}U/{}^{238}U$ (constant); σ = Cross section of ^{235}U for fission induced with thermal neutrons.

The neutron fluence is related to the induced track density of the standard glass' external mica detector:

$$\emptyset = B\rho_D \quad [2]$$

B = constant of proportionality; ρ_D = Induced track density in external detector mica against the standard glass.

$$\zeta = \sigma IB/\lambda_f \quad [3]$$

Incorporation of the zeta factor (ζ, Hurford and Green, 1982, Green, 1985) reduces bias in the calculation that may result from subjective counting between researchers and/or equipment differences. Zeta calibration involves empirically calibrating the system against age standards thus avoiding the need to calculate constants in [1] which may involve error. Standards have to satisfy various criteria outlined in Hurford and Green (1983). In this study, the Fish Canyon, Mt Dromedary and Durango apatites were used as standards in the zeta calibration (see appendix B).

Thus:

$$t_u = 1/\lambda_D \ln [1 + \lambda_D \zeta (\rho_s/\rho_i) \rho_D] \quad [4]$$

t_u = unknown age of sample; ρ_s/ρ_i = Spontaneous and induced track densities respectively; ρ_D = track density of glass monitor (standard); ζ = zeta calibration factor.

4.1.2.5 Measuring Track Lengths

As mentioned in section 4.1.1, track lengths supply information regarding the cooling (or heating) history of the mineral. To measure the distribution of track lengths in an apatite crystal only horizontal, confined tracks are measured from grain surfaces that are oriented parallel to the C-axis (Laslett *et al.*, 1982; Gleadow *et al.*, 1986, 2002). Confined tracks do not intersect the crystal surface and are etched as a result of intersection by a crack or dislocation or another track, which acts as a conduit for the acid. Track length measurements in this study were made using a drawing tube-digitising tablet arrangement calibrated against a stage micrometer.

4.1.3 Complexities

4.1.3.1 Meaningful age?

"A fission track age does not generally reflect a discrete event" (Gallagher, 1995, 421).
It is simplistic to consider the fission track age as the time at which the sample cooled below its 'closure temperature'. In reality the cooling history may be far more complex. If a sample cools slowly through the PAZ tracks are annealed/ shortened, and thus are less likely to intersect the surface used to count their density. In this case, the calculated fission track age is younger than the time at which it cooled through its 'closure temperature'. A fission track age can only be regarded as representing a discrete cooling event if the sample has cooled rapidly through the PAZ and has a resulting mean confined track length of ~14- 15 μm and a standard deviation of track length distribution of ~1 μm (Green, 1988).

Some annealing occurs even at low temperatures (~20 to 30°C) resulting in spontaneous (natural) tracks that are always shorter than induced tracks (produced in the laboratory) (Green, 1980). In 10 Myrs, tracks of a sample subjected to 20°C will shorten by ~1 μm in length according to Laslett *et al.*'s 1987 annealing model (Green, 1988). Likewise, an apatite that has never been heated above ~50°C will show track lengths that are shorter than induced track lengths (Green 1980, 1988; Gleadow *et al.*, 1986).

A further complication is that samples collected from deep boreholes may have present day temperatures in the range where initial annealing occurs much faster (Ketcham *et al.*, 1999). Thus the closure temperature is both a function of cooling rate as described above, as well as the ambient temperature of the sample collection site (Ketcham *et al.*, 1999).

For this reason modelling thermal histories (thermochronology) depends on track length distribution rather than simply the fission track age determination (see section 4.5).

4.1.3.2 Pressure

Wendt *et al.* (2002) carried out experiments to determine the effect of pressure, stress and temperature on the annealing properties of apatite. They concluded that (1) as pressure increases, annealing rates in apatite decrease and (2) increased stress leads to an increased annealing rate. Most importantly, in their opinion, there is no typical annealing behavior for apatites and therefore the standard methodology of extrapolating fission track data to geological time scales cannot be applied (Wendt *et al.*, 2002).

Kohn *et al.* (2003) criticize the study of Wendt *et al.* (2002) on the basis of poor experimental design and procedure as well their lack of consideration of previous fission track annealing experiments. Annealing models that have been based on analysis of annealing behaviour of apatites from deep borehole studies (e.g. Gleadow and Duddy, 1981; Gleadow *et al.*, 1983, Hammerschmidt *et al.*, 1984, Arne and Zentilli, 1994) are in broad agreement with those derived from experimental laboratory data (Kohn *et al.*, 2003). Since models derived from deep borehole samples already encompass any effect of pressure on annealing, the effect of pressure must be minor (Kohn *et al.*, 2003).

Donelick *et al.*, (2003) conducted similar experiments as Wendt *et al.*, (2002) to determine the effect of pressure on the annealing properties of apatite. They observed no effect of pressure on track annealing in samples subjected to 1bar to 1kbar of pressure and could not reproduce the data of Wendt *et al.* (2002) at similar conditions.

4.1.3.3 Apatite Composition

Green (1985) proposed that the annealing properties of apatites are controlled by their chlorine/fluorine (Cl/F) ratio. Therefore compositional differences may explain why different grains respond differently to temperature (Green *et al.*, 1985, 1986; Arne and Zentilli, 1994; Gallagher, 1995; Carlson *et al.*, 1999; Ketcham *et al.*, 1999; Barbarand *et al.*, 2003a,b). In particular, the degree of track annealing may vary from grain to grain. Apatites rich in chlorine are more resistant to annealing than fluorine-rich apatites (Green *et al.*, 1985, 1986; Arne and Zentilli, 1994). Thus fluorine-rich samples show complete annealing at lower temperatures (~90-100°C) than those of chlorine-rich samples whose closure temperatures vary between 110 and 150°C (Gleadow et al., 2002). Chlorine-rich

apatites may retain more short tracks than those rich in fluorine and hence have shorter mean track lengths (Gleadow *et al.*, 2002). Little is known about the role of OH^- ion in the annealing process (Gallagher, 1995). Recent work by Carlson *et al.* (1999) has shown that additional compositional variations (chemical substitution for Ca for example) may also be important in determining annealing rates. New annealing models have been developed to take composition differences into account (Crowley *et al.*, 1991; Galbraith and Laslett, 1993; Ketcham *et al.*, 1999).

4.1.4 Theoretical models of borehole age and track length profiles

Thermal histories are modelled using computer software described in section 4.5. However, from the analysis of borehole plots of mean track length and fission track age versus depth, much information regarding the timing and extent of changes in denudation can be ascertained. This section describes the theoretical shape of borehole plots of fission track age and mean track length versus depth, expected for changes in denudation rate. This section also discusses how mean track length varies with varying fission track age for a thermal history involving a period of increased denudation.

4.1.4.1 Fission track age vs. depth

In a stable region, where the denudation rate is low, the profile of fission track age with increasing depth has a characteristic concave up shape, which is controlled by increasing temperature with depth (Figure 4.4a, after Brown, 1992). The steepest gradient (i) reflects ages of samples that are located above the PAZ(I) (<60°C). Above the PAZ(I) little annealing occurs with increasing depth, thus ages are similar. The shallowest gradient (ii) corresponds to the PAZ(I) (60-110°C) where the temperature dependent annealing of tracks occurs. Tracks subject to the highest temperatures will be more highly annealed (shorter), resulting in younger ages for deeper samples.

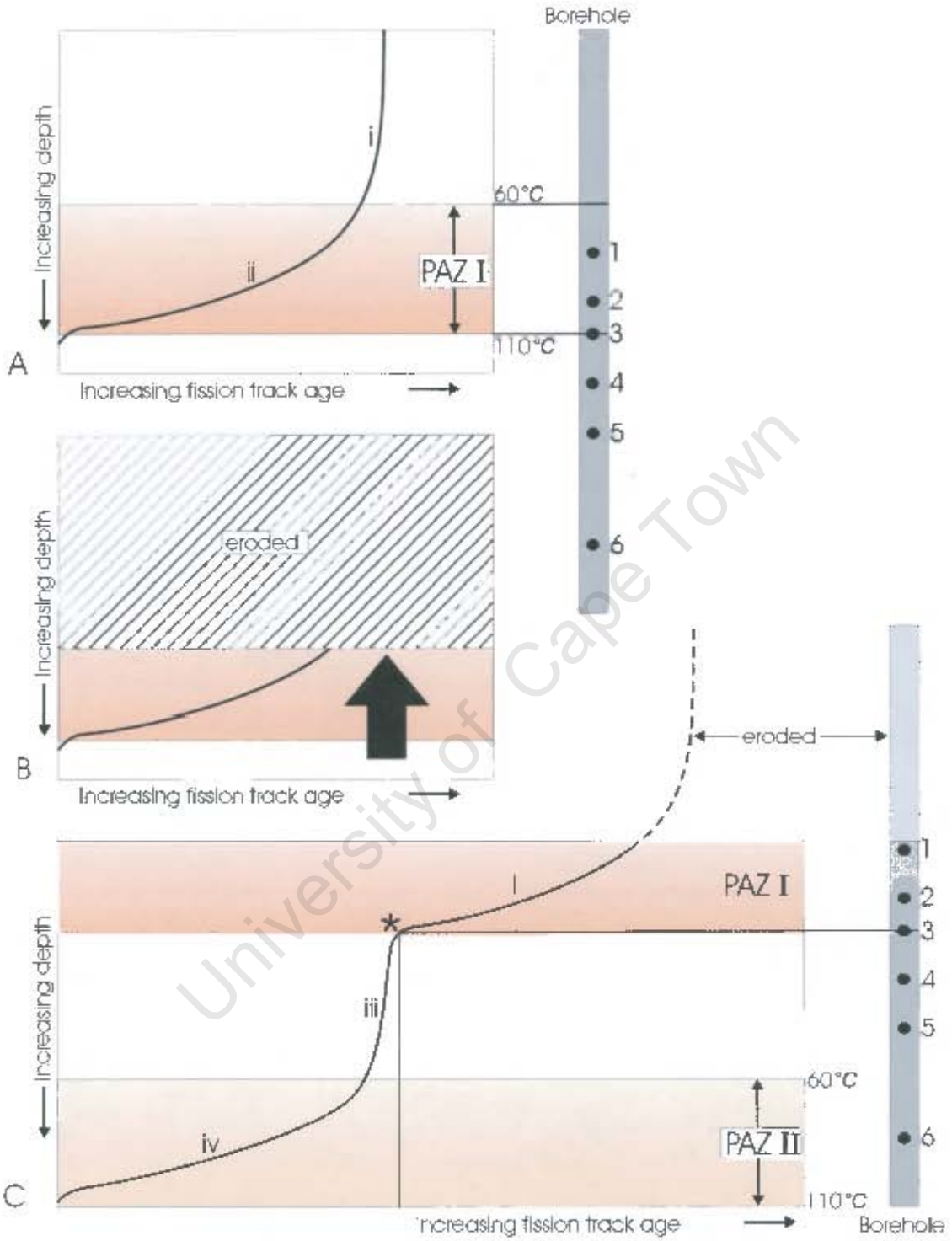

Figure 4.4: (A) Age-depth model profile for a constant low denudation rate. (B) The shaded area is removed during a period of increased denudation. (C) The resultant new age-depth profile post uplift. Note the preservation of the paleo-partial annealing zone, PAZ(I), at the top of the borehole.

If this stable setting is disturbed by a subsequent increase in denudation (Figure 4.4b) then a more complex age-depth profile will result (Figure 4.4c). Again, the new steepest section is <60°C (iii) and shallowest gradient is through the present day partial annealing zone, PAZ(II) (iv). Note that the remaining, uneroded, paleo-partial annealing zone, PAZ(I), i) is retained at the top of profile in figure 4.4c. The inflection point (*) between the two parts of the profile marks the base of the PAZ(I) (~110±10°C). The age at this point (i.e. the age of sample 2) gives the time at which the acceleration in denudation began (from Brown, 1992).

4.1.4.2 Mean track length vs. depth

The variation of mean track lengths with depth reflects an increase in denudation rate. In the simple example of a sudden increase in denudation rate (section 4.1.4.1), prior to the denudation, within the PAZ, mean track lengths decrease with increasing depth. For example, sample 3 (Figure 4.4) will have a shorter mean track length than sample 2 and 2 a shorter mean track length than 1 (all are within the PAZ(I)). The annealing that shortened these tracks took place before the denudation. In this scenario, rapid denudation will cause samples 4 and 5 to cool rapidly through the PAZ. With less time for these samples' tracks to anneal, they will have longer mean track lengths than 1, 2 and 3 above. After denudation, the samples that now lie within the present day PAZ(II) (e.g. sample 6) will be annealing at present and therefore will have shortened mean track lengths.

4.1.4.3 Boomerang plots (Mean track length vs. fission track age)

The relationship between fission track age and mean track length has been referred to in the literature as a boomerang plot. The 'boomerang' describes the shape of the concave up trend in samples from a region that has experienced one discrete phase of accelerated denudation (see Gallagher and Brown, 1999b). This scenario is shown graphically in figure 4.5. In figure 4.5a the sample from the top of a borehole (1) cools from a temperature less than 60°C, thus has the oldest age (it has never been thermally reset) and long mean track length as none of its tracks have been subjected to temperatures high enough to result in significant annealing. Sample (1) will not record the acceleration in denudation. Sample (2) cools from a temperature within the PAZ, thus will be partially reset. It will have a younger fission track age with shorter mean track length, because

tracks formed while the sample was within the PAZ will have been annealed. Prior to denudation, sample (3) was below the PAZ, and at a temperature of >110 ± 10°C. Rapid denudation resulted in its rapid cooling through the PAZ during which little track annealing occurred. As a result, this sample has the youngest age, and like (1), has a long mean track length (Figure 4.5b).

After a description of how the samples were acquired (section 4.2) and the FTA results (section 4.3), section 4.4 will compare the fission track data to these theoretical models described in 4.1.4.

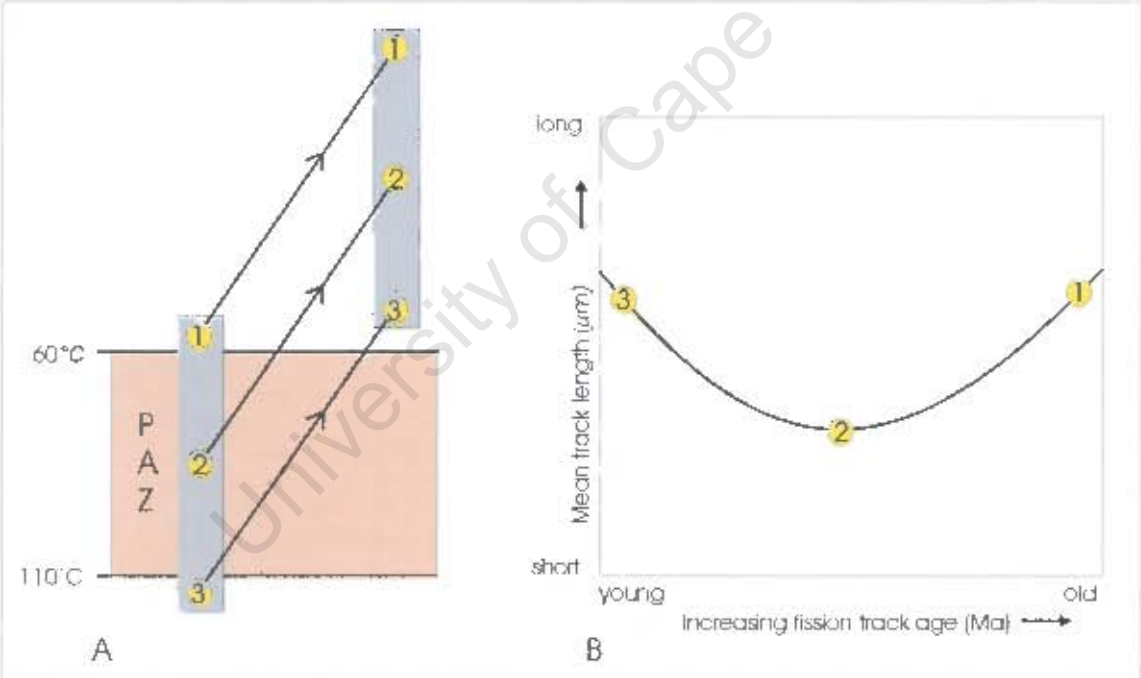

Figure 4.5: (A) Schematic figure showing how a "boomerang" trend (B) in fission track age vs. mean track length is produced.

4.2 Data

4.2.1 Fission track samples

Twenty-five outcrop samples (Figures 1.1 and included in appendix C) yielded sufficient apatite to calculate a fission track age. These were collected along a N-S transect that extends from Victoria Bay along the south coast, across the Cape Fold Belt and E-W trending faults (both normal and reverse) associated with the assembly and break-up of Gondwana. It crosses the Cango inlier (<518 ± 9 Ma- top of Cango Group, Barnett *et al.*, 1997), the Oudtshoorn basin (150-130 Ma, age of Uitenhage Group) and finally, the Great Escarpment. The transect extends into the Karoo basin (Beaufort and Ecca Groups) and ends at Marydale (~200 km SE of Upington). Nineteen sedimentary rocks were sampled from the following stratigraphic groups: The Cango, Dwyka, Ecca, Beaufort and the Brulpan Groups. Six igneous samples were obtained including the George granite (~550-530 Ma, Rozendaal *et al.*, 1999), the Skalkseput Group granite (2718 ± 8 Ma, McCourt *et al.*, 2000) and the Karoo dolerites (183 ± 1 Ma, Duncan *et al.*, 1997). Apatite yield was stratigraphically controlled. The largest yield was from the Beaufort Group samples and no apatite at all was recovered from Table Mountain Group samples. Appendices D, E and F give locations, descriptions and photographs of the samples, respectively.

Thirty-one samples from three boreholes were sampled at a depth interval of ~300 m. From west to east these boreholes are SA1/66, KW1/67 and CR1/68, situated south of the escarpment (Figures 1.1 and Figure 4.6, crosses). All samples were separated, prepared and counted at the University of Melbourne's fission track laboratory. Eight borehole samples were recounted at the University of Cape Town's fission track laboratory. The results of the fission track analysis follow in section 4.3.1.

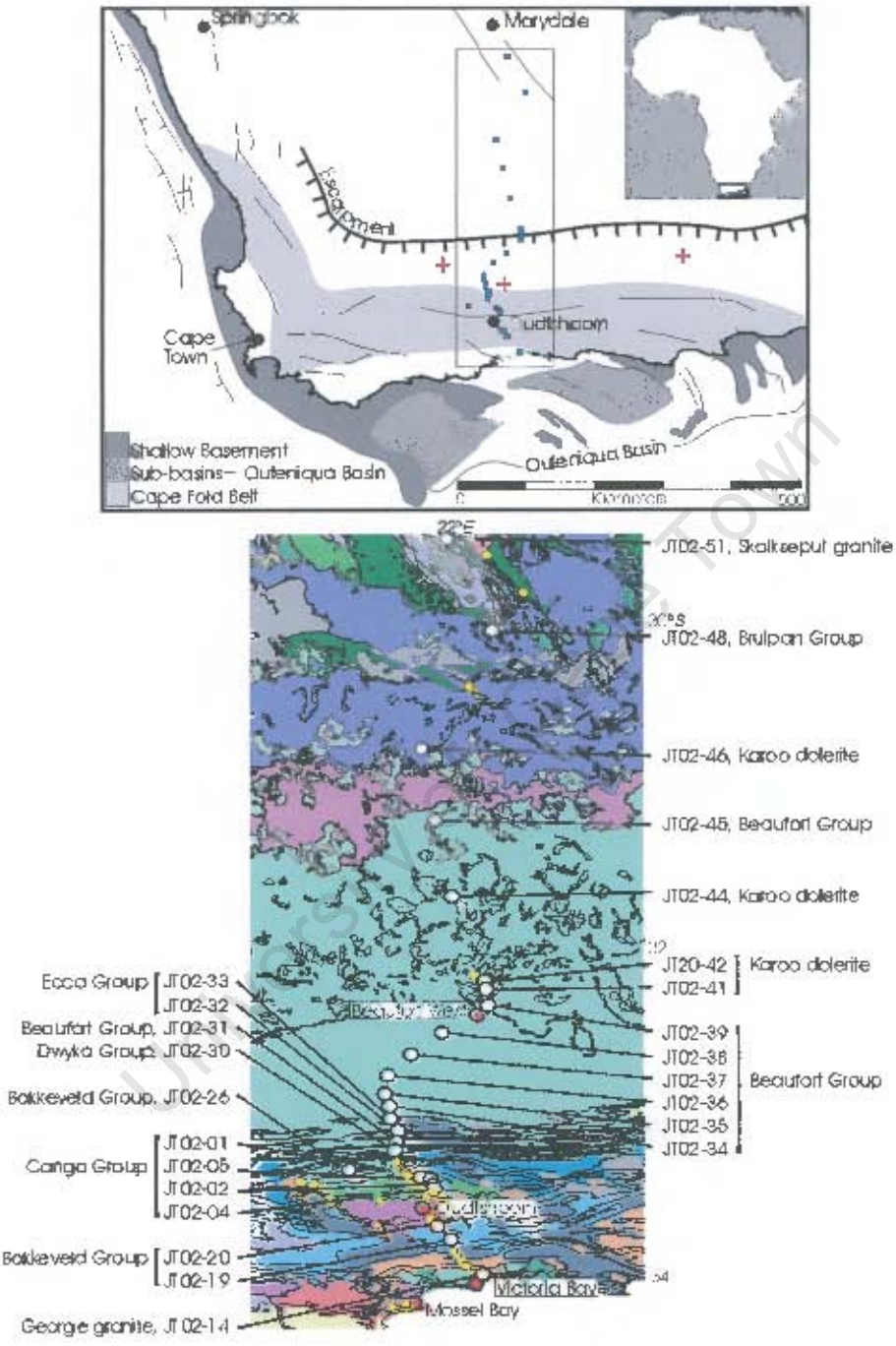

Figure 4.6a: Location of outcrop samples (squares) and boreholes (crosses). Inset enlarged in b: unsuccessful (yellow dots) and successful (white dots) samples. Red dots= towns. Geology according to the legend in Figure A-1 (Appendix A).

4.2.2 Microprobe analysis of apatite

Twenty grains from each selected sample were chemically analysed at Geotrack International, Melbourne, Australia to test the possible effect of compositional differences on apatite annealing characteristics. Chlorine content, converted to weight %, was measured using a JEOL JXA5A electron microprobe on twenty of the same grains originally counted to obtain the fission track age. The JEOL JXA5A microprobe is equipped with a computer-controlled X-Y-Z stage and three computer controlled wavelength dispersive crystal spectrometers with an accelerating voltage of 15kV and beam current of 25nA, defocused to 20μm diameter. Chlorine count rates are converted to wt% Cl by reference to those from a Durango apatite standard (0.43 wt% Cl). Eleven samples were probed including 3 dolerite samples (JT02-41, 44 and 46), the top and bottom samples from borehole SA1/66 (JT03-60 and 74) and six samples from borehole KW1/67 (JT03-75, 77, 79, 82, 86 and 88). Samples were selected in order to obtain representative chlorine content for all stratigraphic groups. The microprobe results are included in section 4.3.2.

4.3 Results

4.3.1 Fission track analysis

4.3.1.1 Representation of results

The fission track results for the boreholes and outcrop samples are given in table 4.1a and b and shown graphically as radial plots and track length histograms (Appendix C). The radial plot (Appendix C), described in Galbraith (1990), shows graphically the spread and precision of individual grain ages within a sample. The position of the plot on the x-axis is a measure of its precision (1 sigma error), which depends on the number of tracks counted. The further to the right each individual grain plots, the more precise the single grain age is.

In the external detector method, fission track ages are an average estimate of the individual grains that make up the samples. These averages are quoted as the pooled, mean and central ages. The pooled age is the sum of spontaneous track counts divided by the sum of induced track counts. The mean age is the arithmetic mean of the individual grain ages, i.e. the individual ratios of spontaneous to induced tracks. The central age is the weighted mean of the log normal distribution of single grain ages (Galbraith and Laslett, 1993). When the population is consistent with a Poisson distribution then the three age estimates should be roughly the same (Gallagher *et al.*, 1998).

To test if the apatite grains are from a single source that has experienced one thermal history and thus has one true age, a chi^2 test is applied. If there is over-dispersion of individual grain ages (the variation in the track count is inconsistent with variation expected for a poisson distribution) then the pooled age estimate is not valid and the sample will fail the chi^2 test (Green, 1981). In appendix C, those samples that have a chi^2 value (expressed as a percentage) of <5% have failed this test. A sample may fail the chi^2 test for a variety of reasons. Apatites from a sedimentary rock may have been derived from more than one source. Thus the grains may have a variable chemical properties causing different annealing characteristics, different track lengths and hence varying track counts (Green *et al.*, 1986, 1989; Arne and Zentilli, 1994; Gleadow et al., 2002). Green (1981) suggested the use of the mean age as an interim measure in cases of over-dispersion in individual grain ages. The mean age however is not sensitive to

differences in actual size of the track counts between individual grains (all grains are equal), so Galbraith and Laslett (1993) recommended that age dispersion and the central age be routinely calculated. The central age is used in table 4.1a and b.

4.3.1.2 Outcrop samples

Fifty-five samples were collected along a north-south transect across the southern Cape into the interior, of which 25 yielded enough apatite to calculate a fission track age (Figure 4.6). The results for these 25 samples are listed in table 4.1a. Figure 4.7 is a topographic and geological cross-section including sample sites and their fission track ages.

Apatite fission track ages range from 89± 6 Ma (Cango Group) to 157 ± 14 Ma (Karoo dolerite at the top of the escarpment) and have chi^2 valued of > 5 % (and in most cases >> 5%). Mean track lengths vary from 11.86 to 14.23 μm. Track length distributions vary from unimodal to dispersed to bimodal. This variation is reflected in their standard deviations: the more broadly dispersed the lengths, the greater the standard deviation. Standard deviations vary between 1.18 (JT02-30, Dwyka tillite) and 2.73 μm (JT02-46, Karoo dolerite). All track length distributions (except JT02-30) are negatively skewed and have a tail of shorter track lengths.

Outcrop samples

Sample number	Group	Strat. Age (Ma)	Lithology	Location Lat. (S), Long. (E)	Elevation (m)	Number of grains	Standard track density ($x10^6$ cm^{-2})	Fossil track density ($x10^5 cm^{-2}$)	Induced track density ($x10^6 cm^{-2}$)	Uranium content (ppm)	Chi square probability %	Fission track age*† (Ma)	Mean track length† (μm)	Std. dev. (μm)
JT02-01	Cango	~560-500	arkose	33.39732, 22.20072	630	23	1.033 (4505)	8.295 (378)	1.725 (786)	20.9	94.9	**89 ± 6**	12.66 ± 0.2 (101)	1.62
JT02-02	Cango		greywacke	33.42906, 22.25193	619	30	1.053 (4505)	2.378 (136)	0.416 (238)	4.9	99.04	**108 ± 12**	12.62 ± 0.24 (100)	2.4
JT02-04	Cango		greywacke	33.46415, 22.2539	473	10	1.094 (4505)	2.81 (75)	0.618 (165)	7.1	40.39	**92 ± 15**	13.1 ± 0.14 (98)	1.39
JT02-05	Cango		greywacke	33.42154, 22.24128	550	23	1.114 (4505)	6.528 (515)	1.145 (903)	12.8	39.85	**114 ± 7**	12.9 ± 0.12 (102)	1.18
JT02-14	George	~540	granite	34.00468, 22.55245	52	20	1.175 (4505)	4.739 (230)	0.937 (455)	10.0	99.98	**107 ± 9**	11.86 ± 0.25 (28)	1.3
JT02-19	Bokkeveld	~ 390-375	shale	33.78127, 22.342	526	28	1.216 (4505)	9.885 (317)	1.643 (527)	16.9	95.97	**131 ± 10**		
JT02-20	Bokkeveld		shale	33.69149, 22.27118	472	30	1.256 (4505)	6.232 (462)	0.979 (726)	9.7	98.62	**143 ± 9**	12.35 ± 0.15 (100)	1.55
JT02-26	Bokkeveld		shale	33.34867, 21.74986	785	21	1.017 (3503)	14.102 (250)	2.155 (382)	26.5	53.58	**119 ± 10**	12.12 ± 0.43 (33)	2.49
JT02-30	Dwyka	~350-275	tillite	33.22082, 22.02561	633	30	1.036 (3503)	6.258 (739)	1.129 (1333)	13.6	45.18	**102 ± 6**	13.4 ± 0.13 (77)	1.18
JT02-31	Beaufort	~252-238	arkose	33.16909, 22.03302	550	23	1.056 (3503)	5.623 (425)	0.955 (722)	11.3	44.74	**112 ± 7**	14.23 ± 0.13 (104)	1.32
JT02-32	Ecca	~275-252	arkose	33.11368, 22.04922	660	25	1.075 (3503)	5.658 (348)	0.951 (585)	11.1	77.85	**115 ± 8**	13.27 ± 0.15 (93)	1.41
JT02-33	Ecca		arkose	33.0271, 22.00091	519	24	1.095 (3503)	7.292 (364)	1.326 (662)	15.1	94.17	**108 ± 7**	13.16 ± 0.19 (100)	1.89
JT02-34	Beaufort	~252-238	arkose	32.96303, 21.98609	514	23	1.114 (3503)	6.784 (356)	1.193 (626)	13.4	9.79	**114 ± 9**	13.51 ± 0.16 (100)	1.61
JT02-35	Beaufort		arkose	32.87557, 21.96231	542	24	1.134 (3503)	4.547 (344)	0.687 (520)	7.6	76.39	**134 ± 10**	13.53 ± 0.21 (101)	2.1
JT02-36	Beaufort		arkose	32.76956, 21.97837	547	24	1.153 (3503)	6.875 (428)	1.373 (855)	14.9	35.94	**104 ± 7**	12.82 ± 0.17 (101)	1.72
JT02-37	Beaufort		arkose	32.65132, 22.11732	623	26	1.172 (3503)	4.659 (399)	0.777 (665)	8.3	78.0	**126 ± 8**	12.99 ± 0.19 (100)	1.88
JT02-38	Beaufort		arkose	32.51006, 22.29901	734	22	1.192 (3503)	6.53 (308)	1.317 (621)	13.8	93.35	**106 ± 8**	12.72 ± 0.22 (100)	2.21
JT02-39	Beaufort		arkose	32.30865, 22.57172	903	30	0.905 (3966)	5.343 (512)	0.843 (808)	11.6	90.51	**103 ± 6**	12.62 ± 0.17 (100)	1.75
JT02-41	Karoo dolerites	183 ± 1Ma, Duncan *et al.*, 1997	dolerite	32.20749, 22.55805	1326	33	0.942 (3966)	2.182 (141)	0.331 (214)	4.4	99.93	**111 ± 12**	13.08 ± 0.26 (101)	2.65
JT02-42	Karoo dolerites		dolerite	32.18589, 22.54947	1487	24	0.961 (3966)	4.039 (110)	0.492 (134)	6.4	99.95	**137 ± 20**		
JT02-44	Karoo dolerites		dolerite	31.6817, 22.35845	1460	31	0.998 (3966)	3.965 (254)	0.451 (289)	5.7	97.3	**157 ± 14**	13.22 ± 0.17 (93)	1.68
JT02-45	Beaufort	~252-238	arkose	31.22582, 22.2631	1427	30	1.017 (3966)	7.514 (428)	1.095 (624)	13.5	41.83	**127 ± 9**	13.08 ± 0.17 (100)	1.67
JT02-46	Karoo dolerites	183 ± 1Ma, Duncan *et al.*, 1997	dolerite	30.79967, 22.16619	1158	18	1.035 (3966)	4.518 (110)	0.608 (148)	7.3	89.43	**138 ± 18**	12.69 ± 1.57 (3)	2.73
JT02-48	Brulpan	~1900-1750	quartzite	30.08138, 22.61431	1059	28	1.072 (3966)	3.659 (610)	0.551 (919)	6.4	94.72	**128 ± 7**	13.45 ± 0.23 (100)	2.25
JT02-51	Skalkseput granite	2718±8 McCourt *et al.*, 2000	granite	29.52769, 22.33132	1024	14	1.091 (3966)	4.736 (117)	1.004 (248)	11.5	90.2	**93 ± 11**	13.02 ± 0.23 (54)	1.66

Table 4.1a: Age and track length data for outcrop samples. Numbers in brackets show number of tracks counted and measured. Standard and induced track densities measured on mica external detectors and fossil track densities on internal grain surfaces. FT Ages calculated using the zeta method for dosimeter glass CN-5 (362 ± 21). § All FT ages are central ages, † One sigma error used. See Chapter 2 for strat. age references.

Borehole Samples

Sample number	Group	Strat. Age (Ma)	Location Lat. (S), Long. (E)	Depth (m)	Number of grains	Standard track density ($x10^6$ cm^{-2})	Fossil track density ($x10^5 cm^{-2}$)	Induced track density ($x10^6 cm^{-2}$)	Uranium content (ppm)	Chi square probability %	Fission track Age §† (Ma)	Mean track length† (µm)	Std. dev. (µm)
SA1/66			32.6667 21.3333										
JT03-60 *	Beaufort	~252-238		28.35	20	1.000 (3314)	7.952 (512)	1.275 (821)	16.9	36.49	**112 ± 9**	12.7 ± 0.2 (100)	2.04
JT03-61 *	Beaufort			319.43	20	1.014 (3314)	4.612 (341)	0.837 (619)	10.6	79.36	**100 ± 9**	12.44 ± 0.22 (101)	2.17
JT03-62 *	Beaufort			602.28	20	1.028 (3314)	3.609 (255)	0.744 (526)	9.98	99.82	**90 ± 9**	12.43 ± 0.19 (100)	1.88
JT03-63 *	Beaufort			941.22	19	1.042 (3314)	4.589 (271)	1.011 (597)	12.34	98.66	**85 ± 8**	12.34 ± 0.23 (101)	2.26
JT03-64 *	Beaufort			1210.06	20	1.056 (3314)	4.456 (274)	1.127 (693)	13.05	79.74	**75 ± 7**	12.53 ± 0.24 (100)	2.38
JT03-66 *	Ecca	~275-252		1880.62	20	1.070 (3314)	1.813 (117)	0.441 (282)	5.28	99.32	**80 ± 10**	12.11 ± 0.24 (100)	2.39
JT03-69	Dwyka	~350-270		3037.33	30	1.183 (4411)	0.944 (120)	1.02 (1296)	10.8	0.16	**19 ± 3**	9.82 ± 0.21 (99)	2.11
JT03-71	Dwyka			3350.97	30	1.236 (4411)	0.597 (62)	1.132 (1175)	11.4	0.08	**13 ± 2**	10.04 ± 0.21 (100)	2.07
JT03-72	Dwyka			3635.65	30	1.263 (4411)	0.548 (54)	1.557 (1534)	15.4	42.01	**8 ± 1**	8.51 ± 0.49 (36)	2.93
JT03-73	Dwyka			3921.86	30	0.965 (4390)	0.344 (29)	1.211 (1020)	15.7	96.67	**5 ± 1**	8.83 ± 0.3 (66)	2.4
JT03-74	Dwyka			4104.44	19	0.992 (4390)	0.399 (14)	2.597 (912)	32.7	0.08	**3 ± 1**	5.45 ± 0.71 (19)	3.12
KW1/67			32.9833, 22.3333										
JT03-75 *	Beaufort	~252-238		394.11	20	1.015 (3161)	4.513 (242)	0.793 (425)	10.29	89.52	**106 ± 11**	12.68 ± 0.19 (100)	1.93
JT03-76 *	Beaufort			713.23	20	1.027 (3161)	4.810 (191)	0.980 (389)	13.3	94.38	**93 ± 10**	12.64 ± 0.12 (97)	1.93
JT03-77	Beaufort			1005.84	30	1.072 (4390)	6.002 (348)	1.407(816)	16.4	63.9	**82 ± 5**	12.45± 0.17 (100)	1.75
JT03-78	Beaufort			1310.64	21	1.099 (4390)	4.183 (205)	1.02 (500)	11.6	9.58	**82 ± 8**	12.39 ± 0.2 (102)	2.06
JT03-79	Beaufort			1659.64	30	1.125 (4390)	5.053 (455)	1.197 (1078)	13.3	81.58	**85 ± 5**	11.92 ± 0.2 (100)	2.01
JT03-81	Beaufort			2357.63	16	1.179 (4390)	5.279 (173)	1.523 (499)	16.1	42.66	**74 ± 7**	11.72 ± 0.2 (99)	2.0
JT03-82	Ecca	~275-252		2725.52	15	1.205 (4390)	6.135 (180)	1.755 (515)	18.2	87.27	**76 ± 7**	10.9 ± 0.2 (101)	2.65
JT03-83	Ecca			3063.24	17	1.232 (4390)	4.231 (104)	1.827 (449)	18.5	10.68	**53 ± 7**	10.0 ± 0.34 (55)	2.51
JT03-84	Ecca			3516.48	4	1.258 (4390)	3.204 (23)	1.532 (110)	15.2	29.79	**47 ± 11**	8.63 ± 0.46 (42)	3.0
JT03-86	Ecca			4179.72	31	0.948 (4137)	1.649 (92)	1.769 (987)	23.3	0.66	**19 ± 3**	8.12 ± 0.26 (81)	2.33
JT03-88	Dwyka	~350- 270		4664.35	30	0.989 (4137)	0.644 (66)	1.493 (1530)	18.9	82.82	**8 ± 1**	8.53 ± 0.36 (36)	2.15
JT03-89	Dwyka			4969.76	30	1.009 (4137)	0.425 (44)	1.501 (1554)	18.6	6.13	**5 ± 1**	7.59 ± 0.52 (38)	3.19
JT03-90	Dwyka			5215.74	9	1.03 (4137)	0.1 (5)	0.711 (356)	8.6	81.87	**3 ± 1**		
CR1/68			32.4833, 25.0167										
JT03-91	Beaufort	~252-238		205.74	33	1.05 (4137)	6.704 (306)	1.31 (598)	15.6	79.01	**97 ± 7**	12.86 ± 0.21 (100)	2.08
JT03-92	Beaufort			353.87	28	1.071 (4137)	7.209 (234)	1.565 (508)	18.3	93.17	**89 ± 7**	12.67 ± 0.27 (64)	2.16
JT03-93	Beaufort			803.15	30	1.091 (4137)	5.281 (471)	1.063 (948)	12.2	78.41	**98 ± 6**	11.66 ± 0.22 (101)	2.23
JT03-94	Beaufort			1179.88	17	1.111 (4137)	5.415 (120)	1.164 (258)	13.1	92.44	**93 ± 10**	11.32 ± 0.36 (56)	2.67
JT03-95	Beaufort			1829.41	15	1.132 (4137)	4.683 (114)	1.035 (252)	11.4	82.18	**92 ± 11**	11.04 ± 0.29 (77)	2.56
JT03-96	Ecca	~275-252		2146.10	29	1.152 (4137)	5.767 (216)	1.786 (669)	19.4	0.67	**74 ± 8**	11.19 ± 0.52 (23)	2.51
JT03-100	Ecca			3446.37	13	1.172 (4137)	3.825 (77)	1.51 (304)	16.1	2.86	**56 ± 10**	9.25 ± 0.67 (13)	2.42

Table 4.2b: Age and track length data for borehole samples. Numbers in brackets show number of tracks counted and measured. Standard and induced track densities measured on mica external detectors and fossil track densities on internal grain surfaces. FT ages calculated using the zeta method for dosimeter glass CN-5 (362 ± 21). § All FT ages are central ages, † One sigma error used. * Slides recounted at the University of Cape Town. References for strat. ages in Chapter 2.

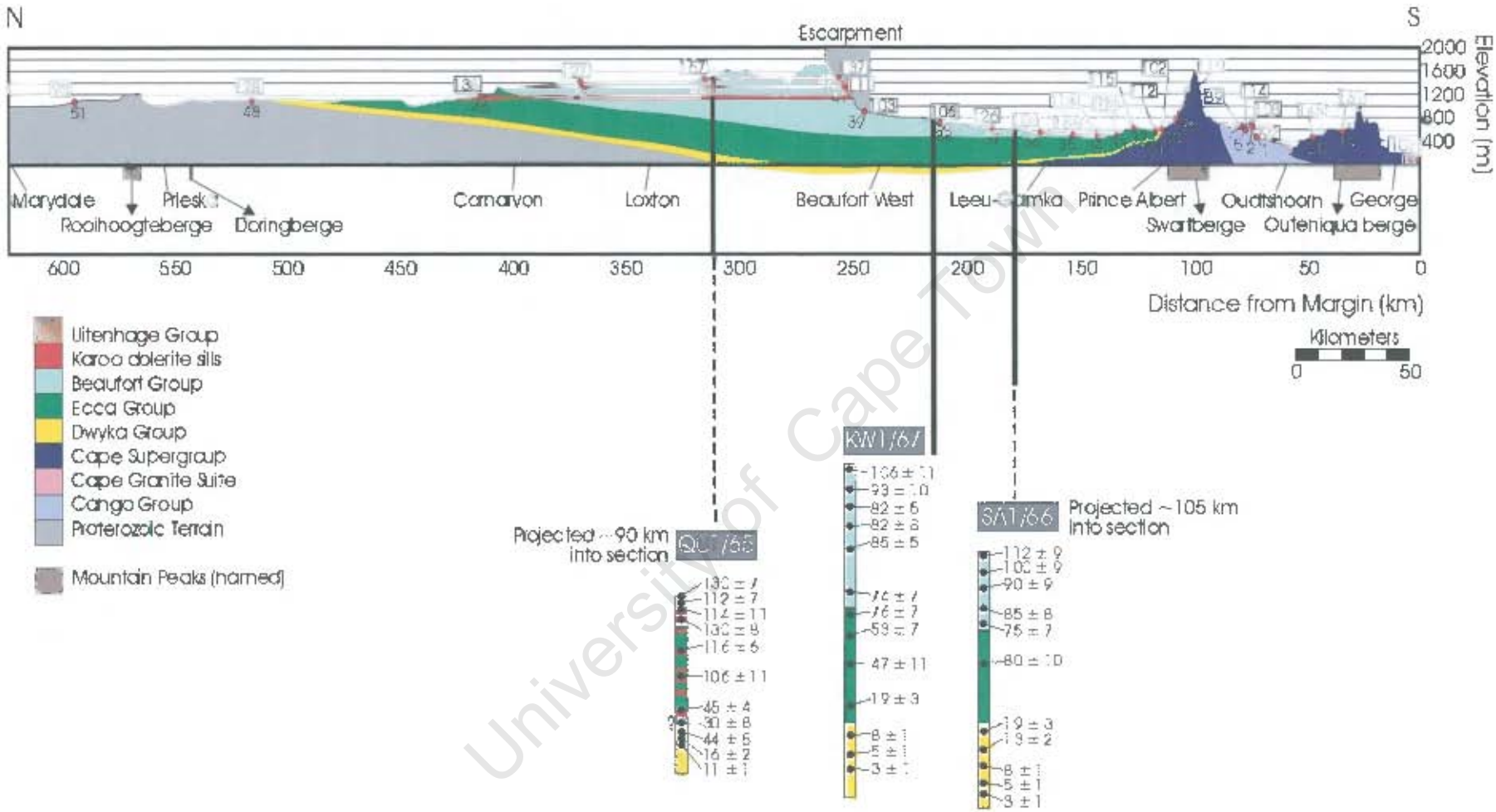

Figure 4.7: Geological cross-section of study transect showing location (red dots) and fission track age (box above) of outcrop samples. Outcrop ages vary between 89 and 157 Ma. The oldest ages are from the top of the escarpment.

4.3.1.2.a Interpretation

Key first points arising from data:

1. All outcrops samples have fission track ages that are younger than their stratigraphic ages. This indicates that all samples have experienced elevated paleotemperatures.
2. All outcrops samples have Cretaceous fission track ages, implying that significant cooling of up to and possibly exceeding 110 ± 10°C has occurred since this time. Owing to the distance of these samples from the rift margin (up to 600 km), cooling is unrelated to the thermal processes related to rifting. Cooling of this onshore region is more likely to be related to its denudation (see Gallagher and Brown, 1999b).
3. The lack of AFT Tertiary ages for outcrop samples indicates that *major* cooling was over by ~65 Ma.
4. All outcrop samples have a chi^2 value of >> 5 %. Thus the distribution of single grain ages measured in each sample is consistent with them being from a population with a single age. Any possible differences in apatite chemistry, for example chlorine content, have not resulted in a wide spread of single grain ages.
5. The tail of shorter tracks present in most track length distributions may indicate a prolonged residence time of the sample within the partial annealing zone. Alternatively short tracks could be retained from a prior thermal history implying that the sample has not been completely reset. However, dolerite samples JT02-41 and 44 (the latter from an elevation of 1460 m) that intruded the Karoo sediments at 183 ± 1 Ma (Duncan, 1997), *also* have a tail of short tracks (Figure 4.8) that cannot be inherited. Therefore all short tracks below this elevation (which includes all the outcrop and borehole samples) must be due to prolonged residence time, at relatively high temperatures, within the partial annealing zone.
6. The shortest tracks measured from the dolerite samples are indicative of the maximum temperature to which the sample has been subjected. Sample JT02-41 (at elevation of 1326 m) has several tracks in the 3-4 µm range, reflecting highly elevated paleotemperatures (~>90°C). Thus all samples at elevations <1326 m have likely experienced temperatures near to, or above 110°C.

7. Below this elevation all single grain ages for all samples are younger than their stratigraphic age, further substantiating the total resetting of all samples below ~1300 m.

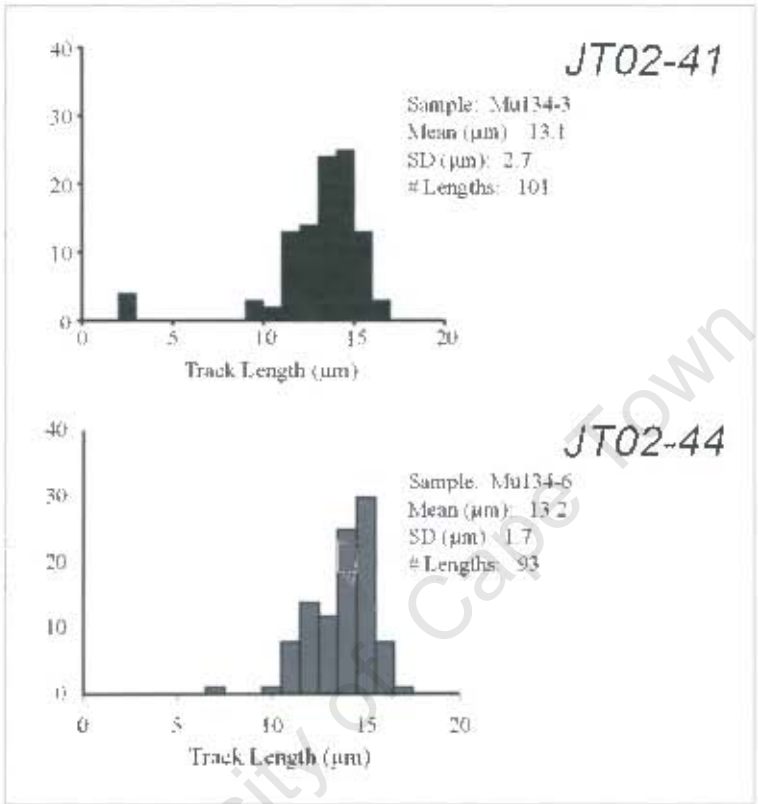

Figure 4.8: Negatively skewed, track length distribution of two Karoo dolerite samples, JT02-41 and 44, showing tail of short tracks that signal prolonged residence time at elevated temperatures.

4.3.1.3 Borehole samples

A total of 31 samples were analysed from the boreholes SA1/66, KW1/67 and CR1/68 (red crosses on figure 4.6). Samples were taken at an interval of ~300 m.

4.3.1.3.a Borehole SA1/66

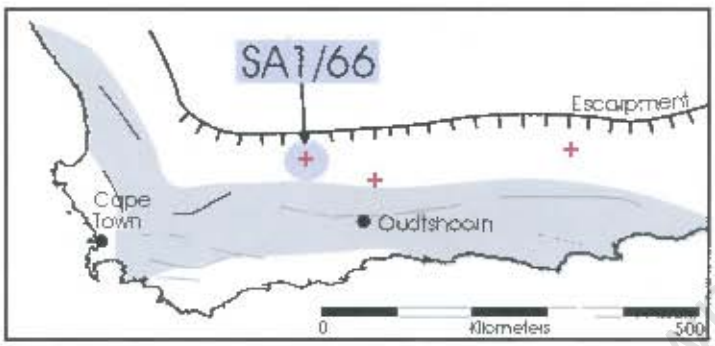

Figure 4.9: Location of borehole SA1/66. Grey= the extent of the Cape Fold Belt.

Borehole SA1/66 is located ~20 km from the Northern Cape/ Western Cape border and ~115 km NW of Oudtshoorn (Figure 4.6, 4.7, 4.9). The top of the borehole is at 738 m above sea level. The borehole intersects samples from the Beaufort Group (samples JT03-60 to 64), the Ecca Group (JT03-66) and the Dwyka Group (JT03-69, 71, 72, 73 and 74). All apatites were extracted from solid core samples.

Fission track ages for the 11 samples of SA1/66 show a non-linear decrease in age with increasing depth (curve in Figure 4.10), from 112 ± 9 Ma near surface to 3 ± 1 Ma at 4104 m depth. The curve has inflection points (*'s, Figure 4.10) at ~1500 m and ~2750 m. The curve is convex up between 0 and ~1500 m, concave up between ~1500 and ~2750 m and convex up again below ~2750 m. Mean track lengths decrease with increasing depth, from 12.7 ± 0.2 μm to 5.45 ± 0.71 μm. Like the outcrop samples, the borehole samples are negatively skewed and have a tail of shorter tracks. This dispersed track length distribution is shown in standard deviations that vary between 1.88 μm and 3.12 μm. For the latter sample though, only 19 track lengths were measured. 3 samples below a depth of 3000 m failed the chi^2 test. This probably reflects the inclusion of single '0' aged grains into the central age count. Radial plots (Appendix C-1f and g) show good clustering of the single grain ages of these samples that failed the chi^2 test.

Sample Number	Depth (m)	Age (Ma)	Error on age (Ma)	Length (µm)	Error on length (µm)
JT03-60	28.35	112.1	9.3	12.7	0.2
JT03-61	319.43	100.3	9.1	12.44	0.22
JT03-62	602.28	89.6	8.1	12.43	0.19
JT03-63	941.22	85	8.1	12.34	0.23
JT03-64	1210.06	75.2	7	12.53	0.24
JT03-66	1880.62	79.9	10	12.11	0.24
JT03-69	3037.33	18.8	2.7	9.82	0.21
JT03-71	3350.97	13	2.3	10.04	0.21
JT03-72	3635.65	8	1.1	8.51	0.49
JT03-73	3921.86	5	0.9	8.83	0.3
JT03-74	4104.44	3.1	1.3	5.45	0.71

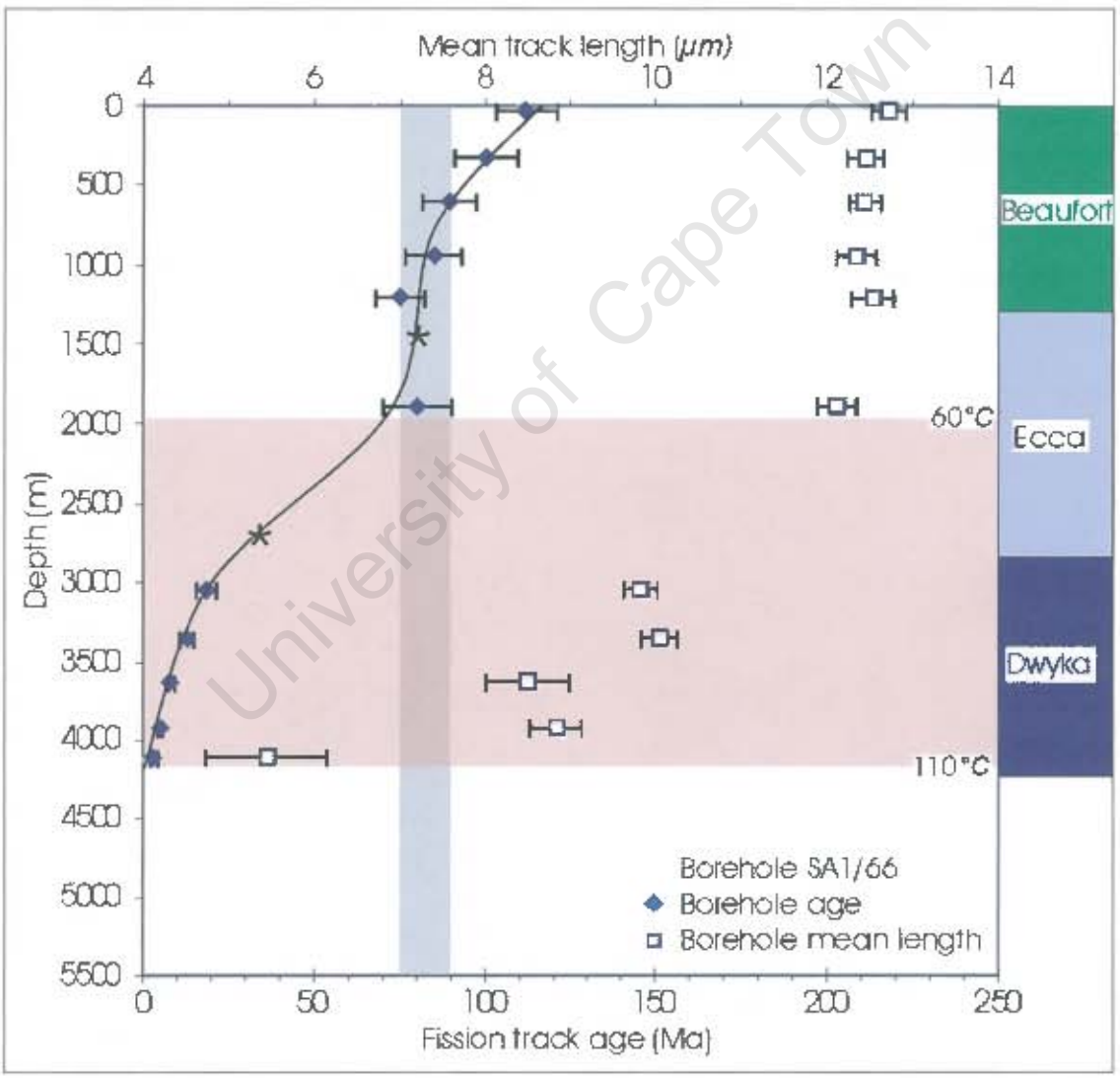

Figure 4.10: Age-depth-mean track length plot of borehole SA1/66. Pink shading= PAZ (measured, Gough, 1963). Grey shading= rapid cooling (see section 4.3.1.3.d). *: see text.

4.3.1.3.b Borehole KW1/67

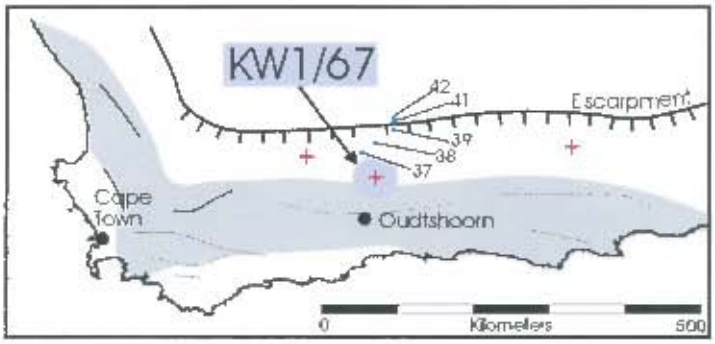

Figure 4.11: Location of borehole KW1/67. Blue squares show the location of the 5 outcrop samples projected into the borehole profile (Figure 4.12). Grey= the extent of the Cape Fold Belt.

Borehole KW1/67 is located nearest to the outcrop transect, ~55 km NNE of Oudtshoorn (Figure 4.11). It is over 5500 m deep, though the deepest sample of 13 in total was acquired at ~5200 m. The top of the borehole is at 964 m above sea level. Like SA1/66, KW1/67 is <70 km south of the escarpment. It intersects rocks of the Beaufort Group, Ecca Group and bottoms out in the Dwyka Group. The Dwyka/ Ecca contact is ~1500 m deeper here than it is in SA1/66, ~120 km to the WNW. Apatites of JT03-76, 77, 78, 81 and 83 are from percussion chip samples, the remainder are from solid core.

Figure 4.12 shows the elevation of KW1/67 borehole samples rather than their depth below the surface as in figure 4.10 (borehole SA1/66). The profile has been extended by the addition of 4 outcrop samples of differing elevations, all located within 60 km of KW1/67 (blue squares on figure 4.12).

Apatite ages from borehole KW1/67 decrease with increasing depth (Figure 4.12). Fission track ages of outcrop samples range from 137 ± 20 Ma to 103 ± 6 Ma. The shallowest borehole sample, JT03-75 (394 m depth) has a fission track age of 106 ± 11 Ma, the deepest, JT03-90 (5216 m depth) has a fission track age of 2.6 ± 1.2 Ma. Similarly to SA1/66, this relationship is non-linear, and the curve (Figure 4.12) is of the same shape as that of SA1/66 (Figure 4.10). The curve (including the outcrop samples) has three inflection points (*'s, Figure 4.12) at +300 m elevation (~600 m

depth), –1500 m elevation (~2500 m depth) and –3000 m elevation (~4000 m depth). The latter two inflection points are at greater depths than those of SA1/66 (~1.5 km and ~2.75 km, Figure 4.10).

Mean track lengths decrease with increasing depth from 13.1 ± 0.26 μm (outcrop sample) to 12.68 ± 0.19 μm (top borehole sample) to 7.59 ± 0.52 μm (deepest borehole sample). Track length distributions are varied between unimodal for the samples <2400 m depth (standard deviations between 1.8 and 2.1 μm) to more broadly distributed for samples >2400 m depth (standard deviations between 2.2 and 3.2 μm). These latter high standard deviations may reflect the low number of tracks counted for samples at greater depth. The track distributions of all samples are negatively skewed with a tail of short track lengths. Tracks as short as ~4 μm are measured from samples at only ~700 m depth.

All samples pass the chi^2 test (except JT03-86) and are thus statistically part of the same population. The radial plot for JT03-86 sample shows good clustering of the single grain ages. Thus, as for the three deep samples of SA1/66, failure of the chi^2 test in this case may be due to the inclusion of several '0' aged grains in the central age calculation.

Sample Number	Depth (m)	Age (Ma)	Error on age (Ma)	Length (µm)	Error on length (µm)
JT02-42	1487	136.9	19.7		
JT02-41	1326	111.4	12.2	13.1	0.26
JT02-39	903	103	6	12.6	0.17
JT02-38	734	106.1	7.6	12.7	0.22
JT02-37	623	126.1	8.3	13	0.19
JT03-75	575.1694	106.1	10.7	12.7	0.19
JT03-76	256.04381	92.6	9.9	12.6	0.12
JT03-77	-36.564182	82.2	5.4	12.5	0.17
JT03-78	-341.38417	82.1	7.9	12.4	0.2
JT03-79	-690.36016	85.4	4.9	11.9	0.2
JT03-81	-1388.3521	73.5	6.6	11.7	0.2
JT03-82	-1756.2457	75.8	6.7	10.9	0.2
JT03-83	-2093.9641	52.8	6.5	10	0.34
JT03-84	-2547.2017	47	11.2	8.6	0.46
JT03-86	-3210.4465	18.5	2.5	8.1	0.26
JT03-88	-3695.0785	7.7	1	8.5	0.36
JT03-89	-4000.4881	5.2	0.8	7.6	0.52
JT03-90	-4246.4616	2.6	1.2		

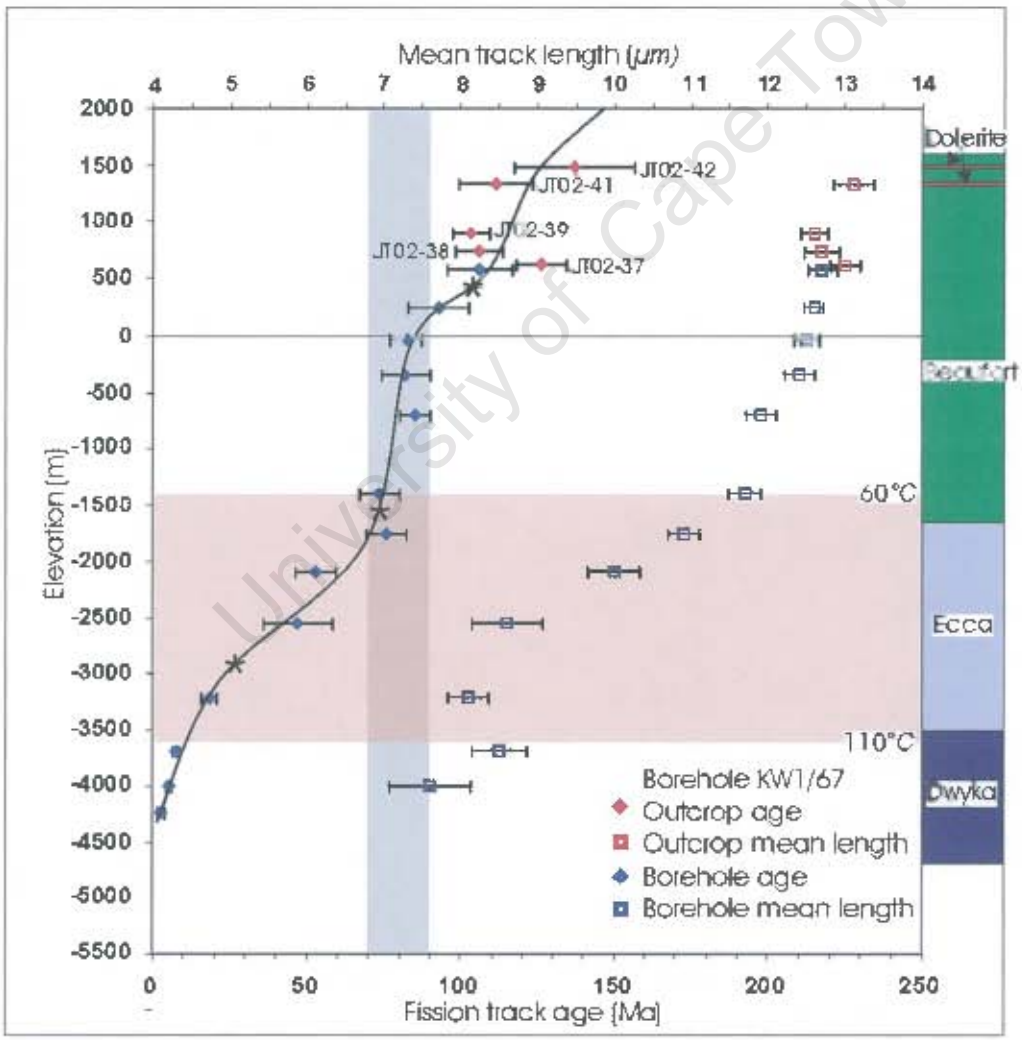

Figure 4.12: Age-depth-mean track length plot of borehole KW1/67. Top of borehole at 969 m elevation. Pink shading= PAZ (measured, Gough, 1963). Grey shading= rapid cooling (see section 4.3.1.3.d). *: see text.

4.3.1.3.c Borehole CR1/68

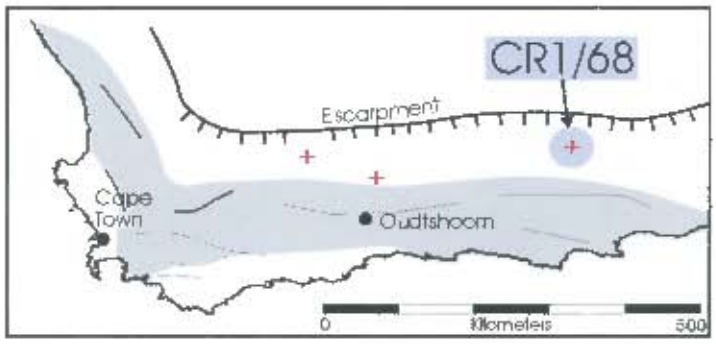

Figure 4.13: Location of borehole CR1/68. Grey= the extent of the Cape Fold Belt.

Borehole CR1/68 is ~300 km ENE of Oudtshoorn, ~400 km E of SA/166 and ~280 km E of KW1/67 (Figure 4.13). Like KW1/67 and SA1/66, CR1/68 is located south of the escarpment (~30 km). The top of the borehole is at 793 m above sea level. 7 samples were analysed, of which all but 2 were from the Beaufort Group. JT03-96 and 100 were from the Ecca Group. Samples JT03-91 and 93 are percussion chip samples, the remainder are solid core.

Fission track ages decrease with increasing depth from 97 ± 7 Ma at 206 m to 56 ± 10 Ma at 3446 m (Figure 4.14). The curve of decreasing age with increasing depth is shown in figure 4.14. The youngest ages (<20 Ma) encountered at depths of > 3000 m in SA1/66 and > 4000 m in KW1/67 are not intersected by CR1/68 and this may account for the lack of the second (deeper) inflection point noted at 2750 m and 4000 m for SA1/66 and KW1/67, respectively. The shallower inflection point noted from these two other curves is also less distinct in CR1/68, but there is a break in slope at ~2250 m (* in Figure 4.14).

Mean track lengths are between 12.86 ± 0.21 and 9.25 ± 0.67 µm. Track length distributions are highly variable, though again, all have a tail of short tracks. A track of ~3 µm was measured from JT03-91 at only 206 m depth. Standard deviations for track length distributions vary from 2.1 to 2.6 µm. All but the two deepest samples (JT03-96 and 100) pass the chi^2 test. Single grain ages of up to ~200 Ma were measured for JT03-96 and from 0 Ma up to ~ 160 Ma for JT03-100. Therefore these last two samples are not composed of grains of two single statistical populations. This may be

due to differences in apatite mineral chemistry and thus in annealing characteristics. Unfortunately, the chemical composition of these two samples is unknown.

Sample Number	Depth (m)	Age (Ma)	Error on age (Ma)	Length (μm)	Error on length (μm)
JT03-91	205.73999	96.9	7.1	12.86	0.21
JT03-92	353.87279	88.6	7.1	12.67	0.27
JT03-93	803.14797	97.9	5.9	11.66	0.22
JT03-94	1179.8808	92.9	10.4	11.32	0.36
JT03-95	1829.4095	92	10.5	11.04	0.29
JT03-96	2146.0967	73.8	7.9	11.19	0.52
JT03-100	3446.3735	53.5	7.5	9.25	0.67

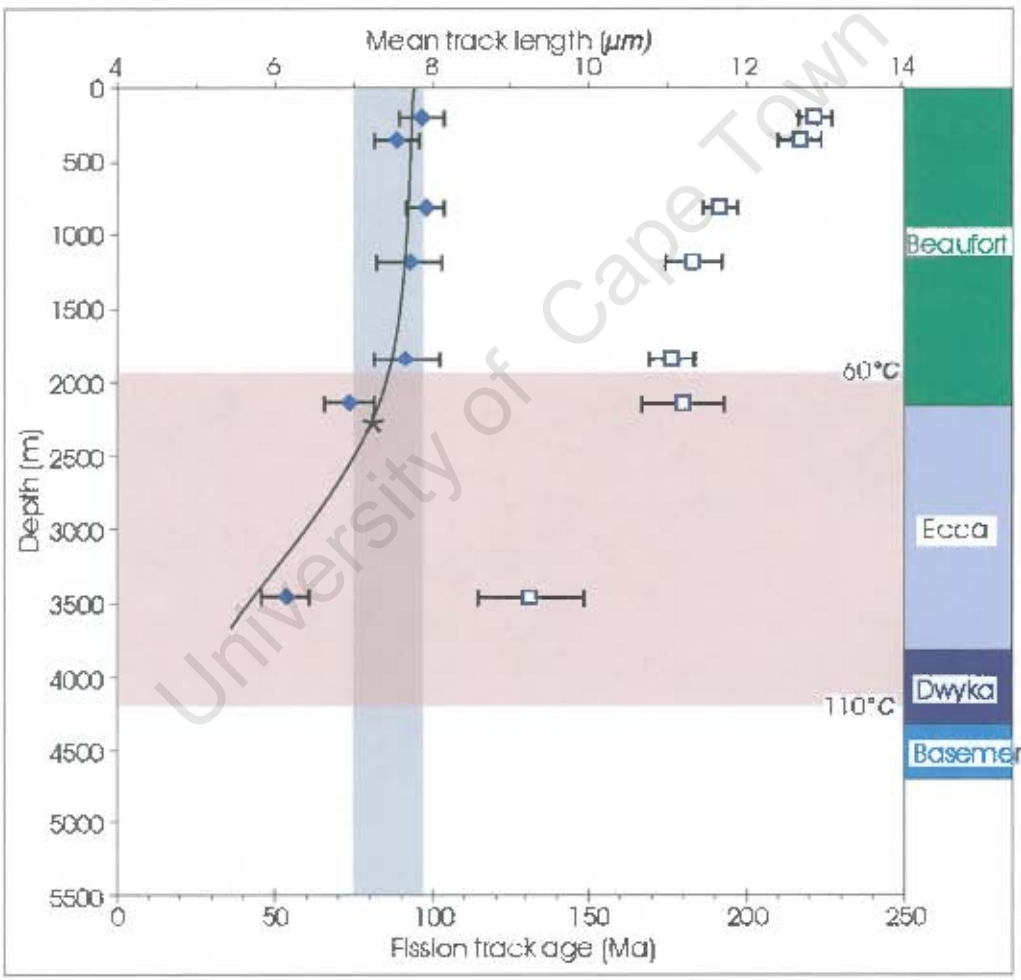

Figure 4.14: Age-depth-mean track length plot of borehole CR1/68. Pink shading= PAZ (measured, Gough, 1963). Grey shading– rapid cooling (see section 4.3.1.3.d). *: see text.

4.3.1.3.d Interpretation

Key first points arising from the data

1. All borehole samples have fission track ages that are significantly younger than their stratigraphic ages, indicating that the samples have experienced elevated paleotemperatures.
2. All samples from the three boreholes have been reset (as explained in section 4.3.1.2). The elevation of the top most sample from all the borehole samples is ~710 m, which is ~600 m lower in elevation than lowest dolerite sample from which short tracks were measured (JT02-41, 1326 m).
3. The presence of very short tracks (eg. 3-4 μm in JT03-91) in shallow samples (205 m for JT03-91) suggests a period of slow cooling through the PAZ. Measuring of track lengths is biased towards the longer track lengths (Green, 1988) therefore even one or two measured short tracks are significant.
4. The gradient of decreasing age with increasing depth (equivalent to the cooling rate) is non-linear.
5. This gradient provides a first estimate of cooling history that is expanded in chapter 4.5 and 5. The shallow gradient at <500 m depth for SA1/66 indicates slow cooling between ~112 and 90 Ma. Similarly, the shallow gradient at depths <750 m for KW1/67 indicates slow cooling from >106 to 90 Ma. The age-depth curve for all three boreholes steepens indicating maximum cooling rates between 90 and 75 Ma (SA1/66), 90 and 70 Ma (KW1/67) and >97 and 74 Ma (CR1/68) (grey shading in Figures 4.10, 4.12 and 4.14). Cooling rates decrease again after ~70 to 75 Ma at depths from 2250 m (SA1/66) to 2800 m (KW1/67). Beyond ~2 km the age-depth curve reflects the present day transition to the partial annealing zone (>60°C). The calculation of the present day geothermal gradient is given in section 4.5.
6. The steep gradient through 4 outcrop samples added to borehole profile KW1/67 shows an earlier period of accelerated cooling between ~137 and 110 Ma.

4.3.2 Halide chemistry of the apatites from microprobe results

Probe results listed in table 4.1 show that the average chlorine content for all the Beaufort Group samples is higher (0.6, 0.49, 0.44 wt%) than that of the standard, Durango (0.43 wt%). Individual apatite grains within each Beaufort sample show great

variability in Cl content. For example, in JT03-60, Cl content varies from 0 to 2.2 wt%. Ecca Group samples are lower in Cl than the standard Durango (0.27, 0.09). The Dwyka Group apatites have the lowest average Cl content of 0.02 to 0.06 wt%. Apatite mineral chemistry has been shown to have an effect on its annealing characteristics (see section 4.1.3.3). Further discussion on how chemistry may affect these samples fission track age follows in section 4.4.

Table 4.2a Chlorine data for selected samples determined by microprobe. Strat* row denotes samples' stratigraphic group: B= Beaufort Group, D= Dwyka Group, E= Ecca Group. Analytical uncertainty given in table 4.2b below.

Grain #	Boreholes									Dolerites		
	Borehole SA1/66		Borehole KW1/67									
	JT03-60	74	75	77	79	82	86	88	89	41	44	46
Strat.*	B	D	B	B	B	E	E	D	D			
1	0.90	0.05	0.03	0.77	0.70	0.14	0.01	0.00	0.00	0.65	1.29	0.48
2	0.04	0.00	0.42	0.05	0.85	0.36	0.03	0.00	0.04	0.68	1.20	0.16
3	0.00	0.02	0.22	0.99	0.66	0.45	0.11	0.04	0.01	0.35	1.04	0.07
4	0.75	0.00	1.59	0.30	0.61	0.15	0.18	0.02	0.02	0.99	1.15	0.29
5	2.2	0.09	1.29	0.07	0.13	0.40	0.22	0.01	0.02	0.80	1.20	0.59
6	0.55	0.04	1.05	0.06	0.04	0.11	0.01	0.06	0.00	0.55	1.17	0.49
7	0.68	0.00	0.67	0.38	0.00	0.00	0.19	0.00	0.05	0.50	1.06	0.35
8	0.83	0.03	0.04	0.82	0.51	0.45	0.18	0.00	0.00	0.55	1.03	0.43
9	0.86	0.29	0.02	0.06	0.75	0.07	0.01	0.02	0.02	0.52	1.09	0.45
10	0.05	0.02	0.60	0.54	0.00	0.72	0.05	0.00	0.00	0.84	1.00	0.45
11	0.92	0.00	1.02	0.64	0.71	0.31	0.21	0.02	0.25	0.83	1.02	0.39
12	0.97	0.00	0.13	0.37	0.47	0.00	0.05	0.07	0.00	0.70	1.17	0.52
13	0.51	0.16	0.16	0.07	0.34	0.42	0.00	0.06	0.00	0.82	0.88	0.37
14	0.42	0.04	0.13	1.07	0.10	0.43	0.02	0.06	0.00	0.66	1.00	0.22
15	0.37	0.05	0.58	0.86	0.39	0.00	0.17	0.04	0.00	0.60	1.17	0.25
16	0.03	0.03	0.25	0.68	0.43		0.09	0.00	0.02	0.30	0.92	0.55
17	0.49	0.00	0.43	0.2	0.41		0.04	0.00	0.00	0.64	1.04	
18	1.2	0.26	0.75	0.28	0.80		0.05	0.00	0.04	0.24	0.91	
19	0.23	0.02	0.26	0.85	0.47		0.04	0.08	0.00	0.74	1.30	
20	0.06		0.09	0.67	0.44			0.00	0.00	0.77	1.30	
Ave. Chlorine	0.60	0.06	0.49	0.49	0.44	0.27	0.09	0.02	0.02	0.64	1.09	0.36

Table 4.2b: Percent errors in chlorine content (P.Green, pers comm.. 2005)

Chlorine content wt%	0.01	0.02	0.05	0.1	0.2	0.5	1.0	1.5	2.0	2.5	3.0
Error (%)	9.3	8.7	7.3	6.1	4.7	3.2	2.3	1.9	1.7	1.5	1.4

4.4 Interpretation of the fission track data

4.4.1 Outcrops

Outcrops sampled over large lateral distances are more difficult to use than borehole samples when constructing a regional thermal history. This is because a ~4 km borehole is less likely to intersect faults, across which the thermal history may differ, than a ~600 km long horizontal transect. Rapid changes in outcrop fission track ages over short lateral distances may be due to elevation changes between samples (thus, recording a different section of thermal history), or to reactivation of faults originally associated with the assembly and break up of Gondwana or to faulting associated with the intrusion of dolerite sills and dykes, north of the Cape Fold Belt. Section 4.4.1.4 details an example of a change in fission track age across the Cango inlier.

4.4.1.1 Fission track age vs. elevation

A close examination of how mean track length, standard deviation of length etc. varies with fission track age can aid in the interpretation of the outcrop data.

For the outcrop samples, there is a tentative correlation between age and elevation (Figure 4.15) and the best-fit linear regression gives an r^2 value of 0.1737. A general rule in a simple thermal history of uninterrupted, constant denudation is that a sample from a high elevation cools through the closure temperature earlier, hence has the oldest age. In this study, however the correlation between age and elevation is tentative, perhaps indicating a more complicated thermal history. Due to the length of the sampled transect (~600 km), all samples along this transect are unlikely to have had the same simple thermal history. For example, the sample transect crosses the Great Escarpment. The landscapes seaward and landward of this divide have likely had different denudation histories (Chapter 3).

Borehole data on the other hand show a clear decrease in fission track age with depth below surface (Figures 4.10, 4.12, 4.14). This is not surprising given that, if we assume that there are no low angle faults that cut the borehole, there is no horizontal separation between samples. Provided the borehole does not transect faults at depth, structure plays no role in 'disturbing' fission track ages as it may do between outcrop samples. Several samples from a single borehole should reflect a single thermal history, a point that is important when modelling such data (section 4.5).

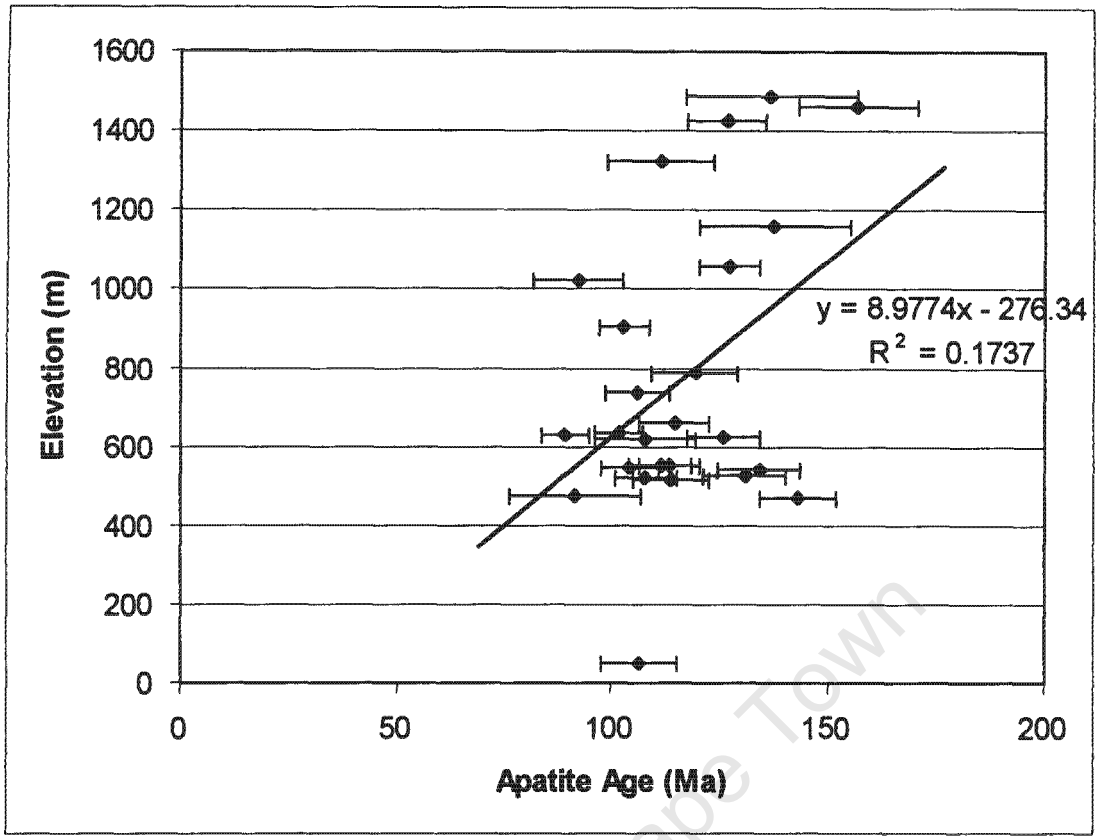

Figure 4.15: Graph of fission track age versus elevation for outcrop samples. Equation of the linear regression trend is as shown. R^2 of linear trend= 0.1737.

4.4.1.2 Fission track age vs. distance from the margin

If King was correct in his suggestion of constant rate of escarpment retreat since its formation (see Chapter 3), then the associated denudation (and cooling) first occurred adjacent to the rift margin and progressed inland. In this scenario the oldest fission track ages are from samples closest to the rift margin, and the youngest closest to the escarpment. The outcrop sample's fission track ages are not correlated to distance from the margin (Figure 4.16), showing that the escarpment has not retreated slowly since the Cretaceous. The fission track evidence suggests that if the escarpment had retreated, its retreat was rapid and took place shortly after rifting. Therefore King's model cannot be correct.

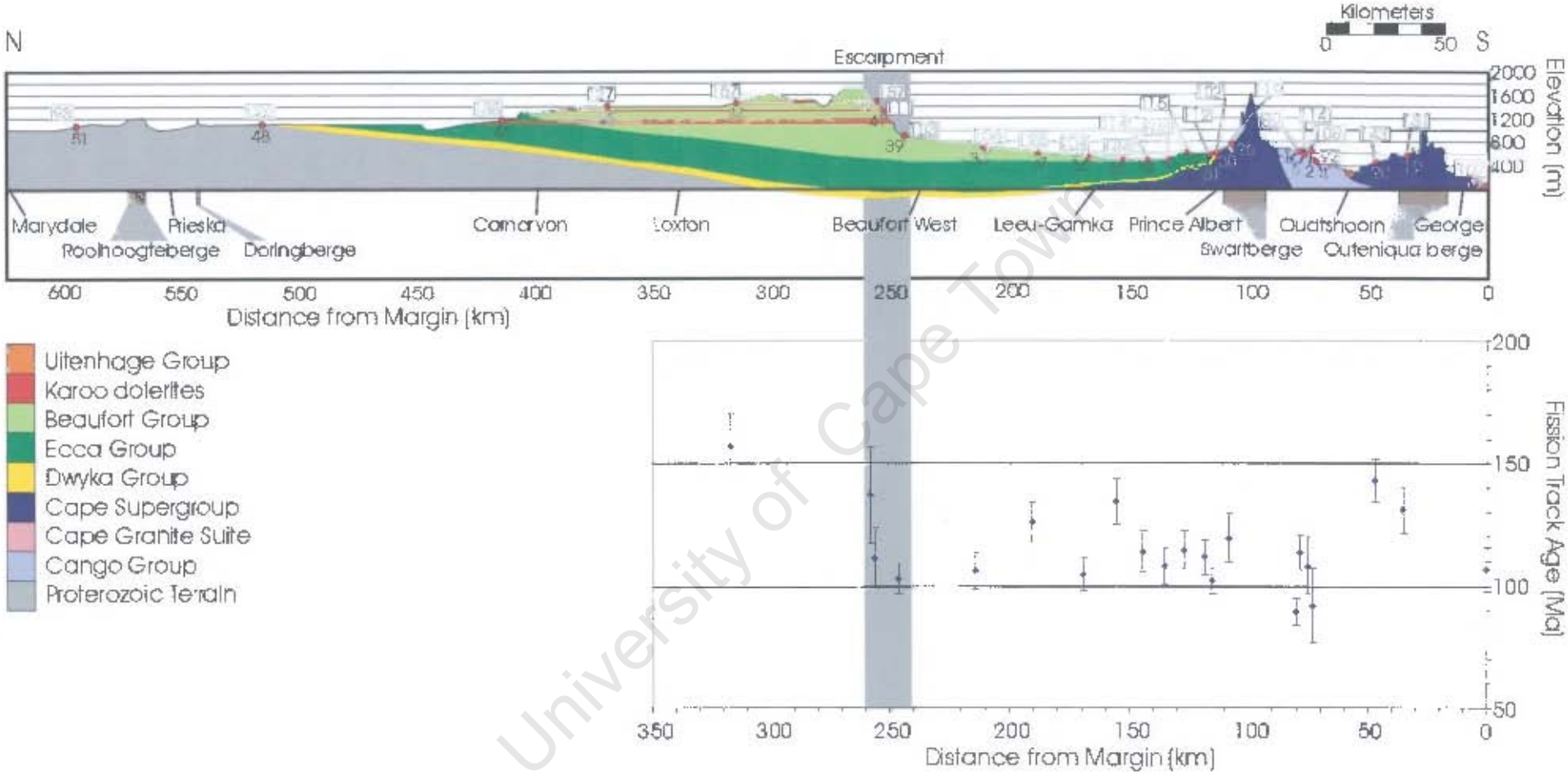

Figure 4.16: Fission track age vs. distance from the margin for outcrop samples. Note the lack of correlation between fission track age and distance from the margin. The oldest ages are measured from the top of the escarpment, e.g. 156.8 ± 13.7 Ma (JT02-44) and a group of younger ages is measured for the Cango inlier (see section 4.4.1.6).

4.4.1.3 Mean track length vs. fission track age (Boomerang plots)

The variation in mean track length with fission track age for the outcrop samples of this study is shown in figure 4.17. No "boomerang" trend is evident (described in section 4.1.4.3), suggesting that the denudation history recorded by the outcrop samples from varying elevations does not reflect a simple one-phase denudation. All the outcrops sampled in the study are completely reset (see Chapter 4.3.1.2.a, point 5) therefore sample 1 (from Figure 4.5, section 4.1.4.3) has been eroded. In addition, there has been more than one period of accelerated denudation. In one possible scenario, the deepest sample (3 in figure 4.5) cools rapidly during a first phase of accelerated denudation to temperatures still >60°C. Denudation slows, resulting in track annealing. A second phase of increased denudation then brings the sample to the surface. Mean track length of this sample (3 in figure 4.5) and others below it, therefore depends on the length of time in the PAZ and the temperature at which annealing occurred. Again, because the sample transect extends over ~600 km, a single thermal history is unlikely to be shared by all the samples.

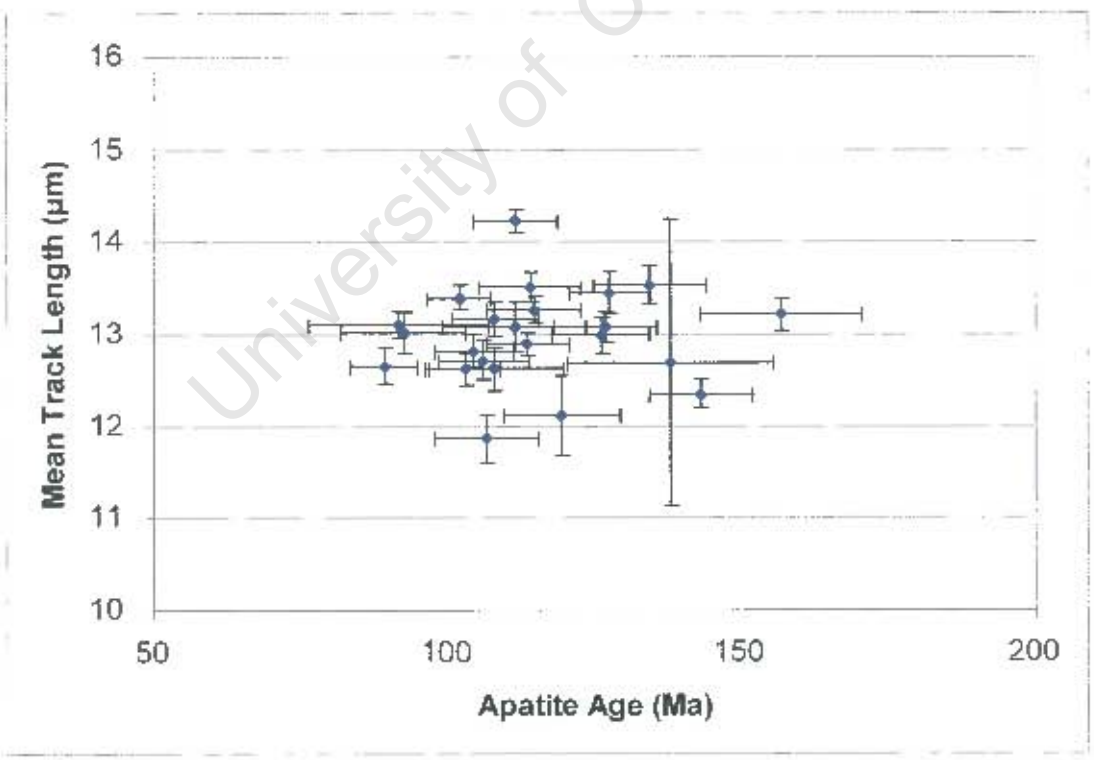

Figure 4.17: Graph of mean track length vs. fission track age for outcrop samples.

4.4.1.4 Mean track length vs. standard deviation of track lengths

Figure 4.18 shows the comparison between mean track length and standard deviation of the track length distribution of the outcrop samples. Standard deviation is high when the track lengths are broadly distributed. Regionally there is an inverse relationship between mean track length and standard deviation (excepting the George granite sample (JT02-14) from which only 28 lengths were measured). This suggests that there is a factor controlling both the mean track length and its standard deviation. This may reflect the anisotropy of track shortening. Those tracks that are oriented perpendicular to the crystallographic C-axis will anneal faster that those that are parallel to the c-axis (Brown, 1992). Thus the higher the temperature to which a sample is subjected, the greater the degree of annealing, the shorter the mean track length and the larger the standard deviation as those tracks oriented perpendicular to the C-axis will anneal faster.

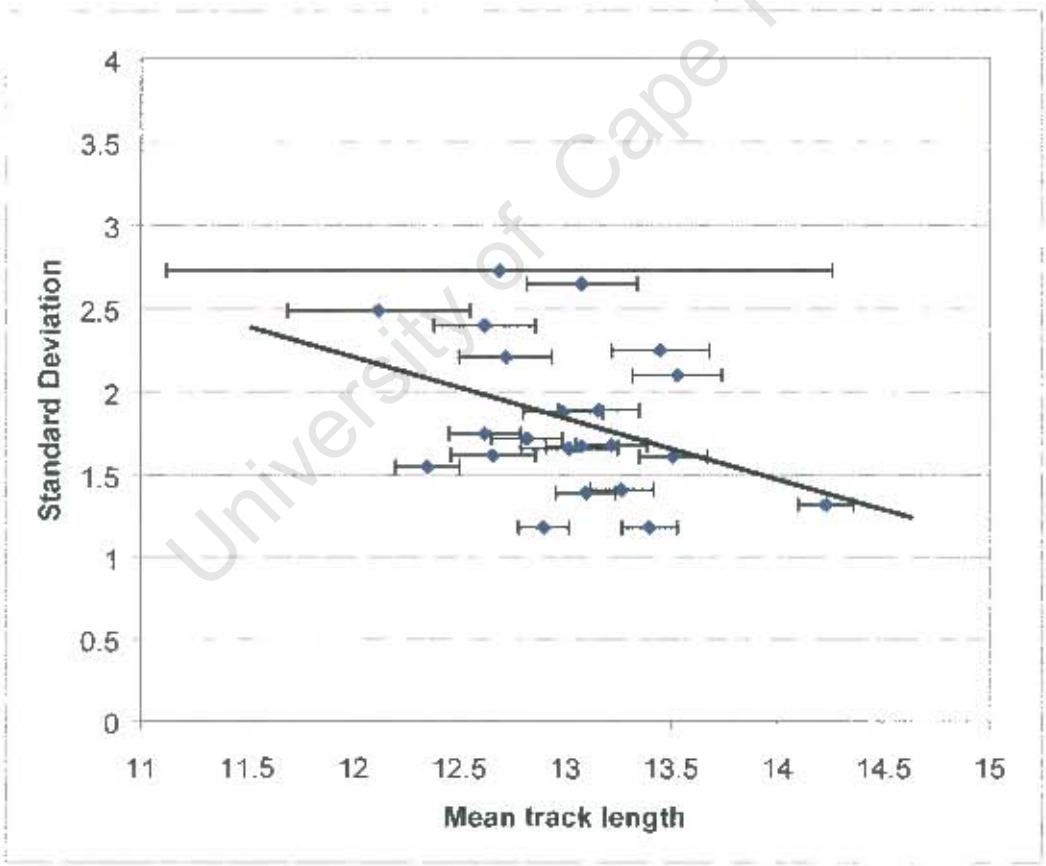

Figure 4.18: Graph of mean track length vs. standard deviation for outcrop samples. Regression line is drawn omitting JT02-14 where only 28 track lengths were measured. R^2 of linear trend = 0.1356.

Other factors that may influence track length distribution include the apatite's chemical composition and/ or protracted cooling within the PAZ. Individual grains of variable apatite composition within a sample increase the standard deviation of the track length distribution of that sample (as tracks within more Cl-rich grains anneal more slowly) but are unlikely to result in a simultaneous decrease in mean track length. Extended residence of the sample within the PAZ, however, will both decrease the fission track age (by shortening the newly forming tracks) and increase the standard deviation (because each newly added track will have experienced a different maximum temperature therefore will be of different length). Thus the samples have likely cooled slowly through the PAZ.

4.4.1.5 Standard deviation of track lengths vs. Chi^2 (%)

Comparing standard deviation of track length distribution to the samples chi^2(%) value (an indication of whether the grains are from one population) may help to understand the reasons for track length dispersion. Apatite compositional variations and/or the presence of inherited tracks are two possible causes of a broad track length distribution (high standard deviation). An increase in standard deviation caused by either of the above would also be accompanied by a decrease of the chi^2(%) of the sample. A sample with inherited tracks or varying apatite chemistry may thus have both a broad track length distribution (standard deviation) and a low chi^2(%) value (because the single apatite grains are not part of the same population).

An inverse correlation between standard deviation and chi^2 value suggests that track length dispersion may be related to apatite composition or incomplete thermal resetting. Figure 2.19 shows no inverse correlation between standard deviation and chi^2(%).This suggests that the factor influencing standard deviation of the track length distributions and the sample's chi^2(%) is not apatite chemistry, or the presence of inherited tracks. An alternative control on the standard deviation of track lengths is protracted cooling within the PAZ. This will increase the standard deviation of the track length distribution without altering its chi^2(%). Protracted cooling, therefore, may be a better explanation for the outcrop sample's wide dispersion of track lengths (and correspondingly high standard deviation).

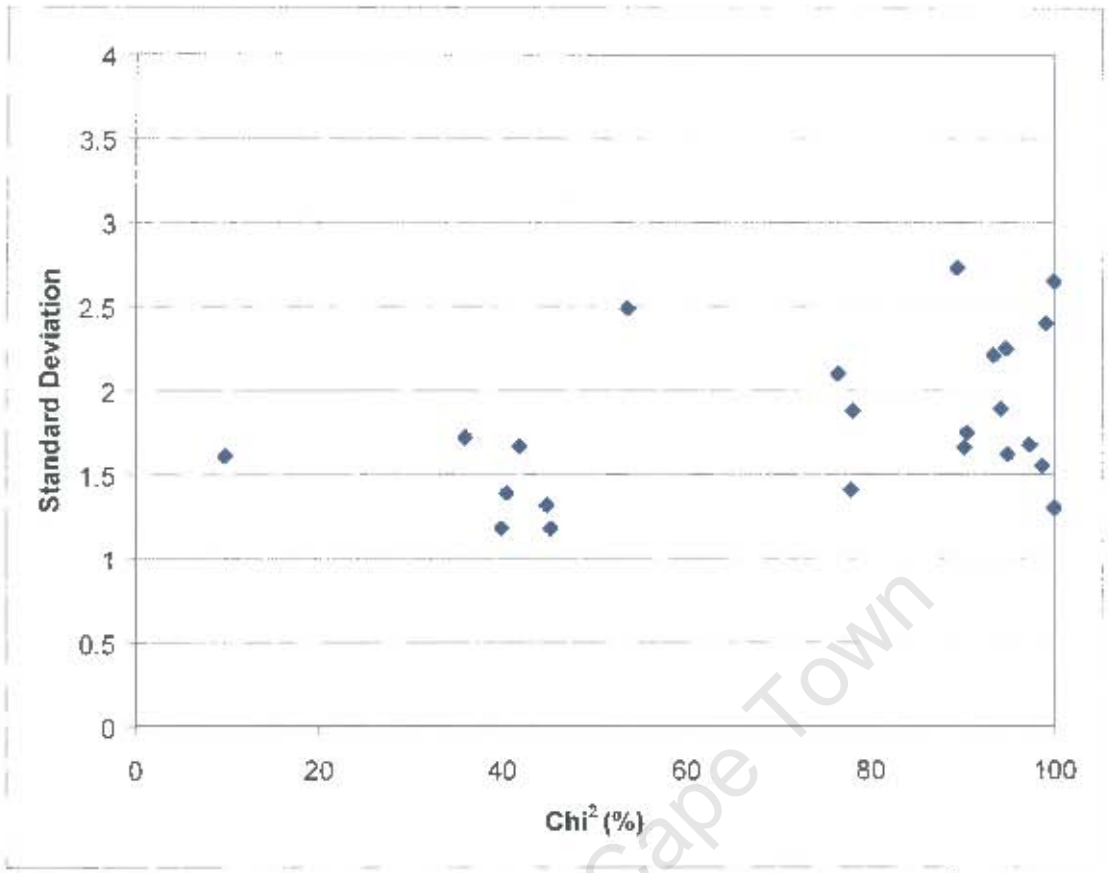

Figure 4.19: Graph of standard deviation of track lengths vs. Chi^2%.

4.4.1.6 Younger Cango Group ages

Fission track ages calculated for the Cango Group outcrop samples, JT02-01, 2, 4 and 5 (89 ± 6 Ma, 108 ± 12 Ma, 92 ± 15 Ma and 114 ± 7 Ma, respectively) are on average younger than the surrounding ages (Figure 4.20). Samples JT02-19 and 20 are ~25 km to the south of the Cango samples and are dated at 131 ± 10 Ma and 143 ± 9 Ma, respectively. Karoo Supergroup samples from similar elevations to the north range from 102 Ma to 134 Ma. The Enon Formation, Uitenhage Group, which is geographically closer to the Cango Group unfortunately yielded no apatite, therefore could not be dated.

Brown (1992) noted similar abrupt changes in fission track age in the southwestern Cape across several faults (the Worcester fault, the Saldahna-Franschoek fault zone and the Piketberg-Wellington fault zone) and observed that ages within each structural block were uniform. Brown (1992) attributed these age differences across structural blocks to significant vertical displacement along these faults synchronous with, or post dating mid Cretaceous cooling.

The relatively younger ages for the Cango inlier may be explained in the same way. Tectonic unroofing may be the cause (shown in Figure 4.20). The Table Mountain Group on the north side of the Cango inlier is overturned by folding during the Cape Orogeny (~250 Ma, Figure 4.20b). Extension between ~140 and 130 Ma as South America rifted away from Africa resulted in the reactivation of previously reverse faults as listric normal faults. This movement created accommodation space into which the Uitenhage Group was deposited (Figure 4.20c). In this model renewed extension at ~≤90 Ma displaced the hanging wall of the TMG and Uitenhage Group relatively downward to the south and thus unroofed the Cango inlier (Figure 4.20d). A similar scenario of younger thermal ages exposed due to tectonic exhumation and unroofing is described in the southern Basin and Range Province by Foster and John (1999) who also used thermochronological techniques (^{40}Ar-^{39}Ar and zircon/ apatite fission track analysis).

Alternatively, the Cango Group may contain apatites with higher fluorine content than those of the Karoo Supergroup, thus preserves younger ages. The Cango samples were not probed to determine their chemical composition, however, based on evaluation of the size of their track etch pits (thus indirectly their chemical composition), this latter explanation appears inadequate to explain the observed differences in ages.

Figure 4:20 (over the page): (A) Relatively young fission track ages of samples from the Cango inlier. Abbreviated sample numbers (e.g. JT02-31 to 31) are shown below the red dots and their fission track ages are shown above. Inset (B) to (E): A tectonic history consistent with the thermal data. (C) Table Mountain and Cango Groups were folded during the Cape Orogeny, at ~250 Ma. (D) Listic normal movement along faults during the onset of the break-out of Africa from Gondwana resulted in the deposition of the Enon Formation in the newly created accommodation space (~140-130 Ma). (E) Tectonic unroofing/ exhumation occurred when reactivation of the normal faults resulted in the displacement of the TMG/ Enon hanging wall relatively downward to the south (at ~90 Ma).

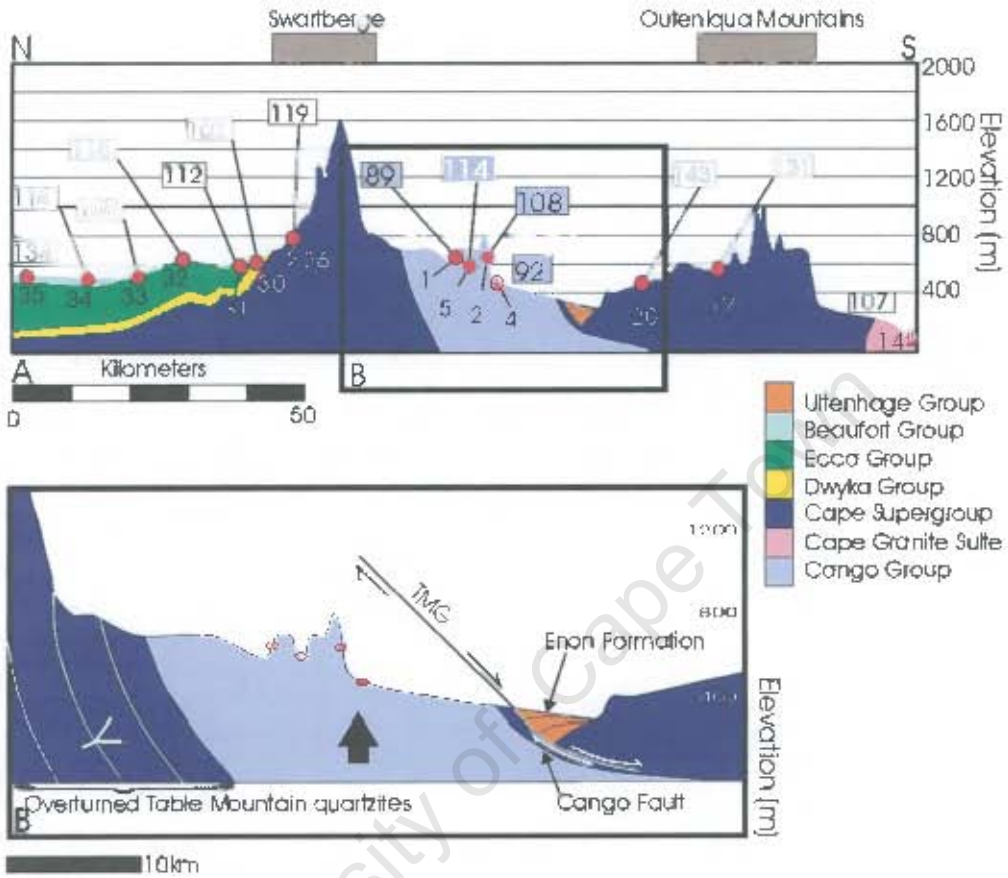

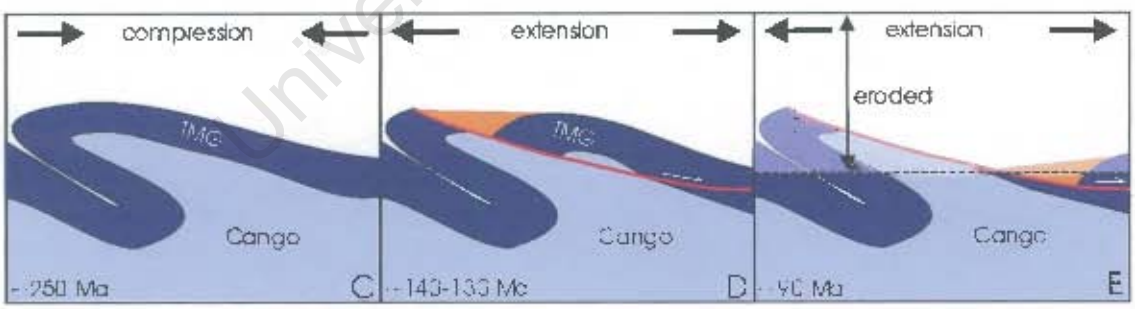

4.4.2 Boreholes

In this section, the borehole's variation in fission track age and mean track length with increasing depth is discussed. The shapes of these plots (Figure 4.10, 4.12, 4.14) are compared to that of the theoretical model an 'ideal' borehole that is subject to sudden increase in denudation (Figure 4.4, outlined in section 4.1.4.1 and 2).

4.4.2.1 Fission track age vs. depth

The trend of fission track age vs. depth for the three boreholes (Figure 4.21) is similar in overall shape to that of the theoretical borehole described in section 4.1.4.i (Figure 4.4). This suggests that for these three areas at least, rapid denudation may have followed a slow period of denudation. The top ~500-750 m of boreholes SA1/66 and KW1/67 may be a preserved PPAZ with the inflection point (*'s on Figure 4.21) marking its base. The fission track age at this inflection point for both boreholes is ~90 Ma, and, in view of the model outlined in section 4.1.4.i, records the onset of accelerated denudation. The steep gradient between ~90 Ma and 70-75 Ma is also present in borehole CR1/68, though it appears that the PPAZ has been completely eroded. Thus the onset of accelerated denudation in this location must have been at >97 Ma (age of the top sample from CR1/68). The steep gradient through the added outcrop samples (KW1/67) is evidence of an earlier period of uplift between ~137-110 Ma (shaded in blue on figure 4.21).

Figure 4.21 (over the page): Changing mean track length (squares) and fission track age (diamonds) with depth for boreholes (A) SA1/66, (B) KW1/67 and (C) CR1/68 (blue) and four outcrop samples (red). Gradient of age with depth is steepest, indicating faster cooling, between ~137 and 110 Ma (KW1/67, shaded blue) and ~95 and 70 Ma (all boreholes, shaded yellow). Elevations (above sea level) of the tops of the boreholes are as shown.

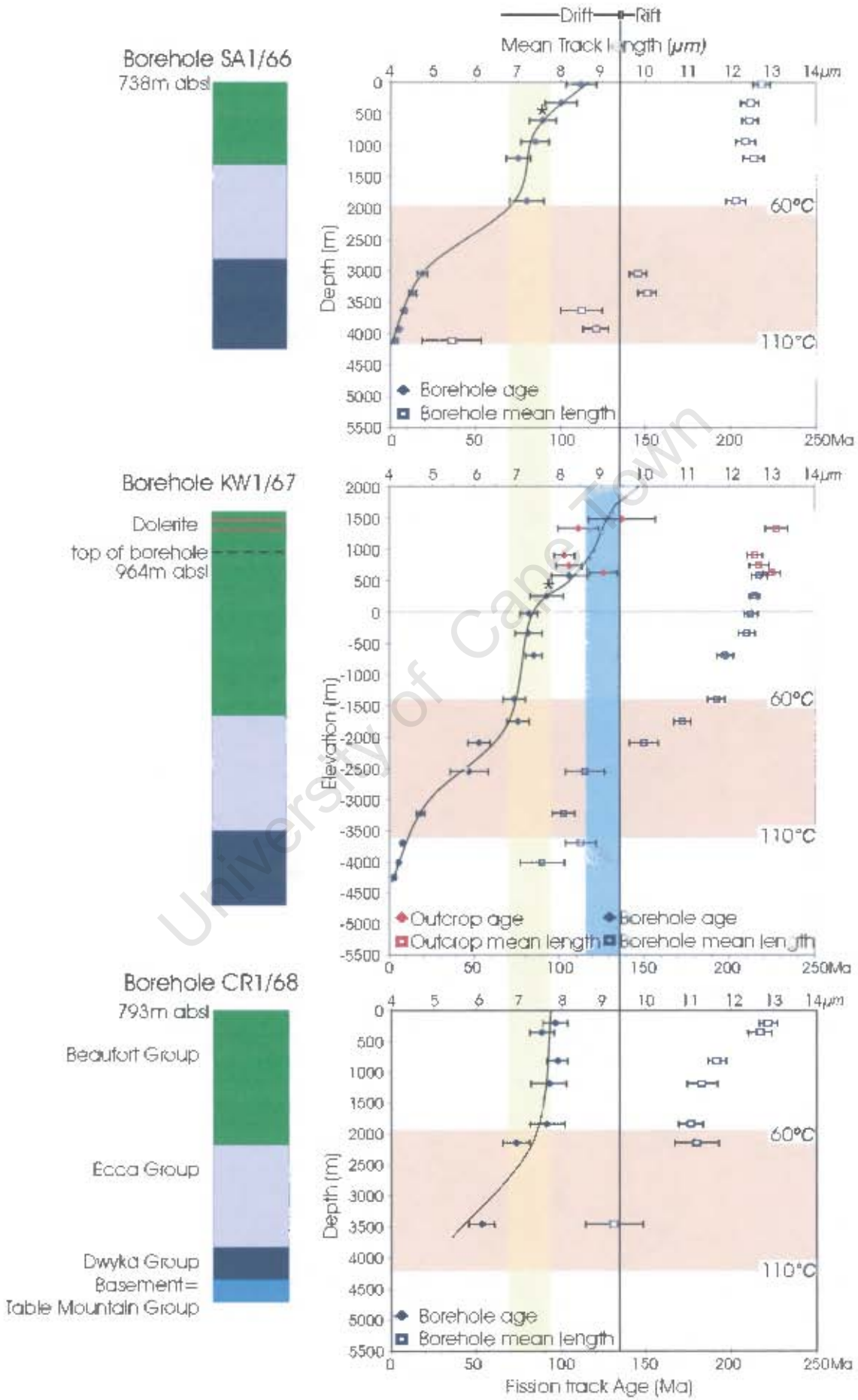

4.4.2.2 Fission track age vs. mean track length

Though the fission track age-depth profiles for the three boreholes (Figure 4.21) are similar in shape to the model profile of figure 4.4, the variation of mean track length with depth is different. Where stability is followed by an increase in denudation rate, samples originally at temperatures >110 ± 10°C will cool quickly through the PAZ and hence have long mean track lengths. Those samples at depths within the PAZ prior to the rapid denudation will have shorter mean track lengths. If the inflection point (*) at ~90 Ma for boreholes SA1/66 and KW1/67 marks the base of the PPAZ, then the samples below this point should show an increase in mean track length. In borehole KW1/67 and SA1/66 the mean track lengths do not increase below '*' (Figure 4.21). The mean track lengths are similar until depths >~2 km, after which they decrease into the present day PAZ.

Thus, the shape of the *fission track age vs. depth profile* suggests that there has been increased denudation beginning at ~95 Ma. However, the discrepancy between expected and actual mean track lengths for this scenario may indicate that the thermal history is not so simple and may involve more than one period of increased denudation. A fourth borehole, Qu1/65 from north of the escarpment (from Brown, 1992, Figure 4.22) is evidence for an earlier period of rapid denudation in the early Cretaceous (~137-110 Ma).

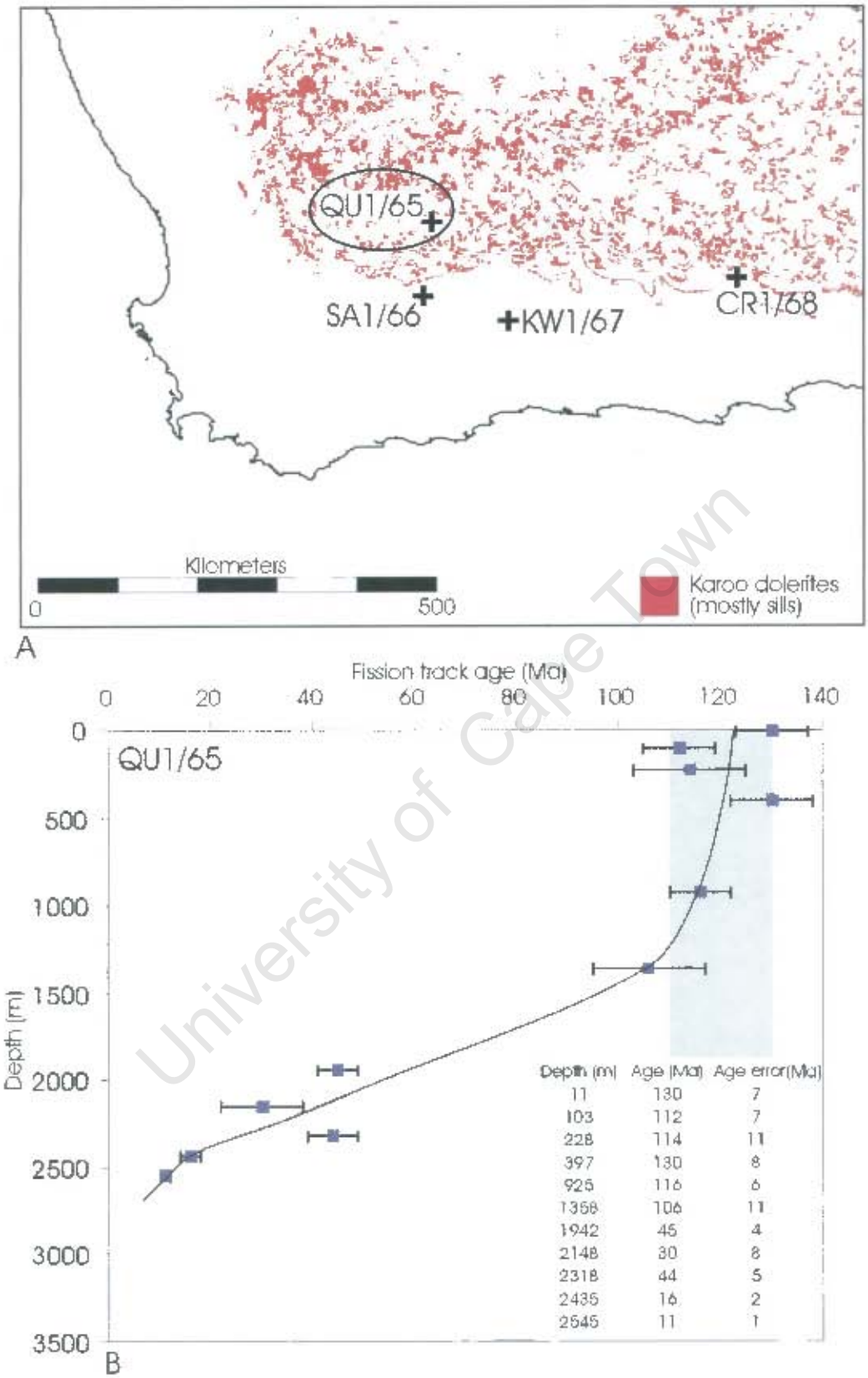

Figure 4.22: Location (A) and age versus depth plot (B) of borehole Qu1/65 (from Brown, 1992). Grey band indicates a period of rapid cooling associated with high denudation rate in the early Cretaceous (~137-110 Ma).

4.4.3 Apatite composition

Tracks within apatite grains that are rich in chlorine are more resistant to annealing than those of fluorine-rich apatites and tend to have older fission track ages (see section 4.1.2.3). Dolerite sample JT02-44 has a fission track age that is ~30 Myrs older than an adjacent Beaufort Group sample (JT02-45) from a similar elevation. This age difference may be due to the dolerite's high chlorine content (average of 1.094 wt%).

The effect of chlorine content of a sample on its fission track age is tested by comparing single grain ages within selected samples with the each grain's respective chlorine content. As chlorine content increases so the single grain ages should increase. Figure 4.23 shows that this is not always the case. Two of the Karoo dolerite samples and one of the borehole samples in fact show the reverse trend of decreasing age with increasing chlorine content. The remaining samples show a decrease in age with decreasing chlorine content but in some examples the points are scattered and the relationship is unconvincing. As mentioned in section 4.1.2.3, the role of the OH^- ion and other additional composition variations in the annealing process is poorly understood (Gallagher, 1995; Carlson *et al.*, 1999). Perhaps the conditions under which the dolerite samples (JT02-41 and 44) containing chlorine-rich apatite crystallised, also resulted in other chemical changes within the apatite, negating the expected decrease in annealing rates. Figure 4.23 shows that, at least in the case of these nine samples, the relationship between apatite chlorine content and annealing rates/ fission track age is not simple.

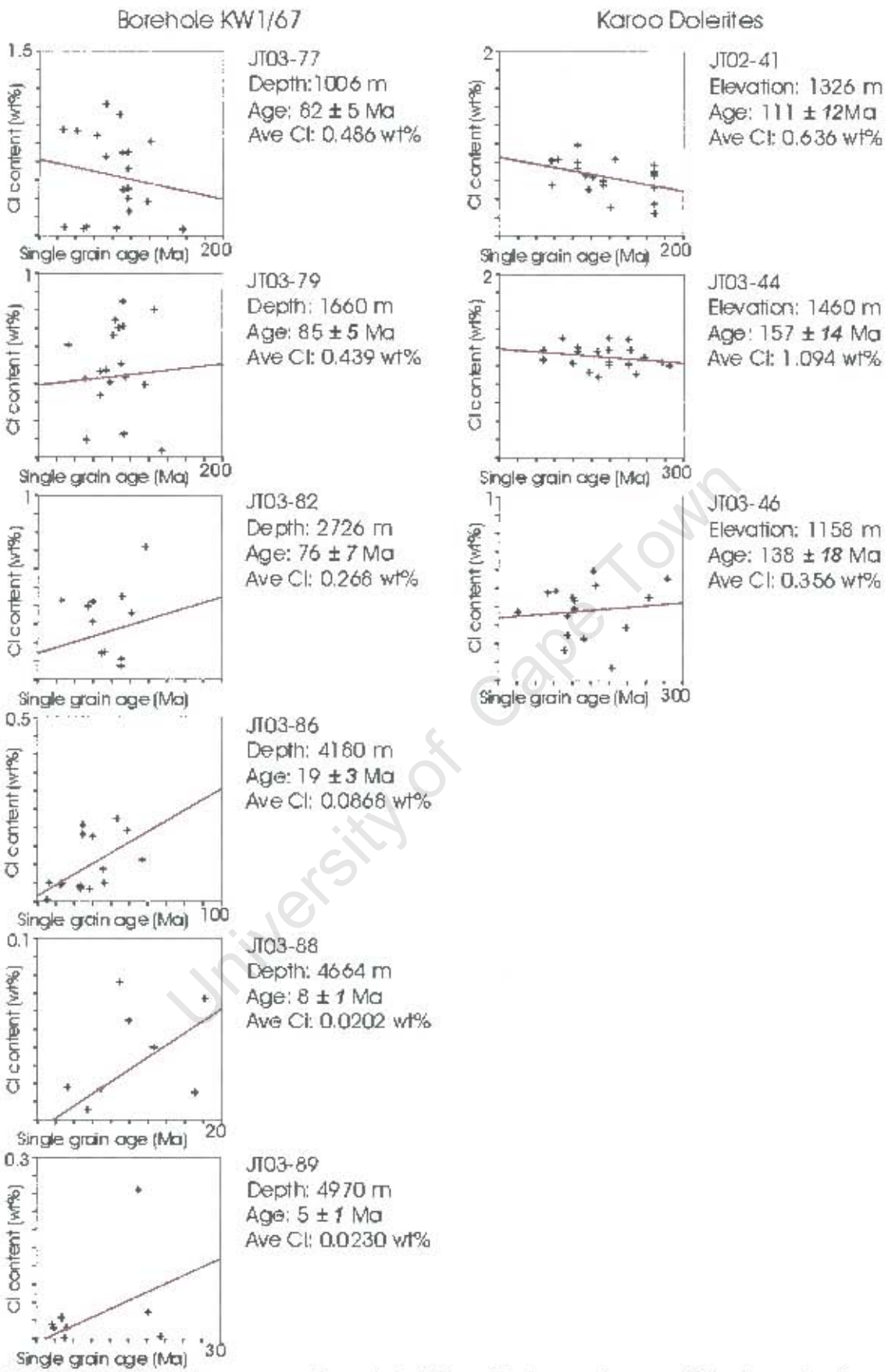

Figure 4.23: Chlorine content (in weight %) vs. fission track ages of single grains from borehole KW1/67 and 3 Karoo dolerite samples. Red line= linear regression line. Note: y-axis changes in scale with decreasing chlorine content at the bottom of the borehole.

4.5 Modelling of fission track data

4.5.1 Introduction

Modelling of fission track data is the process by which a thermal history is obtained from apatite fission track ages and their track length distributions. Apatite fission track data may be used to quantify an approximate thermal history since the sample was at its maximum temperature. Modelling theory is outlined in 4.5.2. Section 4.5.3 discusses model constraints. Required model input including initial track length and geothermal gradients is outlined in section 4.5.4 and 4.5.5. Boreholes KW1/67 and SA1/66 are modelled in section 4.5.6 and 4.5.7 respectively. Section 4.5.8 summarizes the model results.

4.5.2 Annealing models and software

Different modelling approaches use different annealing algorithms. These annealing algorithms are based on laboratory experiments which attempt to describe the annealing of induced fission tracks with varying time and temperature conditions (Fleischer *et al.*, 1965a, 1974; Naeser, 1967, Naeser and Faul, 1969). The results are then extrapolated to geological time scales. A second technique involves the observation of spontaneous track annealing in samples under well-documented geological conditions, for example, deep boreholes (Gleadow and Duddy, 1981; Gleadow *et al.*, 1983; Hammerschmidt *et al.*, 1984; Arne and Zentilli, 1994; Wagner *et al.* 1997), or those samples with a well-constrained geological history using independent evidence (Kohn *et al.*, 2003).

In the late 1980's quantitative annealing models based on experiments involving the Durango apatite standard were developed (Laslett *et al.*, 1987; Duddy *et al.*, 1988; Green *et al.*, 1989). Carlson (1990) and Crowley *et al.* (1991) expanded these models, the latter incorporating apatite composition and deriving a model for fluorine-rich apatite.

Ketcham *et al.* (1999) introduced the term 'kinetic' variation to replace 'compositional' variation. Subsequent models (multi-kinetic models) have attempted to take compositional differences between apatite grains within a single sample into account (eg. Galbraith and Laslett, 1993; Ketcham *et al.*, 1999 using experimental data from Carlson *et al.*, 1999, Donelick *et al.*, 1999). Ketcham *et al.* (1999) uses the diameter of the etch pits on the

polished surface of the apatite crystal (Dpar) to estimate kinetic variability rather than using a microprobe to determine chemical composition. Ketcham *et al.* (1999) cites several problems with monokinetic annealing models (those that assume the same annealing behaviour for all apatites in the same sample). Firstly, the monokinetic model assumes that the apatites modelled have the same annealing characteristics as the apatite upon which the model is based. For example, Laslett *et al.*'s (1987) model is only appropriate for sample apatites that anneal the same way as the Durango standard apatite. Secondly, by taking a central age, the individual ages from perhaps variable kinetic populations are pooled which will obscure the thermal history for each population (Ketcham *et al.*, 1999).

"It is still a matter of debate as to which algorithm is most appropriate" (Gallagher, 1995). In both the forward and inverse modelling the monokinetic annealing model of Laslett *et al.* (1987) is used, because for most of the samples the apatite chemistry is unknown. The approach to modelling presented here involves proposing an exhumation history that best fits the fission track data. The model is constrained by interpretation of the borehole fission track data (see sections 4.3.1.iii and 4.4.2) and then incorporates any available geological constraints, for example resetting of apatites at ~250 Ma during the Cape Orogeny (Chapter 5). Finally, taking into account ideas for the denudation history outlined in chapter 3, chapter 5 proposes a detailed denudation history for the southern Cape region.

Computer programs that have been developed to model fission track data include AFTsolve 1.3.1 (Ketcham *et al.*, 2000), and HeFTy 2.0 (Ketcham, 2004) for PC's, and Monte Trax (Gallagher, 1995) and Thermotrack (developed by Brown, described in Brown *et al.*, 1994) for Macintoshes. Borehole KW1/67 is modelled using Thermotrack (section 4.5.6). Thermotrack is a forward modelling program that produces a thermal history for a set of evenly spaced vertically offset samples (e.g. in a borehole) for a given burial/exhumation history. This can then be compared with measured changes in fission track age and mean track length with depth. The term 'exhumation' describes the path of rocks that were once deeply buried to the surface, due to the erosion of rocks above (Green *et al.*, 2002). The top 6 samples of borehole SA1/66, from shallower depths than today's

partial annealing zone, are modelled using the inverse modelling software, Monte Trax (Gallagher, 1995) (section 4.5.7). Both Thermotrack and Monte Trax are used to test whether a similar thermal history can be generated from both.

4.5.3 Model constraints from the fission track data

This section is focused on the borehole samples, as the zero horizontal offset between samples in a borehole is an additional constraint on the choice of the thermal model. The thermal history for the shallowest sample must be consistent with that experienced by the deepest sample (only at consistently higher temperatures). Any chosen burial history used in a forward modelling approach (e.g. for KW1/67 and Thermotrack) has to result in a thermal history that gives fission track model results that fit reasonably with the observed fission track ages and lengths of all of the vertically offset samples in the borehole. Thus, thermal history models generated from boreholes are generally more robust.

The interpretation of two episodes of increased denudation (~137-110 Ma and ~100-70 Ma) made from the borehole profiles (Figures 4.10, 4.12 and 4.14) and borehole QU1/65 (section 4.4.2.2), helps to constrain the sample's thermal history. The steep gradient of the curve of the borehole plots between ~95 and 70 Ma (Figures 4.10, 4.12 and 4.14) indicates that the region experienced a second episode of accelerated denudation around this time. However the exact timing of both periods of accelerated denudation can only be established from thermal modelling. This is so because the presence of short tracks in the apatites sampled results in a younger fission track age than the true time at which it cooled through the annealing temperature. This is because short tracks are less likely to intersect the surface of the crystal that is counted (see section 4.1.3.1). Even though the exact timing of accelerated denudation is uncertain, these two episodes of accelerated denudation must be incorporated into the thermal history model of the region.

From the presence of short tracks measured in the outcropping dolerite samples, it is proposed that all samples from elevations lower than ~1300 m have been completely reset (section 4.3.1.2). This is further supported by a comparison to Brown *et al.* (2002)'s fission track data from the Drakensberg escarpment. Modelling of their borehole SW1/67, located seaward of the escarpment, showed that the top 5 samples (elevation 870 m to

1648 m above sea level) were partially reset at maximum temperatures <110°C. The bottom three samples at elevations of 630 m, -82 m and –1132 m were all completely reset (e.g. >110°C). If the south coast has experienced a similar thermal history to the east coast then all samples from <~650 m elevations have also been completely reset. Since all borehole samples except the top sample from borehole SA1/66 are from elevations of <600m, these have also been reset. The fact that a borehole from South Africa's east coast still retains samples that have been incompletely reset suggests that less erosion may have occurred there.

Based on this initial interpretation of the borehole profiles, the thermal model is constrained by two episodes of accelerated denudation (cooling) in the early-mid Cretaceous and late Cretaceous and the complete resetting at some stage of all borehole samples.

4.5.4 Initial track length

A required input into any modelling procedure is the initial track length. Tracks induced in the laboratory have a mean track length of ~16.3 μm. Spontaneous tracks from rapidly cooled samples have a mean track length of ~15.5 μm. This reduction in mean track length is because tracks are annealed even at low temperatures over long geological time spans (~10 Myrs) (see section 4.1.3.i). Induced tracks will also vary in length depending on the apatite chemistry (Carlson *et al.*, 1999).

There is no consensus among fission track modellers as to what initial track length to use. A common model artifact following the application of Laslett *et al.* (1987)'s algorithm using an initial track length of 16.3 μm, is a period of Miocene cooling from ~60°C to surface temperatures (Stephenson *et al.*, 2004). This model artifact is most pronounced for older ages, >150 Ma and short mean track lengths, 11-12 μm (Stephenson *et al.*, 2004). It is for this reason that some fission track modellers use a reduced initial track length in their models. Proponents of using a shorter initial track length claim that this removes the erroneous Miocene cooling (e.g. Grist *et al.*, 2004 who use an initial track length of 15 μm). Green (2004), however, claims that using a shorter initial track length in the Laslett *et al.* (1987) model will cause inaccuracies at the high temperature end of the thermal

history. Based on the apatite's chemical control on initial track length, Carlson *et al.* (1999) propose modelling lengths individually depending on the grain's Cl content.

Most modelling software allows the user to vary the initial track length. Although in this study several borehole samples were probed to ascertain their Cl content, only 20 grains from each sample were analyzed. These 20 grains are used to calculate the sample's fission track age. Track lengths, however, were measured from several other apatite grains of unknown chemistry on each slide. Thus the approach of varying initial track length depending on apatite chemistry (Carlson *et al.*, 1999, Ketcham *et al.*, 1999) cannot be used. For borehole KW1/67 and SA1/66 an intermediate initial track length of 15.5 μm (section 4.5.6 and 4.5.7) results in a thermal model that best fits the fission track data.

4.5.5 Geothermal gradients

Fission track thermal modelling requires an estimate of present and paleo-geothermal gradient of the area. In this section the present day geothermal gradient is calculated from heat flow and conductivity measurements and is then compared to those measured directly while drilling was in progress and after drilling. Section 4.5.5 is concluded with a discussion of the paleogeothermal gradient.

4.5.5.1 Present day geothermal gradient

The calculation of the current geothermal gradient of the southern Karoo area, south of the escarpment uses data from Gough (1963). Gough (1963) measured heat flow in several boreholes in the southern Karoo. The location of four of these boreholes, south of the escarpment, is shown in figure 4.24. The western Sambokkraal borehole of Gough (1963) (number 2 in figure 4.24) is SA1/66. (It was originally drilled in the 1940's and deepened in 1966). The borehole Kalkkop, KA1/66 (green cross on Figure 4.24) lies to the west of CR1/68.

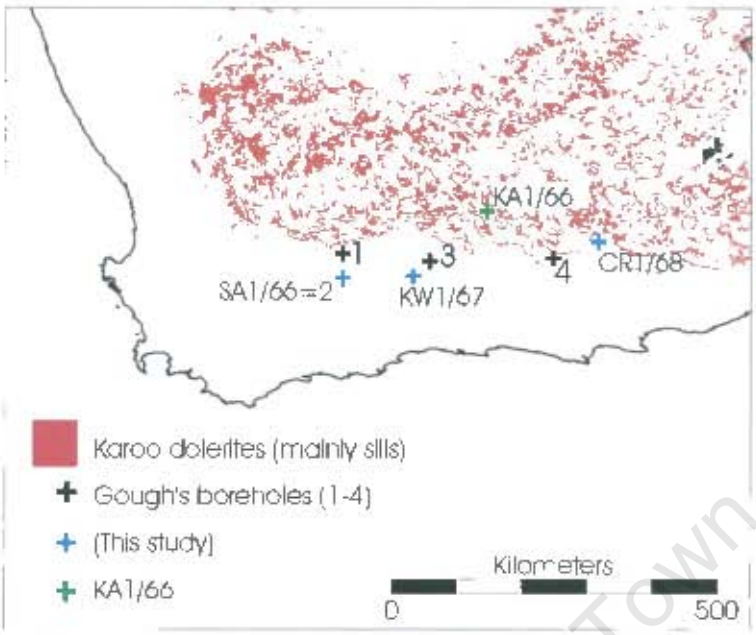

Figure 4.24: Location of the 4 boreholes used to measure heat flow (black crosses, from Gough, 1962). Blue crosses= boreholes SA1/66, KW1/67, CR1/68 and green cross= KA1/66.

Assuming no radiogenic heat production over the depth interval, the geothermal gradient for boreholes KW1/67 and CR1/68 is calculated using the following heat equation:

$$\mathbf{T = T_0 + q_0 x / K}, \text{ where} \qquad [1]$$

T_0= *Surface Temperature.*

Q_0= *Measured surface heat flow.*

Calculated from the average heat flow measured by Gough (1963) from 4 boreholes (Table 4.3).

K= *Thermal conductivity.*

The ratios of shale to sandstone to siltstone for the various stratigraphic groups were obtained from the borehole logs of CR1/68 and KW1/67. Using these proportions, as well as Gough's (1963) average thermal conductivity values for Karoo sandstone, siltstone and shale (converted to W/m/K, Table 4.3), a weighted average thermal conductivity for each stratigraphic group (which corresponds to a

depth interval) was calculated (Table 4.4). This thermal conductivity was then used in the above equation to calculate geothermal gradient (Table 4.4) and the temperature at various depths for borehole KW1/67 and CR1/68 (Table 4.4, final column).

X= *Depth*.

Table 4.3 Average heat flow and thermal conductivity of Karoo rocks (from Gough, 1963).

Heat flow		
Old units ($\mu cal.cm^{-2}$)	Converted units ($W.m^{-2}$)	
1.33	55.77	
Thermal conductivity		
Lithology	Old units (10^4 $cal.cm^{-1}.degC^{-1}$)	Converted units ($W.m^{-1}.°C^{-1}$)
Shale	61.3	2.57
Siltstone	65.4	2.74
Sandstone	76	3.18

Table 4.4: Conductivity and heat flow values used in calculation of geothermal gradient. * from Gough (1963).

KW1/67	Thick-ness (m)	Cumul-ative depth (m)	% Shale	% Sand-stone	% Silt-stone	Conduct-ivity ($W.m^{-1}°C^{-1}$)	Heat Flow ($W.m^{-2}$)*	Temp. gradient (°C/km)	Temp. at cumulat-ive depth (°C)
Lower Beaufort	2685	2685	29.2	27.5	43.3	2.81	55.77	19.84	73.26
Ecca-Seekoegat	990.6	3675.6	60.4	12.6	27	2.69	55.77	20.71	93.78
Ecca-Koup	684.6	4360.2	56.5	25	18.5	2.75	55.77	20.25	107.64
Dwyka	1194	5554.2	100	0	0	2.57	55.77	21.70	133.55
Total depth (m)	5554.2								
CR1/68									
Beaufort-Middleton	1311	1311	31.4	38.9	29.7	2.86	55.77	19.52	45.58
Beaufort-Koonap	826.6	2137.6	25.1	48.3	26.6	2.91	55.77	19.17	61.43
Ecca-FortBrown	1534	3671.6	86	1.7	12.3	2.60	55.77	21.44	94.32
Dwyka	618.7	4290.3	100	0	0	2.57	55.77	21.70	107.74
Bokkeveld	227.1	4517.4	3.5	96.5	0	3.16	55.77	17.66	111.75
Table Mountain	140.8	4658.2	0	100	0	3.18	55.77	17.54	114.22
Total depth (m)	4658.2								

4.5.5.2 Comparison to other estimates of present day geothermal gradient

Actual downhole temperatures were measured by Gough (1963) after original drilling in the 1940's. Borehole temperatures were also measured with thermometers strapped to drilling equipment while the second stage of drilling was in progress in the 1960's. Table 4.5 compares these data with that calculated in table 4.4. The data are presented graphically in figure 4.25. Note, the geothermal gradient measured while drilling is higher than that measured after drilling (Gough, 1963) and higher than that calculated using the heat equation above. Heat measurements made while drilling is in progress are inaccurate because of a number of factors including the use of drilling fluids, friction, convective heat loss etc. Therefore in this study a present day geothermal gradient of ~20°C/km is used (grey interval on figure 4.25).

Table 4.5: Geothermal data measured while drilling boreholes SA1/66, KW1/67 and CR1/68 (Soekor), after drilling boreholes 1-4 (location- figure 4.24, Gough, 1963) and calculated in this thesis (based on heat flow and conductivity measurements).

Measured during drilling in the 1960's	Borehole KW1/67		CR1/68		KA1/66			
	Depth (m)	Temp. (°C)	Depth (m)	Temp. (°C)	Depth (m)	Temp. (°C)	Depth (m)	Temp. (°C)
	1250	58	2489	86	1981	65.56		
	3048	102	3666	131	2594	85.56		
	4023	126	4658	160				
	4572	137						
	5547	160						
Measured after drilling (Gough, 1963)	Borehole 1		2		3		4	
	242.6	26.8	242.7	25.9	242.3	24.14	239.2	24.93
	545.9	33.14	546.2	31.36	545.9	28.94	300.2	26.02
	728.2	36.83	728.5	34.51	728.5	32.18		
	849.2	39.5	849.8	37.14	849.5	34.34		
	1032	43.3			1031	37.71		
	1276	47.81			1274	42.52		
	1517	53.51			1457	46.14		
	1760	60.14						
Calculated (this study)	Borehole KW1/67		CR1/68					
	2685	73.26	1311	45.58				
	3675.6	93.78	2137.6	61.43				
	4360.2	107.64	3671.6	94.32				
	5554.2	133.55	4290.3	107.74				
			4517.4	111.75				
			4658.2	114.22				

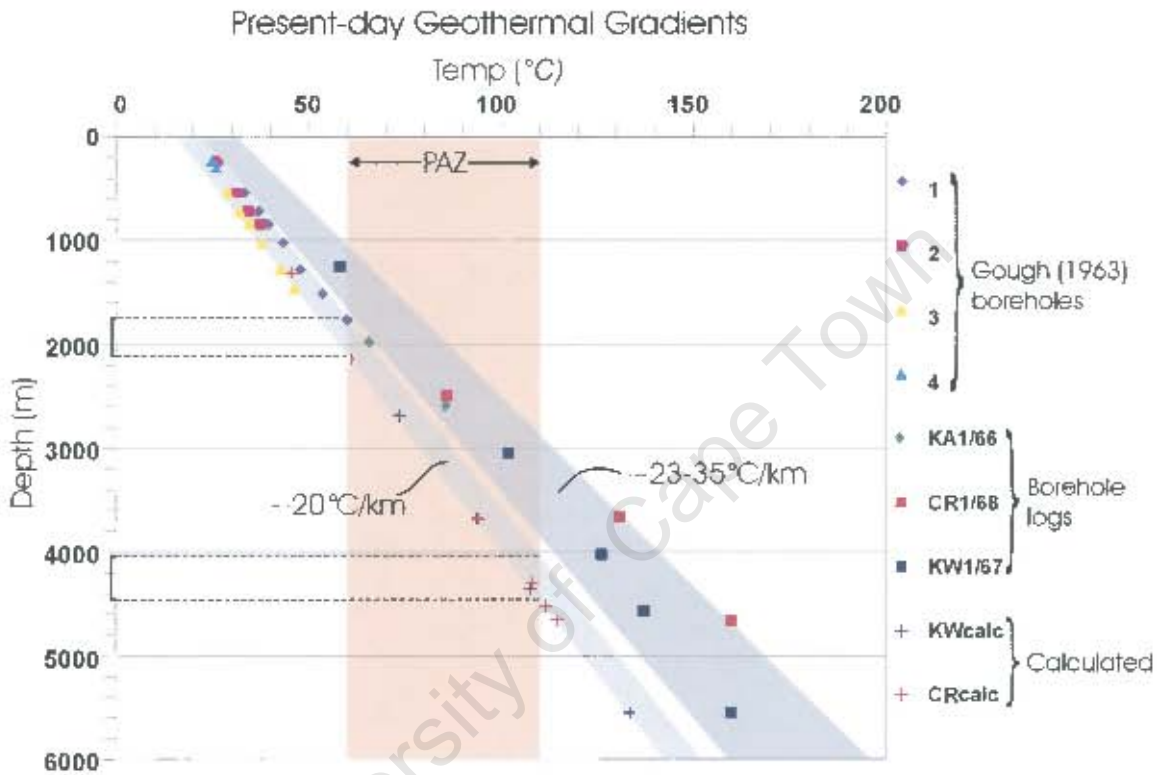

Figure 4.25: Present day geothermal gradient measured during drilling, dark grey (borehole logs), after drilling (Gough, 1963) and calculated from the heat flow equation (1). Light grey band= range of present day geothermal gradients, ~20°C/km. Orange= present day partial annealing zone. Dashed lines indicate range of depths equivalent to 60°C and 110°C.

4.5.5.3 Paleo-geothermal gradient

Paleotemperatures down a borehole may be constrained by combining fission track data with vitrinite reflectance (VR) data (Bray *et al.*, 1992). Unfortunately, the scarcity of Karoo VR data precludes this approach. However the paleogeothermal gradient in the early Cretaceous may be estimated by first calculating heat production at that time, using equation (2) of Kramers *et al.* (2001):

$$\mathbf{Ht = \rho\,[3.48*10^{-6}*C_K*e^{0.554t} + 0.0256*C_{Th}*e^{0.0495t} + C_U*}$$
$$\mathbf{(0.9929*0.0918*e^{0.1551t} + 0.0071*0.576*\,e^{0.98485t})|,}\ \text{where} \qquad \mathbf{[2]}$$

ρ= rock density= 2460 kg.m^{-3} for Karoo (average of shale and sandstone densities, 2540 ± 40 kg.m^{-3} and 2380 ± 80 kg.m^{-3}, respectively, Jones, 2003)

Ht= Heat production in μWm^{-3}

C_K, C_{Th}, C_U= Present day concentrations of K, Th and U in ppm

t= time (Ga)

Very little is published on U, Th and K concentrations of rocks from the Karoo Supergroup. Beeson (1980) investigated the geochemistry of siltstones and mudstones in the Beaufort Group. Average values of 4 ppm U, 16 ppm Th and 31554 ppm K (converted from 3.8 wt%) were calculated for the region in which boreholes SA1/66 and KW1.67 were drilled. Zawada (1988) measured the trace element composition of the Ecca and Beaufort Group mudstones. His values of K_2O range between 2.1 and 4.3 wt%, which are similar to those of Beeson (1980). The concentrations measured by Beeson (1980) are used in the equation of Kramers *et al.* (2001) for t= 0 and t= 140 Ma. Heat production calculated in this way is 2.2578 μWm^{-3} at 140 Ma and 2.2148 μWm^{-3} at t= 0 Ma. To show how this decrease in heat production over 140 Myrs affects the geothermal gradient, equation (3) is solved for the upper 2865 m of borehole KW1/67. Equation (3) is the heat flow equation, (1), adapted to include constant heat production.

$$T(x) = T_0 + q_0x/K - H_0x^2/2K, \text{ where} \quad [3]$$

T(x)= temperature (°C) at depth x (km)

T_0= surface temperature= 20°C

q_o= heat flow (55.77 $W.m^{-2}$, see table 4.4)

K= thermal conductivity (2.81 $Wm^{-1}.°C^{-1}$)

H_0= heat production (2.2578 μWm^{-3} at t= 140 Ma, 2.2148 μWm^{-3} at t= 0)

Solving this equation for H_0= 2.2578 μWm^{-3} (t= 140 Ma), gives a temperature of 70.39°C at a depth of 2685 m (base of Beaufort Group), which translates to a geothermal gradient of 18.77°C/km through this unit. Solving the equation for H_0= 2.2148 μWm^{-3} (t= 0 Ma) gives a temperature of 70.45°C, which translates to a geothermal gradient of 18.79 °C/km. This difference is negligible. Therefore decreased heat production since 140 Ma has had no appreciable effect on the region's geothermal gradient. Thus, in forward modeling of the fission track data (section 4.5.6), the palcogeothermal gradient is assumed unchanged from the present day geothermal gradient, calculated from figure 4.25.

4.5.6 Forward modelling of borehole KW1/67 with Thermotrack

Thermotrack is a 1-D numerical forward modelling program (see Brown *et al.*, 1994 for model details and Fitzgerald *et al.*, 1999 for an example of its application). For a given burial/exhumation history, Thermotrack produces a thermal model and then lists the fission track ages and mean track lengths of a series of vertically offset samples expected for that model. These model values are then compared to the measured fission track data from borehole KW1/67 to assess how realistic the input burial/exhumation model is. Since all samples have been completely reset (see section 4.5.3) it is only possible to model the exhumation history (i.e. time since the sample was at its maximum temperature) and not the sample's burial history. The geothermal gradient is set at 20°C/km (see section 4.5.5).

4.5.6.1 Quantifying denudation since 80 Ma

Thermotrack is first used to quantify late-stage denudation (<80 Ma). The forward model is constrained by the observation of two episodes of accelerated cooling in the early Cretaceous and mid Cretaceous (see section 4.5.3). Assuming denudation of 2 km in the early Cretaceous and 3 km in the mid Cretaceous, 6 forward models of varying denudation

since 80 Ma are produced. Denudation since 80 Ma of 0 km (C), 0.5 km (B), 0.75 km (A), 1 km (D) and 2 km (E) are modelled. In (F) denudation of 3 km since 30 Ma is modelled. The values used in these models and the resultant model curves generated by Thermotrack are given in table 4.6 and figure 4.26 respectively. These curves are compared to the measured curve of fission track age with depth to assess which value of denudation since 80 Ma is most realistic.

Table 4.6: Model parameters used to estimate late-stage (<80 Myr) denudation. Numbers are in km.

	180 Ma	140 Ma	120 Ma	100 Ma	80 Ma
A	0	2	0	3	0.75
B	0	2	0	3	0.5
C	0	2	0	3	0
D	0	2	0	3	1
E	0	2	0	3	2
			80 Ma	65 Ma	30 Ma
F			0	0	3

The model curves generated by varying denudation since 80 Ma are very different to each other. Qualitatively, A, B and D (0.5 to 1 km of denudation since 80 Ma) best fit the fission track age measurements. C, E and F are poor fits to the measured data. (A statistical analysis of the fit of the curves to the measured data follows at the send of this section).

The general shape of the modelled mean track length curves for A, B and D is similar to that of the measured values, but is displaced to the right (longer mean track lengths, Figure 4.26). Modelled mean track lengths for A, B and D are consistently ~1μm too long. The likely reason for this discrepancy is that Thermotrack uses an initial track length (16.3 μm), which cannot be changed without changing the program code. Section 4.5.4. explains that the preferred initial track length used in this study is 15.5 μm.

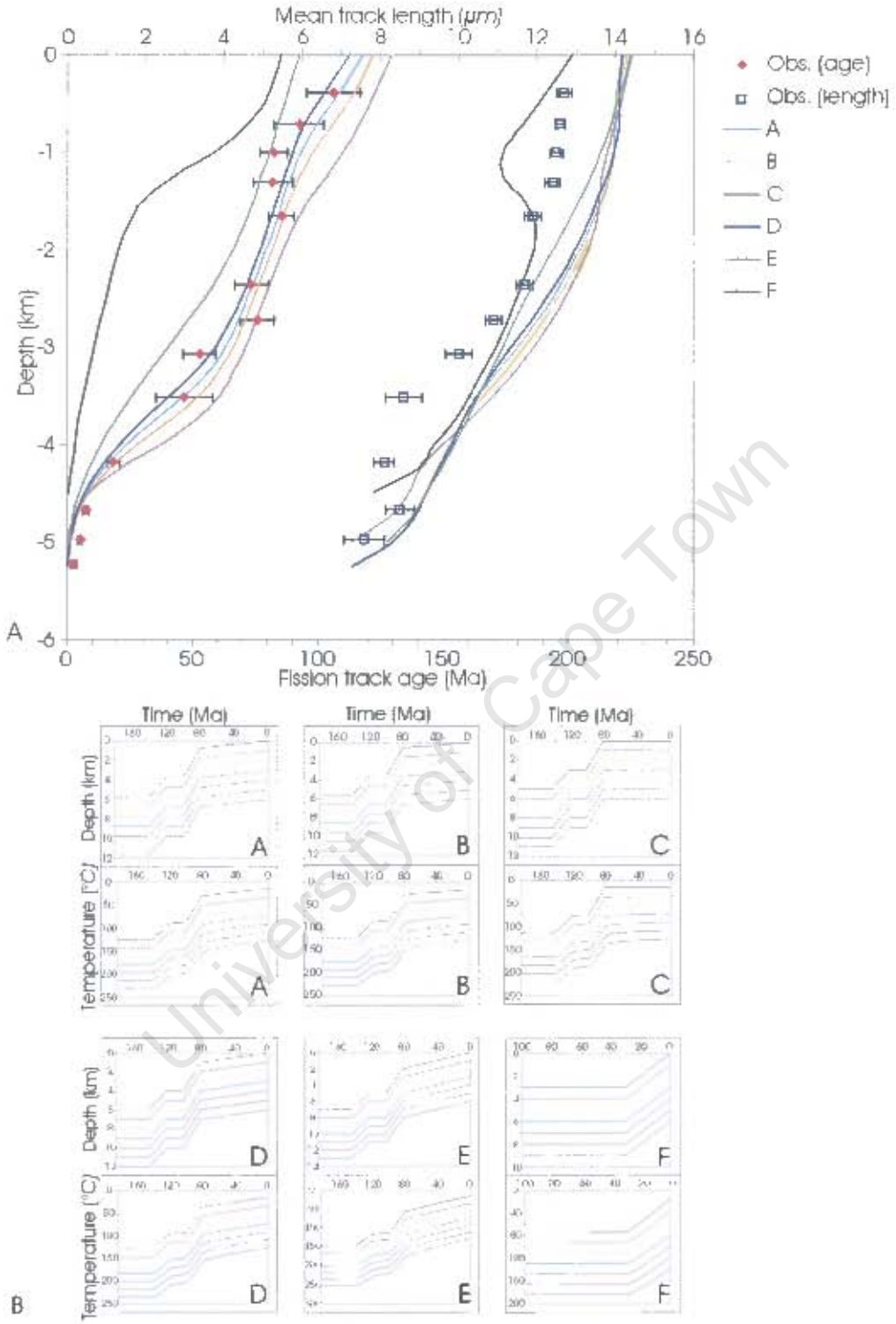

Figure 4.26: (A) Comparison between model curves of fission track age and mean track length vs. depth generated in Thermotrack for varying denudation since 80 Ma, and the measured fission track ages and mean track lengths from borehole KW1/67. (B) Exhumation and cooling paths of selected, evenly spaced samples from each model.

This may account for the observed consistent differences between the modelled and measured mean track lengths. Mean track length curves for model E and F do not match, or mimic the shape of the measured mean track length curve.

'F' models uplift as a recent, post 30 Ma phenomenon (c.f. Burke, 1996, Chapter 3). The resultant curve is clearly a poor fit to the measured fission track ages. Also, the shape of the mean track length curve poorly fits the observed mean track lengths. Thus, significant denudation did not occur after 80 Ma. The maximum post-80 Myr uplift that fits the borehole data is 1 km. Thus, these data do not support a model of extensive denudation post 30 Ma, as advocated by Burke (1996).

4.5.6.2 Quantifying denudation in the Cretaceous

The second modelling step involves fixing the post-80 Myr uplift at 1 km and varying the degree of denudation earlier in the Cretaceous. First, mid Cretaceous uplift (100-80 Ma) is fixed at 3 km and early Cretaceous uplift is varied between 1 and 2 km (K, D and J, Table 4.7 and Figure 4.27). Curves generated for varying amounts of early Cretaceous denudation are very similar and close to the observed values (J, K and D, Figure 4.27).

Table 4.7: Model parameters used to estimate early Cretaceous (140-120 Ma) and mid Cretaceous (100-80 Ma) uplift.

		180 Ma	140 Ma	120 Ma	100 Ma	80 Ma	
J	Varying early Cretaceous uplift	0	1	0	3	1	Figure 4.27
K		0	1.5	0	3	1	
D		0	2	0	3	1	
H	Varying mid Cretaceous uplift	0	1.5	0	2.5	1	Figure 4.28
K		0	1.5	0	3	1	
L		0	1.5	0	3.5	1	
I	Varying mid Cretaceous uplift	0	2	0	2	1	
D		0	2	0	3	1	
G		0	2	0	3.5	1	

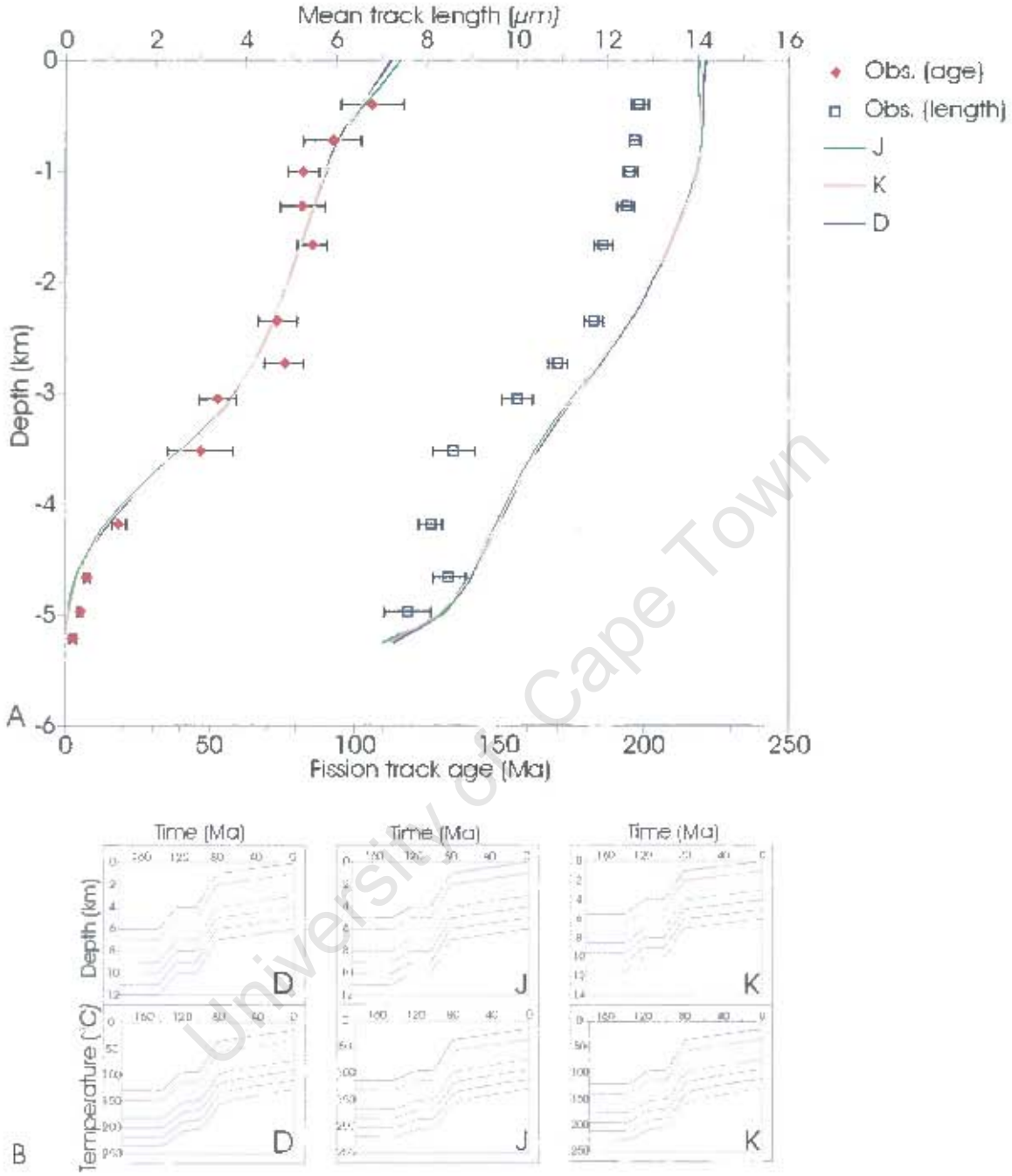

Figure 4.27: (A) A comparison between model curves of fission track age and mean track length vs. depth generated for varying denudation in the early Cretaceous (models J, K and D), and the measured fission track ages and mean track lengths from borehole KW1/67. Denudation since 80 Ma is fixed at 1 km. Denudation in the mid Cretaceous is fixed at 3 km. (B) Exhumation and cooling paths of selected, evenly spaced samples from each model.

Early Cretaceous denudation is fixed at 1.5 km and 2 km in models H, K, L and I, D, G, respectively. Mid Cretaceous denudation is varied between 2 and 3.5 km. Varying mid Cretaceous denudation results in a wider spread of curves (Figure 4.28), indicating that mid Cretaceous cooling is an important control on the overall shape of the model curves and thus on the thermal history of the samples. Of the six curves (Figure 4.28) K, L, D and G are the best fit to the measured fission track ages. Again, mean track lengths are systematically too long, by ~1 μm.

A least squares statistical analysis is undertaken to assess which of all the model curves (A to L, Figure 4.29) is the best fit to the measured fission track age data, and thus is the best approximation of borehole KW1/67's thermal history. The results of this analysis are presented graphically in figure 4.30a. The best fitting model, A (circled in red), involves denudation of 2 km in the early Cretaceous, 3 km in the mid Cretaceous and 1 km since 80 Ma. Other models that are also a good fit include J, K, L, G and D, in which there is denudation of 1 to 2 km in the early Cretaceous, 3 to 3.5 km in the mid Cretaceous and 1 km since 80 Ma. Models E, F, H, I, B and C are poor fits to the measured fission track data.

Although model mean track lengths differ from measured length (because initial track length was set at 16.3 μm), the model curve that is the most similar in shape to the measured lengths best approximates the thermal history of the sample. In this statistical analysis, the distance between measured mean track length and each model length was measured. The standard deviation of these distances for each model reflects how similar each model curve is to the measured values. The lowest standard deviation indicates the most similarly shaped curve. The results of these calculations are shown in figure 4.30b. Model curves for D, J, H, I, A and B are the most similar in shape to the measured mean track lengths (best fit for H, circled in red). As in figure 4.30a, models C, E and F (where denudation since 80 Ma is 0, 2 and 3 km respectively) are the poorest fit to the measured data. Figure 4.30c is composed from 4.30a and b to assess which models best fit both the age and mean length data. The best fitting models are A, J and D (they plot closest to the origin on figure 4.30). Thus 1 to 2 km of denudation occurred in the early Cretaceous, 3 km in the mid Cretaceous and 0.75-1 km in the last 80 Myrs.

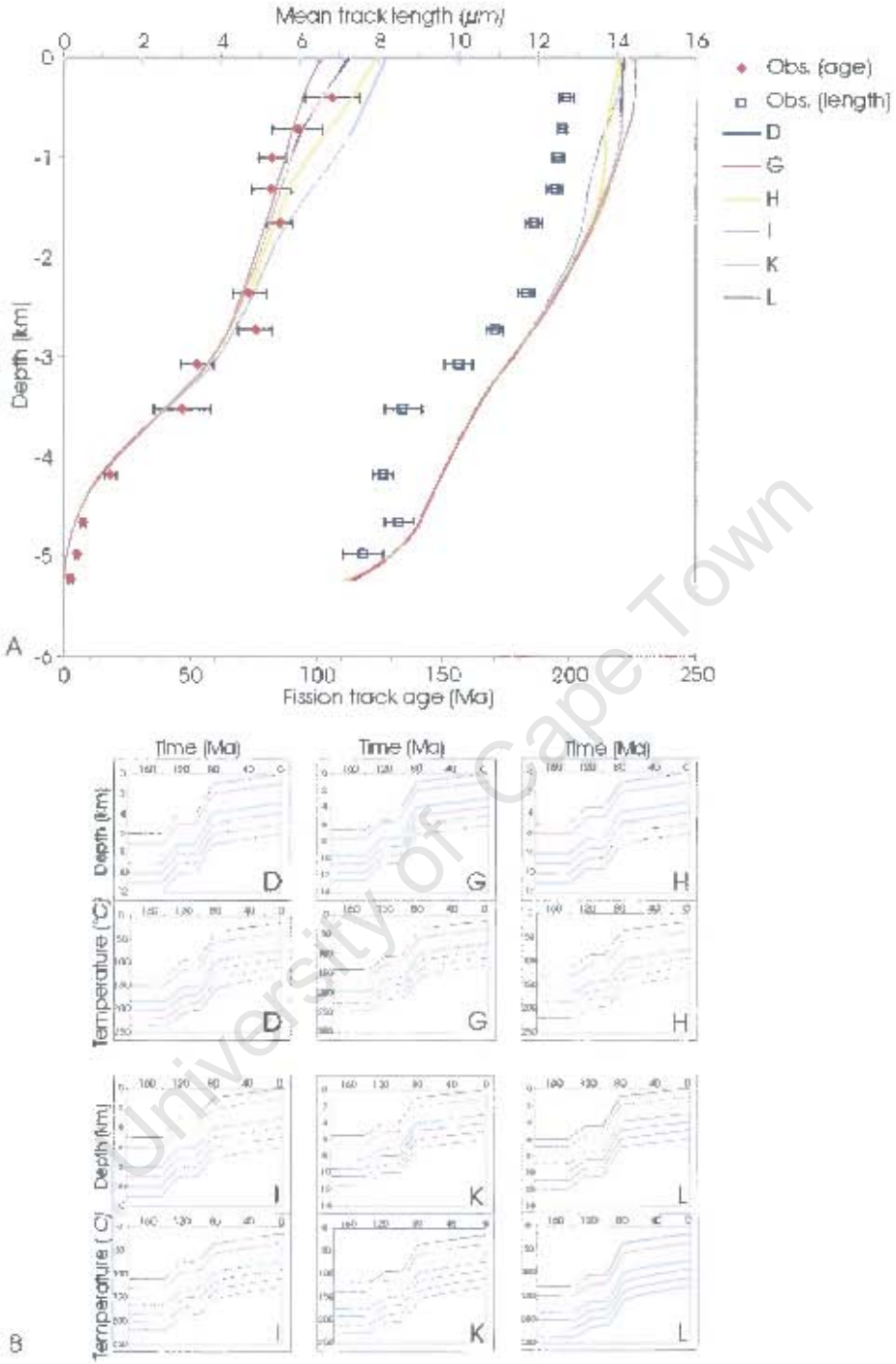

Figure 4.28: (A) A comparison between model curves of fission track age and mean track length vs. depth generated for varying denudation in the mid Cretaceous, and the measured fission track ages and mean track lengths from borehole KW1/67. Denudation since 80 Ma is fixed at 1 km. Denudation in the early Cretaceous is fixed at 1.5 km (models H, K and L) and at 2 km (models I, D and G). (B) Exhumation and cooling paths of selected, evenly spaced samples from each model.

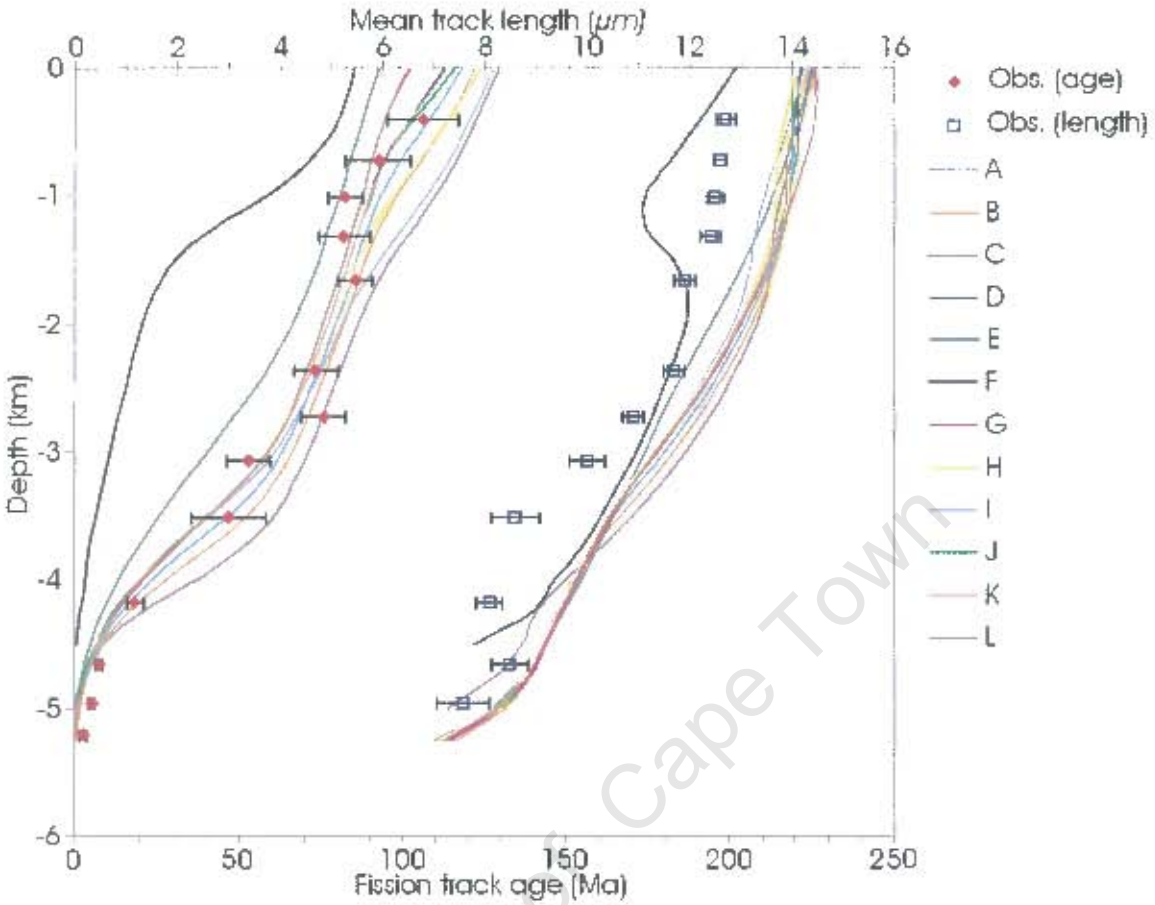

Figure 4.29: All model curves (A to L) generated by varying denudation in the early and mid Cretaceous and since 80 Ma.

Figure 4.30 (over the page): (A) A least squares statistical assessment of goodness of fit between model curves and measured fission track age data (best fits shown in red letters). Models A to L are listed along the x-axis. The y-axis is a measure of how well the model curves fit the measured curve. (B) Standard deviation of difference between model curves for mean track lengths and measured mean track lengths. Low standard deviation indicates that the curves are of similar shape (shown by red letters). These models best approximate the borehole's thermal history. Best fitting models from figure 4.30a and b are circled in red (A and H). (C) A combination of (A) and (B) shows that models D, A and J (red dots and letters) are the best fit to the measured fission track data. Thus 1 to 2 km of denudation occurred in the early Cretaceous, 3 to 3.5 km in the mid Cretaceous and 0.75-1 km since 80 Ma.

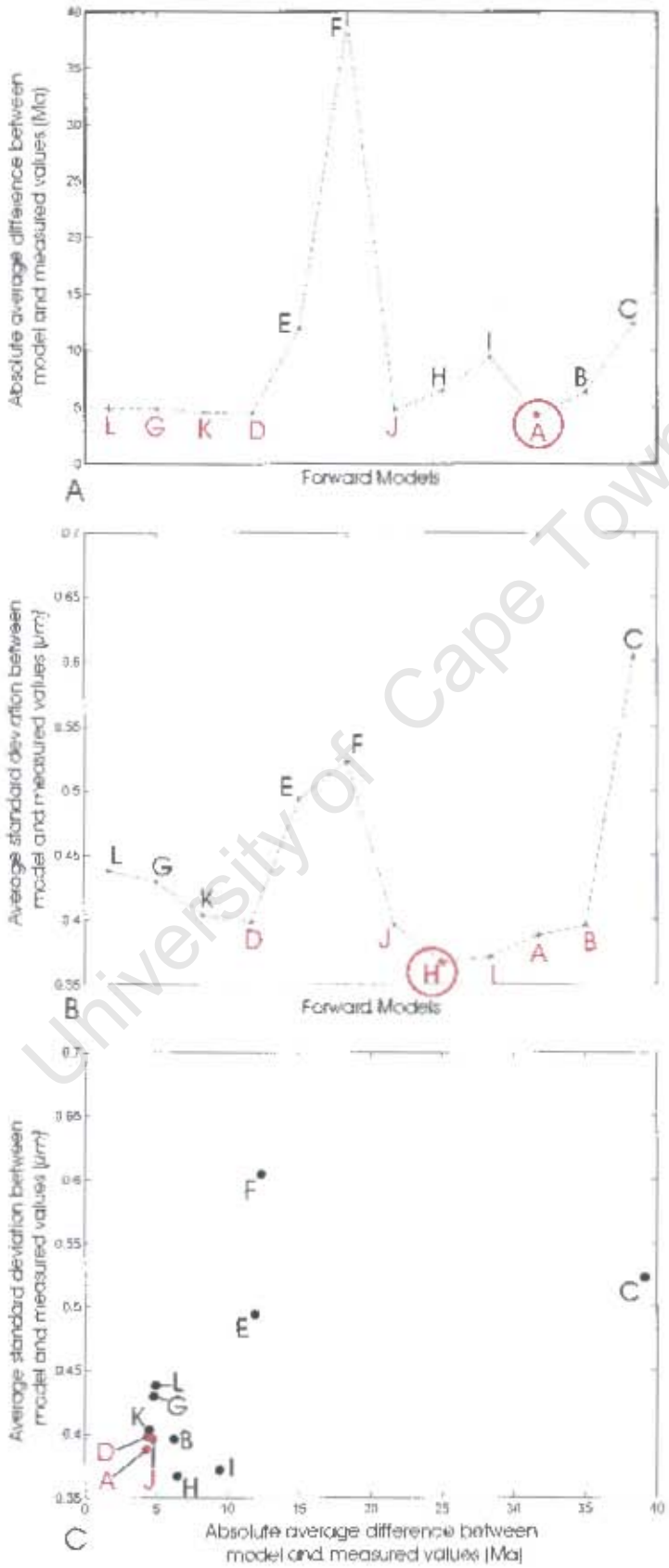

4.5.7 Inverse modelling of borehole SA1/66 with Monte Trax

Inverse modelling of fission track data does not provide a unique thermal history. Several thermal histories may result in exactly the same fission track age, mean track length and track length distribution of the sample, although modelling a series of vertically offset samples does offer a further constraint. The inverse modelling procedure is used here as a way to exclude possible thermal histories. It is also used to test whether a thermal history involving denudation in the early and mid Cretaceous can produce the range of fission track ages and lengths that are measured from borehole SA1/66.

The Monte Trax software (developed by K. Gallagher and explained in Gallagher, 1995) works as follows. The fission track single grain age and track length data (mean length and distribution) for each sample of borehole SA1/66 are imported into the program. The user then inputs any available geological constraints on the burial/exhumation history of the sample by specifying temperature-time 'boxes' which must be incorporated into the thermal model Through an iterative procedure (Monte Carlo simulation) Monte Trax then produces a set of thermal models that best fit the data. The predicted model results can then be compared to the observed fission track age and track length distributions.

The purpose of using this software is to test whether an exhumation history involving denudation in the early Cretaceous (~140-120 Ma), quiescence from ~120 to 100 Ma, renewed rapid denudation from ~100 Ma to ~80 Ma and minor denudation since ~80 Ma may be adequate to explain the observed variation in fission track age and track lengths with depth. The intention was not to prove that this is the *only* exhumation history possible for all six samples from borehole SA1/66, but rather that the samples could have been exhumed in this way. It was also hoped that Monte Trax's inverse modelling approach could be used to corroborate Thermotrack forward model results (section 4.5.6).

As in section 4.5.6, Monte Trax modelling only considers the exhumation history and not the prior burial history of the samples. The model setup is given in table 4.8. The geological constraints (boxes 1 to 5) outline the thermal history to be tested. Their positions are fixed with respect to time but vary with respect to temperature. Sample JT03-60 at the onset of the proposed early-mid Cretaceous uplift is at 120 to 160°C. This

temperature range was chosen to force the sample to completely reset. At this time, sample JT02-66, which is 1850 m deeper, is ~40°C hotter (given a geothermal gradient of ~20°C/km, see section 4.5.5). Therefore box 1 for sample JT03-66 is between 160 and 200°C in the early Cretaceous. Monte Trax cannot constrain cooling at temperatures greater than 110°C therefore early cooling at these high temperatures is suggested, rather than supported by the fission track data. The initial track length is set at 15.5 µm.

Table 4.8: Monte Trax model setup.

Sample	JT03-60	JT03-61	JT03-62	JT03-63	JT03-64	JT03-66
Depth (m)	28	319	602	941	1210	1881
Stratigraphy	Beaufort Group	Beaufort Group	Beaufort Group	Beaufort Group	Beaufort Group	Ecca Group
Fission track age (Ma)	112 ± 9	100 ± 9	90 ± 9	85 ± 8	75 ± 7	80 ± 10
Mean track length (µm)	12.7 ± 0.2	12.44 ± 0.22	12.43 ± 0.19	12.34 ± 0.23	12.53 ± 0.24	12.11 ± 0.24
Box 1 145-120 Ma	120-160°C	125-165°C	135-175°C	140-180°C	145-185°C	160-200°C
Box 2 135-110 Ma	80-120°C	85-125°C	95-135°C	100-140°C	100-155°C	120-160°C
Box 3 105-80 Ma	80-120°C	85-125°C	95-135°C	100-140°C	100-155°C	120-160°C
Box 4 100-80 Ma	10-50°C	15-55°C	25-65°C	30-70°C	35-75°C	50-90°C
Box 5 0 Ma	10-30°C	15-35°C	25-45°C	30-50°C	35-55°C	50-70°C

4.5.7.1 Monte Trax results

The results of inverse modelling are presented graphically for each sample in figure 4.31a to f and in table 4.9. A comparison of observed to predicted variations in fission track age/ track length with depth is shown in figure 4.32.

Figure 4.31 (over the page): Monte Trax inverse modelling results for samples JT03-60 to JT03-66 of borehole SA1/66. Grey= 50 of the best fitting thermal models of which red= the best fit to the fission track data. Yellow= the average thermal model and the smaller boxes bracket the error on the average model.

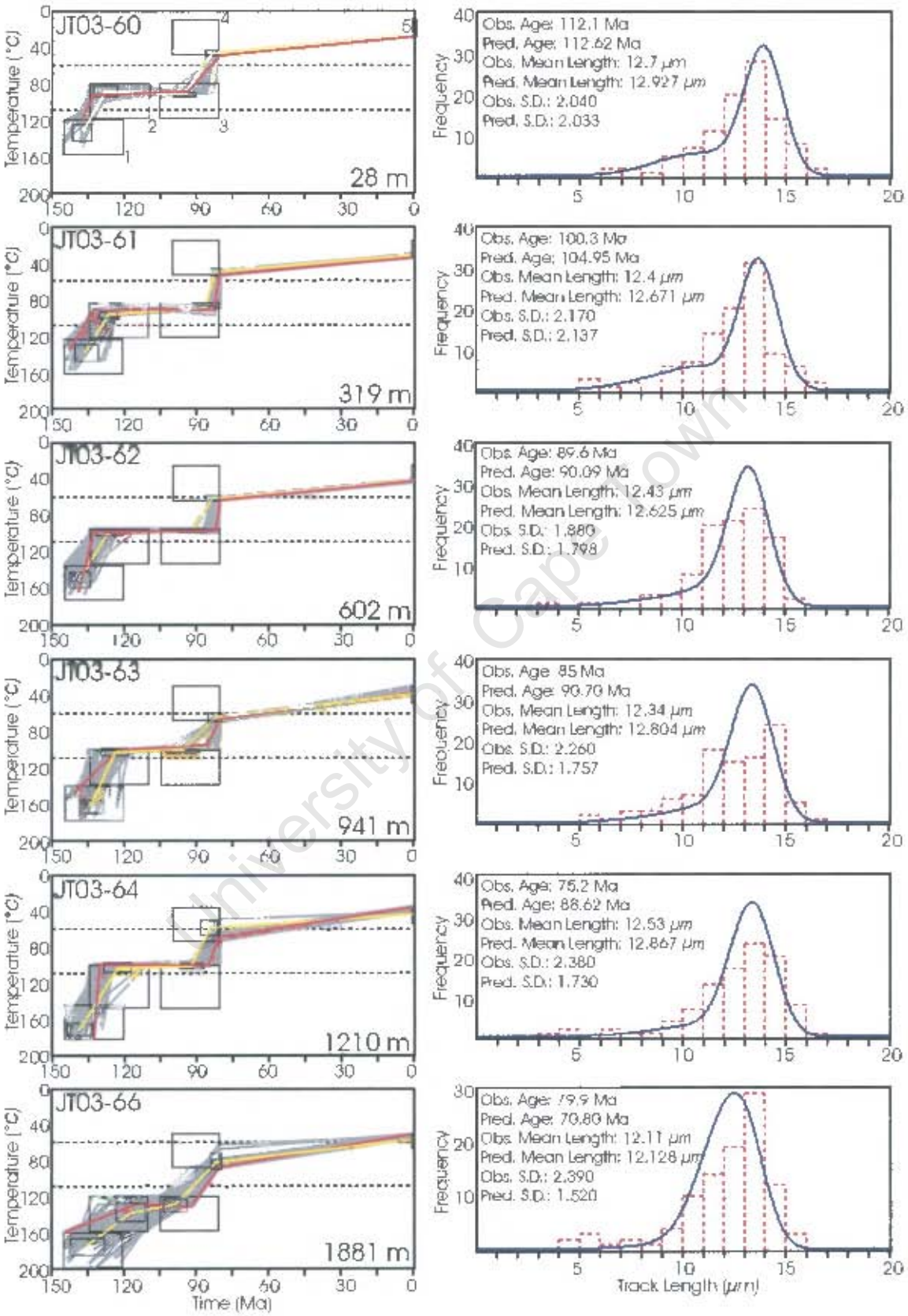

Table 4.9: Monte Trax inverse modelling results.

	Fission track age (Ma)		Mean track length (μm)		Standard deviation (μm)	
	Observed	Predicted	Observed	Predicted	Observed	Predicted
JT03-60	112.10	112.62	12.70	12.93	2.040	2.033
JT03-61	100.30	104.95	12.44	12.67	2.170	2.137
JT03-62	89.60	90.09	12.43	12.63	1.880	1.798
JT03-63	85.00	90.70	12.34	12.80	2.260	1.757
JT03-64	75.20	88.62	12.53	12.87	2.380	1.730
JT03-66	79.90	70.80	12.11	12.13	2.390	1.520

Figure 4.31 shows that for all the samples, the thermal model tried to keep the sample within the PAZ for as long as possible (between boxes 2 and 3). This period of slow cooling gives rise to the shorter tracks. It also necessitates a rapid cooling before and after this slow cooling phase. This fits well with what is expected from the shape of the borehole plots and with Thermotrack model results. Figure 4.32 shows that there is a good fit of the thermal model to both fission track age and mean track length. However, the fit of the model to the standard deviation of mean track lengths is good for the top three samples, and poor for the lower three. The reason for this is unclear. Variable apatite chemistry is one possible explanation. The lower samples may contain grains of varying Cl/F. Grains with higher Cl content are more resistant to annealing than Fl rich grains, thus tracks measured from a variety of grains are anticipated to show great spread in track lengths. However, varying apatite chemistry between grains will also result in a large spread in single grain ages (and a low chi^2 %). Samples JT03-63, 64 and 66 pass the chi^2 test and are therefore each considered as from a single population.

Several alternative models were attempted, some of which produced a better fit to one or two samples but were unsuccessful in fitting all 6 samples. Despite the poor fit of this thermal model to the standard deviation of track lengths for the lower three samples, it results in a good fit to the age and mean length fission track data of all 6 samples.

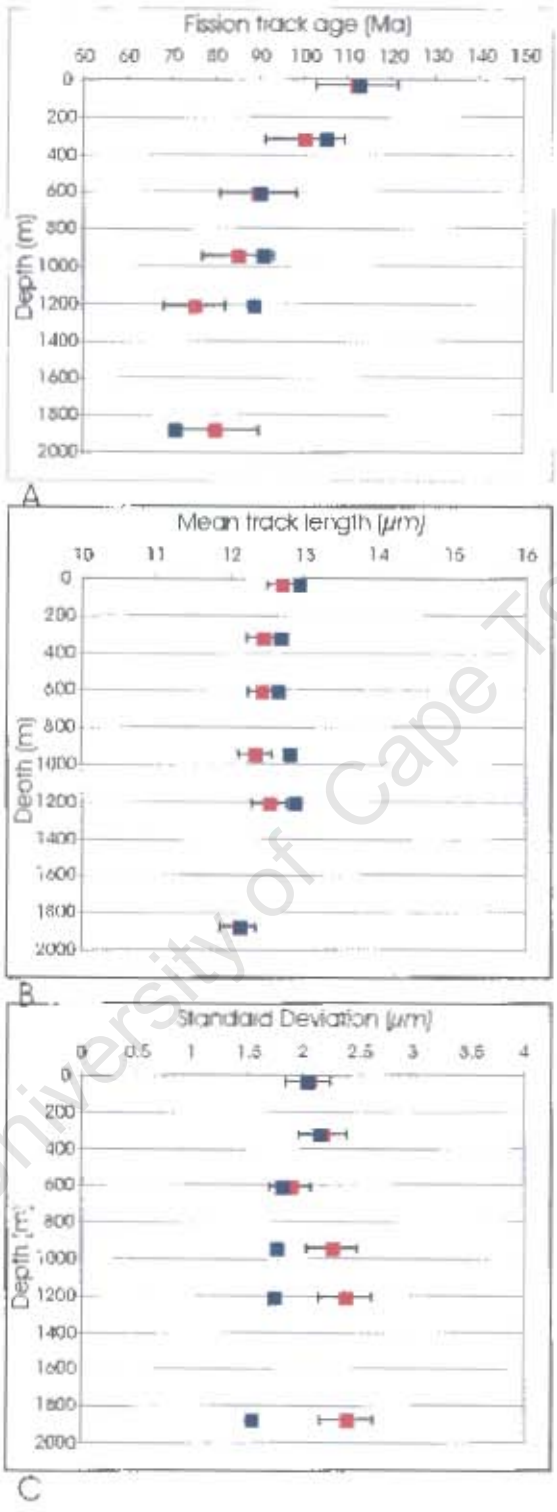

Figure 4.32: A comparison of observed (red) to predicted (blue) variations in fission track age and mean track length with depth of borehole SA1/66. Note model fits fission track age (a) and mean track length (b) observations better than standard deviation (c).

4.5.7.2 Denudation estimates from Monte Trax modelling and paleogeothermal gradients

A summary of the results of Monte Trax inverse modelling procedure is given in table 4.10. Figure 4.33 illustrates the parameters t0 etc. set out in table 4.10.

Table 4.10: Summary of modelling results for various time intervals outlined in figure 4.34. cooling from t0 to t1 occurs at >110°C, therefore is not constrained by the FT data. When subtracting values, e.g. t0-t1, the square root of the sum of errors squared is added to the difference, t0-t1. This assumes that t0 and t1 are independent variables.*

Sample number	t0 (Ma)	T0 (°C)	t1 (Ma)	T1 (°C)	t0-t1 (Ma)	T0-T1 (°C)
JT03-60	138 ± 5	134 ± 11	128 ± 6	90 ± 7	10 ± 8	44 ± 13
JT03-61	136 ± 5	140 ± 11	127 ± 4	98 ± 5	9 ± 6	42 ± 12
JT03-62	139 ± 5	153 ± 10	127 ± 6	99 ± 5	12 ± 8	54 ± 11
JT03-63	134 ± 6	163 ± 9	124 ± 6	103 ± 6	10 ± 8	60 ± 11
JT03-64	139 ± 6	173 ± 8	123 ± 6	103 ± 7	16 ± 8	70 ± 11
JT03-66	136 ± 8	176 ± 11	118 ± 7	139 ± 11	18 ± 11	37 ± 16
				Average	**13 ± 3**	**51 ± 5**
Sample number	t1 (Ma)	T1 (°C)	t2 (Ma)	T2 (°C)	t1-t2 (Ma)	T1-T2 (°C)
JT03-60	128 ± 6	90 ± 7	95 ± 5	92 ± 4	33 ± 8	-2 ± 8
JT03-61	127 ± 4	98 ± 5	86 ± 4	90 ± 4	41 ± 6	8 ± 6
JT03-62	127 ± 6	99 ± 5	92 ± 6	98 ± 5	35 ± 8	1 ± 7
JT03-63	124 ± 6	103 ± 6	96 ± 7	101 ± 3	28 ± 9	2 ± 7
JT03-64	123 ± 6	103 ± 7	92 ± 5	102 ± 4	31 ± 8	1 ± 8
JT03-66	118 ± 7	139 ± 11	99 ± 5	130 ± 9	19 ± 9	9 ± 14
				Average	**31 ± 3**	**3 ± 4**
Sample number	t2 (Ma)	T2 (°C)	t3 (Ma)	T3 (°C)	t2-t3 (Ma)	T2-T3 (°C)
JT03-60	95 ± 5	92 ± 4	84 ± 3	48 ± 4	11 ± 6	44 ± 6
JT03-61	86 ± 4	90 ± 4	82 ± 2	51 ± 6	4 ± 4	39 ± 7
JT03-62	92 ± 6	98 ± 5	84 ± 3	62 ± 4	8 ± 7	36 ± 6
JT03-63	96 ± 7	101 ± 3	83 ± 3	65 ± 7	13 ± 8	36 ± 8
JT03-64	92 ± 5	102 ± 4	85 ± 4	60 ± 11	7 ± 6	42 ± 12
JT03-66	99 ± 5	130 ± 9	82 ± 3	82 ± 10	17 ± 6	48 ± 13
				Average	**10 ± 3**	**41 ± 4**
Sample number	t3 (Ma)	T3 (°C)	t4 (Ma)	T4 (°C)	t3-t4 (Ma)	T3-T4 (°C)
JT03-60	84 ± 3	48 ± 4	0	27 ± 3	84 ± 3	21 ± 5
JT03-61	82 ± 2	51 ± 6	0	32 ± 4	82 ± 2	19 ± 7
JT03-62	84 ± 3	62 ± 4	0	42 ± 3	84 ± 3	20 ± 5
JT03-63	83 ± 3	65 ± 7	0	40 ± 4	83 ± 3	25 ± 8
JT03-64	85 ± 4	60 ± 11	0	44 ± 5	85 ± 4	16 ± 12
JT03-66	82 ± 3	82 ± 10	0	57 ± 5	82 ± 3	25 ± 11
				Average	**83 ± 1**	**21 ± 3**

* This assumption is invalid. However, since correlation between t0 and t1 is unknown, the correct formula for the subtraction of errors cannot be applied [var(X±Y)= var(X) + var(Y) ± 2cos(X,Y)]. The application of the correct formula results in an error that is ± 2 units (or ± 2 Ma in the case of t0-t1) different to that calculated assuming independence.

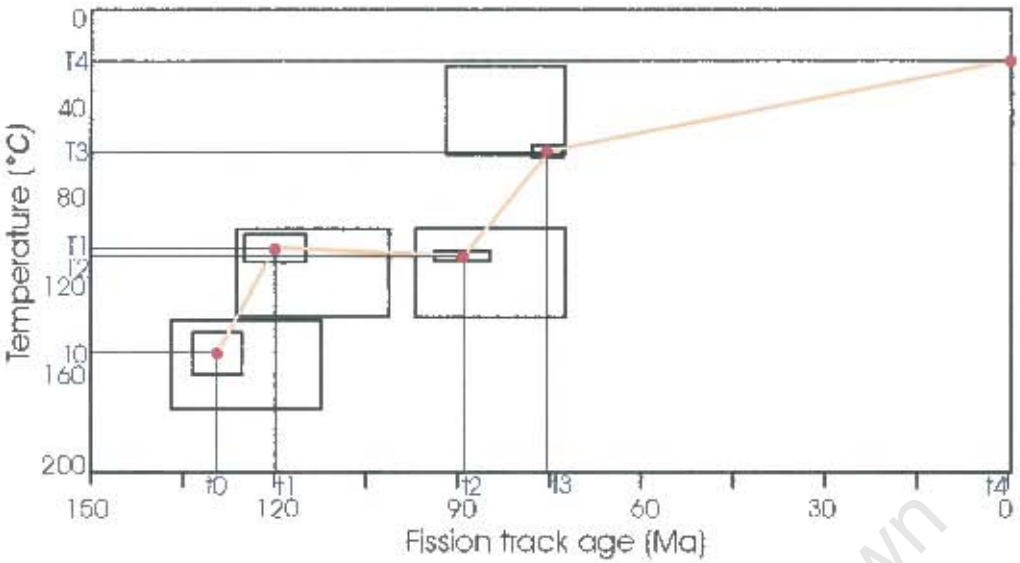

Figure 4.33: T0, T1, T2, T3 and T4 are the model temperatures of the sample at times t0, t1, t2, t3 and t4, respectively.

Table 4.10 gives the average amount of cooling over four time intervals (~137-~125 Ma, ~125-~93 Ma, ~93-~83 Ma and ~83-0 Ma). To convert cooling in degrees to denudation in kilometers, the paleogeothermal gradient of each time interval is required. In the forward model using Thermotrack, a paleogeothermal gradient of 20°C/km was assumed. Monte Trax does not assume a paleogeothermal gradient. Instead, the paleogeothermal gradients at various times are calculated from a plot of the maximum temperatures experienced by the samples (from table 4.11, calculated by Monte Trax) versus each sample's current depth (Figure 4.34). In figure 4.34 regression (or best fit) lines are drawn through the data points and the model geothermal gradients at ~125 Ma (t1), ~93 Ma (t2) and ~83 Ma (t3) are read from the slope of these lines. The geothermal gradient at ~137 Ma (t0) is not plotted as it is calculated above 110°C, a temperature above which FT data cannot constrain.

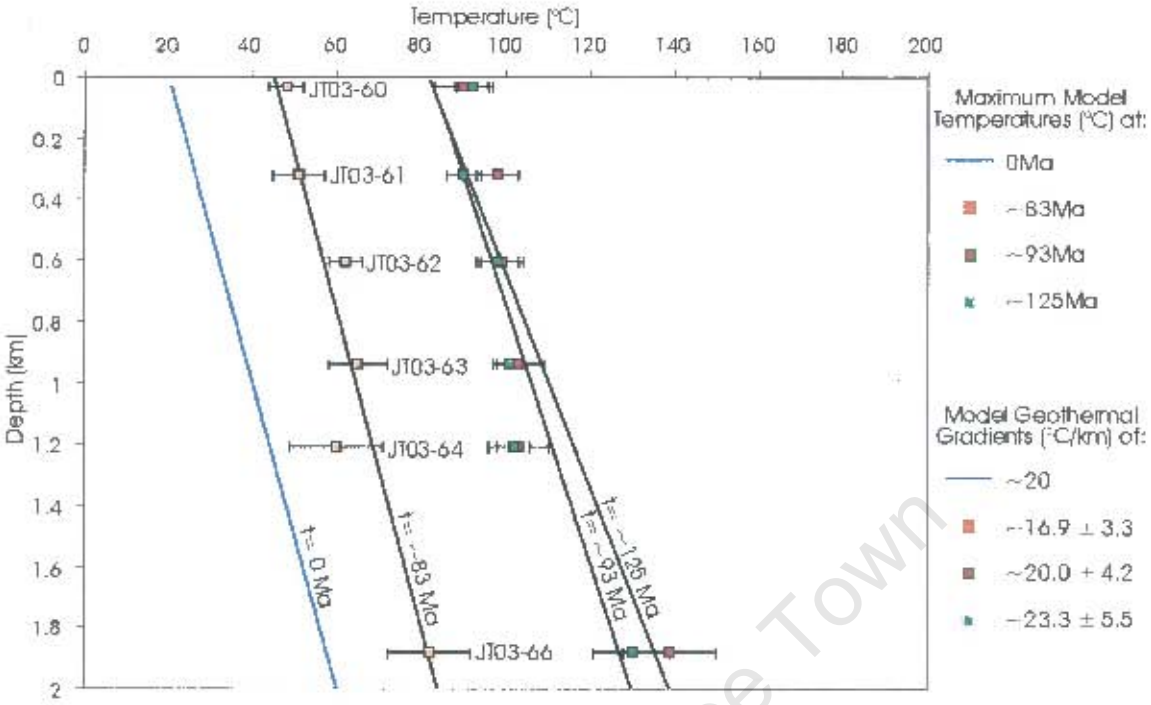

Figure 4.34: Paleogeothermal gradients calculated by Monte Trax inverse modelling software vary over time from ~23.3 ± 5.5°C/km at ~125 Ma to ~16.9 ± 3.3°C/km since 80 Ma.

According to Monte Trax modelling, the paleogeothermal gradient varies between ~23.3 ± 5.5°C/km (at ~125 Ma) and 16.9 ± 3.3°C/km (at ~80 Ma) (Figure 4.34). In table 4.11, denudation is calculated by first assuming a constant paleogeothermal gradient (of 20°C/km as for the Thermotrack model, (*) and then by allowing the geothermal gradient to vary over time as calculated by the Monte Trax program (**) from figure 4.34. Total denudation calculated using a variable geothermal gradient (5.6 ± 0.32 km) only differs by ~400 m from that calculated using a fixed geothermal gradient of 20°C/km (6 ± 0.41). Given the large errors on the paleogeothermal gradients derived from Monte Trax, (up to 5.5°C/km) and the small difference in denudation a variable geothermal gradient actually makes, total onshore denudation, estimated from the Monte Trax model, is estimated as 6 ± 0.41 km.

Table 4.11: Calculations of degree and timing of denudation * using a fixed paleogeothermal gradient of 20°C/km and ** a variable geothermal gradient based on maximum temperatures of samples at each step (from Figure 4.34). Cooling in the early Cretaceous at temperatures above 110°C is not constrained by the FT data.

	Time interval (Ma)	Temp. interval (°C)	Denudation * (km)	Denud-ation rate * (m/Ma)	Palegeo-thermal gradient (variable)	Denudation ** (km)	Denudation rate ** (m/Ma)
Rapid cooling in early Cretaceous	13 ± 3	51 ± 5	2.6 ± 0.25	200	24.7 ± 3.9	2.1 ± 0.19	162
Quiescence in early-mid Cretaceous	31 ± 3	3 ± 4	0.15 ± 0.2	4.8	23.3 ± 5.5	0.13 ± 0.03	4.2
Rapid cooling in mid Cretaceous	10 ± 3	41 ± 4	2.1 ± 0.2	210	20.0 ± 4.2	2.1 ± 0.24	210
Slow cooling since late Cretaceous-Tertiary	83 ± 1	21 ± 3	1.1 ± 0.15	13	16.9 ± 3.3	1.24 ± 0.09	15
Total			**6 ± 0.41**			**5.6 ± 0.32**	

4.5.8 Comparing the Thermotrack and Monte Trax models

The results of both modelling approaches are shown together in figure 4.35, though they are not strictly speaking directly comparable since they are applied to two different boreholes. The two models do, however, show a similar pattern of increasing and decreasing denudation since ~140 Ma because they have been deliberately constrained to produce this pattern. The model constraints are provided by the fission track data itself. Steep gradients on all three boreholes plots of fission track age versus depth imply rapid cooling in the mid Cretaceous (~100-80 Ma). An early Cretaceous period of rapid cooling (~140-120 Ma) is suggested by steep gradients through the outcrop samples plotted on KW1/67 and from the borehole QU1/65 (Figure 4.24). Short tracks measured from the dolerite samples suggest that all the borehole samples have been completely reset.

Most importantly, these two models are a good fit to all the samples of both borehole SA1/66 and KW1/67. While it is impossible to rule out all alternative untested thermal models, it is very difficult to match the fission track data of 6 samples of borehole SA1/66

and 13 samples of borehole KW1/67 with one model. Many unsuccessful alternative models were attempted.

Inverse modelling of borehole SA1/66 using a constant paleogeothermal gradient of 20°C/km suggests denudation of 2.6 ± 0.25 km in the early Cretaceous, 2.1 ± 0.2 km in the mid Cretaceous and 1.1 ± 0.15 km since 83 ± 1 Ma, giving a total of 6 ± 0.41 km (Table 4.11). This estimate falls within the 4.75-6.5 km calculated by forward modelling borehole KW1/67, that also used a paleogeothermal gradient of 20°C/km (section 4.6). According to Thermotrack forward modelling, 1-2 km of denudation occurred in the early Cretaceous, 3-3.5 km in the mid Cretaceous and 0.75-1 km since 80 Ma. Combining these two model results gives denudation of 1-2.6 km in the early Cretaceous (~140-120 Ma), 2.1-3.5 km in the mid Cretaceous (~100-80 Ma) and 0.75-1.1 km since the late Cretaceous (~80 Ma). 4.75-6.5 km has been denuded from above boreholes SA1/66 and KW1/67 since the early Cretaceous (~140 Ma). Chapter 5 investigates the geological and geomorphic implications of this exhumation history.

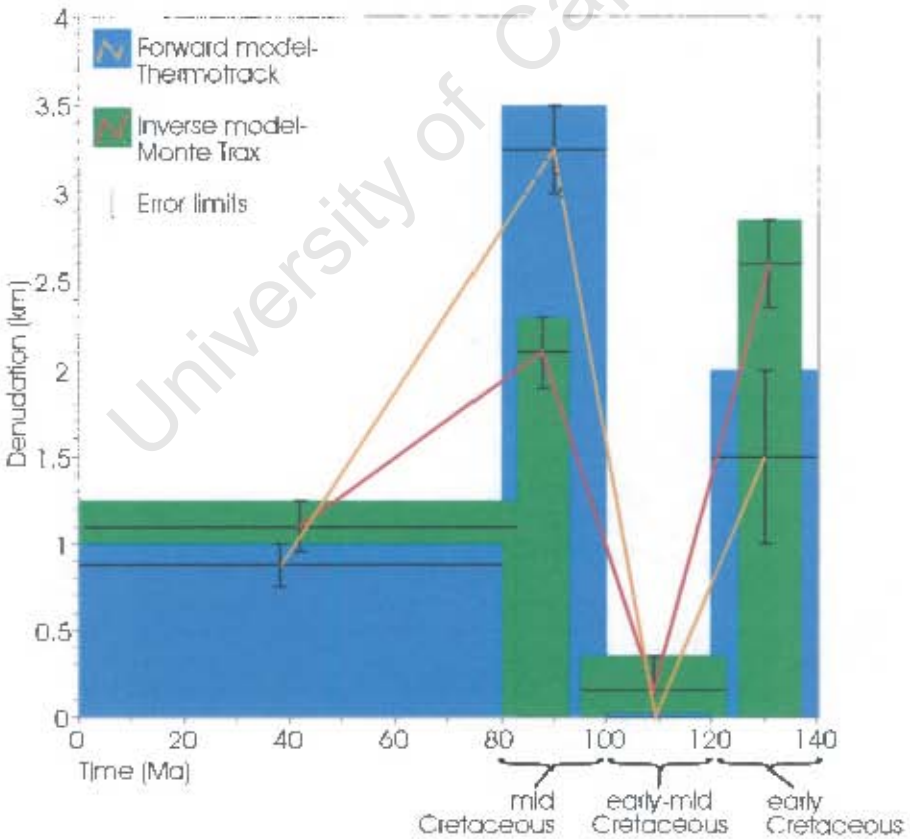

Figure 4.35: Graphical comparison of the results of Thermotrack modelling (blue) for borehole KW1/67 and Monte Trax modelling (green) for borehole SA1/66.

Chapter 5: Denudation of the southern Cape

5.1 Geologic input

Exhumation involving denudation of ~1-2.6 km of rock in the early Cretaceous, ~2.1-3.5 km in the mid Cretaceous and ~0.75-1.1 km since 80 Ma is proposed from thermal modelling of fission track data (section 4.5). This can be tested against all available onshore geological evidence. The incorporation of independent information about the tectonic history of the geological region is vital to understanding and modelling fission track data (Wagner, 1981; Gallagher, 1995). This section evaluates how various tectonic and magmatic episodes may have affected the thermal history of the sampled region. It includes a discussion of the Cape Orogeny (~250 Ma), burial by the upper Karoo Supergroup (~245->183 Ma), thermal effects of the Karoo magmatic event (183 ± 1 Ma, Duncan *et al.*, 1987), further burial by the Drakensberg Group volcanics and/or unknown stratigraphic units (183-140 Ma) and exhumation from 140 Ma.

5.1.1 The Cape Orogeny (~250 Ma)

Fluid inclusion work by Egle (1996) in the south west Cape Fold Belt and Karoo basin has shown that large volumes of fluids were mobilised during the Cape Orogeny resulting in a peak temperature for the Cape and Karoo Supergroups of 150-170°C. Localised peak temperatures for the Beaufort Group may have reached 270°C and 240-410°C for the basement sediments, including the Cango Group (Egle, 1996). Frimmel *et al.* (2001) present geothermometry data that support low-grade metamorphism (lowermost greenschist facies, ~300°C) during the Cape Orogeny. These temperatures of >110°C are sufficient to reset the apatites of all stratigraphic groups affected by the Cape Orogeny (Cango Group, Cape Granite Suite, Cape Supergroup and the lower Karoo sediments). North-northwesterly paleocurrent directions for the upper Beaufort Group imply that the southern branch of the Cape Fold Belt was a significant provenance for this Group (Cole, 1992; Cole and Wipplinger, 2001). Since the Karoo Supergroup (below the Stormberg Group) is either deformed in the Cape Orogeny or derived from sediments that were deformed, then all apatites were reset at ~250 Ma and thus have lost any inherited tracks that may have accumulated prior to ~250 Ma. The lack of any single grain fission track ages of >250 Ma in the samples is consistent with this (see Figure 4.7 a to j).

5.1.2 Burial by Karoo Supergroup (~245-183 Ma)

How thick was the Beaufort Group in the southern Cape region?

The Triassic and Jurassic strata of the main Karoo Basin "represent an erosional outlier of the Karoo Supergroup of what was probably a considerably more extensive original development" (Dingle *et al.*, 1983, 14). Dingle *et al.* (1983) propose that ~3.5-4.5 km of Karoo sediment (Upper Permian to Middle and Upper Triassic) in the southern Cape has been removed by erosion. The extent of the Main Karoo Basin preservation is shown in figure 5.1. The tops of boreholes SA1/66, KW1/67 and CR1/68 outcrop in the Adelaide Subgroup of the Beaufort Group (Figure 5.1). The thickness of the Adelaide Subgroup in borehole SA1/66, KW1/67 and CR1/68 is ~1300 m, ~2300 m and ~2150 m, respectively. Johnson *et al.* (1997) propose a maximum thickness of 5000 m for the Adelaide Subgroup in the southeast which decreases rapidly towards the center and then gradually farther to the north. If the southwest was similarly thick, then the boreholes were originally covered with up to ~2700-3700 m additional Adelaide Subgroup rock. Smith (1990), however, proposes that the Adelaide Subgroup is ~2800m thick in the southwest. If this estimate is accurate then 500-1500 m of Adelaide Subgroup rock has been eroded from above the boreholes (Table 5.1).

Unconformably overlying the Adelaide Subgroup is the Tarkastad Subgroup (outcrop shown in Figure 5.1). Assuming the Tarkastad Subgroup originally covered the southern Cape region, a total of 3700-4700 m of Beaufort Group rock has been eroded from above the boreholes (Table 5.1). Burial by >4.5 km of rock is sufficient to reset fission track ages (assuming a geothermal gradient of 20°C/km). By the end of Beaufort Group deposition (~240 Ma) samples of borehole SA1/66 (covered by 4700 m of rock) plus samples at >800 m depth in boreholes CR1/68 and KW1/67 would have been thus reset. The lack of single grain ages from any borehole samples >200 Ma (see Figures 4.7 a to j) suggests that burial continued beyond 240 Ma.

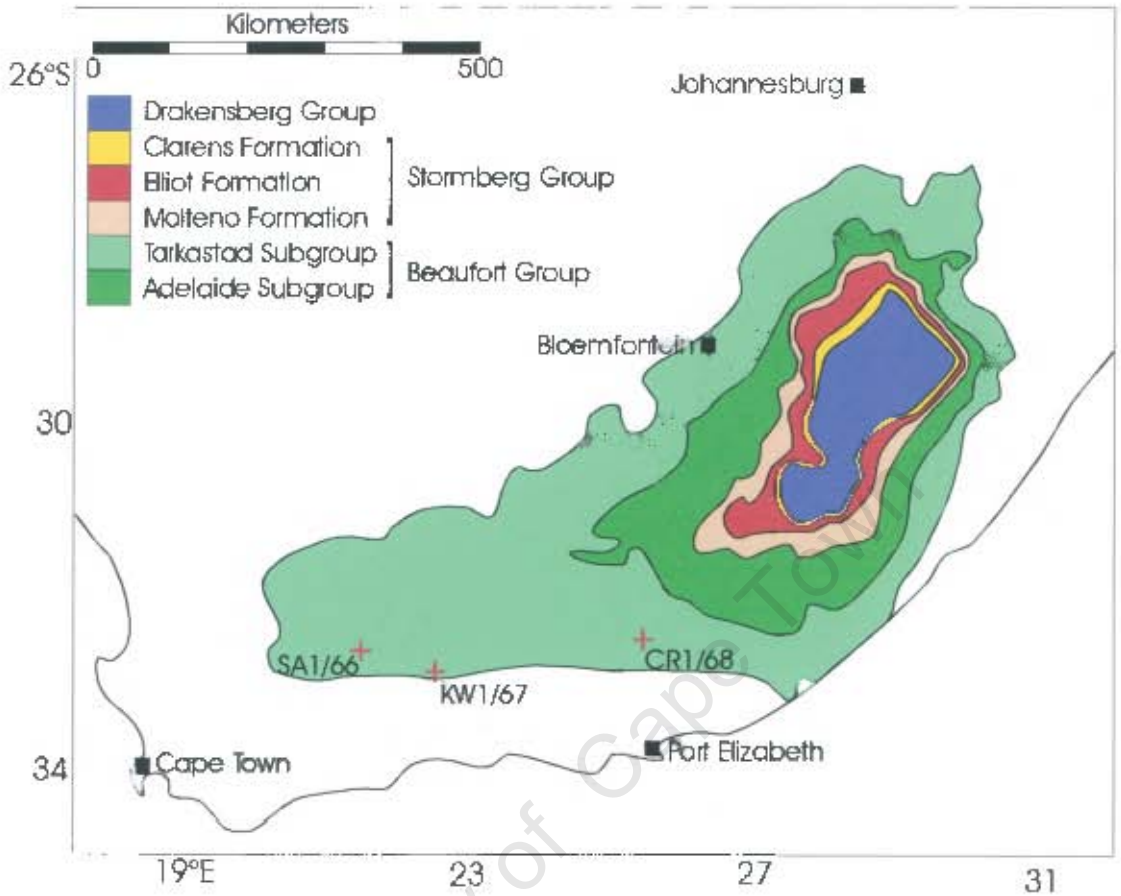

Figure 5.1: Outcrop of Adelaide and Tarkastad Subgroups of the Beaufort Group and Molteno, Clarens and Elliot Formations (adapted from Johnson *et al.*, 1996). Position of boreholes SA1/66, KW1/67 and CR1/68 are marked with red crosses.

How far south and west did the Molteno, Elliot and Clarens Formations extend?

Unconformably overlying the Beaufort Group are the Molteno, Elliot and Clarens Formations of the Stormberg Group (~460 m, ~480 m and ~280 m thick, respectively, totaling ~1220 m, Visser, 1984; or ~1100 m according to Dingle *et al.* 1983). An isopach map of the Stormberg Group in Dingle *et al.* (1983) shows it preserved as a south-east thickening wedge of sediments. The southern part of the original depocentre has been removed by syndepositional or post-depositional erosion. Its maximum thickness is 1100 m, south-east of Elliot (Dingle *et al.*, 1983).

Catuneanu *et al.*, (1998) suggest that the Stormberg basin limits are close to its present day preservational area. The Catuneanu *et al.* (1998) model of Karoo deposition describes a hinge line, separating distal from proximal deposition, which migrates craton-ward during Cape Fold Belt orogenic loading in Late Carboniferous-Middle Triassic (Dwyka to Beaufort Group deposition) and southward during unloading in the Late Triassic-Middle Jurassic (Stormberg Group deposition). Orogenic unloading causes uplift of the proximal foreland and subsidence of the distal foreland, thus according to Catuneanu *et al.* (1998), the Stormberg basin was separated from the Cape Fold Belt by a zone of syndepositional bypass and reworking of older Dwkya, Ecca and Beaufort rocks. This reworking is supported by provenance studies of the Molteno sandstones (Catuneanu *et al.*, 1998). In the Catuneanu *et al.* (1998) model, it is unlikely that the Stormberg Group deposition extended to the southern and south western Cape. However, a weakness of this model is that it hinges on unreliable K-Ar and Ar-Ar whole rock ages of Cape Fold Belt paroxysms (ages in Halbich *et al.*, 1983 and Gresse *et al.*, 1992) (see chapter 2.1.3) and does not use newer, more reliable, U-Pb ages to define the chronostratigraphy of the Karoo Basin (de Wit, pers. comm. 2004). The Karoo Basin is poorly dated at present, using vertebrate paleontology (biostratigraphy).

Turner (1999) proposes that the upper Karoo is not related to foreland basin tectonics as claimed by Catuneanu *et al.* (1998). His alternative involves the uplift of the Molteno source area due rifting prior to continental breakup and opening of the South Atlantic (Turner, 1986, 1999). Turner (1999) suggests that the dominant source of the Molteno sediments is the Maurice Ewing Bank, north of the Falkland Plateau, which was uplifted prior to rifting. Paleocurrent directions measured by Cole (1992) support such a sediment source to the south and east. Northerly and easterly to north-easterly paleocurrent directions, however, are measured from the unconformably overlying Lower and Upper Elliot Formation, respectively (Bordy *et al.*, 2004). These authors favour a recycled-orogen provenance from a southerly and south-westerly source for the Elliot Formation and call for long distance transport across and oblique to the strike of the foreland system (Bordy *et al.*, 2004).

There is still much uncertainty with regards to the source of the Stormberg sediments and the tectonic framework in which they were deposited, therefore an enlarged original depositional area cannot be ruled out. If the entire Karoo sequence up to and including the Stormberg Group originally covered the southern Cape region, then ~5-6 km of sedimentary rock has been eroded from above the boreholes since the end of Stormberg Group deposition at ~183 Ma (Table 5.1). This is consistent with the fission track results (Chapter 4).

Table 5.1: Estimates of thickness of Karoo sediment eroded from above boreholes SA1/66, KW1/67 and CR1/68. Estimates vary depending on how much of the upper Karoo Supergroup was originally deposited in the southern Cape and whether this region was covered by the Drakensberg basalts.

Stratigraphy above boreholes	Sedimentary thickness above boreholes	Sediment eroded from above boreholes (m)		
		SA1/66	KW1/67	CR1/68
Remainder of Adelaide Subgroup	Estimate from Smith (1990)= ~2800 m	1500	500	650
	Estimate from Johnson *et al.* (1997)= ~5000 m	2700	1700	1850
Remainder of Beaufort Group (Adelaide + Tarkastad Subgroup)	Estimate of the entire Beaufort Group from Johnson (1991)= ~7000 m	4700	3700	3850
Remainder of Beaufort Group + Stormberg Group (Molteno, Elliot and Clarens Formations)	Estimate of the Stormberg Group from Dingle *et al.* (1983)= 1100 m	5800	4800	4950
	Estimate of Stormberg Group from Visser (1984)= ~1220 m	5920	4920	5070
Beaufort Group + Drakensberg basalts	Estimate of Drakensberg basalt thickness= 1650 m (Duncan and Marsh, in press)	6350	5350	5500
Beaufort Group + Stormberg Group + Drakensberg basalts	Using the Dingle *et al.* (1983) estimate of maximum Stormberg thickness	7450	6450	6500

5.1.3 The Karoo Igneous Event (183 ± 1 Ma, Duncan et al., 1997)

The Karoo basalts are extremely voluminous (~2.5 * 10^6 km^3 for the Karoo and Ferrar Provinces together, Duncan *et al.*, 1997) and at least 1650 m thick (Duncan and Marsh, in press). Their emplacement has two possible thermal effects on the underlying Karoo sediment. Firstly, contact metamorphism between basalts/ dolerites and country rock may reset apatites in adjacent country rock. Secondly, Karoo magmatism may have generated convective hydrothermal systems that distribute heat throughout the basin (Duane and Brown, 1991; Brown *et al.*, 1994a). In the first case, contact heating has a highly localized effect. In the second case the heating effect of mobilized fluids has a greater range.

What effect has the Karoo magmatic event had on the borehole samples?

The southern Cape region, south of the escarpment was apparently not intruded by the Karoo dolerites (Figure 5.2). Figure 5.2a shows the location of 3 boreholes north of the escarpment, QU1/65, AB1/65 and KA1/66 and 4 boreholes south of the escarpment, KL1/65, SA1/66, KW1/67 and CR1/68. Figure 5.2b shows a vertically exaggerated cross section taken along a north-south line shown in figure 5.2a. Boreholes QU1/65, AB1/65, SA1/66 and KW1/67 are projected onto this line. Several dolerites sills intrude the Beaufort, Ecca and Dwyka Groups, drilled by boreholes QU1/65 and AB1/65, north of the escarpment. Borehole KA1/66, also located north of the escarpment, intersects several dolerite sills that have intruded the Beaufort Group in this location.

Boreholes SA1/66 and KW1/67, south of the escarpment, do not intersect any dolerite sills. Borehole KL1/65, also south of the escarpment, intersects one dolerite sill that intruded the Cape Supergroup. North of the escarpment, the boreholes intersect numerous Karoo-aged dolerite sills (e.g. the 3000 m deep QU1/65 borehole intersects 9) therefore it is surprising that borehole KL1/65, 3457 m deep, intersects only one. This sill may belong to the suite of dolerites that are associated with the Etendeka volcanics, Namibia, described and dated at 132 ± 6 Ma by Reid *et al.* (1991) (K-Ar age). The Karoo dolerites that are so numerous in the boreholes north of the escarpment do not extend to boreholes SA1/66 and KW1/67, ~100 km to the south. This suggests that the dolerite's original lateral extent is similar to their current position and that the region south of the escarpment was not intruded by dolerites. As a corollary, the coinciding of the escarpment with first

appearance of the dolerites is highly suggestive of the dolerite's roll as a barrier to escarpment retreat (further discussion in section 5.2.2 and in chapter 7).

Since the Karoo dolerites may not have extended far beyond their present day position, apatites from borehole samples south of the escarpment have not been reset by elevated temperatures associated with contact metamorphism. Whether they have been reset by the hydrothermal systems activated by Karoo volcanism is more difficult to assess. Fission track data from detrital zircons from two sedimentary-hosted uranium ore deposits suggests that these deposits have experienced maximum paleotemperatures of at least 250 ± 50°C at ~190 ± 10 Ma (Brown *et al.*, 1994a). Three of these samples are from the Rietkuil uranium deposit located south of the escarpment and <100 km from the boreholes. Thermal modelling of these data suggests that magmatically driven hydrothermal systems dissipated excess heat over a larger thickness of stratigraphic sequence than would be expected by conductive heat transfer alone (Brown *et al.*, 1994a). Single grain ages of the outcrop and borehole fission track samples presented here occasionally exceed 180 Ma, suggesting that if resetting by hydrothermal fluids did occur ~100 km south beyond the dolerite intrusions, then it did not effect all of the samples to the same degree.

Figure 5.2 (over the page): (A) Outcrop map showing the Karoo dolerites (mainly sills) and basalts and location of 7 boreholes (black crosses). The north-south cross-section is expanded in (B). The elevation of the top of each borehole is shown. Dolerite sills are marked in red. Note that dolerite sills outcrop across the escarpment and are intersected by the boreholes to the north, but are absent from boreholes SA1/66 and KW1/67. Borehole data are from the original SOEKOR Geological Well Completion Report of Leith (1969) and core logs of SA1/66, KW1/67, QU1/65 and AB1/65. Additional stratigraphic information of the top 630 m QU1/65 and 690 m for AB1/65 is from Cole and Wipplinger (2001). '?' on borehole QU1/65 indicates a transition from the Ecca to the Dwyka Group at an unknown depth.

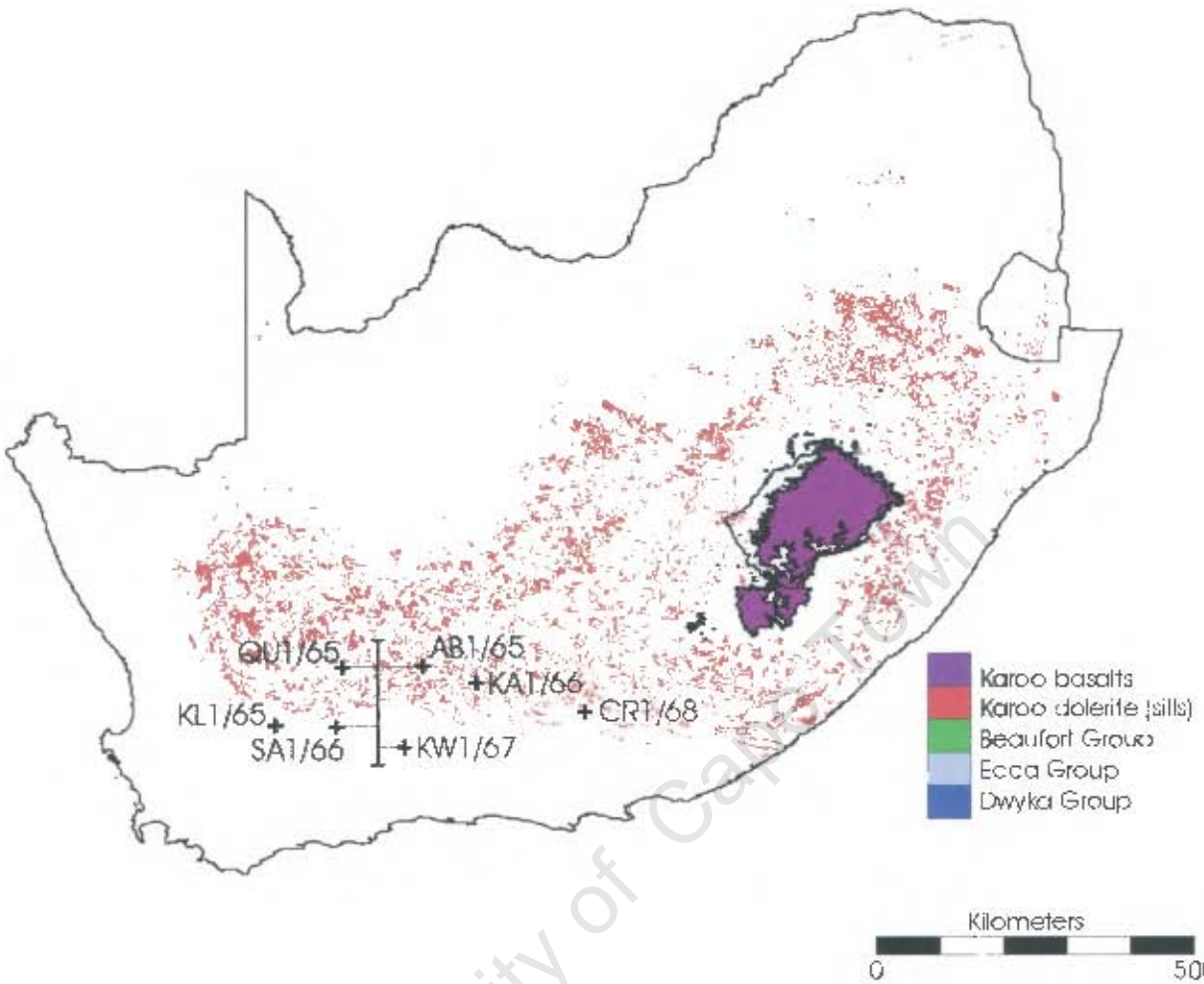

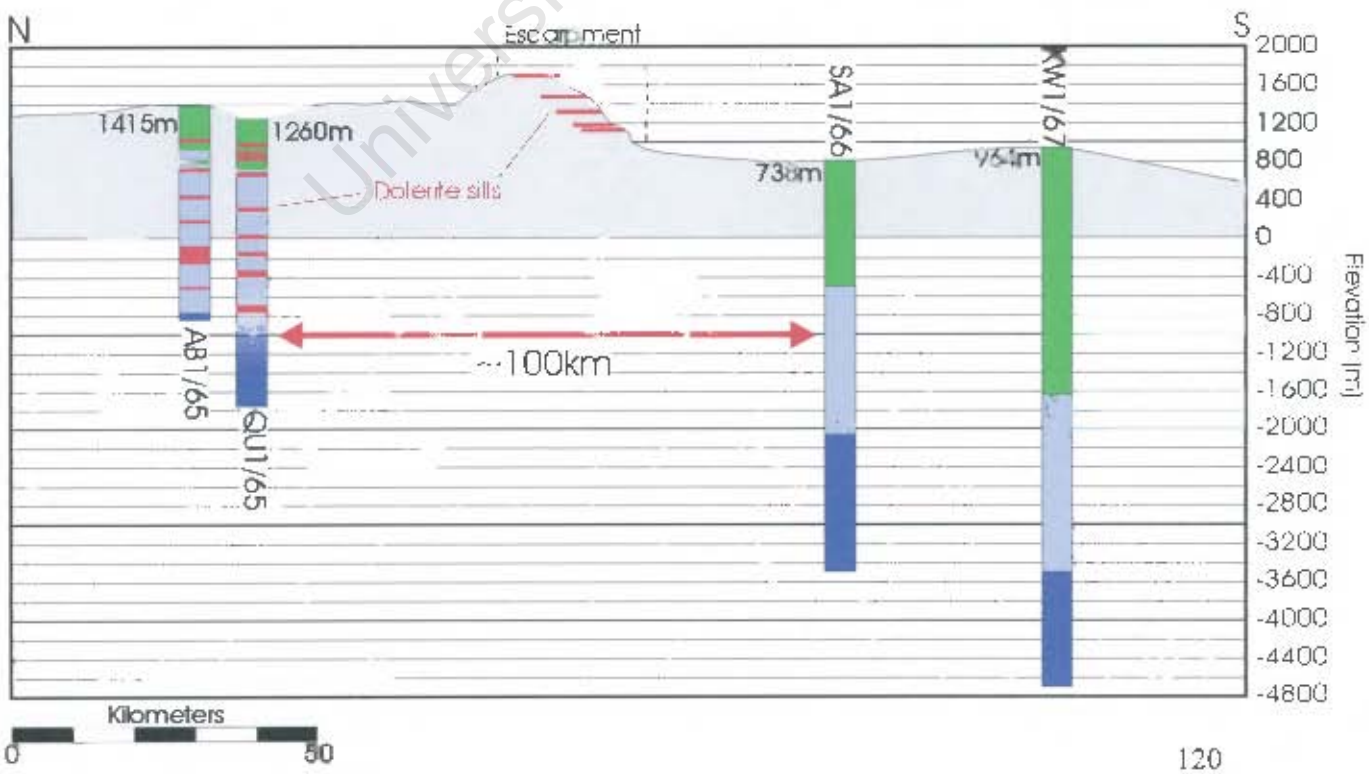

Did the Drakensberg lavas extend south, beyond the intrusive dolerites?

The answer to this question is unknown. In the case of a younger continental flood basalt province, the Columbia River Basalt Group (17-6 Ma), Tolan *et al.* (1989) (referenced in Duncan and Marsh, in press) describe lava flows of over 600 km. If the southern Cape was covered by an additional ~1650 m of Karoo lava (and not covered by the Stormberg Group) then total thickness above the top of boreholes KW1/67, SA1/66 and CR1/68 is 5350 to 6350 m (Table 5.1). This is within the denudation range of 4.75-6.5 km estimated in section 4.5. If both the Stormberg Group and Drakensberg lavas covered the southern Cape then this thickness increases to 6450-7450 m, which exceeds the estimate from fission track analysis.

Cretaceous erosion (described in section 5.2.2) was followed by the deposition of eroded material in extensional rifts associated with continental break-up, e.g. the Uitenhage Basin (onshore) and Outeniqua Basin (offshore). If the Drakensberg lavas once covered the southern Cape region and Cape Fold Belt and were subsequently eroded, then intuitively basaltic clasts should form a component of the infill of these basins. In the north-west Algoa Basin, Enon conglomerate clasts are composed of well rounded orthoquartzites, sandstones, shale and vein quartz derived from the basement, Table Mountain quartzites, Witteberg quartzites and Bokkeveld shales (Dingle *et al.*, 1983). Rare pebbles of amygdaloidal basalt, agate and tuff derived from the underlying Suurberg volcanics (of unknown age) also occur (Dingle *et al.*, 1983). There are no reports of any Drakensberg Group basaltic clasts within the infilling sediment of these Cretaceous grabens. This is supported by personal observation of the Enon Formation in the Cango Basin.

5.1.4 Evidence for further burial?

The ~250 Ma Cape Fold Belt is likely an exhumed mountain belt (Tinker *et al.*, 2004). Numerous paleoterraces at elevations of up to 1700 m above present river level (Figure 5.3) suggest that there has been downcutting of at least 1.7 km. Since the terraces are not dated, fission track thermochronology is used to estimate the extent of burial and the age of downcutting. The highest peaks in the Cape Fold Belt are formed by Table Mountain quartzites that contain no apatite and could not be dated. However, dating the overlying Bokkeveld Group (at lower elevation) resulted in fission track ages of 119 ± 10 Ma (JT02-

26) to 143 ± 8.8 Ma (JT02-20). The track length distribution of these samples shows a tail of shorter tracks (see Figure 4.7b), indicating that the samples have experience high temperatures (>~80°C). For a geothermal gradient of 20°C/km this equates to a depth of burial of >~3 km. JT02-26 and 20 were sampled from an elevation of 472 m and 785 m respectively and the highest nearest peaks in the Cape Fold Belt are ~1800 m. This suggests that this part of the Cape Fold Belt was originally covered by >2 km of rock.

Figure 5.3: (A) A terrace at 600 m elevation in the Cedarberg Moutains, ~200 km north-northeast of Cape Town. (B) A remnant Cenozoic river valley cut into the dipping Enon Formation in Baviaanskloof, Eastern Cape (see figure 2.9 for location).

A further hint that the Cape Fold Belt is an exhumed mountain range is its drainage pattern. At several locations along the east-west trending arm of the Cape Fold Belt perennial rivers running north-south meander through vertically dipping, highly competent quartzite ridges (Figure 5.4). Meanders are generally a feature of a flat landscape and thus are completely unexpected in this terrain of high relief and highly competent rock. A likely explanation is that the drainage is inherited from a previous river system, originally draining cover rock to the Cape Fold Belt. King (1963) describes a similar situation where the Vaal River transects the competent circular ridges of the Vredefort dome. In this case the drainage was inherited from when Karoo rocks covered the dome. "Such a course cannot conceivably have resulted from the simple process of river erosion acting alone immediately upon a domed structure. We are forced to postulate at least two cycles of erosion" (King, 1963, 195).

Figure 5.4 (over the page): (A) The Gourits, Gamtoos and Sundays Rivers drain the southern Cape and in several places (including Seweweekspoort and Gamkaskloof, enlarged in B) meander through prominent quartzite ridges of the Table Mountain and Cango Groups. (B) Aerial photograph showing the meandering of the Gourits River through steeply dipping quartzites and sandstones in these locations. (C) A view of the Swartberg Pass and of the meanders at ground level. Meanders also cut through folded quartzites at Montague.

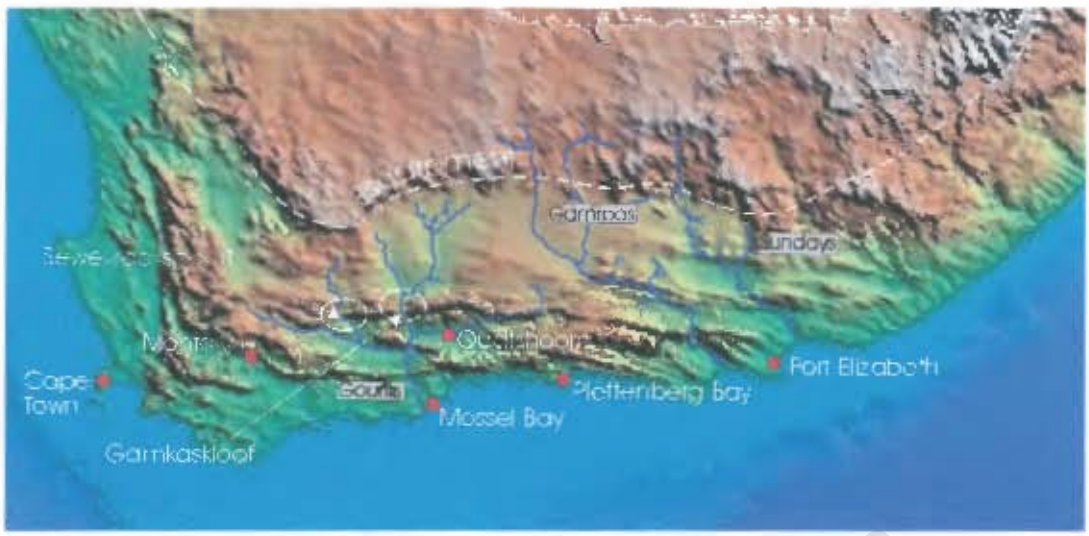

A

B

Kilometers
0 10

Kilometers
0 10

C

What covered the Cape Fold Belt?

Candidates for Cape Fold Belt cover include, the Stormberg Group, the Drakensberg Group or a completely unknown cover rock, contemporaneous with or younger than these two groups, that has been completely removed by subsequent erosion in the early and mid-Cretaceous.

5.1.5 Uplift in the Cretaceous

There is much evidence to support early and mid Cretaceous denudation that is independent of fission track thermochronology (described in detail in Chapter 3). Offshore sediment volumes in particular offer a clear corroboration of an exhumation history involving denudation in the early and mid Cretaceous. The offshore evidence is described in detail in chapter 6.

5.2 Summary of burial and exhumation history

5.2.1 Burial

Figure 5.5 is a schematic model of the tectonic evolution of the southern Cape, prior to the onset of increased denudation (> ~140 Ma).

A) The deposition of the Cape Supergroup occurred along a thermally subsiding passive margin from ~500-330 Ma.

B) The lower Karoo sequence was deposited from ~330-250 Ma (Dwyka, Ecca and lower Beaufort Groups).

C) Orogenic loading during the Cape Fold Belt Orogeny (~250 Ma) caused subsidence in the foreland and deposition of the upper Beaufort Group in the newly created accommodation space.

D) The Stormberg Group is deposited in either (i) a restricted basin or (ii) a larger basin extending to and covering the Cape Fold Belt (~220-183 Ma). The same two scenarios for the Stormberg Group are outlined in (i) and (ii) in E and F.

E) The extrusion and intrusion of Karoo basalts and dolerites occurred at 183 ± 1 Ma (Duncan *et al.*, 1997). The basalts may have extended beyond the intrusion limit of the dolerites, hence the '?'.

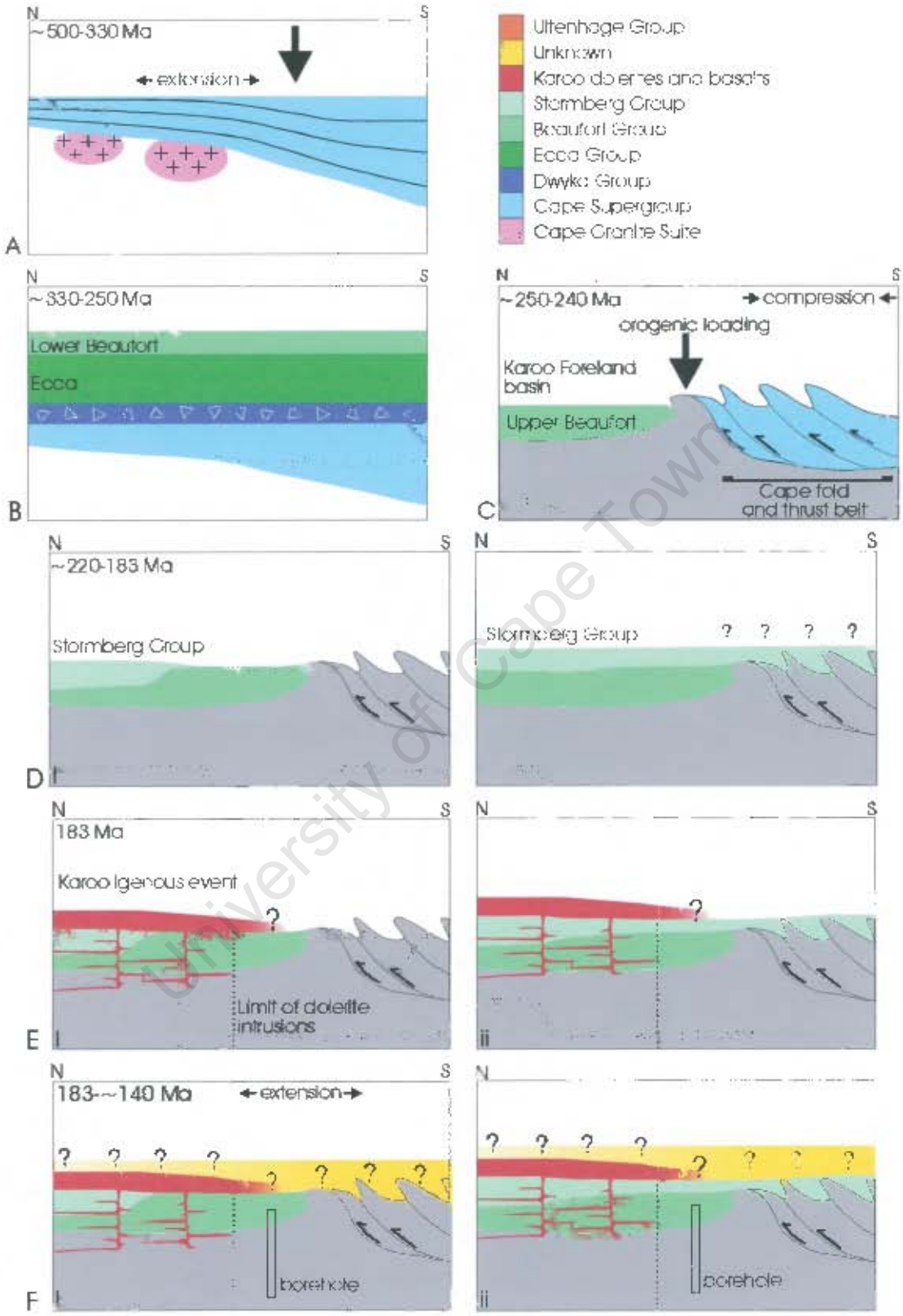

Figure 5.5: Summary figure of the history (including burial) of the southern Cape since ~500 Ma. See text for full explanation.

F) Further burial by unknown rock shown in yellow may have occurred from 183-~140 Ma. Thus, at maximum burial the borehole may have been covered by upper Beaufort, Stormberg and Drakensberg Groups as well by unknown rock (ii) or by any combination of these Groups (one combination shown in (i)).

5.2.2 Exhumation and differential denudation

Figure 5.6 is a comparison between the age-depth profiles of borehole QU1/65, located north of the escarpment, and SA1/66, KW1/67 and CR1/68 all located south of the escarpment. Evidence of accelerated denudation in the early Cretaceous (blue shading) is apparent in borehole QU1/65 and the outcrop samples (red diamonds; from increasing elevations across the escarpment) added to the borehole plot of KW1/67. The borehole samples south of the escarpment do not record the signature of this early period of denudation. Significant mid Cretaceous denudation (100-80 Ma, yellow shading) is recorded by all three boreholes south of the escarpment, but not by QU1/65 to the north.

Figure 5.6 (over the page): A comparison of age-depth profiles of boreholes seaward (SA1/66, KW1/67, CR1/68) and landward of the escarpment (QU1/65). Early Cretaceous rapid denudation is shaded blue, mid Cretaceous rapid denudation is shaded yellow. Blue diamonds= borehole samples. Red diamonds= outcrop samples.

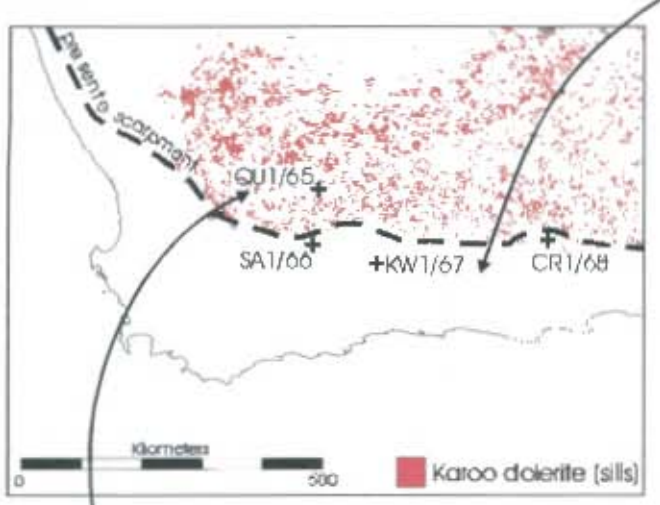

South of the escarpment

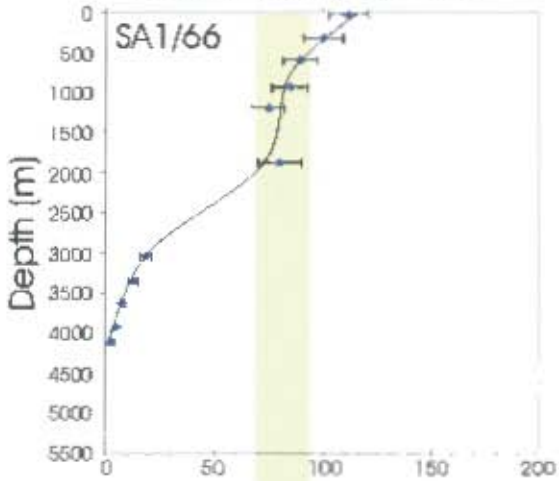

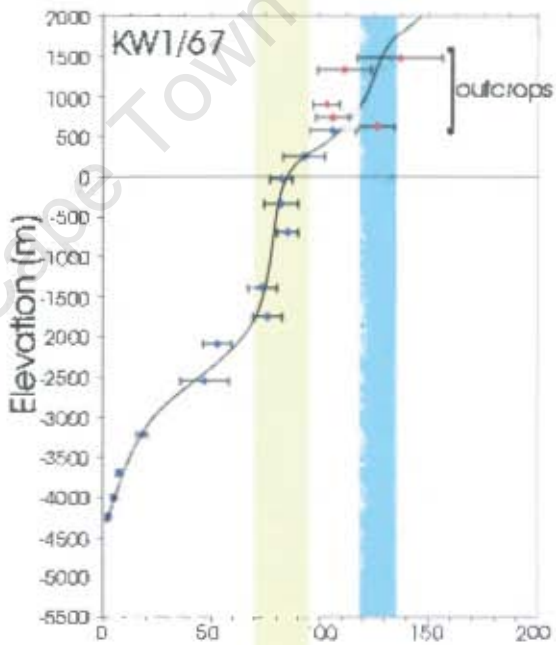

North of the escarpment

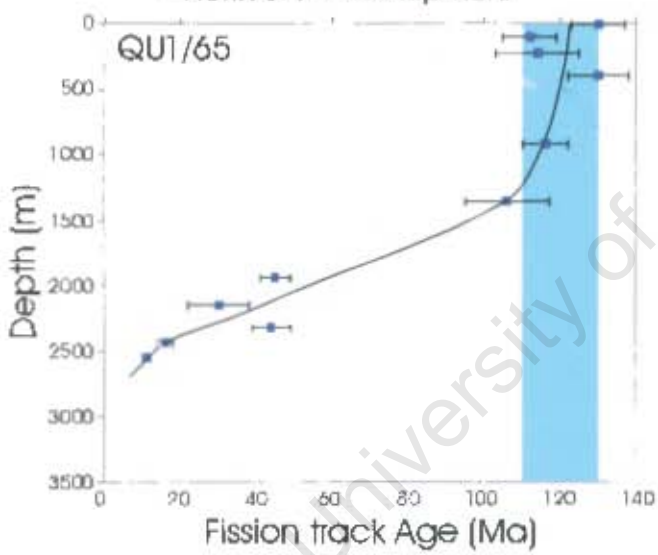

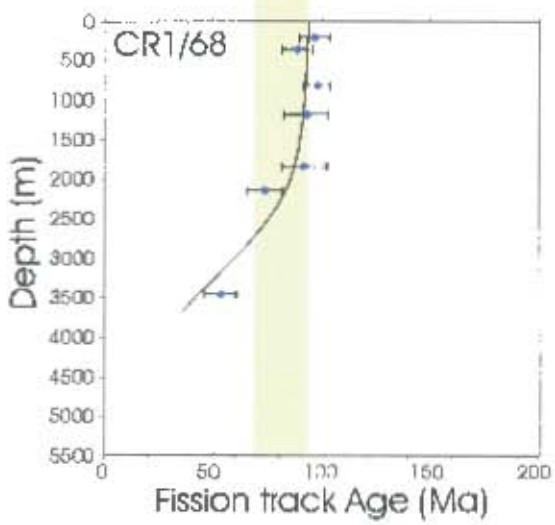

5.2.2.1 Early Cretaceous denudation

The lack of a record of early Cretaceous denudation from the coastal boreholes can be explained in two ways. Either, the coastal zone has not experienced rapid denudation in the early Cretaceous (~140-120 Ma) or, it *has* experienced early Cretaceous rapid denudation, but the signature of this denudation (e.g. the inflection point, * in Figure 4.4) has been removed completely by subsequent erosion in the mid Cretaceous. Successful thermal modelling of the boreholes (Chapter 4.5) incorporating an early phase of increased denudation suggests that the latter is the case. Rapid denudation in the early Cretaceous may be related to the onset of the break-up of Africa and South America (discussed further in Chapter 7). The close proximity of the coastal region to the rift margin suggests that it would have been uplifted and denuded (see the various computer models for rift flank uplift in Chapter 3). Subsequent erosion in the mid Cretaceous (100-80 Ma) has likely removed the signature of earlier denudation in the coastal region.

Early Cretaceous denudation (~140-120 Ma) of 1-2.6 km above the boreholes, (according to fission track modelling), is shown schematically in figure 5.7). North of the dolerite limit the Karoo basalts and possible additional unknown cover rock are eroded. South of the dolerite limit the Karoo sediments and Cape Fold Belt cover are eroded, to produce the first terraces of the Cape Fold Belt. In the early Cretaceous the Uitenhage Group was deposited in half grabens.

5.2.2.2 Mid Cretaceous denudation

Inland, QU1/65 shows no evidence of rapid denudation in the mid Cretaceous. This suggests that either the inland region was never uplifted in the mid Cretaceous or that uplift occurred without rapid denudation that occurred in the coastal region. A possible reason for a decrease in denudation rate may be the presence of Karoo dolerites. Dolerites form cap rocks that shield the softer Karoo sediment beneath from erosion. The dolerite sills, now exposed on the surface, must originally have been covered. Prior to rifting and the onset of denudation (>140 Ma) the inland region is likely to have been covered by 1-2 km of Karoo basalts. In Lesotho, these basalts are vesicular and composed of multiple flows with multiple internal contacts and therefore are more prone to erosion than the massive, crystalline dolerite sills beneath (A.R. Duncan, pers. comm. 2004). If the Karoo

basalts were eroded in the early Cretaceous (~140-120 Ma) leaving only an erosional remnant in Lesotho, then by the mid Cretaceous (~100 Ma) the inland region (north of the escarpment) may have been irregularly covered by many dolerite sills that form a more erosion- resistant cap to the soft sediments beneath (Figure 5.7b). Denudation in the mid Cretaceous would occur at a reduced rate relative to denudation occurring contemporaneously, south of the escarpment (1.7-3.5 km) and to denudation in the early Cretaceous.

In this scenario, fission track data from QU1/65 shows no rapid denudation in the mid Cretaceous, even though the area may have been uplifted. South of the dolerite limit, erosion in the mid Cretaceous continued and 2.1-3.5 km of Karoo sediments were 'scooped' out against the escarpment and the Cape Fold Belt was exhumed (Figure 5.7b). Thus all record of the earlier period of denudation was removed. The 'signature' of early Cretaceous uplift should be preserved in apatites from high elevations in the Cape Fold Belt. Unfortunately, the peaks are formed by Table Mountain quartzites from which no apatite was recovered to test this. Mid Cretaceous denudation (and uplift) may have been coupled with extension and the tectonic exhumation of inliers to the Cape Fold Belt (e.g. the Cango Group, see Chapter 4.4.1.6). This is shown schematically in figure 5.7. Since 80 Ma there has been minor erosion in the southern Cape.

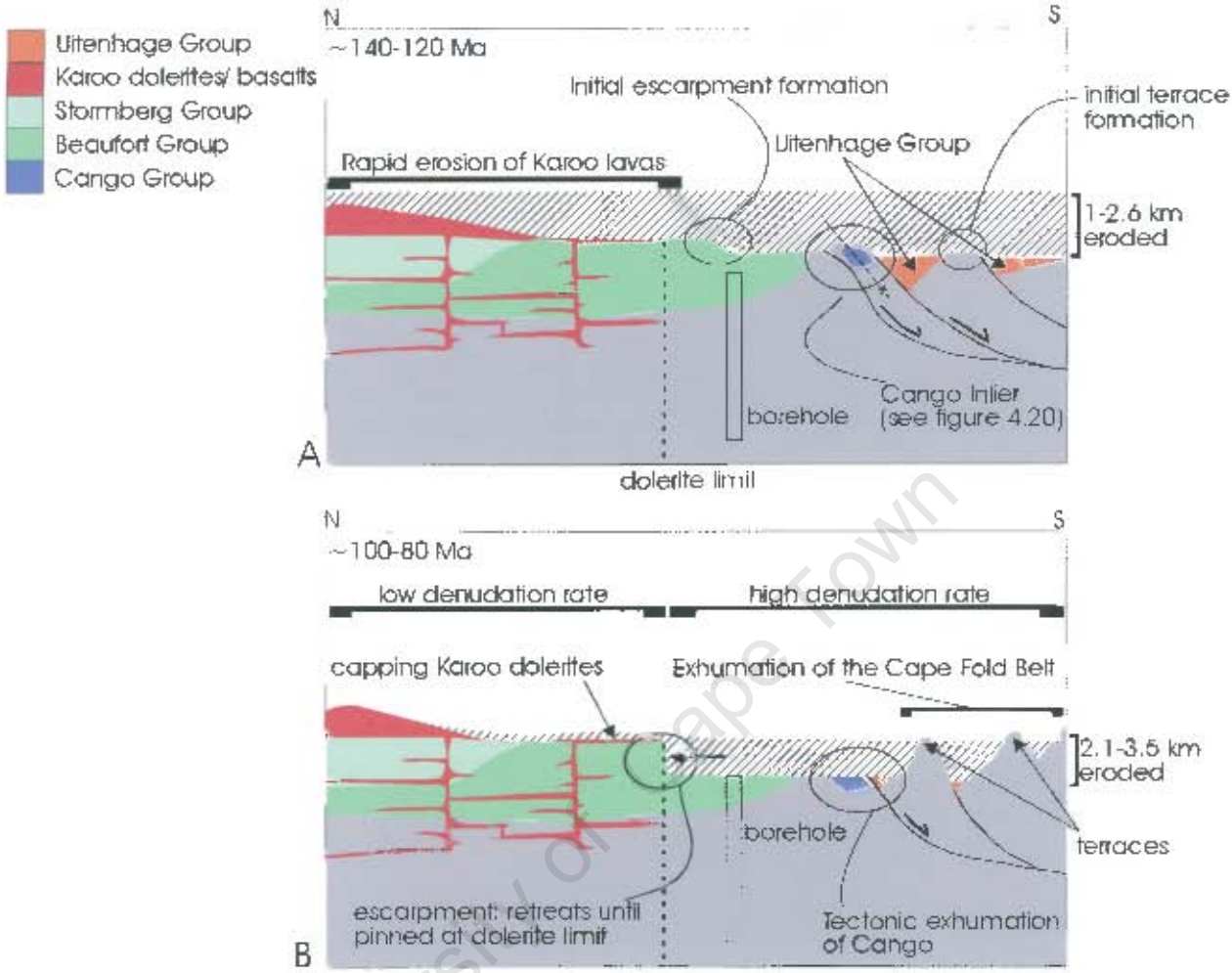

Figure 5.7: Differential denudation in the early and mid Cretaceous. (A) Denudation in the *early Cretaceous* (~140-120 Ma) removes the Drakensberg basalts from the area immediately north of the dolerite limit. The escarpment was initiated just south of the dolerite limit, possibly at a pre-existing drainage divide (see Chapter 3.3). Denudation of 1-2.6 km of rock from above the boreholes was synchronous with the deposition of the Uitenhage Group (orange) in newly created accommodation space adjacent to reactivated faults. Exhumation of the Cape Fold Belt began and the first terraces were formed. (B) Denudation in the *mid Cretaceous* (~100-80 Ma) results in limited escarpment retreat until it was 'pinned' by the erosion resistant dolerite sills. Denudation occurs at a low rate north of the dolerite limit where dolerites protect the soft Karoo sediment below from erosion. To the south, an escarpment is 'scooped out' as 2.1-3.5 km of rock, unprotected by Karoo dolerites, is eroded. Inliers to the Cape Fold Belt (e.g. the Cango Group, purple) are tectonically exhumed during extensional faulting.

5.3 Implications for the Great escarpment

From the fission track analysis it is clear that the escarpment is not a young feature of the South African landscape, and is certainly significantly older than the ~30 Ma age that Burke (1996) assigns it. Gradual recession since its original formation during rifting is also ruled out (Figure 4.17). The fission track data (and cosmogenic analysis) support a model that concludes major escarpment recession by the end of the Cretaceous. Geophysical models described in chapter 3 relate escarpment formation to rifting and its initiation is likely related to the first period of increased denudation in the early Cretaceous (140-120 Ma). However, it is argued here that the escarpment's prominent relief may be due to lithologic inheritance and subsequent denudation in the mid Cretaceous (100-80 Ma). In this second period of denudation, the southern Cape, south of the escarpment, was more easily eroded than its northern counterpart which was capped by competent, erosion-resistant dolerite sills.

Chapter 6: Accumulation of sediment offshore

6.1 Introduction

Since Gondwana breakup and the onset of separation of South America from southern Africa (~140-130 Ma), sediment eroded from the continent has been deposited on the evolving continental shelves surrounding South Africa. This chapter investigates the timing and volume of sediment accumulating off South Africa's south coast.

Since the 1970's, South Africa's offshore has been explored for oil and gas. This exploration has resulted in a wealth of seismic and borehole data that have allowed researchers to unravel the sedimentary and tectonic history of offshore Mesozoic basins. Much of the earlier work is contained in internal company exploration reports. A stratigraphic atlas of the south and west coast, compiled by Brown *et al.* (1995) from detailed seismic stratigraphic studies, summarizes this previous work and compiled maps presented here make use of their stratigraphic framework. For this thesis, the ages of the regional unconformities have been adjusted to reflect new age calibrations for the Cretaceous Period and Cenozoic Era from Gradstein *et al.*, (2004).

Underpinning this study are 10 maps of sediment distribution across the four basins, the Bredasdorp, Pletmos, Gamtoos and Algoa Basins (collectively termed the Outeniqua Basin) off the south coast of South Africa (Figure 6.1). The southern extension of these basins is the Southern Outeniqua Basin. Five of these maps show depths to 5 regional unconformities across the Outeniqua Basin. The unconformities, chosen for their regional distribution and known age, are: 1At1, the rift-drift unconformity for the south coast (~136 Ma), 6At1 (~130 Ma), 13At1 (~120 Ma), 15At1 (~93 Ma) and 22At1 (~67 Ma). Each time interval reflects a particular stage in the development of the offshore Mesozoic basins (described in Chapter 6.2). For example, the onset of thermal subsidence creates a different pattern of sediment distribution across the rift margin. Five additional isopach maps show how sediment thickness varies across the Outeniqua Basin over time. Appendix G describes how all 10 maps are compiled and shows how sediment thickness for the Outeniqua Basin and Southern Outeniqua Basin is calculated.

Section 6.2 discusses the development of the offshore Mesozoic basins (south coast) and section 6.3 gives the results of the calculation of sediment volume over 136 Myrs. A discussion of the implications of these results follows in section 6.4.

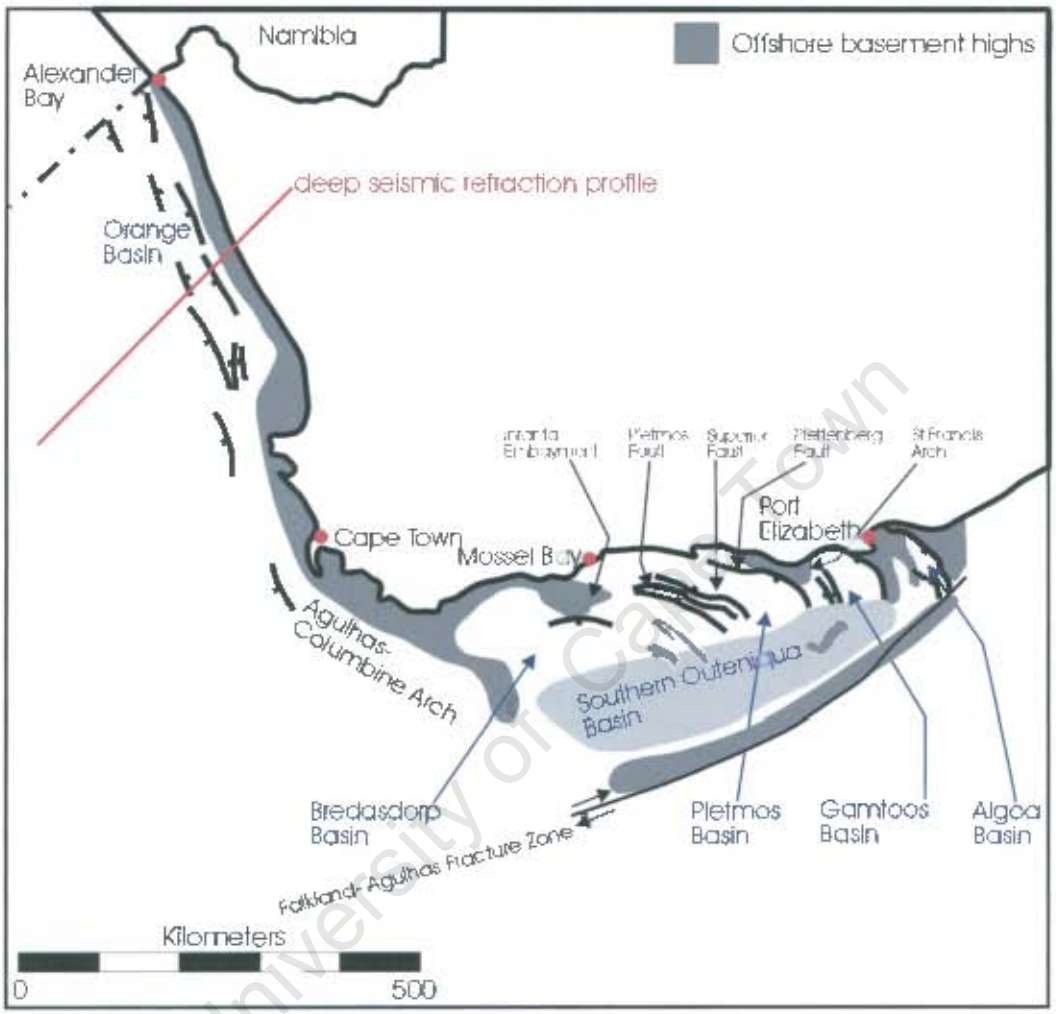

Figure 6.1: Location of Mesozoic basins offshore: Orange Basin (west coast), Bredasdorp, Pletmos, Gamtoos, Algoa Basins (Outeniqua Basin) and Southern Outeniqua Basin (shaded grey). Red line= deep seismic refraction profile of the Inkaba ye Africa Project. Dark grey shading= offshore basement highs. Adapted from the Petroleum Agency (2000).

6.2 The break-up of Gondwana and the development of the offshore basins

6.2.1. Introduction

The rifting of Africa from Antarctica and South America (~140-130 Ma) resulted in the formation of several offshore basins (Figure 6 1) that became the depositories for late Jurassic to Cretaceous sediment eroded from the southern African continent. The temporal and spatial distribution of this sediment can be used to constrain the timing and degree of source area denudation.

Dextral shear stress along the Falkland-Agulhas Fracture Zone (FAFZ) resulted in the separation of the Falkland Plateau from the Mozambique Ridge, thus the break up of Africa and South America during the middle/ late Jurassic to ~136 Ma. During this time, arcuate rift faults gave rise to a horst and graben structure composing the early Outeniqua Basin As outlined in Bate and Malan (1992), the arcuate nature of the bounding faults may have been inherited from the curvature of the Cape Fold Belt in this region (Martin *et al.*, 1981). However, Ben Avraham *et al.* (1993) suggest that the curvature may be a response to clockwise rotation of 'Lafonia', the Falkland microplate away from the Mozambique ridge.

Tectonic readjustments during the breakup of Gondwana have resulted in several prominent and widespread unconformities within the thick drift succession that are identified and correlated from offshore seismic data and paleontological age dating (Brown *et al.*, 1995; McMillan *et al.*, 1997, McMillan, 2003). The regional unconformities are 1At1 at ~136 Ma (Valanginian Stage), 6At1 at ~130 Ma (Hauterivian Stage), 13At1 at ~120 Ma (Early Aptian Stage), at ~103 Ma (Albian Stage), 15At1 at ~93 Ma (Cenomanian Stage), ~80 Ma (Campanian Stage) and 22At1 at ~67 Ma (Upper Maastrichtian Stage).

Sequence stratigraphic work using seismic reflection data has identified highstand and lowstand sedimentary systems tracts and resulted in the fine-scale stratigraphic subdivisions of the basin's infill (Brown *et al.*, 1995, McMillan *et al.*, 1997, McMillan, 2003). Micro paleontological evidence (from Foraminifera) suggests that these systems tracts are a result of variation in rate of margin subsidence or sediment supply (McMillan *et al.*, 1997). The volumes of sediment bounded by these major

unconformities are calculated in section 6.3. Along the south coast, most normal faulting terminated by the early Cretaceous (Brown *et al.*, 1995). Uplift and erosion resulted in the first regional unconformity, the rift-drift unconformity (1At1, ~136 Ma), marking the beginning of the rift-drift transition sequences along the south coast.

The oldest sediment (Late Jurassic) accumulated at the onset of rifting. These sediments were drilled in the Gamtoos and Algoa basins (McMillan *et al.*, 1997). Movement continued along some normal faults post 1At1 and deposition was concentrated in areas of increased localized subsidence (Brown *et al.*, 1995). Figure 6.2 shows the depth to the 1At1/136 Ma unconformity, which is highly variable across the south coast (353 m, Algoa Basin to 4268 m, eastern Bredasdorp Basin). The unconformity is shallowest in the north (Infanta Arch), northeast (St Francis Arch) and southwest (Agulhas Arch) and deepest farther offshore in the Southern Outeniqua basin. The variable depth of 1At1 is partly because the underlying synrift sediment is unevenly thick, due to its localized deposition adjacent to normal faults. Also, the 1At1 unconformity itself is offset by normal faulting (Petroleum Agency SA, 2000).

Figure 6.2 (over the page): Highly variable depth (in meters) below sea floor to unconformity 1At1 (~136 Ma). Shallow depth in red, deepest in blue. Borehole locations used in composition of map marked by crosses. The unconformity is deepest to the south of normal faults bounding the Pletmos and Bredasdorp basins, suggesting that normal movement along these faults continued after the development of the 1At1 unconformity. One area, where 1At1 is shallow is possibly a horst block (circled). Since the same area can be circled on the map of the depth to the 6At1 unconformity (Figure 6.3) but not on Figure 6.4, normal movement may have continued till ~>120 Ma.

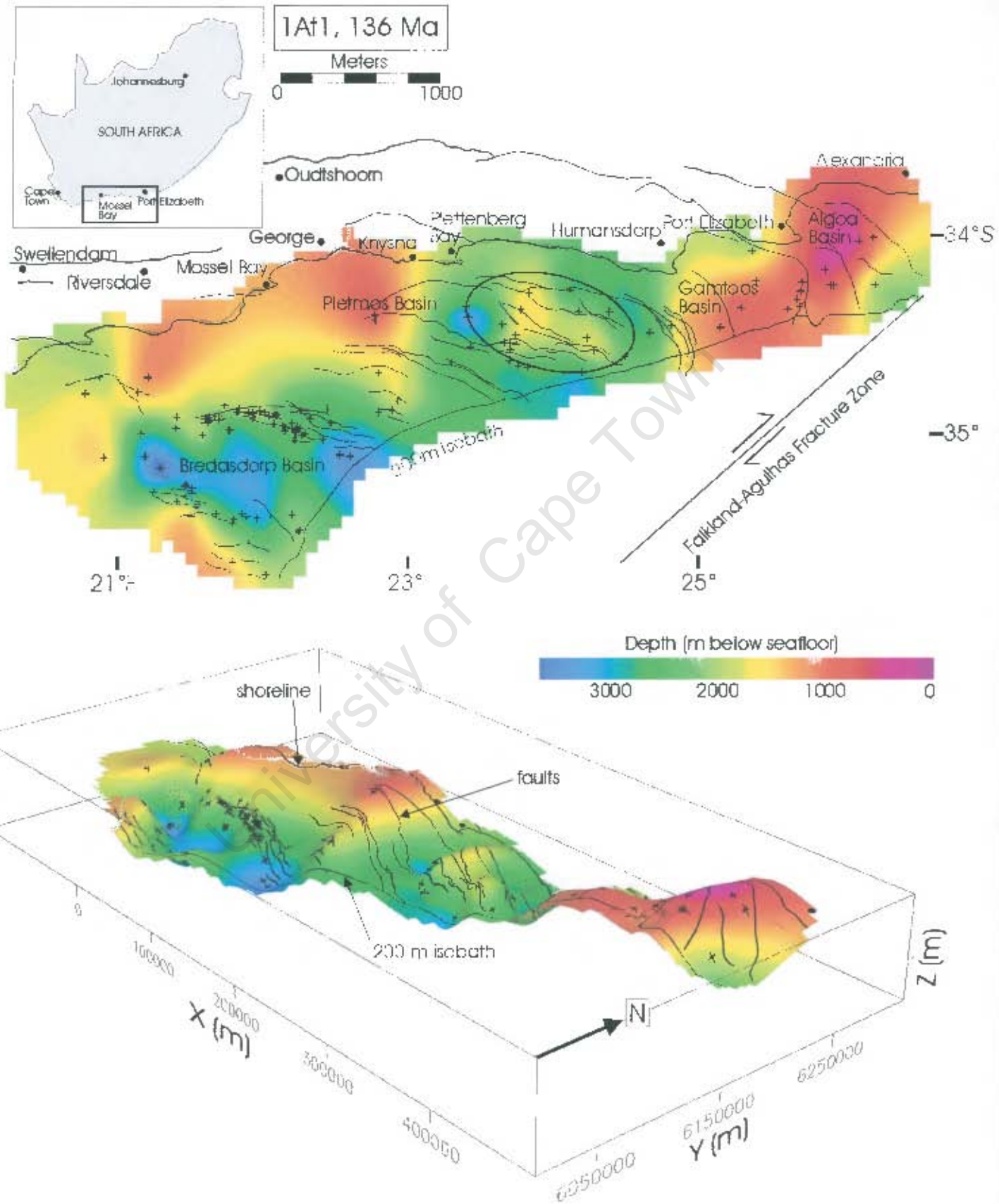

A second period of uplift and subsequent erosion and canyon incision occurred at ~130 Ma (Hauterivian Stage) and produced a second regional unconformity (6At1). 6At1 signals the end of graben infilling and the beginning of shelf sediment progradation as well as the end of active subsidence along the northern onshore Algoa and Pletmos basin margins (McMillan *et al.*, 1997). 6At1 also corresponds to the rift-drift unconformity along the west coast, where normal faulting continued for ~9 Myr after the cessation of most faulting along the south coast (Brown *et al.*, 1995).

From ~130 to 100 Ma (*Albian Stage*) Africa and South America separated ('unzipped') from south to north along the west coast, which occurred simultaneously with dextral movement along the FAFZ (Brown *et al.*, 1995). Deposition in the Orange Basin at ~130 Ma (above the rift-drift unconformity) was associated with lower subsidence rates resulting in sediment progradation to form a wedge along the margin (Brown *et al.*, 1995). High subsidence rates along the south coast were reduced between 130 and 120 Ma perhaps due to reduced thermal subsidence during the final phase of transpressional stress along the FAFZ (Brown *et al.*, 1995). After 130 Ma the eastern basins (Gamtoos and Algoa) experienced uplift and erosion (greatest in the latter) while the western basins (Pletmos and Bredasdorp) were subsiding (Brown *et al.*, 1995).

Figure 6.3 shows the depth below seafloor of the 6At1 unconformity that varies between 934 m (St Francis Arch) and 3454 m (Eastern Bredasdorp Basin). As in figure 6.2, figure 6.3 shows the unconformity as generally deepest in the south but also deep in the central Bredasdorp Basin and sections of the Pletmos Basin. The 11a and 11b boreholes (See Figure G-1, Appendix G for location) that drill through the Algoa and Gamtoos Basins mostly do not intersect 6At1 and 13At1. This is likely due to major uplift that led to the erosion of sediments deposited between 130 and 120 Ma in this area (mentioned above and described in more detail in section 6.2.2.3).

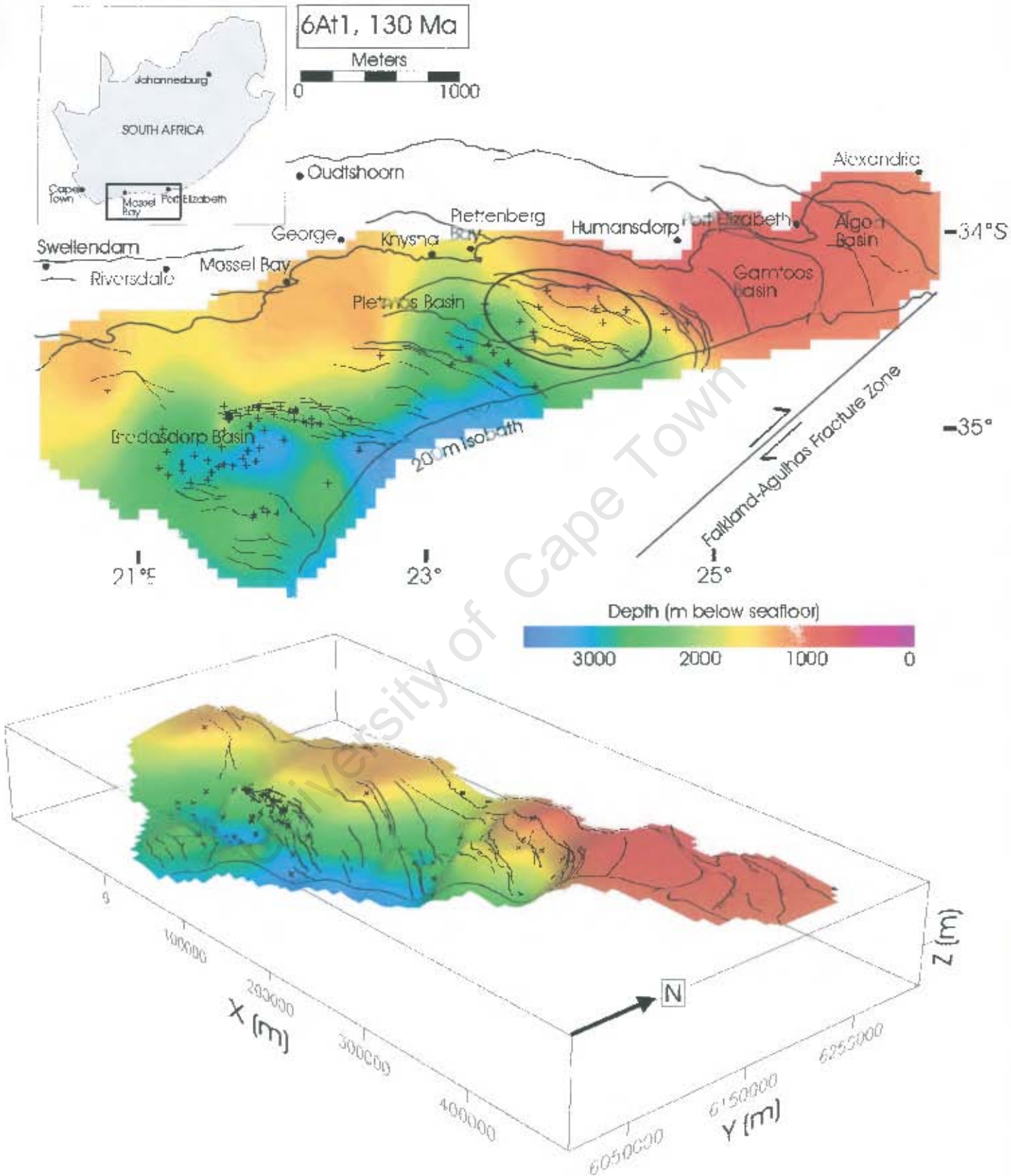

Figure 6.3: Depth (in meters) below sea floor to unconformity 6At1 (~130 Ma). See figure caption 6.2 for explanation of circled area.

A third period of uplift and erosion saw the development of a third regional unconformity, 13At1 (~120 Ma). The regional effect the onset of thermal subsidence (post ~120 Ma) is shown in the constant depth below sea floor of the 13At1 unconformity and also of 15At1 (~93 Ma) above (Figure 6.4 and 6.5, respectively). 13At1 is deepest in the central Bredasdorp Basin and the Southern Outeniqua Basin (~3000 m below seafloor). According to Dingle *et al.* (1983) and Partridge (1998), the Falkland Plateau cleared the Agulhas Bank at ~100 Ma when South America and South Africa finally disengage from each other completely (although this age is debated as outlined in Fouché *et al.*, 1992).

Movement along the FAFZ ended in the mid Cretaceous. The fourth, fifth and sixth regional unconformities developed at 103 Ma (*Albian Stage*), 93 Ma (*Cenomanian Stage*) (Figure 6.5) and 80 Ma (*Campanian Stage*) respectively. From ~80 Ma, subsidence rates decreased and sediment prograded further into the South Atlantic Basin (Brown *et al.*, 1995). In figure 6.5 this is shown in the predominance of pink/red colour close to the coast, indicating shallow 15At1. Successive sediment bypassed these shallower areas and was deposited where there is accommodation space, in deeper water further offshore.

Figure 6.6 shows the depth to the 22At1 unconformity (67 Ma) that approximately marks the beginning of the Cenozoic sediment accumulation. This unconformity is shallow (<700 m below seafloor) across the shelf, indicating that the overlying Cenozoic sediments are relatively thin. (The results of sediment volume calculations are given in section 6.3). This unconformity varies in depth below seafloor, indicating that the Cenozoic sediment above is thickest in discrete areas. This is discussed in further detail in section 6.4.

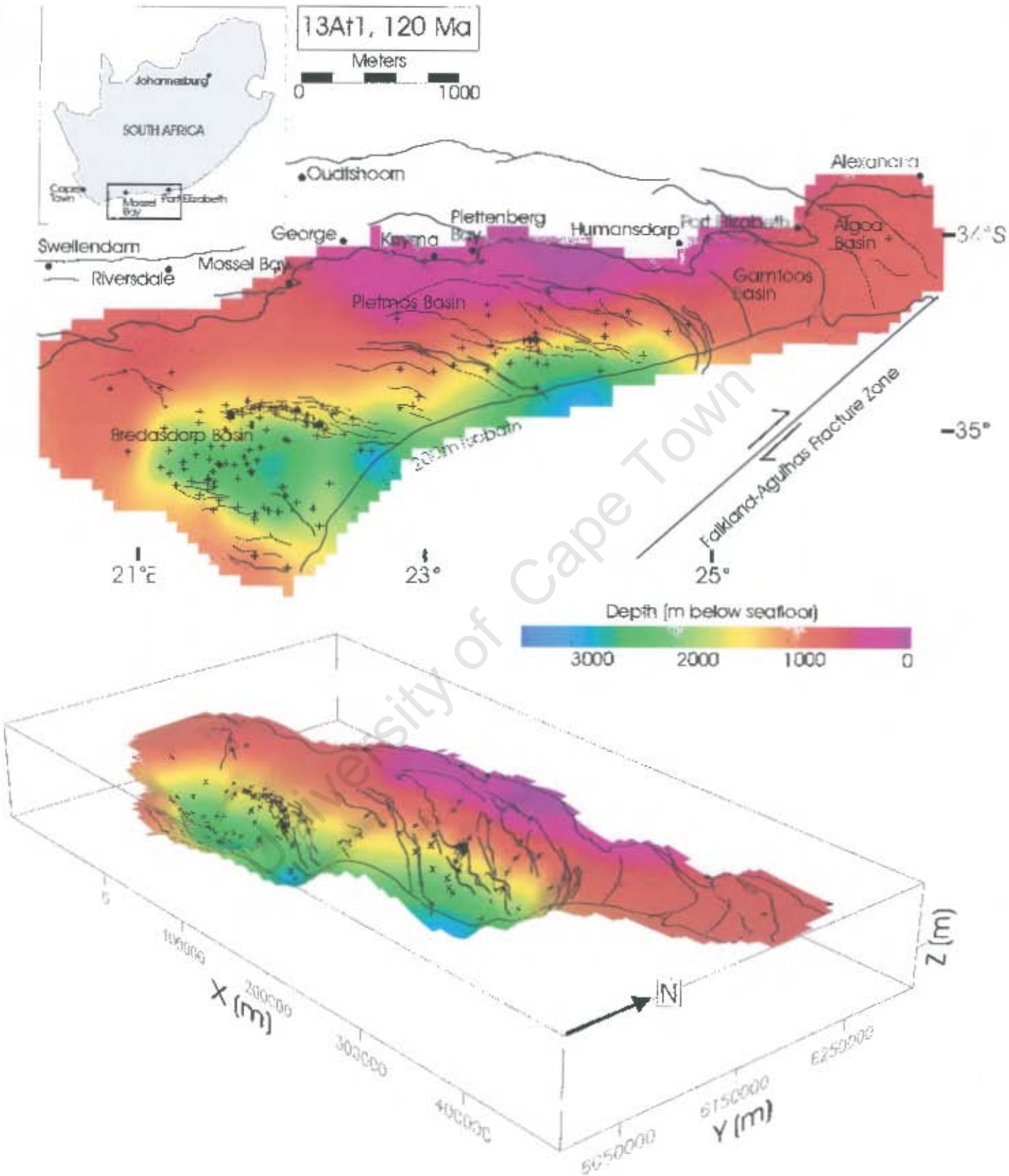

Figure 6.4: Depth (in meters) below sea floor to unconformity 13At1 (~120 Ma).

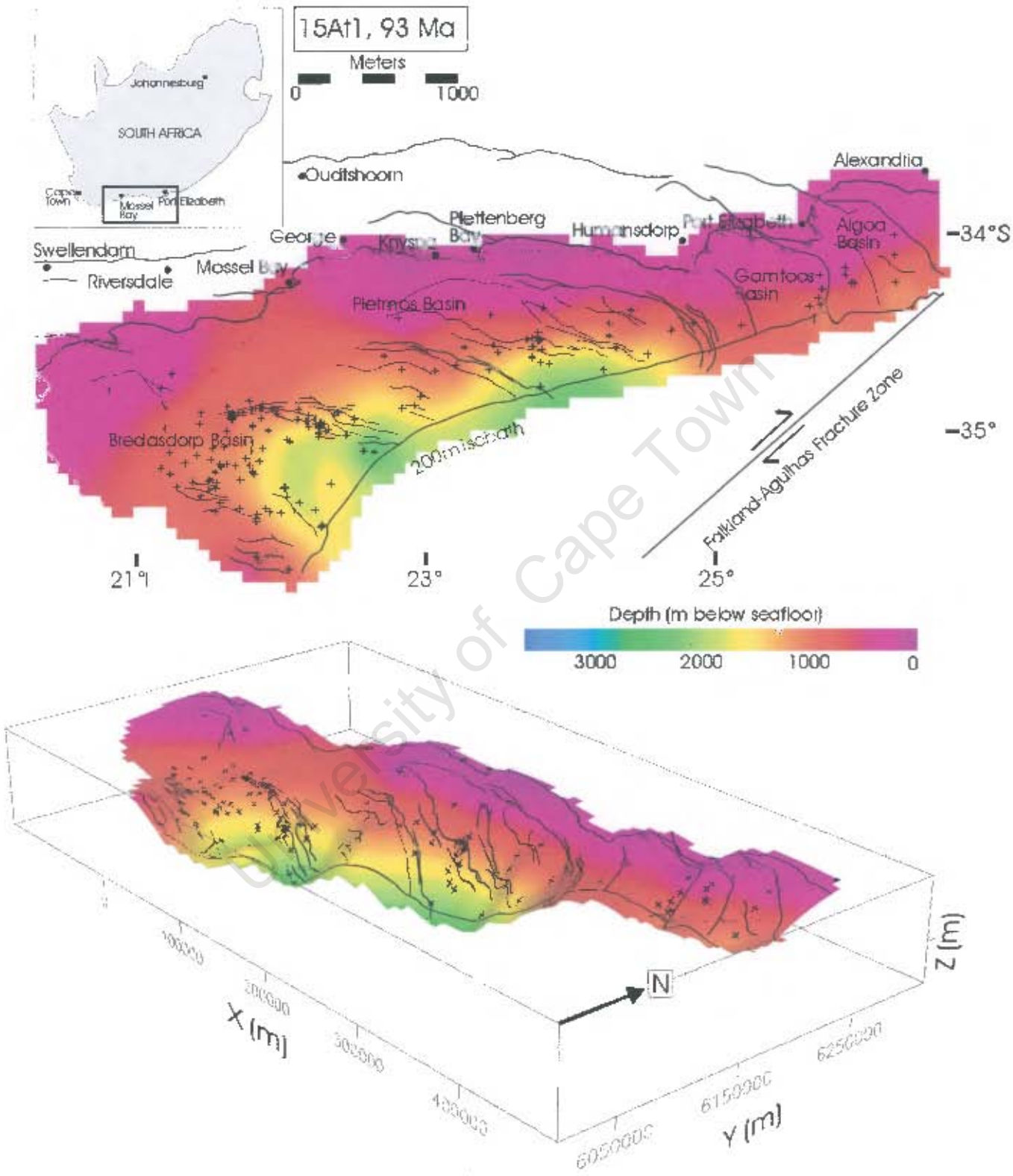

Figure 6.5: Depth (in meters) below sea floor to unconformity 15At1 (~93 Ma).

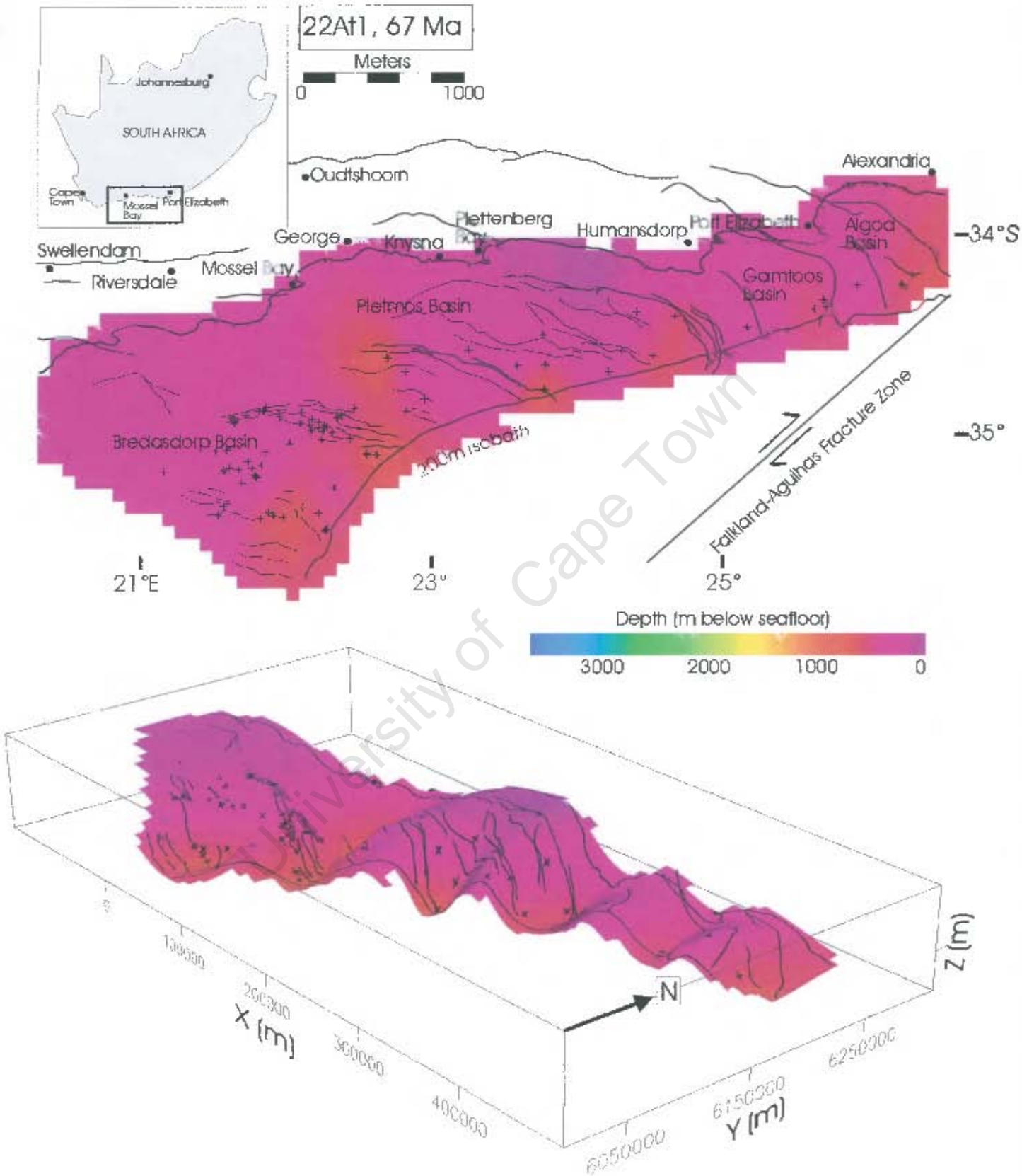

Figure 6.6: Depth (in meters) below sea floor to unconformity 22At1 (~67 Ma).

6.2.2. *The Outeniqua Basin in detail (from west to east)*

6.2.2.1 The Bredasdorp Basin

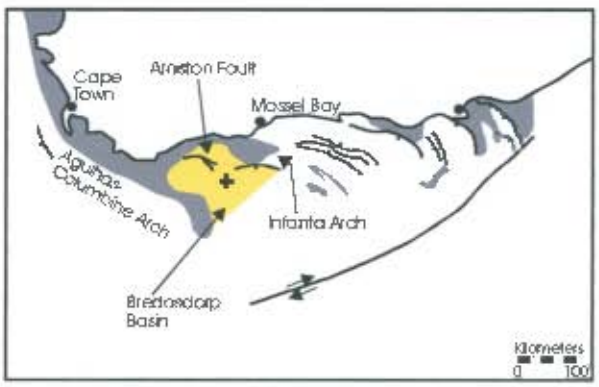

Figure 6.7: Location of the Bredasdorp Basin (yellow). Cross shows the location of the Oribi and Oryx oil fields. Red line= location of section shown in figure 6.8.

6.2.2.1.a Introduction

The Bredasdorp Basin occupies an area of ~18,000 km^2, 200 km long and 80 km wide, southwest of Mossel Bay (Figure 6.7, section in Figure 6.8). The basin is bounded by minor faults defining the Infanta Arch in the northeast and the Agulhas Arch in the southwest and is filled with late Jurassic to Cenozoic sediment (Brown *et al.*, 1995). Basement is at a maximum depth of 7 km and where it is intersected, is composed of the Devonian Bokkeveld Group and (close to the Infanta Embayment) Table Mountain Group quartzites (McMillan *et al.*, 1997).

Exploration by SOEKOR (Pty) Ltd in the Bredasdorp Basin began in the 1970's. In 1987, a borehole targeted a postrift stratigraphic trap and encountered the first potential economic oil field of offshore South Africa (cross on Figure 6.7). Production began in 1993 and entails the piping of gas from a fixed offshore platform to an onshore facility where it is converted to liquid fuel (Brown *et al.*, 1995)

Rifting began in the middle to late Jurassic. Dextral shear stress along the FAFZ caused predominately northwest-southeast striking normal faulting between the Infanta Arch and Agulhas Arch. These listric, normal faults bound synrift graben and half graben basins and detach onto a common decollement surface at depth. Smaller scale

faults of varying ages and varying orientations imply that extension took place in changing stress fields (Van der Merwe and Fouché, 1992).

Mild, localised positive tectonic inversion at three different stages (<1At1, >1At1 and <15At1) is indicated by the reactivation of some pre-existing normal faults and associated folding (Van der Merwe and Fouché, 1992). One out of several possible causes of this inversion may be the build up of stress between adjacent plates across the FAFZ during phases of fault inactivity. A second model proposed involves small changes in plate motion during the break up of Gondwana (Van der Merwe and Fouché, 1992).

The rift-drift unconformity at ~136 Ma separates the synrift sediments from the transitional rift-drift sediments above. The syn-rift sequence is composed of fluvial and shallow marine sediments and the post-rift sequences are dominated by deep marine sediment (Van der Merwe and Fouché, 1992). In general, high initial subsidence rates associated with rifting were replaced by lower rates during the thermal subsidence that followed (Brown *et al.*, 1995). Of the southern basins, the Bredasdorp basin has the thickest Cretaceous drift succession, up to 4000 m (McMillan, 2003).

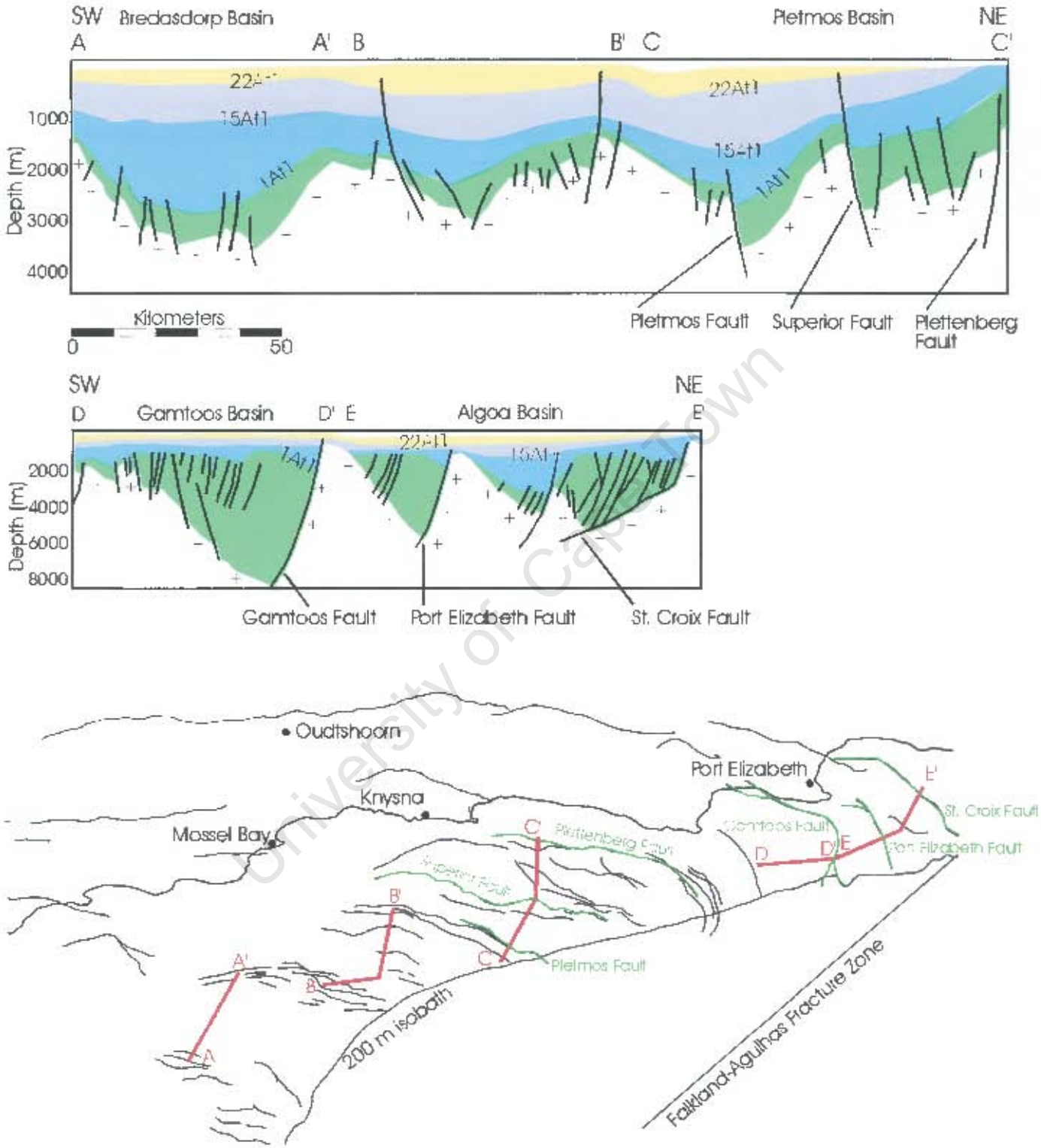

Figure 6.8: A and B: sections (locations in C) of the Bredasdorp (A-A'), Pletmos (C-C'), Gamtoos (D-D') and Algoa (E-E') basins (sections from McMillan *et al.*, 1997, A-C' and Petroleum Agency SA, 2000, D-E').

6.2.2.1.b 136-130 Ma (1At1-6At1)

Initially high subsidence was followed by decreased subsidence over this interval. Sedimentation occurred concurrently and was restricted to several depocentres, along the basin axis, in the centre and south (McMillan *et al.*, 1997). These embayments are related to earlier synrift sub-basins (Brown *et al.*, 1995).

Sediment supply at this time was low and river-dominated deltas from the north did not prograde far into the basin (Brown *et al.*, 1995). As a result, sediment is thickest (up to 1263 m) (yellows in Bredasdorp Basin, Figure 6.9) in proximal areas. The direction of sediment transport into the basins is from the north and west into the Bredasdorp Basin (Figure 6.9). Sediment fill across the northern flank of the Bredasdorp basin is thin (<30 to ~170 m, blue in Figure 6.9). Based on the rarity of benthic faunas (ostracods and foramnifera), McMillan *et al.* (1997) conclude that sedimentation, from 136 to 120 Ma, was mostly deep-marine in a poorly circulating water column with corresponding low oxygen levels near the sea floor.

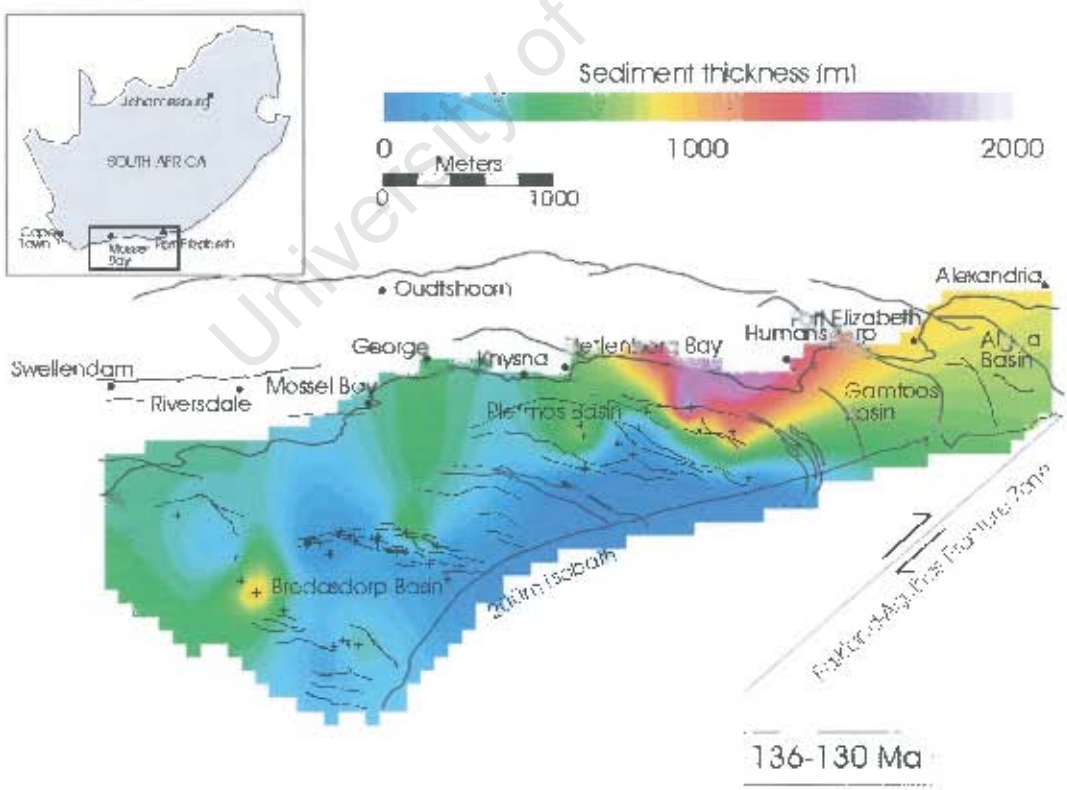

Figure 6.9: Thickness of sediment accumulated between ~136 and 130 Ma.

6.2.2.1.c 130-120 Ma (6At1-13At1)

Initially high subsidence rates were replaced by lower rates at ~120 Ma. At 6At1 displacement ended along Arniston fault to the north (Figure 6.7) (McMillan *et al.*, 1997). The flooding of an enlarged basin integrated the embayments created between 136 Ma and 130 Ma and resulted in a major shift in sedimentation to the north and north-eastern basin flank (Brown *et al.*, 1995; McMillan *et al.*, 1997) (shown in greens in Figure 6.9). Sedimentation was dominated by turbidity flows into a restricted and poorly oxygenated marine basin (McMillan *et al.*, 1997). In the latter part of this period subsidence rates declined, sandstones became widespread (highstand tracts proximally, lowstand turbidites distally) and there was an increasing sediment input from the north (McMillan *et al.*, 1997). Less sediment accumulated in the south (blue in Figure 6.9). Sediment thickness for the Bredasdorp Basin between 130 and 120 Ma, ranges from 138 m (south) to 939 m (central) (Figure 6.10).

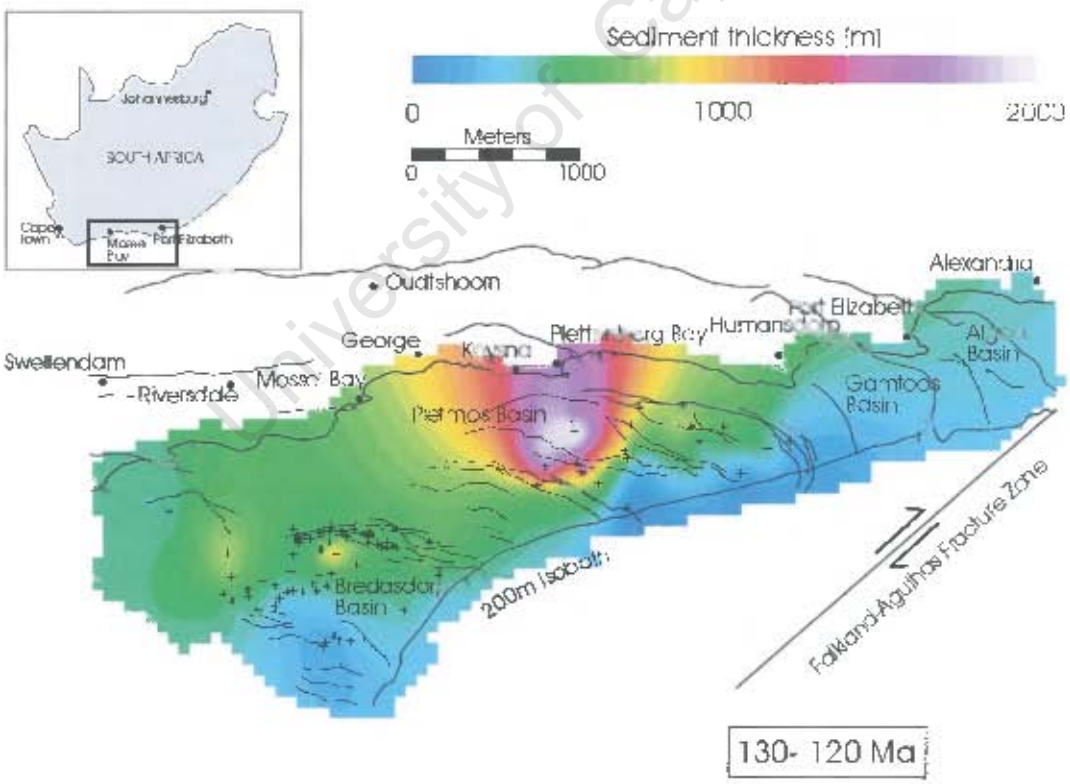

Figure 6.10: Thickness of sediment accumulated between ~130 and 120 Ma.

6.2.2.1.d 120-93 Ma (13At1-15At1)

Extensive uplift and subaerial erosion around the basin margin created an unconformity at 120 Ma (13At1). Erosion at greater basin depths resulted in a 5 by 50 km channel which trends eastwards across the central basin (McMillan *et al.*, 1997). Brown *et al.* (1995) proposes that as the Falkland Plateau cleared the Agulhas Arch, there was full connection to the southern Outeniqua Basin, resulting in marine circulation and increasing wave action over previously dominating fluvial processes. The basin expanded and became increasingly connected to the newly forming southern Atlantic Ocean (Brown *et al.*, 1995). Sedimentation and subsidence rates were reduced in the northeast while in the northwest clastic sediment input remained high. Progradation into the central basin from the northwest is shown by the preservation of highstand shelf sandstones that are thickest toward the basin axis (McMillan *et al.*, 1997). At 15At1 (~93 Ma) high sediment input and subsidence of the Bredasdorp basin ended (McMillan, 2003).

The thickness of sediment that accumulated between 120 and 93 Ma is shown in figure 6.11. The thick accumulation in the centre of the Bredasdorp basin shows up clearly in yellow/ orange. Overall, sediment thickness varies in the Bredasdorp basin from 280 m (northeast) to 1579 m (central). From the series of isopach maps (Figures 6.9, 6.10, 6.11, 6.12 and 6.13) it is clear that maximum accumulation of sediment took place from 120 to 93 Ma in the Bredasdorp Basin.

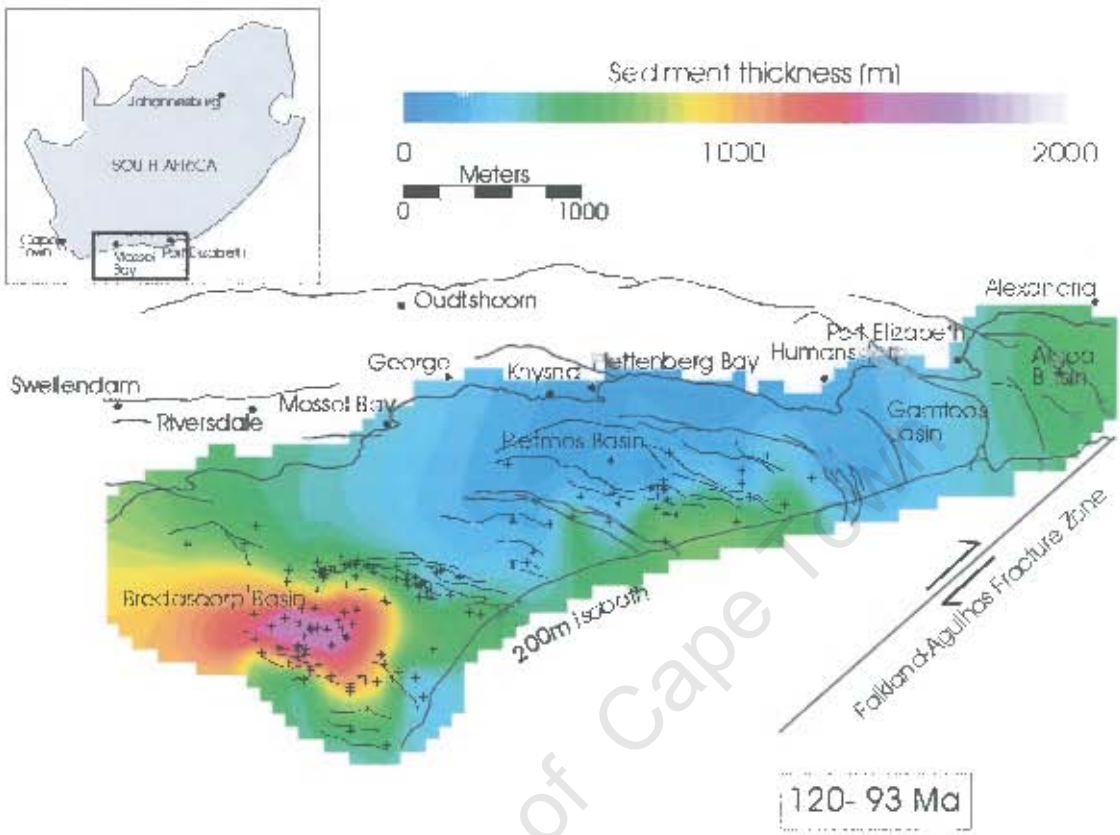

Figure 6.11: Thickness of sediment accumulated between ~120 and 93 Ma.

6.2.2.1.e 93-67 Ma (15At1-22At1)

Maximum erosion associated with the 15At1 unconformity occurred distally in the east (McMillan *et al.*, 1997). Above this unconformity there is an episode of progradation that is also identified in the Pletmos Basin. This progradation occurred primarily in the east (McMillan *et al.*, 1997) and is shown in yellow/orange (highest accumulation) in figure 6.12. Succeeding this episode, clastic input was reduced and biogenic sedimentation dominated. Across the basin, the Late Cretaceous sediments were deposited in non-marine environments (McMillan, 2003). In the southeast of the basin towards the end of the Cretaceous, a domal structure formed which may be associated with intrusions also in that area (McMillan *et al.*, 1997) (circled on Figure 6.12).

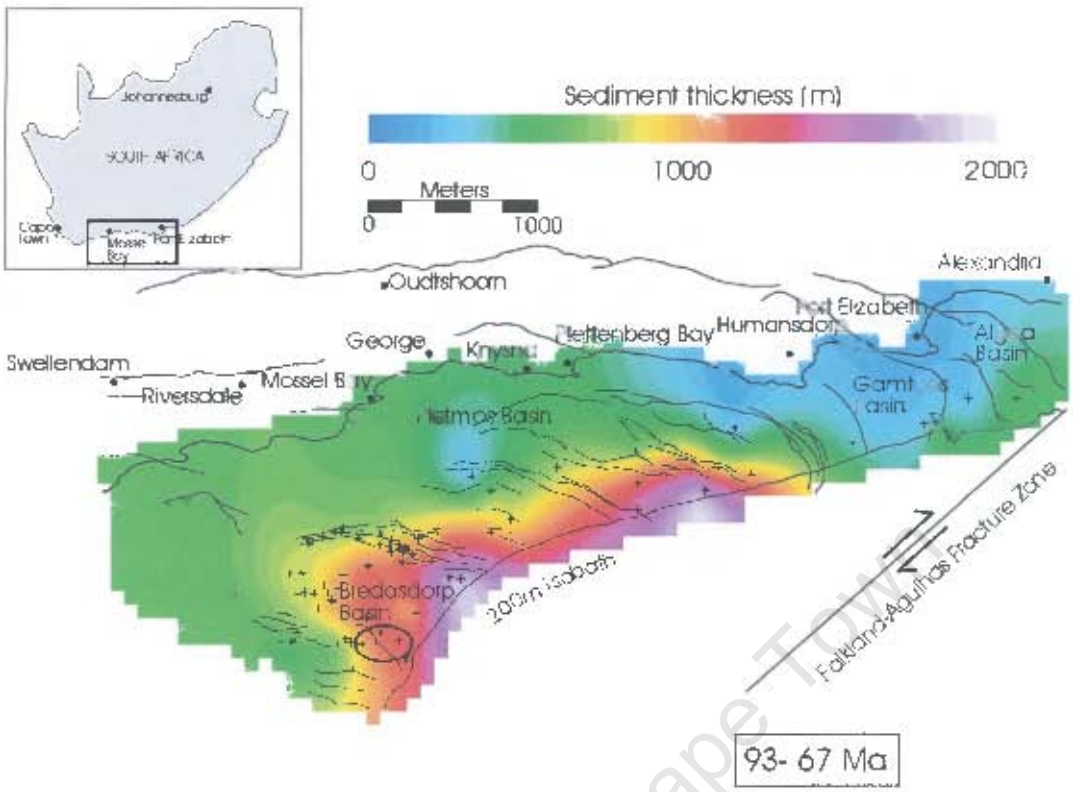

Figure 6.12: Thickness of sediment accumulated between ~93 and 67 Ma. A domal structure (circled) in southeast Bredasdorp Basin may be associated with intrusions in this area (McMillan *et al.*, 1997).

6.2.2.1.f Cenozoic

Tertiary sediment (200-700 m thick, Figure 6.13) is dominated by highstand shelf deposits of occasional sand, glauconitic and biogenic clays (widespread) (McMillan *et al.*, 1997, McMillan, 2003). The youngest sediment is a thin, up to 1m cover of Holocene-Pleistocene material that unconformably overlies Miocene rock (McMillan *et al.*, 1997).

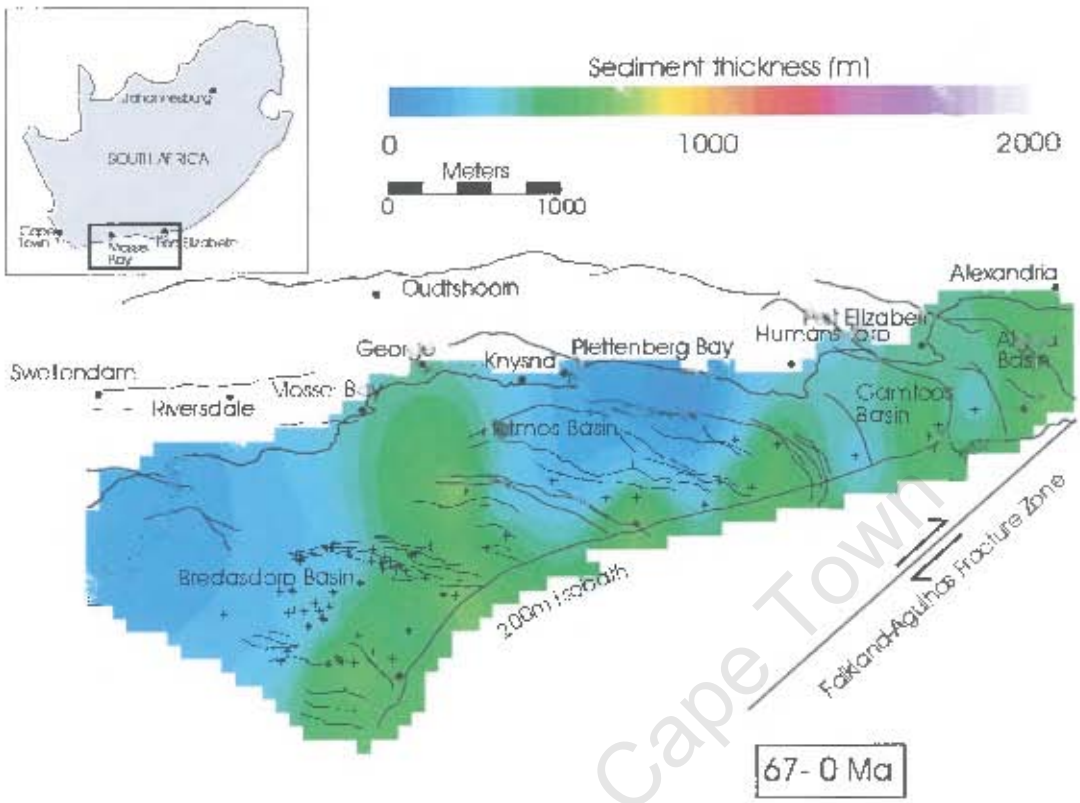

Figure 6.13: Thickness of sediment accumulated between ~67 Ma and the present.

6.2.2.2 The Pletmos Basin

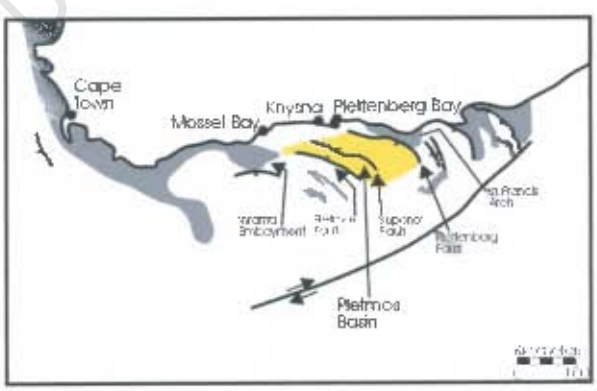

Figure 6.14: Location of the Pletmos Basin (yellow).

6.2.2.2.a Introduction

The Pletmos Basin (12500 km^2) is located offshore between Mossel Bay and Cape St Francis. It is the largest of the southern offshore basins and is 270 km long and 110 km wide (McMillan *et al.*, 1997). The basin trends northwest-southeast and is bordered by the Plettenberg Fault to the northeast and the Plemos Fault to the southwest. The Superior Fault divides the basin into two sub-basins to the north and south with different development during the rift phase. The Infanta Arch separates it from the Bredasdorp Basin to the west and the St Francis arch from the Gamtoos Basin in the east. Basement, where intersected, is composed of Table Mountain quartzites (McMillan *et al.*, 1997). The Pletmos Basin extends onshore at Mossel Bay, Plettenberg Bay and Knysna. Onshore lithologies comprise non-marine claystones and shallow marine claystones and sandstones (McMillan *et al.*, 1997). An idealized section through the Pletmos Basin is shown in figure 6.8.

Exploration for hydrocarbons has been underway since the 1970's resulting in some discoveries of sub-economic gas. Commercial oil has not been discovered.

Right lateral movement along the FAFZ was associated with normal faulting (Plettenberg, Pletmos and Superior Faults) trending northwest-southeast. The development of horst and grabens during rifting resulted in the variable accumulation of synrift sediment, particularly just south of the Plettenberg Fault (up to 5000 m), north of the Superior Fault and north of the Pletmos Fault (McMillan *et al.*, 1997). The Cretaceous succession (up to 2240 m) in the Pletmos basin is thinner than that in the Bredasdorp basin (McMillan, 2003).

6.2.2.2.b 136-130 Ma (1At1-6At1)

The first preserved sediment accumulated as restricted fan deltaic systems, first in the Plettenberg sub-basin and then later in the Northeastern sub-basin. The Northern and Southern sub-basins were relatively deep marine embayments, isolated from fluvial discharge (Brown *et al.*, 1995).

Rapid subsidence resulted in high positive accommodation rates and the aggradational stacking of sediments in the Plettenberg Sub-basin (south of the Plettenberg Fault) (McMillan *et al.*, 1997). Adjacent to this fault, sedimentation rates were high (>200 m/Ma) (McMillan *et al.*, 1997) and up to 3200 m of sediment accumulated (Bate and

Malan, 1992). This thick accumulation of sediment in the northeast Pletmos Basin shows up in red/orange in figure 6.9. Suspension settling dominated deep-water deposition (Brown *et al.*, 1995). Reduced deep-water oxygen levels led to an accumulation of organic rich claystones (McMillan *et al.*, 1997, McMillan, 2003).

A deceleration of subsidence rates led to a decrease in aggradation and an increase in progradation of sediment input (Brown *et al.*, 1995). Overall the period from 1At1 to 6At1 was regressive with the sediment becoming progressively sandier (McMillan *et al.*, 1997). In figure 6.9, the Pletmos Basin's 136-130 Ma succession is up to 2196 m thick.

6.2.2.2.c 130-120 Ma (6At1-13At1)

A second unconformity formed during the Hauterivian Stage (130 Ma) when transpressional uplift resulted in erosion, enhancement of basement anticlines, and the rotation of existing rifts (Brown *et al.*, 1995). Erosion stripped most of the earlier sediment deposited in the central and southern part of the Pletmos Basin between 136 and 130 Ma (shown in blue in Figure 6.9) (Brown *et al.*, 1995). The most complete record of the 1At1-6At1 sequences is found in the northern margin of the Pletmos Basin (orange/red in Figure 6.9).

During uplift at 130 Ma subsidence rates declined north of the Superior Fault and movement along the bounding faults ended (McMillan *et al.*, 1997). At this time the northern sub-basin was filled with proximal, coarser sediment and the south filled with finer, distal clays (McMillan *et al.*, 1997).

Renewed subsidence after uplift at 130 Ma resulted in the flooding and expansion of marine embayments of the Northern and Southern sub-basins (north and south of the Superior high) and the deflection of drainage patterns into these sub-basins (Brown *et al.*, 1995). Sediment sources shifted from the north to the northwestern margin of the basin and sediment prograded down the two axis of the sub-basins (McMillan *et al.*, 1997). This shift in sediment source from the north to the northwest of the Pletmos Basin is shown clearly in the differing locations of the orange/red in figure 6.9 and 6.10. In figure 6.9 the thickest sediment accumulation is in the north, along the south side of the Plettenberg Fault. In figure 6.10, sediment is now thickest in the northwest

of the Pletmos Basin (up to 2310 m thick). The Superior high caused sediment starvation in the southern basin (McMillan *et al.*, 1997). This is shown in blue on figure 6.10, indicating sediment thickness of <50 m in this area. By the 13At1 unconformity, the Pletmos Basin had ended as a substantial depocentre (McMillan, 2003).

6.2.2.2.d 120–93 Ma (13At1- 15At1)

Uplift and erosion produced a third regional unconformity during the early Aptian Stage (Brown *et al.*, 1995) (120 Ma). Sedimentation rates during this period were reduced across a slowly subsiding widened continental shelf (McMillan *et al.*, 1997). Borehole evidence shows that the thickness of sediment that accumulated during this interval varies from 113 m in the north of the Pletmos Basin (shown in blue in Figure 6.11) to 732 m to the south (green in Figure 6.11). Figure 6.11 shows that sediment thickness across the entire basin is thin compared to the Bredasdorp Basin at this time. In general, sediment accumulation was 300-500 m thicker in the south of the Pletmos Basin than in the north.

6.2.2.2.e 93-67 Ma (15At1-22At1)

After the uplift and erosion that saw the development of the 15At1 unconformity there was substantial progradation of sediment into deeper water (till ~89 Ma) (McMillan *et al.*, 1997). This progradation is evident from the yellows, oranges and red in figure 6.11, showing thick accumulation of sediment (up to 1823 m) in the south of the Pletmos Basin.

From ~89 Ma to the mid-Campanian (~78 Ma) sedimentation rates were reduced. At this time (mid-Campanian) a transgression occurred during which subsidence rates were elevated and sedimentation occurred at a faster rate. This interval was halted by tectonic activity at the end of the Maastrichtian, ~67 Ma (McMillan *et al.*, 1997).

6.2.2.2.f Cenozoic

Cenozoic deposition (up to 703 m thick, Figure 6.12) initially consisted of glauconitic claystones, overlain by biogenic clays in the Eocene and then by glauconitic clays in the early Oligocene (McMillan, 2003). Glauconite is an indicator of very slow sedimentation (Birch, 1975). Miocene biogenic clays unconformably overly the Oligocene sediments that are in turn overlain by a thin veneer of Pleistocene and

Holocene sediment (McMillan *et al.*, 1997). The 'thicker' Cenozoic sediments are located in the south and east of the Pletmos basin (green in Figure 6.12). Thus, the Cenozoic is dominated by biogenic, rather than allogenic sedimentation, suggesting a dramatic decrease in sediment supply rate from the continent.

6.2.2.3 The Gamtoos and Algoa Basins

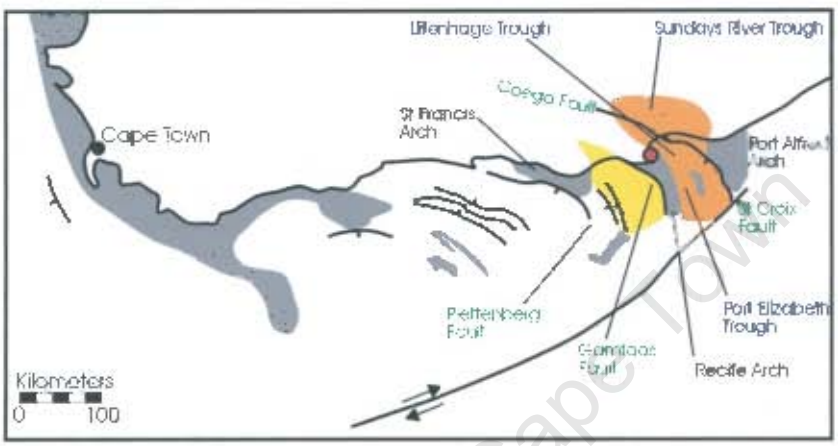

Figure 6.15: Location of the Gamtoos (yellow) and Algoa (orange) Basins. Arches labeled in black, faults in green and troughs in blue. Red dot= Port Elizabeth.

6.2.2.3.a Introduction

The Gamtoos Basin (5000 km^2), located south west of Port Elizabeth (Figure 6.15, section in Figure 6.8), is significantly smaller than the Bredasdorp and Pletmos basins, but it has a similarly thick sediment infill (McMillan *et al.*, 1997). It is bounded by the Gamtoos Fault in the northeast and the St. Francis Arch in the west. The Gamtoos Fault extends on land where it has a throw of ~3 km. Offshore this fault extends to a depth of ~12 km (McMillan *et al.*, 1997) and has a throw of 10 km (Bate and Malan, 1992).

The Algoa Basin (8200 km^2) is the eastern-most of the southern offshore basins (Figure 6.15). Like the Gamtoos Basin, it is smaller than the Bredasdorp and Pletmos Basins. It is located east of Port Elizabeth and is subdivided into the Sundays River Trough, the Uitenhage Trough and the Port Elizabeth Trough. The first two are extended onshore, the latter is only offshore. The Algoa Basin is bordered to the east by the Port Alfred Arch and to the west by the Recife Arch.

Basement of both basins, where intersected, is composed of Table Mountain quartzites and slates of the Bokkeveld Group, which are aligned parallel to the Cape Fold Belt (McMillan *et al.*, 1997). Onshore drilling in the Algoa Basin has reached Table Mountain Group basement in the Uitenhage Trough and Bokkeveld Group in the Sundays River Trough (McMillan *et al.*, 1997).

In both the Gamtoos and Algoa Basins tectonic subsidence and sedimentation rates were high in the initial drift stage. In the latter intervals (except 13At1-15At1) sediments are thinner than in the Bredasdorp and Pletmos Basins (McMillan *et al.*, 1997). The Gamtoos Basin contains ~7000 m of undrilled sediment which may be Middle to Late Jurassic in age (McMillan *et al.*, 1997).

6.2.2.3.b 136-130 Ma (1At1-6At1)

Little is left of any sediment deposited between ~136 and 130 Ma due to major uplift and erosion between ~130 and 120 Ma. The estimate of sediment thickness from ~136 to 130 Ma for these two basins is poorly constrained because none of boreholes used to produce figures 6.9, 6.10, 6.11, 6.12 and 6.13, intersect all the unconformities. Maximum preservation of these sediments is in structurally low areas in the central part of the Gamtoos Basin (McMillan *et al.*, 1997). In the Algoa basins early sediment is preserved offshore against the St. Croix Fault and onshore against the Coega Fault and in the centre of the Sundays River Trough (McMillan *et al.*, 1997). Sediments range from claystones and interbedded sandstones deposited under well-oxygenated conditions along the northern basin margins, to deeper slope, poorly oxygenated clay and turbidite deposits in the south (McMillan *et al.*, 1997). In both the Gamtoos and Algoa Basin there are structural features that indicate tectonic strain along the FAFZ. These include (in the Gamtoos Basin) the Gamtoos Anticline, reverse faults, inversion features, strike-slip displacement and (in the Algoa Basin) a basement arch (McMillan *et al.*, 1997).

5.2.2.3.c 130-120 Ma (6At1-13At1)

The evolution of the Gamtoos and Algoa Basins appears different to the Pletmos Basin during this interval. The eastern basins experienced uplift and erosion while the western basins were subsiding (Bate and Malan, 1992). In the Algoa Basin major erosion created incised channels and a large canyon 60 km long, 30 km wide and 1 km

deep which eroded sediments and exposed basement in the Uitenhage Trough (Bate and Malan, 1992; McMillan *et al.*, 1997). Evidence of similar though reduced uplift and erosion in the Gamtoos Basin is a small canyon close to the Gamtoos Fault that partially eroded the Gamtoos anticline (McMillan *et al.*, 1997).

6.2.2.3.d 120-93 Ma (13At1-15At1)

The 13At1 unconformity developed during the peneplanation of a widespread area of synrift sediments of the Algoa and Gamtoos Basins (Bate and Malan, 1992). Canyon infilling then began and these sediments include mainly claystones, minor sandstones and dolomites (McMillan *et al.*, 1997). From limited borehole data, sediment in the Algoa Basin is 520 m thick at least in one location (Figure 6.11).

6.2.2.3.e 93-67 Ma (15At1-22At1)

The 13At1 and 15At1 unconformities are a result of basin tilt creating uplift along the basin margins in the north and relative subsidence of the basins centres (Bate and Malan, 1992).

The 15At1 sequence atop the 15At1 unconformity is developed over the southern half of the Gamtoos and Algoa Basins and indicates the first marine transgression since prior to 6At1 (McMillan *et al.*, 1997) (~130 Ma). Glauconitic claystones with minor sandstones were deposited in the southern part of the basins (McMillan *et al.*, 1997). Sediments of the late Cretaceous interval are thinner in the Gamtoos and Algoa Basins than synchronous sediment of the Pletmos and Bredasdorp Basins (McMillan *et al.*, 1997). The thin late-Cretaceous sediments (214 m to 545 m) of the Algoa and Gamtoos Basins show up as blue as opposed to the yellows and oranges indicating thicker sediment in the western basins in figure 6.12.

The thin, late-Cretaceous sediment indicates minimal shelf subsidence (McMillan, 2003). At Mid-Campanian (~78 Ma) the northern Gamtoos and northeastern Pletmos basins subsided, causing a marine transgression (McMillan, 2003). The last sediment to be deposited prior to ~67 Ma is composed of glauconitic claystones and sandstones that unconformably overlie pre~130 Ma aged sediment in the proximal parts of the basin (McMillan *et al.*, 1997). Distally they are composed of shelf claystones and microfaunal evidence suggests normal oxygen conditions at the seafloor (McMillan *et al.*, 1997). McMillan (2003) suggests that Cenozoic uplift and erosion has resulted in

only small remnants of this latest Cretaceous sediment, which originally would have been regionally distributed across the shelf.

6.2.2.3.f Cenozoic

Paleocene sediments of the Gamtoos Basin consist of a thin veneer of glauconitic claystone overlain by biogenic clays of the Eocene, a thick interval of Oligocene silty glauconitic clays, and a thin veneer of Quaternary sediment (McMillan *et al.*, 1997). Cenozoic sediments of the Algoa Basin include clays of the Paleocene, Eocene and Oligocene. Early Miocene sediments are restricted to the distal regions of the Algoa Basin. Overlying Pliocene and early Pleistocene clays and shelly sands are indicative of renewed subsidence in the Algoa Basin (McMillan *et al.*, 1997). Cenozoic sediment is up to 593 m thick in the Algoa Basin and up to 559 m thick in the Gamtoos Basin (Figure 6.13).

6.2.2.4 The Southern Outeniqua Basin

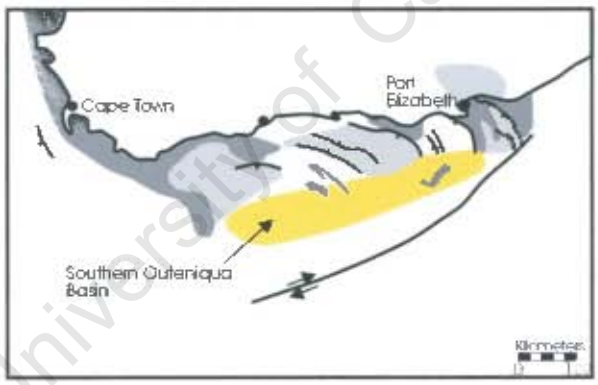

Figure 6.16: Location of the Southern Outeniqua Basin (yellow).

The Southern Outeniqua Basin is situated off the south coast of South Africa and consists of the south eastern deep water extensions of the Bredasdorp, Pletmos, Gamtoos and Algoa Basins, beyond the 300 m isobath (Roux, 1997). It is ~330 km long and ~60 km wide, occupying an area of ~20 000 km^2 (Figure 6.16). It is a relatively unexplored basin. It has reasonable seismic reflection coverage but no boreholes.

Figure 6.17 shows a schematic section through this basin (adapted from Roux, 1997). Roux (1997)'s interpretation of the Southern Outeniqua Basin is based on geological models that are in turn based on boreholes through the southern extent of the inner basins. Thus much of the interpretation which follows remains untested. Figure 6.17 shows highly localised synrift sediment unconformably overlain in places by sediment accumulated between ~136 and ~130 Ma. These sediments are likely the fine-grained, distal deposits (shales) of their more proximal near-shore equivalents. Sediments which accumulated between ~130 and ~120 Ma are more laterally continuous and may contain deep marine fan and channel sandstones (Roux, 1997). These are unconformably overlain by an extensive lowstand wedge followed by shales deposited between ~120 and ~93 Ma (Roux, 1997). Sediments deposited between ~93 and ~67 Ma are relatively thick, in contrast to the thin Cenozoic sediment above, which does not extend far into the Southern Outeniqua Basin.

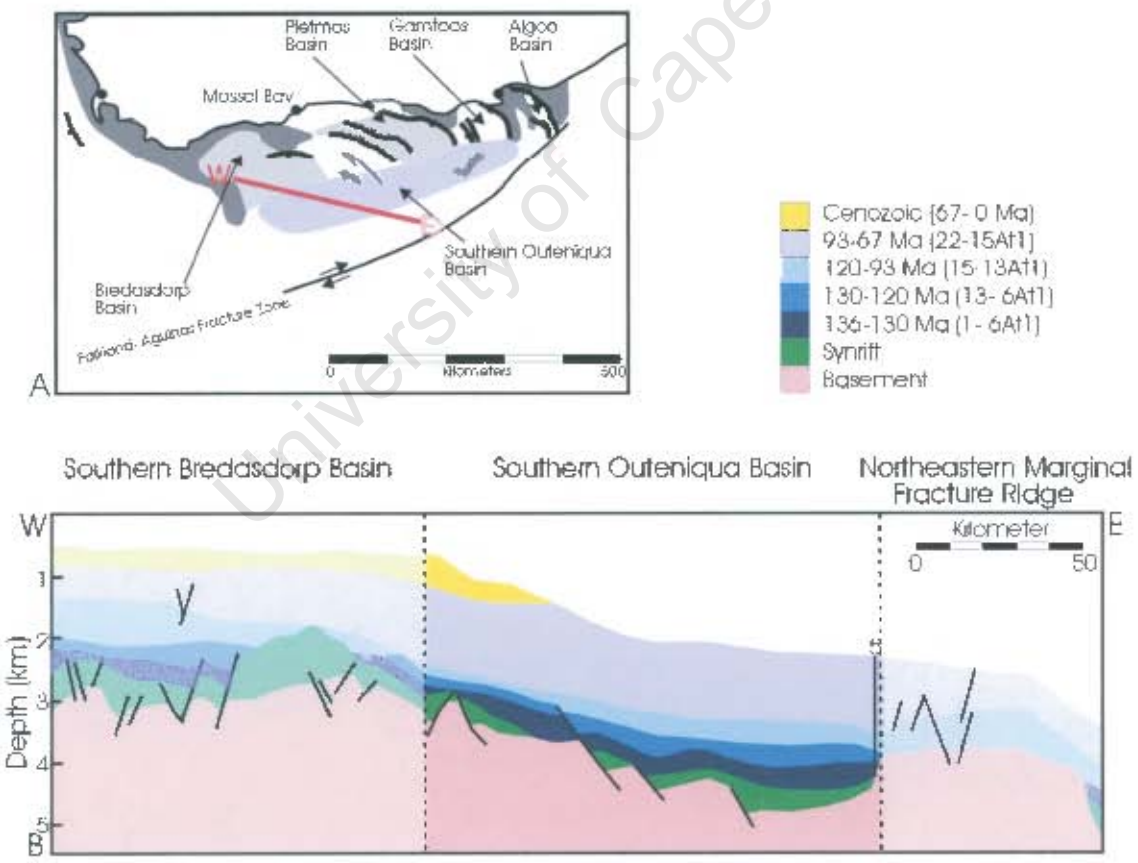

Figure 6.17: (A) The location of (B), a schematic section across the Southern Outeniqua Basin shown in darker colours (adapted from Roux, 1997).

6.3 Sediment Volumes

6.3.1 Outeniqua Basin

The volume of sediment accumulated in 5 time intervals was calculated using Oasis Montaj's grid volume utility. This function calculates the volume under a grid produced for each time interval by the minimum curvature gridding method (described in section 6.2). The area over which sediment is distributed is 74 630 km^2. The results of these calculations are listed in table 6.1.

Table 6.1: Sediment volumes and accumulation rates for the Outeniqua Basin. Accumulation rates are averaged over period of sedimentation.

Bounding Unconformities	Age range (Ma)	Time Span (Ma)	Measured Volume (km^3)	Accumulation rate (km^3/Ma)
1At1-6At1	136-130	6	29429	4904.8
6At1-13At1	130-120	10	38601	3860.1
13At1-15At1	120-93	27	31547	1168.4
15At1-22At1	93-67	26	46522	1789.3
22At1-seafloor	67-0	67	25225	376.49
TOTAL	136-0	136	171 324	1259.7 (average-total/ 136 Ma)

6.3.1.1 Compaction

The original borehole information upon which the isopach maps are based did not factor in the effect of compaction. Depending on porosity, sediment will compact to a varying degree, thus the original thickness of each interval in each borehole was undoubtedly greater prior to its burial. Compaction increases with depth, therefore the sediment volumes listed in table 6.1 are underestimated to the greatest degree for the earlier (and deeper) time intervals, ~136-130 Ma and ~130-120 Ma. Accumulation rates were highest between ~136 and 120 Ma (Table 6.1). Thus the general reduction in the rate of sediment accumulation with time from ~136 Ma to the present is likely even greater.

The established method to remove the effect of compaction is to 'backstrip' the borehole, layer by layer, restoring each section to its original thickness (e.g. Steckler and Watts, 1978). It is impractical to attempt this with all 173 boreholes.

Therefore, to approximate compaction, the following formula is applied:

$$Vsurf = Vbur + (Psurf - Pbur)^* Vbur \quad [1]$$

Vsurf= Volume at surface

Vbur= Volume at a certain depth

Pbur= Porosity of rock at depth

Psurf= Porosity of rock at the surface (R.Brown, pers. comm. 2005)

For direct comparison to estimated onshore eroded rock volumes the equivalent volume of rock is given by:

$$Vrock = Vsurf\,(1 - Psurf)$$ (R.Brown, pers. comm. 2005) [2]

Volume at a certain depth is calculated by multiplying the average thickness of the layer by the basins' extent, 74630 km^2. Porosity at that depth and at the surface is estimated by comparing the borehole data presented here to a borehole (COST B-2) through the continental margin off New York (Steckler and Watts, 1978). In their paper, the authors calculate the subsidence of this margin by removing the contribution of sediment loading and the effects of compaction, amongst others. These data were chosen because the tectonic setting (a Jurassic-aged passive margin) and sediment age is similar.

Steckler and Watts (1978) assume that irrespective of their lithology, the porosity of sediment will follow a depth-porosity curve as the overburden pressure increases. This curve (Figure 6.18) was produced from in-situ measurements of porosity with increasing depth (Rhodehamel, 1977 in Steckler and Watts, 1978). To compare the south coast borehole data to the curve in figure 6.18, the average depth to each sedimentary unit (~136-130 Ma etc.) was calculated by summing the average depth to the two bounding unconformities and dividing by 2. The porosity % (Pbur) for each unit is then estimated from figure 6.18 (after Steckler and Watts, 1978). An 'uncompacted' volume is calculated using equation 1 with Psurf= 0.55 and the equivalent rock volume (assuming volume of allochthonous cement is negligible) is calculated using equation 2. The original volumes, porosity estimates and the newly calculated 'uncompacted' sediment volume and rock volume equivalent for each unit

are listed in table 6.2. These new volumes are then summed to give an approximation of the rock volume before compaction.

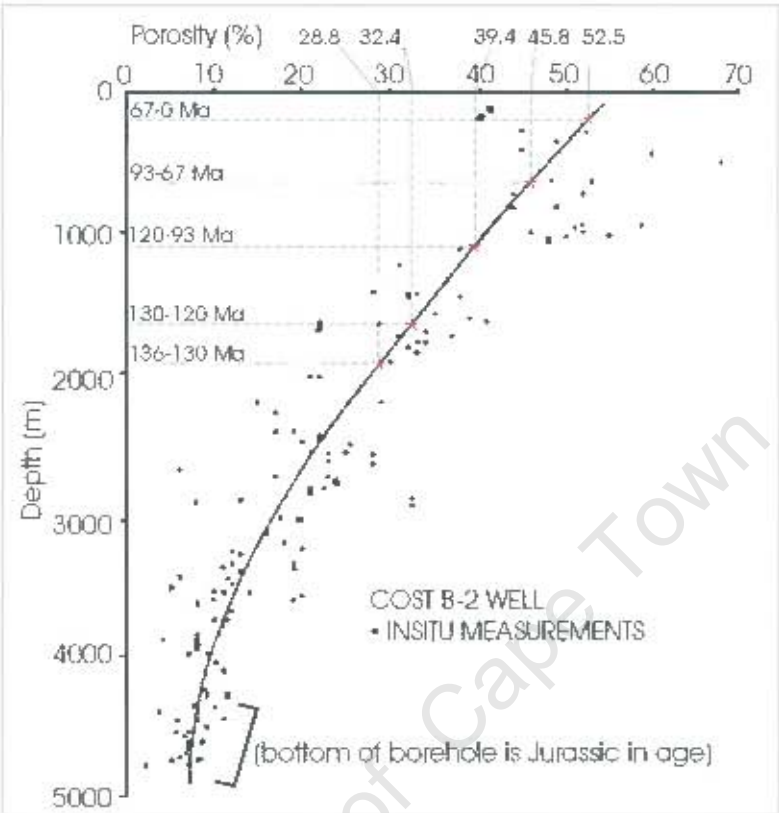

Figure 6.18: Curve plotted through insitu borehole measurements showing decreasing porosity with increasing depth (Adapted from Steckler and Watts, 1978).

Table 6.2: Estimate of sediment volume and accumulation rates in the Outeniqua Basin for 5 time intervals, taking the effect of compaction into account (see text for details). Accumulation rates are averaged over period of sedimentation.

Age Range (Ma)	Average Depth (km)	Average Thickness (km)	Est. Porosity (%)	Diff. in porosity (%)	Corrected Average Thickness (km)	Corrected Volume (km^3)	Acc. Rate (km^3/ Ma)	Effective Rock Volume (km^3)
136-130	1.982	0.4387	28.8	26	0.5528	41253	6876	18564
130-120	1.664	0.5586	32.4	23	0.6871	51276	5128	23074
120-93	1.100	0.4624	39.4	16	0.5364	40030	1483	18014
93-67	0.6411	0.6854	45.8	9	0.7471	55755	2144	25090
67-0	0.1934	0.3718	52.5	3	0.3829	28579	427	12861
					TOTAL	216893	1595	97603

6.3.2 The Southern Outeniqua Basin

Table 6.3: Sediment accumulation in the Southern Outeniqua Basin. The area of basin is ~20 000 km^2 (Roux, 1997). Porosity at depth estimated from figure 6.18.

Age range (Ma)	Est. Average depth (km)	Est. Average Thickness (km)	Est. Porosity (%)	Diff. in porosity (%)	Corrected average thickness (km)	Corrected Volume (km^3)	Acc. Rate (km^3/ Ma)	Effective Rock Volume (km^3)
136-130	2.084	0.295	27.1	28	0.3776	7552	1259	3398
130-120	1.811	0.251	31.4	24	0.3112	6225	623	2801
120-93	1.535	0.301	34.5	21	0.3642	7284	270	3278
93-67	0.755	1.258	44.1	11	1.396	27928	1074	12568
67-0	0.063	0.126	54.0	1	0.127	2545	38	1145
136-0					TOTAL	51534	379	23190

Table 6.3 lists the accumulated sediment volume and equivalent rock volume in the Southern Outeniqua Basin for the 5 time intervals. These volumes have been corrected for compaction using equations 1 and 2 in section 6.3.1.

In the Southern Outeniqua Basin the highest volume of sediment was deposited between ~93 and 67 Ma (27928 km^3) at a rate of 1074 km^3/Ma. This rate of accumulation is just slightly less than the maximum for this basin of 1259 km^3/Ma during the interval of ~136 to 130 Ma. Figure 6.12 (section 6.2) shows that the thickest sediment accumulated along the southern margin of the Outeniqua Basin at this time (pinks and reds in Figure 6.12). Thus it is not surprising that farther offshore in the Southern Outeniqua Basin this interval is similarly thick.

The Cenozoic cover in the Southern Outeniqua Basin is very thin (as in the Outeniqua Basin) and deposited at a rate that is 2 orders of magnitude lower than the maximum accumulation rate in the early Cretaceous.

6.3.3 Total Sediment Volume

Table 6.4 lists the total volume of sediment for the Outeniqua Basin and Southern Outeniqua Basin together and figure 6.19 shows this graphically. The maximum volume of sediment accumulated offshore between ~93 and 67 Ma (83683 km^3). However, the accumulation rate was highest for the earlier time intervals, ~136 to 130 Ma (8134 km^3/Ma) and ~130 to 120 Ma (5750 km^3/Ma) (Figure 6.19). These rates are more than double the average rate of 1974 km^3/Ma over ~136 Myrs. Sediment accumulation rate increases significantly (almost doubles) from the early-mid Cretaceous (~120-93 Ma) to mid-late Cretaceous (~93-67 Ma). The lowest volume of sediment (31124 km^3) accumulated at the lowest rate (465 km^3/Ma) during the Cenozoic.

Table 6.4: Total sediment volumes and accumulation rates for the Outeniqua and Southern Outeniqua Basins. Total area across which sediment is accumulated =94 630 km^2.

Bounding Unconformities	Age range (Ma)	Time Span (Ma)	Measured Volume (km^3) (Outeniqua Basin)	Estimated Volume (km^3) (Southern Outeniqua Basin)	Total Volume	Total Accumulation rate (km^3/Ma)
1At1-6At1	136-130	6	41253	7552	48805	8134
6At1-13At1	130-120	10	51276	6225	57501	5750
13At1-15At1	120-93	27	40030	7284	47314	1752
15At1-22At1	93-67	26	55755	27928	83683	3219
22At1-seafloor	67-0	67	28579	2545	31124	464.5
TOTAL	136-0	136	216893	51534	268427	1974 (average over 136 Myrs)

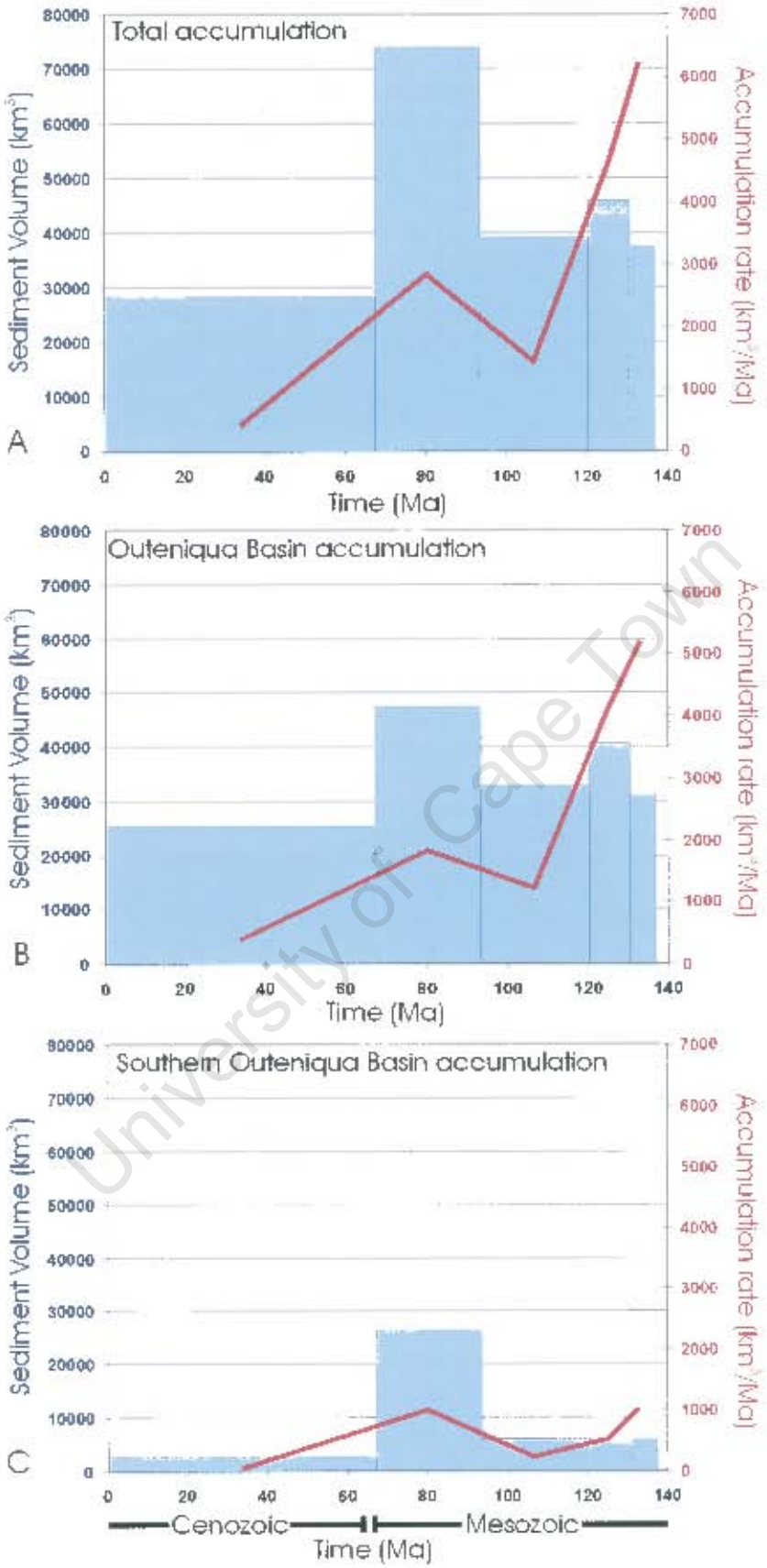

Figure 6.19: Varying sediment accumulation volume (shaded blue, left axis) and rate (red line, right axis) over ~136 Myrs for (A) the Outeniqua and Southern Outeniqua Basins combined, (B) the Outeniqua Basin and (C) the Southern Outeniqua Basin.

6.4 Uncertainties and implications of offshore sediment volumes

6.4.1 Minimum values

The sediment volumes calculated in section 6.3 and listed in tables 6.1 to 6.4 are minimum values for the following reasons:

6.4.1.1 Sediment accumulation not deposition

Sediment accumulation is always volumetrically less than sediment deposition. It is impossible to quantify how much sediment has been 'lost' at each of the major (and several minor) offshore unconformities. The onset of current activity in the newly created southern Atlantic Ocean (e.g. the Agulhas Current) may have exacerbated this erosion. Reworking of sediment may have been confined to each basin to some degree. For example, in the Algoa and Gamtoos Basins, sediment deposited prior to ~120 Ma was eroded, reworked and redeposited after ~120 Ma (see section 5.3). Calculation of earlier sediment accumulation (~136-130 Ma) in these basins, therefore, underestimates original sediment deposition. The successive time interval (~120-93 Ma) may overestimate sediment volume originally sourced from the continent.

6.4.1.2 Sediment bypass and deposition on the Falkland Plateau

In the early Cretaceous, sediment may have bypassed the African continental shelf to accumulate in deeper waters offshore or on the Falkland Plateau, which is known to have accumulated significant volumes of Cretaceous to recent sediments (Lorenzo and Mutter, 1988). It is impossible to quantify sediment that may have accumulated beyond the boreholes used here to calculate sediment volume in the inner basins and beyond the seismic data coverage used to estimate accumulated volume in the Southern Outeniqua Basin.

Sediment may have continued to bypass the continental shelf after clearing of the Agulhas Bank by the Falkland Plateau and the development of open ocean circulation (Late Albian, Dingle *et al.*, 1983; Martin and Hartnady, 1986). These sediments may have been transported beyond the shelf by turbidity currents (and thus are likely to be volumetrically significant), or alternatively may have settled out of suspension (volumetrically minor). However, bypassing sediments in both the early and late Cretaceous would also have had to clear the Northeastern Marginal Fracture Ridge (named by Robson and Dingle, 1986, renamed the Diaz Ridge in Ben Avraham *et al.*,

1993) (Figure 6.17) and the Agulhas Marginal Fracture Ridge (created early in the development of the region, Lorenzo and Mutter, 1988). Basement outcrops may have acted as a barrier to sediment migration into deeper waters (>3000 m water depth).

6.4.2 Resolution issues

The precision and resolution of the 10 contour maps produced (Figures 6.2 to 6.6 and 6.8 to 6.12) is reliant on the distribution of borehole data. Basins that have been better explored for hydrocarbons (e.g. the Bredasdorp Basin) have more borehole data. Thus variation in sediment thickness across the Bredasdorp and Pletmos Basins is better constrained than across the Gamtoos and Algoa Basins. In the unexplored (undrilled) Southern Outeniqua Basin, sediment volume is less well constrained.

6.4.3 Localised versus widely distributed sediment

Where sediment is rift-bounded (e.g. sediment that accumulated between ~136 and 130 Ma) it is locally distributed. In the Outeniqua and Southern Outeniqua Basins younger sediment (~130-0 Ma) is more regionally distributed. Sediment distribution also may be highly localized due to subsequent erosion. For example, erosion between ~136 and 120 Ma in the Gamtoos and Algoa basins left sediment preserved only in canyons (up to 2340 m, McMillan, 2003). Locally distributed sediment is difficult to grid accurately due to abrupt changes in sediment thickness (gridding method described in Appendix G). Calculated sediment volumes for the Outeniqua Basin using gridded data will reflect true sediment volume more accurately for the latter, more regionally distributed sediments (~130 Ma to present). The problem of localised sediment distribution is compounded when the boreholes are unevenly distributed and widely spaced. For example, boreholes that do not intersect the canyons described above will underestimate sediment thickness accumulated between ~126 and 120 Ma in the Gamtoos and Algoa Basins. In this case though, sediment filling these canyons of limited lateral extent is likely to be volumetrically minor.

6.4.4 Sensitivity of grid volume to grid area (Outeniqua Basin)

The grid area for each isopach map was increased by 95% and reduced by 46% to test the sensitivity of grid volume to grid area. Figure 6.20 shows the newly enlarged and reduced area compared with that used in volume calculations for the ~93 to 67 Ma time interval. The results of this test for all time intervals are shown graphically in figure 6.21.

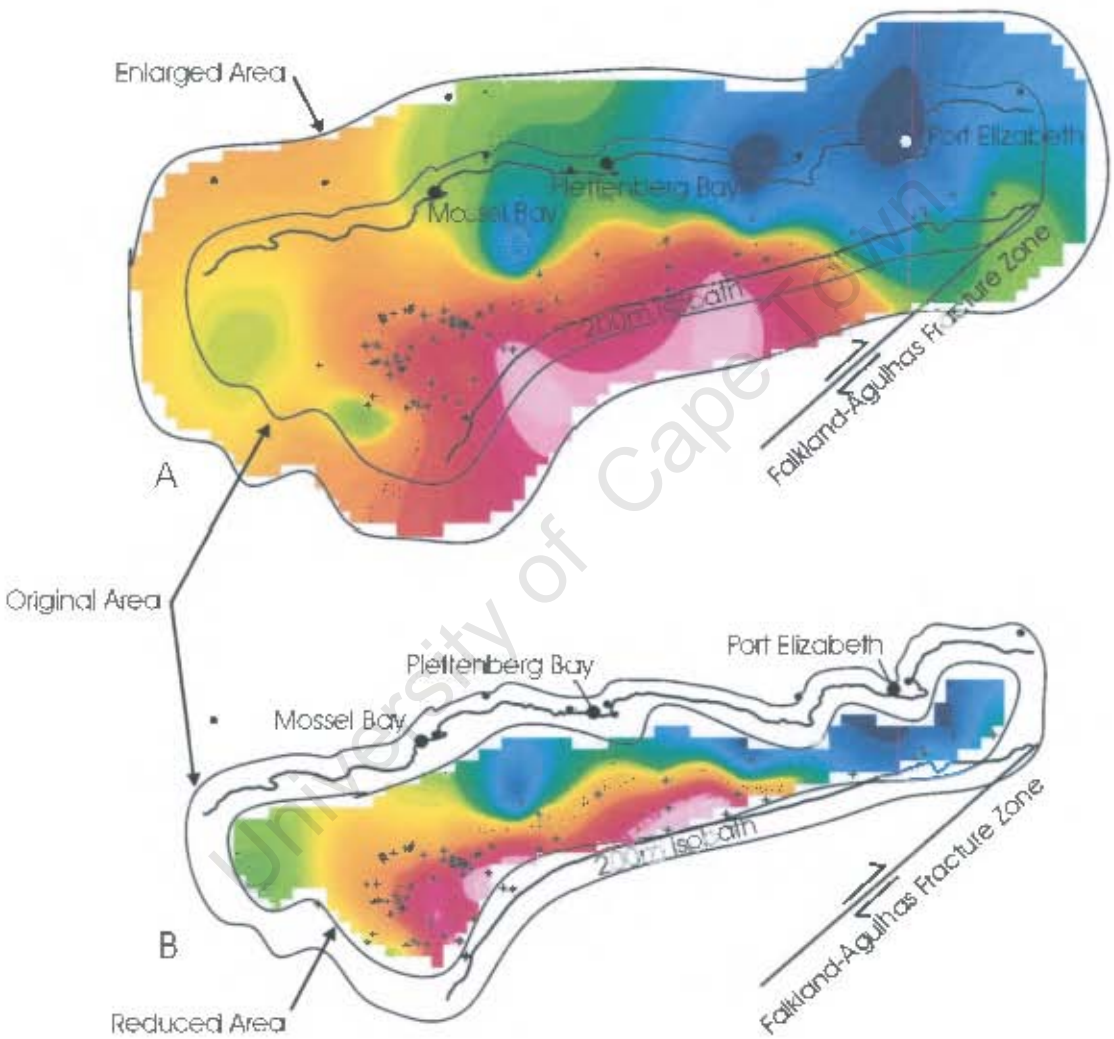

Figure 6.20: Sensitivity test of grid volume and grid area for sediments accumulated between ~93 and 67 Ma in the Outeniqua Basin. (A) Area is enlarged by 95%. (B) Area is reduced by 46%.

Time interval	Adjustments to grid area	Original Volume (km^3)	New Volume (km^3)	% Change
6-1 (136-130 Ma)	Increasing by 95%	29429	68264	132
	Reducing by 46%		12604	57
13-6 (130-120 Ma)	Increasing by 95%	38601	72837	89
	Reducing by 46%		20864	46
15-13 (120-93 Ma)	Increasing by 95%	31547	63444	101
	Reducing by 46%		16651	47
22-15 (93-67 Ma)	Increasing by 95%	46522	96364	107
	Reducing by 46%		23574	49
0-22 (0-67 Ma)	Increasing by 95%	25225	51232	103
	Reducing by 46%		12533	50

Figure 6.21: Results of sensitivity test of grid area. Blue= grid area increased by 95%. Red= grid area decreased by 46%.

In all but one test, increasing or decreasing the grid area leads to an increase or decrease in % volume that is greater than the % change in area (Figure 6.21). This demonstrates the importance of careful selection of grid area. In these calculations the grid area was chosen to fit closely to the data points (boreholes). Extrapolating beyond the better constrained areas introduces unnecessary uncertainty. The grid area was also demarcated for geological reasons. It is bordered to the north by the shoreline, which is the northern limit of offshore sediment deposition. The west and east borders are basement highs, bounding the Bredasdorp and Algoa Basins, respectively which act as barriers to sediment transport. The southern boundary co-incides with the northern boundary of the Southern Outeniqua Basin. The grid area used in calculations of sediment volume was kept the same for all time intervals. Thus although the sediment volume has been shown to be sensitive to the size of the gridded area, the *relative differences* in sediment volume between the time intervals are valid.

6.4.5 Timing of onshore denudation

The largest sediment volume accumulated offshore between ~93 and 67 Ma, implying that onshore denudation was greatest during this period. However, the rate of sediment accumulation was highest immediately succeeding continental break up (~136-120 Ma), implying that the *rate* of onshore denudation occurred was highest during this time. Between these two periods of high denudation and high rate of onshore denudation was a period of both low denudation and low rate of denudation from ~120 to 93 Ma. Offshore sediment volumes for the Cenozoic (~67 Ma to present) are low, suggesting that onshore denudation was at a minimum over this period.

The high rate of denudation immediately after continental breakup suggests significant uplift of the onshore area from ~136 to 120 Ma and the possible mechanisms for this are described in chapter 3 (Gilchrist and Summerfield, 1990; Gilchrist *et al.,* 1994; Kooi and Beaumont, 1994; Van der Beek *et al.*, 2002) and chapter 7. The decrease in both the amount and rate of denudation between ~120 and 93 Ma suggests that these mechanisms of uplift (e.g. marginal topographic upwarp by flexural isostatic uplift due to differential denudation, Gilchrist and Summerfield, 1990) only operated until ~120 Ma. According to the offshore evidence, there is a renewed increase in both the amount and rate of onshore denudation from ~93 to 67 Ma.

6.4.6 Degree of onshore denudation

The thickness of onshore denudation is directly calculated from fission track analysis and thermal modelling in chapter 4. Here onshore denudation is estimated indirectly, from offshore volumes, in order to test whether the onshore-offshore system is in balance. Chapter 7 explores this test further. To calculate onshore denudation from offshore sediment volumes, it is first necessary to identify the source area of the sediment offshore. This is difficult, as the denuded onshore area may have changed in both extent and location over time (Chapter 5).

The assumption made here is that the majority of sediment accumulated in the Outeniqua and Southern Outeniqua Basins has been derived from an onshore area south of the Great Escarpment. It is proposed by Gilchrist *et al.* (1994) (amongst others, see Chapter 3) that synchronous with the break up of Gondwana was the development of two drainage areas, an internal, inward draining region separated from an external, seaward draining region by an escarpment. This escarpment either initially formed near, or rapidly retreated to near its present position in the Cretaceous and has only experienced limited retreat since rifting (Chapter 3). This drainage divide suggests that only the area south of the Great Escarpment has been eroded by rivers oriented perpendicular to the coast to eventually be deposited off the south coast. The area north of the escarpment has been eroded by inward draining rivers, for example the Kalahari and Karoo Rivers and later the Orange River (de Wit, 1999), to be finally deposited off the west coast (in the case of these rivers). The development of this 'early' escarpment is shown in Figure 5.7, Chapter 5).

Thus, in the following calculations of the degree of onshore denudation, the source area for the south coast sediments is bounded in the north by the escarpment (or southern limit of the dolerite intrusions). The western limit of the source area is taken along a diagonal drawn from Cape Hangkip, east of False Bay, inland to the escarpment and first outcropping dolerites. This roughly corresponds to the position of the Cape Fold Belt syntaxis. It is not suggested, though, that the Cape Fold Belt Mountains acted as a watershed or drainage divide as they were, at rifting, buried beneath Jurassic to early-Cretaceous sediment (Chapter 5). The source area's eastern limit extends ~north-south, inland from where the Cape Fold Belt currently meets the Indian Ocean, to the escarpment.

The source area described is ~140 000 km^2. This was calculated in Arcview GIS from a polygon drawn around the estimated source area and over the digitized geology of southern Africa (Figure 6.22). The total offshore sediment volume deposited since rifting (not including synrift sediment) is 268 427 km^3 with an equivalent rock volume of 120 792 km^3 (calculated using equation 2 in section 6.3). Therefore, based on offshore evidence, an average thickness of ~863 m has been removed since ~136 Ma. A breakdown of the thickness of sediment eroded from the source area for each time interval is given in table 6.5. The calculation of onshore denudation from offshore sediment volumes assumes that the system is balanced. Whether this is indeed the case is evaluated further in chapter 7.

Table 6.5: Thickness of sediment and equivalent rock volume eroded from source area for each time interval.

Bounding Unconformities	Age range (Ma)	Time Span (Ma)	Offshore Sediment Volume (km^3)	Equivalent Rock Volume (km^3)	Equivalent Average Onshore Denudation (m)
1At1-6At1	136-130	6	48805	21962	157
6At1-13At1	130-120	10	57501	25875	185
13At1-15At1	120-93	27	47314	21291	152
15At1-22At1	93-67	26	83683	37657	269
22At1-seafloor	67-0	67	31124	14006	100
TOTAL	136-0	136	268427	120792	863

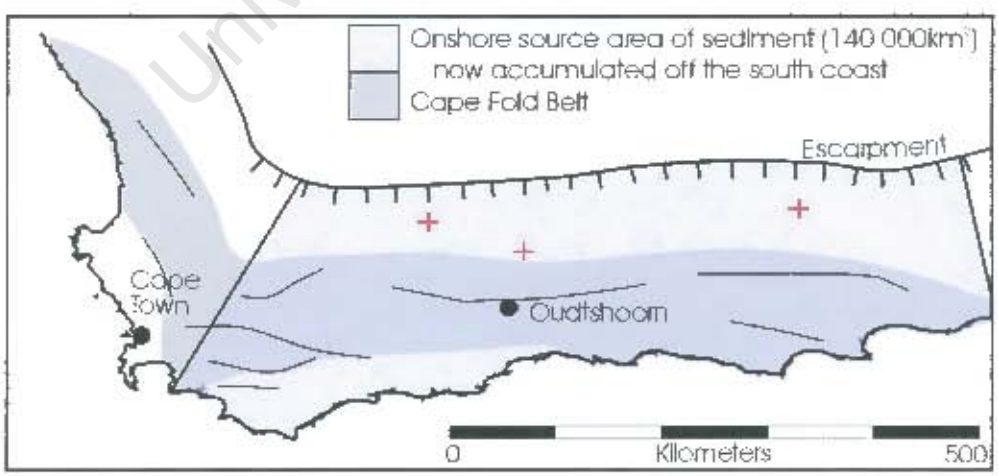

Figure 6.22: Estimated source area (~140 000 km^2) of sediment accumulated off the south coast since ~136 Ma. Red crosses are boreholes sampled for fission track analysis (Chapter 4).

6.4.7 A Comparison to sediment accumulation rates across the west coast

Dingle and Hendey (1984) calculated accumulated sediment volume in the Orange Basin (West Coast) from seismic data and compared it to source area denudation. They found that sediment accumulation rate was highest in the late Cretaceous and decreased in the Paleogene and further still in the Neogene. This, coupled with their calculated decrease in yield from the catchment areas, was used as evidence that there has been a "gross reduction in continental erosion rates over the period" (Dingle and Hendey, 1984).

Offshore sedimentation estimates in Brown *et al.* (1990) were obtained (and corrected for compaction) from SOEKOR borehole records. 4 Boreholes located in the north and centre of the Orange Basin along the South African west coast, (Kudu 9A-1, K-A1, K-A2 and K-A3), show initially high sediment accumulation rates in the early Cretaceous and then a decrease in rate by ~120 Ma (Brown *et al.*, 1990). Very low rates of ~11-58 m/Ma in the Cenozoic are determined from two boreholes located in the north and centre of the Orange Basin (Brown *et al.*, 1990).

Rust and Summerfield (1990) used the same boreholes (described above) and isopach data (from Dingle *et al.*, 1983 and Emery and Uchupi, 1984) to assess *onshore denudation rates* and offshore accumulation rates (Figure 6.23, labeled A and B) for the western margin. They propose a reduction in erosion rate for catchment areas draining to the western margin from 41-82 m/Ma (~152-113 Ma) to 7-9 m/Ma (~37-0 Ma). The average offshore accumulation rate (in km^3/Ma) is highest for the late Cretaceous-early Cenozoic (~113-37 Ma) though this reflects an increase in onshore catchment area (Rust and Summerfield, 1990). If the variation in size of the depositional area is taken into account (i.e. by dividing sediment volume by depositional area), the accumulation rate decreases from 89 m/Ma in the early to middle Cretaceous to 24-35 m/Ma since then. Since the Cretaceous, Rust and Summerfield (1990) estimate that an average of 1.8 km post-rifting erosion for the present day catchment has occurred. This is more than double the 863 m estimated for the south coast hinterland, and more than 2.5 times less than the 4.75-6.5 km calculated from the fission track data (see Chapter 7).

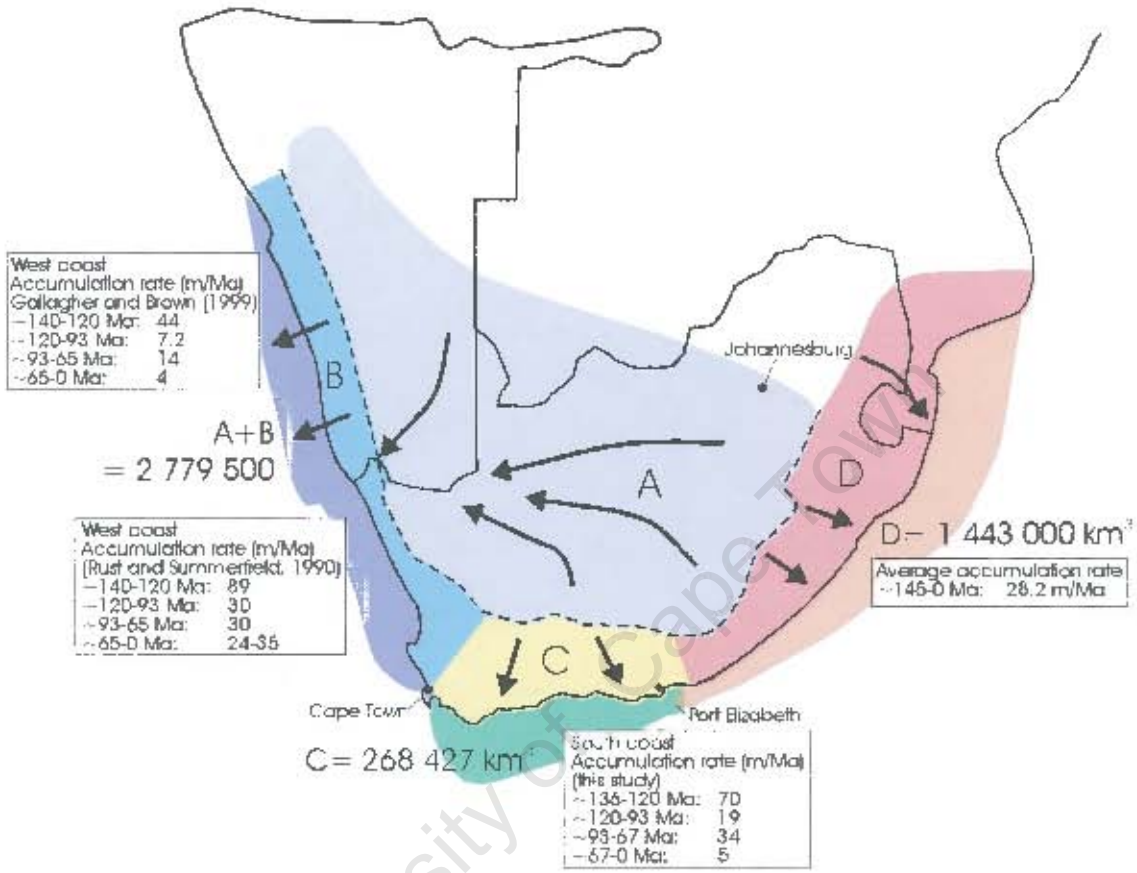

Figure 6.23: Schematic showing the source and quantity of sediment and its accumulation rate off the west coast (A and B, Rust and Summerfield, 1990; Gallagher and Brown, 1999b), the south coast (C, this study) and the east coast (D, Martin, 1987).

Gallagher and Brown (1999b) compare denudation rates estimated from fission track analysis with offshore Namibian sediment accumulation rates (Figure 6.23 labeled C and D) from isopachs calculated from seismic data across the Namib, Walvis, Luderitz and northern Orange Basins (from data in Maslanyj *et al.* (1992); Light *et al.* (1992, 1993); Clemson *et al.* (1997)). Figure 6.24 shows the offshore sediment flux from the Early Cretaceous to the present for the Namibian margin calculated by Gallagher and Brown (1999b). As for the Kudu boreholes from the centre of the Orange Basin, sediment accumulation based on seismic data was highest during the Early Cretaceous (~>11 000 km^3/Ma at ~136 to 132 Ma). A low accumulation rate followed from ~132 to 120 Ma (~1000 km^3/Ma). Accumulation rate then increased from ~120 to 90 Ma (to ~1800 km^3/Ma) with a further increase from ~90 to 65 Ma (to ~3500 km^3/Ma). The Cenozoic is again a period of low sediment accumulation (~1000 km^3/Ma). This variation in sediment accumulation rate is similar to that calculated for the south coast. Taking the area of the depository into account, (=~250 000 km^2, measured from an area parallel and ~170 km from the Namibian coast), gives accumulation rates of 44 m/Ma (~136-132 Ma), 4 m/Ma (~132-120 Ma), 7.2 m/Ma (120-90 Ma) and 14 m/Ma (~90-65 Ma) (Figure 6.24).

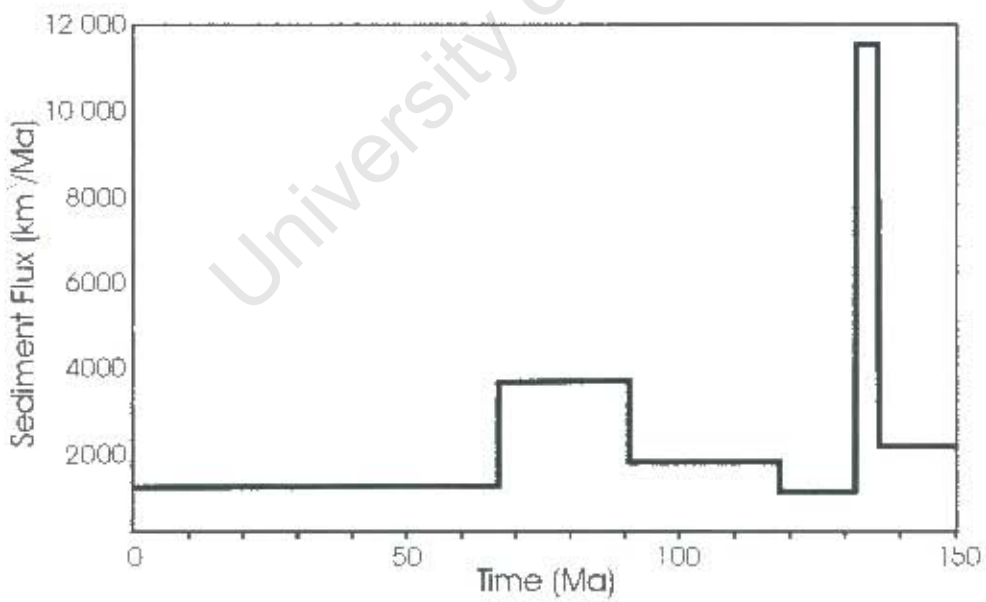

Figure 6.24: Change in sediment accumulation rates since continental breakup for the Namibian margin (from Gallagher and Brown, 1999b).

6.4.8 A Comparison to sediment accumulation rates across the east coast

Martin (1987) estimated sediment volumes for the Mozambique Coastal Plain, Natal Valley and Transkei Basin from seismic reflection and refraction data and drillholes. The results are listed in Table 6.6 and shown grammatically on figure 6.23 (D). According to Martin (1987), a total of ~1 443 000 km^3 of sediment has accumulated off the east coast (including the Mozambique Plain) since ~122.5 Ma at a rate of 11 780 km^3/Ma. This figure is a minimum estimate because in the ~20 Myrs after rifting, sediment may have bypassed the continental shelf and been deposited on the Falkland Plateau. The initiation of the Agulhas Current in the Cenozoic may have eroded sediment and transported it to the south-west, away from the east coast.

Even if the time over which the sediments have been accumulating is 'corrected' to 145 Myrs (when East Antarctica and Africa separated), the accumulation rate is ~5 times higher (9952 km^3/Ma) than the average rate calculated for the south coast (1974 km^3/Ma). This is likely due to the large difference in area over which the sediments have accumulated. The total south coast area is ~95 000 km^2, the east coast area is ~417000 km^2 (Martin, 1987), 4.4 times greater. Based on east coast offshore sediment volumes, Martin (1987) proposes that between 564 and 1033 m of rock has been eroded from the eastern hinterland in the last 100 Myr. This is similar to the ~863 m of material estimated to have been eroded from the south coast hinterland since 136 Ma from offshore volumes, but is inconsistent with that calculated from the fission track data of 4.75-6.5 km (see Chapter 7).

Table 6.6: Volume of sediment accumulated on Mozambique coastal plain and offshore in the Natal Valley and Transkei Basin since continental break-up (from Martin, 1987).

		Sediment Volume (km^3)	Accumulation Rate (km^3/Ma)
Northern Natal Valley and Coastal Mozambique	Offshore	212 800	
	Coastal Plain	284 900	
	Tugela Cone	63 200	
Southern Depocentres	Southern Natal Valley	879 300	
	Port St Johns Basin	2450	
Total		1 443 000	11 780

6.4.9 Comparison Summary

Table 6.7 shows a comparison between estimates of offshore accumulation for the west, south and east coasts. To compare margins with differing depositional areas, the rates given for the south coast (this study) and Namibian margin (Gallagher and Brown, 1999b) have been 'corrected' by dividing their sediment volume accumulation rates in km^3/Ma by the depositional area (km^2) over which they have accumulated (~94 000 km^2 and ~250 000 km^2 respectively). Thus all rates given in table 6.7 and shown graphically in figure 6.25 are in m/Ma. Figure 6.25 shows that sediment accumulation rates were highest for the south and west coasts post-rifting (~140-120 Ma). Accumulation rates then decrease into the middle Cretaceous and increase again into the late Cretaceous. Sediment accumulation rates off the south and Namibian coasts were particularly low during the Cenozoic.

Table 6.7: Offshore sediment accumulation rates (in m/Ma) for the west, south and east coasts[1]. South coast rates calculated over slightly different time intervals (136-120 Ma, 120-93 Ma, 93-67 Ma, 67-0 Ma).

	Rust and Summerfield (1990)	Gallagher and Brown (1999b)	Martin (1987)	Tinker (this study)
Time Interval	West coast	West coast	East coast	South coast
~140-120 Ma	89	44 (early)- 4 (late)		70
~120-93 Ma	30	7.2		19
~93-65 Ma	30	14		34
~65-0 Ma	24- 35	4		5
Total			28	21

[1] Sediment accumulation rate= (sediment volume/ depositional area)/ time (m/Ma). This adjustment is made to take into account the dependence of sediment accumulation volumes on area over which sediment accumulates. Area for south coast= ~94 630 km^2. Area of Namibian offshore deposition= ~250 000 km^2.

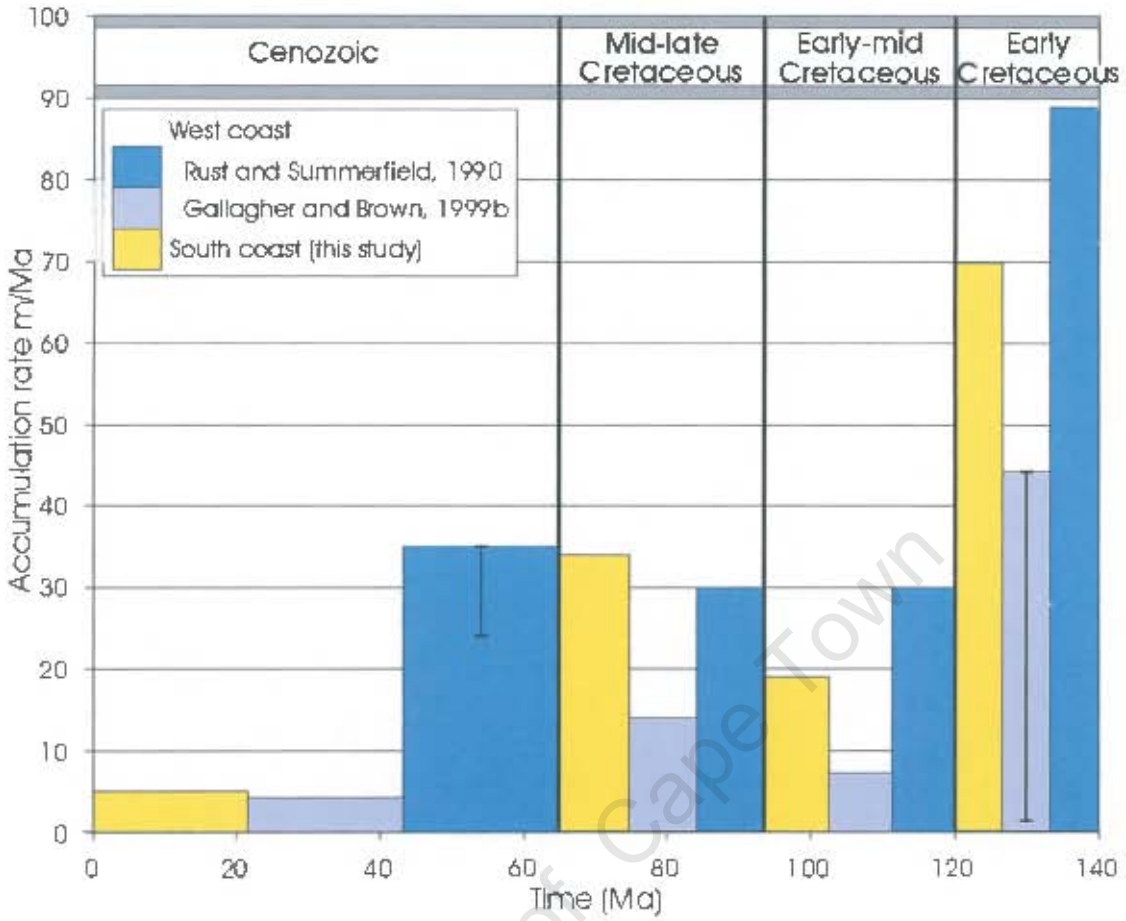

Figure 6.25: Comparison between sediment accumulation rates (in m/Ma) for the west coast (purple and blue) and south coast (yellow) of southern Africa from Table 6.7. South coast rates calculated over slightly different time intervals, though plotted as for the west coast.

6.4.10 Distribution of Cenozoic Sediment

Across the southern Cape, the Cape Fold Belt Mountains are a barrier to moisture-laden winds from the Indian Ocean (Figure 6.26a). Air is forced to rise which results in orographic rainfall along the coastal strip between the Cape Fold Belt Mountains and the sea (Mossel Bay, George, Knysna, Plettenberg Bay area). Thus the average rainfall received by this strip is considerably higher than the national average (Figure 6.26b, *). The highly competent Table Mountain quartzite ridges of the Cape Fold Belt Mountains also act as a physical barrier to rivers draining the area south of the escarpment. However, in places, three rivers, the Gourits, Gamtoos and Sundays Rivers, have cut through these ridges delivering sediment to the Outeniqua Basin (Figure 6.26c). Thus because of the orographic rainfall and hence enhanced erosion, as

well as the discharge from the Gourits River (see Figure 6.26c for location) we expect recent sediment discharge to the Outeniqua Basin to be relatively high offshore of this coastal strip (ellipse in Figure 6.26b and c). This relative increase in offshore sediment volume shows up in green on the isopach map of Cenozoic sediment volume (Offshore between Mossel Bay and Knysna in Figure 6.26c). This suggests that the geomorphological characteristics of the southern Cape that presently result in relatively high sediment discharge into the Outeniqua Basin (i.e. the Cape Fold Belt Mountains acting as a barrier to river transport and moisture-laden air) may have been in place since the early Tertiary.

East of the town of Plettenberg Bay, around Humansdorp, there is no coastal strip of flat land, because the Cape Fold Belt Mountains extend to the coast (Box marked *, Figure 6.26a). Any orographic rainfall will fall out to sea and the rainfall just inland of the coast will be relatively low (box marked *, Figure 6.26b). Rivers in this area tend to flow parallel to, rather than across, the Table Mountain Group quartzite ridges and therefore deliver their sediment further to the east (e.g. a tributary of the Gamtoos River, ▲ in Figure 6.26c). Figure 6.26c shows that sediment volumes accumulated since the beginning of the Tertiary are, as expected, low south of this strip (blues) (Plettenberg Bay to Humansdorp, Figure 6.26c).

East of Humansdorp rainfall increases (Figure 6.26a), the Gamtoos and Sundays Rivers discharge their load into the Outeniqua Basin. The accumulated sediment volumes are relatively high here (greens on Figure 6.26c)

Figure 6.26 (over the page): (A) A digital elevation model (DEM) showing the relief of the Cape Fold Belt Mountains which act as a barrier to moisture-laden air from the Indian Ocean, causing orographic rain along the coastal strip. * marks area where the Cape Fold Belt "meets" the sea. (B) South African rainfall from July 2003 to May 2004 based on preliminary data from the South African Weather Service (their map, www.weathersa.co.za). * marks area where the Cape Fold Belt meets the sea. Block C expanded: (C) The distribution of Cenozoic sediment and the position of three main rivers (the Gourits, Gamtoos and Sundays) that cut through the Table Mountain Group quartzite ridges of the Cape Fold Belt.

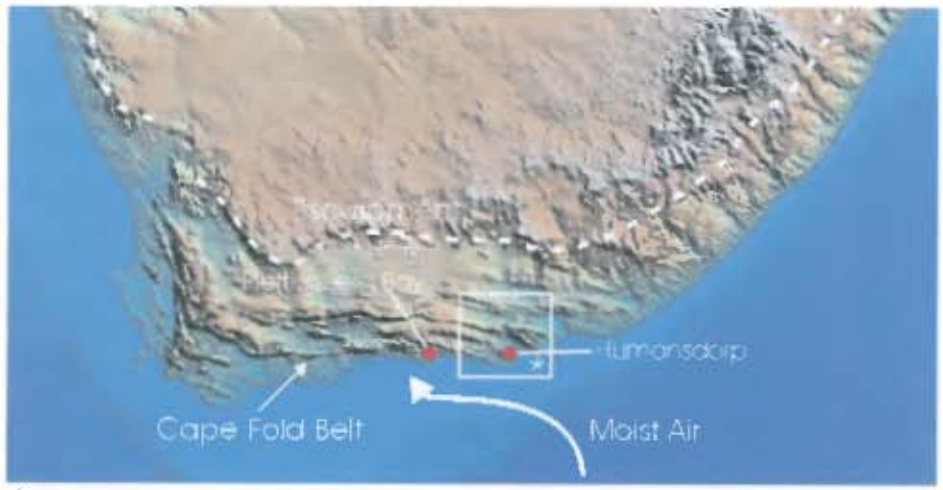

A

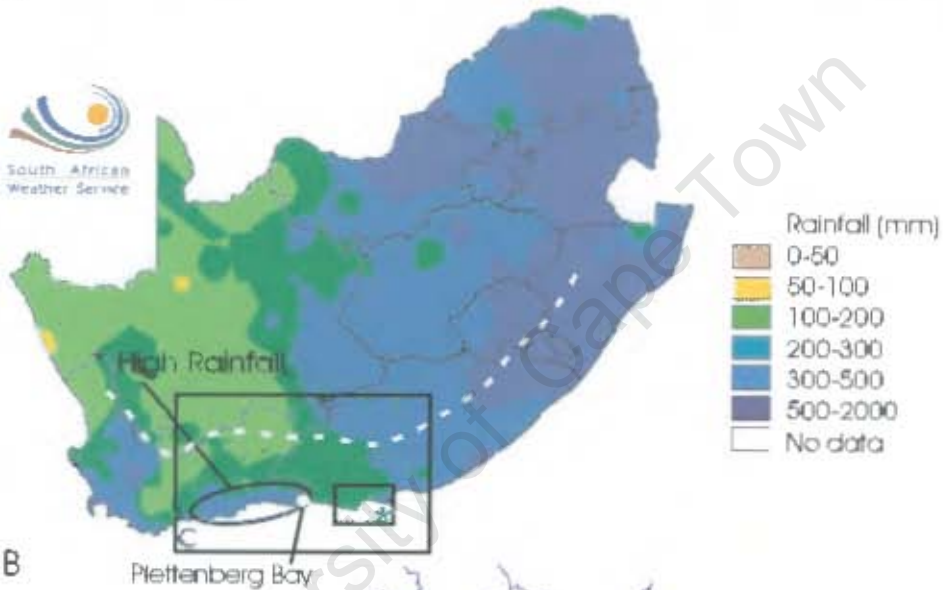

B

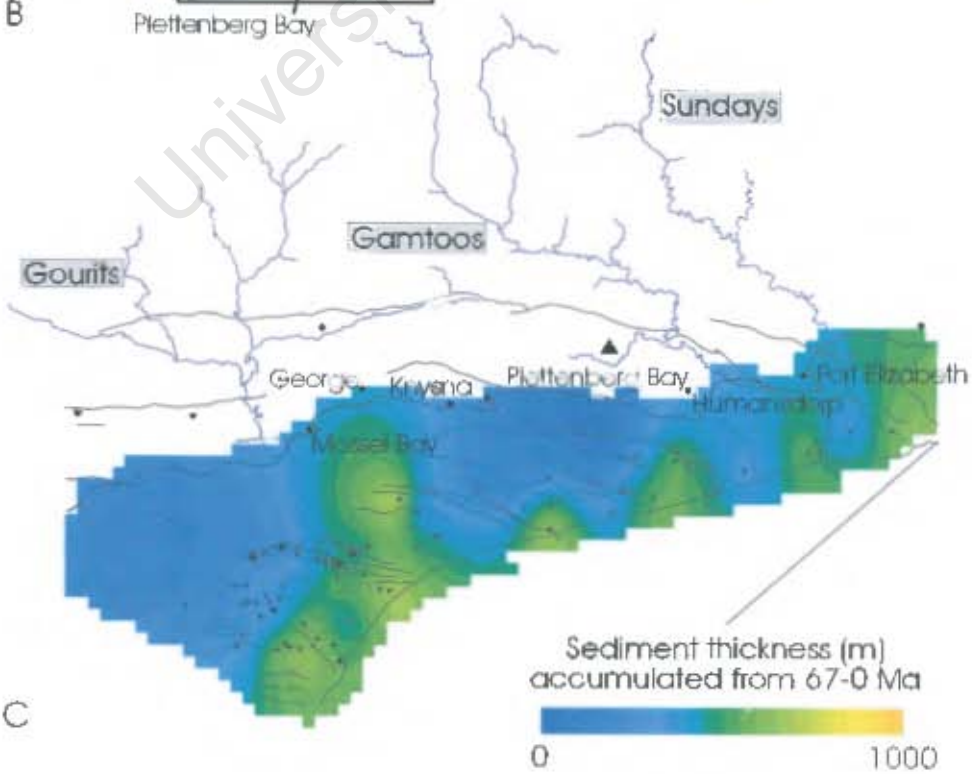

C

Chapter 7: Testing the balance between the onshore and offshore

This chapter first summarizes four observations:

- Onshore denudation exceeds offshore accumulation (7.1).
- The timing of changes in denudation and accumulation are well matched (7.2).
- Early, mid and late Cretaceous high rates of denudation are recorded from fission track data on a regional scale (>1000 km), all around southern Africa (7.3).
- Increased denudation and accumulation are co-incident with peak frequency of kimberlite intrusions (7.4).

The remainder of this chapter (7.5) discusses the implications of these observations on the causal mechanisms for southern African uplift.

7.1 Onshore denudation > offshore accumulation

Based on offshore sediment volumes, a calculated thickness of >863 m eroded from an estimated onshore area of ~140 000 km^2 since ~136 Ma (section 6.4.6). This calculation assumes that what is eroded from the continent is all accumulated on the continent shelf. However, modelling of fission track data suggests erosion of ~4.75 to 6.5 km from above boreholes KW1/67 and SA1/66 since the early Cretaceous (section 4.5.8). These values are 5 to 8 times higher than that estimated from offshore sediment preserved off the south coast. Thus, onshore denudation does not equal the accumulated volume preserved on the continental shelf.

A comparison of onshore denudation to offshore accumulation requires the calculation of total sediment volumes for each region. For the offshore, the sediment volumes are directly calculated (Table 6.4). For the onshore, the *thickness* eroded above boreholes KW1/67 and SA1/66 is calculated. The *volume* of eroded sediment is estimated by multiplying this thickness by the denuded area (~140 000 km^2). Offshore and onshore volumes and rates are shown graphically in figure 7.1 and listed in Table 7.1.

Figure 7.1 shows that calculated onshore denudation is > 3.5 times higher than preserved offshore accumulation. Thus, either onshore denudation is overestimated or offshore accumulation is underestimated.

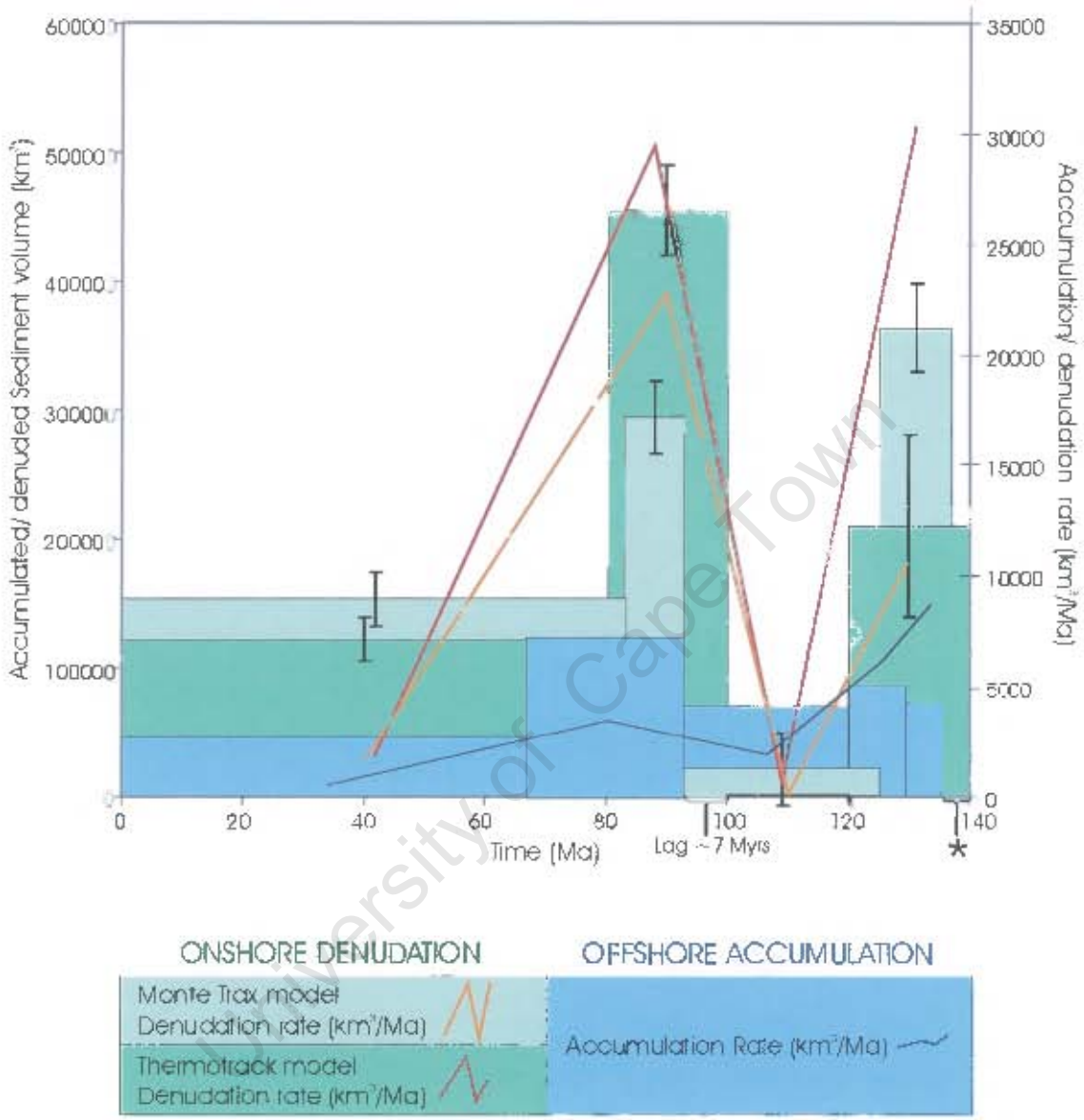

Figure 7.1: A comparison of onshore denudation and denudation rates from the Monte Trax model (light green and orange, respectively) and Thermotrack model (dark green and red) to offshore accumulation (blue). Uncertainties in denudation volumes are shown by error bars. *= Apparent lag time between denudation and accumulation (see section 7.2).

Table 7.1: Comparison of onshore denudation to offshore accumulation. Onshore area= ~140 000 km^2, offshore area= ~94 000 km^2. Onshore denudation is calculated using the thickness estimates from the Monte Trax (1) and Thermotrack (2) models.

ONSHORE				OFFSHORE		
Time (Ma)	Denudation (km^3)	Denudation error (km^3)	Denudation rate (km^3/Ma)	Time (Ma)	Accumulation (km^3)	Accumulation rate (km^3/Ma)
1						
137-125	364000	35000	30333	136-120	106306	6644
125-93	21000	28000	656	120-93	47314	1752
93-83	294000	28000	29400	93-67	83683	3219
83-0	154000	21000	1878	67-0	31124	464.5
2						
140-120	210000	70000	10500			
120-100	0	0	0			
100-80	455000	35000	22750			
80-0	122500	17500	1531			

7.1.1 Uncertainties in onshore denudation

The denuded volume is a rough estimate because of the difficulties in assessing the arial extent of the region that was eroded. In table 7.1 the denuded region is assumed to be restricted to south of the present day escarpment, ~140 000 km^2 (for reasons outlined in section 6.4.6). However, in the early Cretaceous, according to the model of differential denudation proposed in chapter 5 (Figure 5.6), this region may have been larger. Therefore onshore volumes calculated for an area of ~140 000 km^2 (only south of the escarpment, see section 6.4.6) may *underestimate* the true volume of eroded sediment.

The denuded volume is calculated by multiplying the thickness eroded from above two point locations (boreholes) by the denuded area. Lateral variation in degree of erosion over an area of 140 000 km^2 is impossible to resolve from fission track data from two boreholes and one sample transect. Thus, the denuded volume calculated in this way is only a rough guide to the true eroded volume.

7.1.2 Uncertainties in offshore accumulation

The offshore sediment volumes are minimum values for reasons outlined in section 6.4.1. These include the erosion and loss of sediment at offshore unconformities (possibly due to erosion by newly active ocean currents, e.g. the Agulhas Current), sediment bypass by suspension settling and turbidites and sediment deposition on the

Falkland Plateau between ~136 and 100 Ma. As in 7.1.1, lateral variations in sediment thickness are difficult to resolve, particularly in areas of poor borehole coverage.

Onshore denudation is calculated from ~140 Ma. Offshore accumulation is calculated from ~136 Ma, above the rift-drift unconformity along the south coast. The volume of sediment that accumulated during rifting, the synrift sediment (prior to ~136 Ma), is not calculated and added into the total offshore sediment volume. This is because the well reports, from which sediment volumes were quantified, did not include depths to the base of the synrift sediment. From offshore seismic reflection profiles, it is apparent that the synrift sediment is thick (up to 5000 m, Pletmos Basin, McMillan *et al.*, 1997) but highly locally distributed. Sediment volumes, therefore, are difficult to estimate. Addition of the synrift sediment to the volume accumulated offshore would increase the estimate of sediment accumulation in the early Cretaceous, possibly to the level of that expected from onshore denudation estimates from fission track analysis. However, there remains a discrepancy between the expected (from denudation estimates) and actual sediment accumulation since the early Cretaceous (~120-0 Ma).

7.1.3 Addition of the Uitenhage Group

As outlined in the differential denudation model of chapter 5, depositories for sediment eroded in the early Cretaceous include several *onshore* extensional basins (Figure 7.2). Thus to estimate the total volume accumulated in the early Cretaceous the infilling volume of the onshore basins must be added to the offshore volume accumulated. The Uitenhage Group outcrops over an area of ~4500 km^2 (calculated using Arcview GIS 3.2). The thickness of the infilling sediments is variable. In the Oudtshoorn, Algoa and Gamtoos Basins the thickness of the Uitenhage Group exceeds 3.15 km, 2.5 km and 3 km respectively (original sources in McLachlan and McMillan, 1976). According to Dingle *et al.* (1983) thickness may exceed 3 km and 4.1 km for the Oudtshoorn and Algoa Basins respectively. Infilling sediment of the other Uitenhage Group basins ranges from 0.8 km to 2.1 km (McLachlan and McMillan, 1976). Assuming an average thickness of ~2 km, an additional 9000 km^3 of sediment accumulated in the early Cretaceous (~136-120 Ma). This does not make up for the discrepancy between offshore and offshore volumes.

The above calculation is based on present day thickness and area of the Uitenhage Group outcrop. However, according to Viljoen (1992), these basins are likely remnants of a more extensive deposit. The Uitenhage Group was deposited in the early Cretaceous and, according to the differential denudation model (Chapter 5), eroded in the mid Cretaceous. The volume eroded from these onshore basins in the mid Cretaceous is impossible to quantify. Dividing the volume difference between denudation and accumulation (>120 000 km^3, using estimate from Thermotrack model) by the present day volume of the Uitenhage basins (9000 km^3) equals ~13.3. Therefore the basins would have had to have been >13 times larger in volume than their present extent to account for the volume difference between sediment denuded and accumulated.

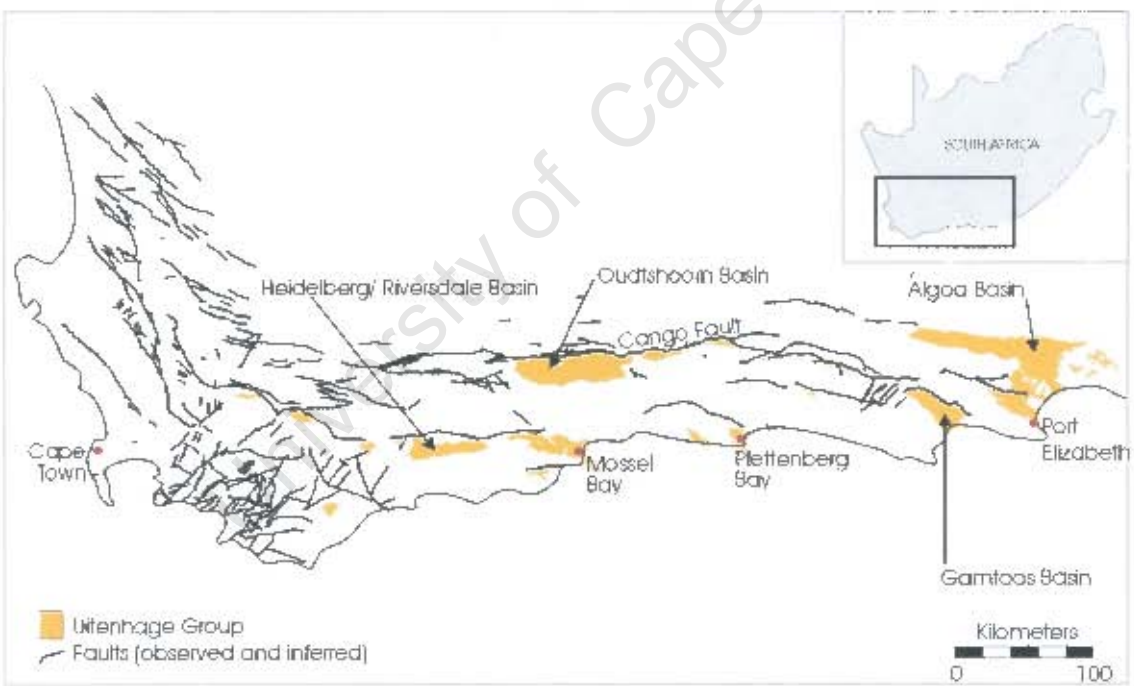

Figure 7.2: Uitenhage Group outcrop.

7.2 Timing of denudation and accumulation fluxes

As is apparent from 7.1, eroded sediment volume does not match sediment volume accumulated. However, the *timing* of changes in denudation and denudation rate matches the *timing* of changes in accumulation and accumulation rate (Figure 7.1). For example, high denudation in the early Cretaceous (~140-120 Ma) is matched by high accumulation (~136-120 Ma). A drop in denudation and denudation rate between ~120 and 100 Ma is coupled to a drop in accumulation and accumulation rate between ~120 and 93 Ma.

Renewed increased denudation and denudation rate in the mid Cretaceous (~100-80 Ma) is mirrored by increased accumulation and accumulation rate, apparently delayed by ~7 Myrs (Figure 7.1), at ~93-67 Ma. If this lag between denudation and offshore accumulation is real then a mechanism is needed to explain it that did not operate in the early Cretaceous when there is no such lag between denudation and accumulation. The 'apparent' lag in the early Cretaceous (marked with a * on figure 7.1) is there because the quantification of offshore sediment only begins ~4 Myrs after the onset of denudation and synrift sediment volumes (deposited prior to ~136 Ma) are not calculated (see section 7.1.2).

Figure 5.6 shows the mid Cretaceous exhumation of the Cape Fold Belt. Perhaps the highly competent, vertical in places, quartzite ridges formed a barrier to the transport of sediment to the margin thus causing a lag in time between erosion and offshore accumulation.

Alternatively, the lag may be just an artefact of averaging offshore sediment accumulation over considerable time intervals (up to ~27 Myrs), bounded by regional unconformities. For example, if there was a sudden increase in sediment accumulation from very low to high values between ~100 to 93 Ma (i.e. at the end of time interval ~120-93 Ma) this may be 'lost' in the averaging of accumulation over the ~27 Myr interval. Likewise, if accumulation was high from ~93 to 80 Ma and then dropped off at ~80 to 67 Ma, this decrease in accumulation may not show up in figure 7.1. Therefore the apparent 'lag' in time between increased denudation and accumulation may be a function of the averaging of volumes over often long time intervals.

A third possibility is that the mid Cretaceous lag between erosion and accumulation is real and is a product of the blockage of the newly exhumed Cape Fold Belt, but is artificially enhanced by the averaging of sediment volumes of long time intervals.

7.3 Denudation across southern Africa from other fission track studies

Using 6 boreholes and numerous outcrop samples from around southern Africa, Brown (1992) proposes three phases of increased denudation. The first at ~140-120 Ma involved >3-4 km erosion of the western and southern continental margins of South Africa and 1.5-2 ± 0.5 km in the interior (orange in Figure 7.3, Brown, 1992). Here I propose 1-2.6 km of early Cretaceous denudation in the southern Cape (light blue in Figure 7.3).

Between ~100 and 80 Ma, the west and south west of South Africa and the eastern continental margin (~2-4 km) was denuded (vertical stripes in Figure 7.3, Brown, 1992). Here I propose 2.1-3.5 km of erosion in the southern Cape (dark blue in Figure 7.3). There is additional evidence of mid Cretaceous cooling (~100-90 Ma) as far north as northern Mozambique (hexagons in Figure 7.3, Dassinnies *et al.*, 2004).

Increased denudation in the late Cretaceous (~80-60 Ma) in Namibia, eastern Natal (~3-4 km) and the eastern interior (~1-2 km) is calculated by Brown (1992) (horizontal stripes in Figure 7.3). Raab *et al.* (2002, 2004) calculate >3.5 km of erosion (at 230 m/Myr) over an area of 600 km long and 160 km wide in central Namibia in response to reactivation of basement structures at ~70 Ma (purple in Figure 7.3, Raab *et al.*, 2004).

Mid-late Cretaceous denudation (~100-60 Ma) is identified across most regions of southern Africa (Figure 7.3). This suggests that the causes of increased denudation at this time operated on a regional (>1000 km) rather than a local scale and therefore that uplift may be associated with dynamic mantle processes affecting the whole of southern Africa.

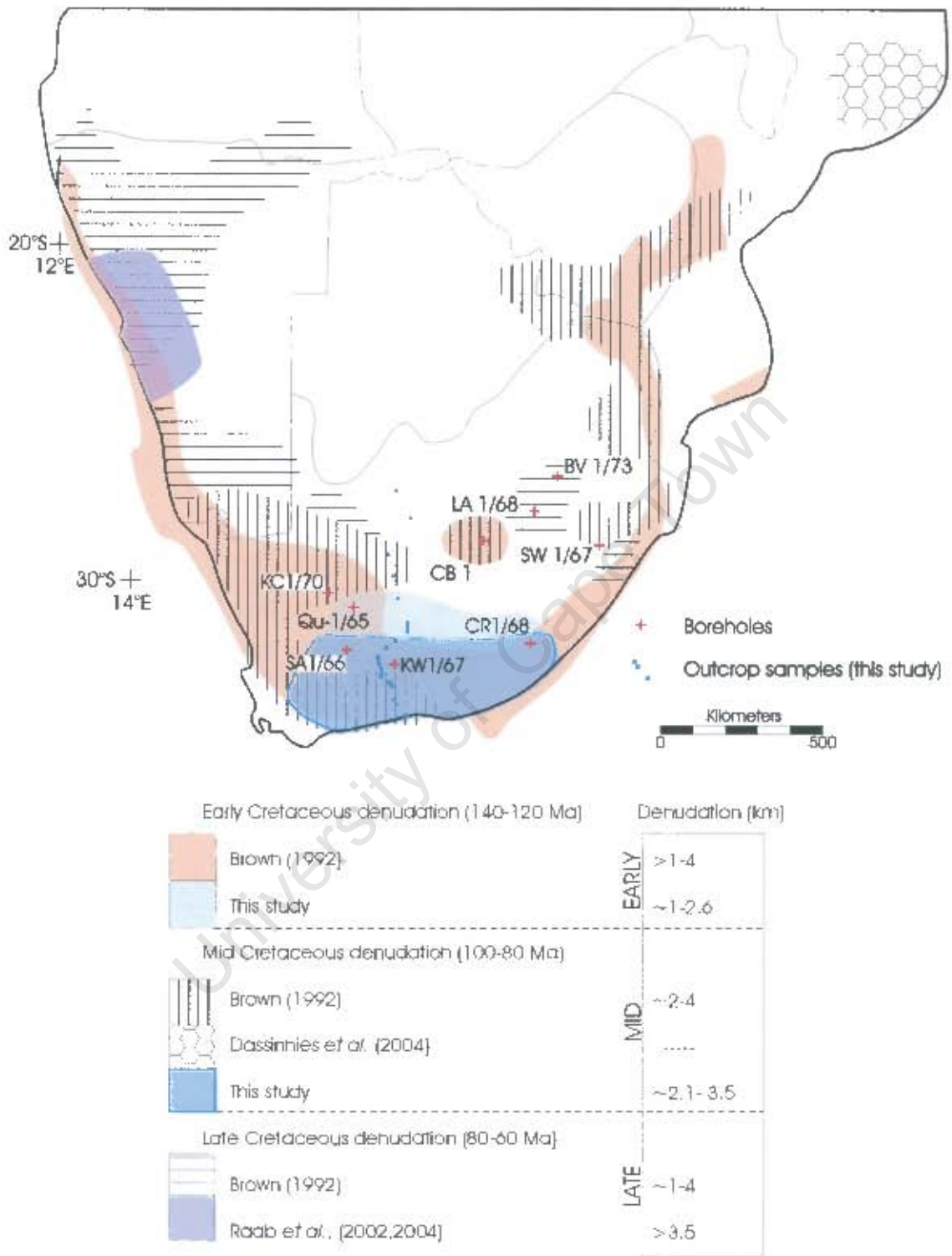

Figure 7.3: Increased southern African cooling (denudation) in the early Cretaceous (~140-120 Ma, orange, light blue shading), mid Cretaceous (~100-80 Ma, hexagons, vertical stripes, dark blue shading), and late Cretaceous (~80-60 Ma, horizontal stripes, purple shading).

7.4 Kimberlite events and the mantle connection

Figure 7.4 shows the frequency of kimberlite and related intrusions since the onset of Gondwana break-up in grey (Jelsma *et al.*, 2004). The blue columns include the De Beers data set, which shows a dramatic increase in the frequency of intrusions at ~120 Ma (Jelsma and Smith, 2004). This is due to the inclusion of a large population of mainly group 1, 120 Ma kimberlites from Angola (Jelsma, pers. comm. 2005). Because the uncertainties in the composition of the De Beer's data set and that the included Angolan kimberlites are far from the area of interest of this study, this discussion uses the published data set (grey in Figure 7.4, Jelsma *et al.*, 2004). The first peak (at 120 Ma) is composed of ~200 Group-2 kimberlites and related intrusions. The second peak (at 90 Ma) involves the intrusion of ~450 Group-1 kimberlites. Figure 7.5 superimposes the age-frequency histogram of kimberlite intrusions from Jelsma *et al.* (2004) on figure 7.1.

The 120 Ma peak of ~200 Group-2 kimberlites and related intrusions co-incides with the end of a period of high denudation, recorded from fission track thermochronology, and high accumulation, recorded from offshore sediment volumes. From ~120 to 100 Ma, during a time of low onshore denudation and offshore accumulation, far fewer kimberlites and related rocks intruded southern Africa (Jelsma *et al.*, 2004, Jelsma and Smith, 2004). Increased denudation and accumulation between ~100 and 80 Ma was *contemporaneous* with the intrusion of ~450 Group-1 kimberlites (Figure 7.5).

Thus there is a correlation between increased onshore denudation, offshore accumulation and onshore kimberlite and related intrusions. Dynamic mantle processes that are responsible for the intrusion of the kimberlites may also have been responsible for the tectonic uplift of southern Africa, thus indirectly increasing onshore denudation and offshore accumulation. The wide distribution of kimberlites (Figure 7.6) suggests that these mantle processes acted regionally, which supports fission track evidence that suggests that mid Cretaceous uplift was regional across the entire southern Africa (Section 7.3).

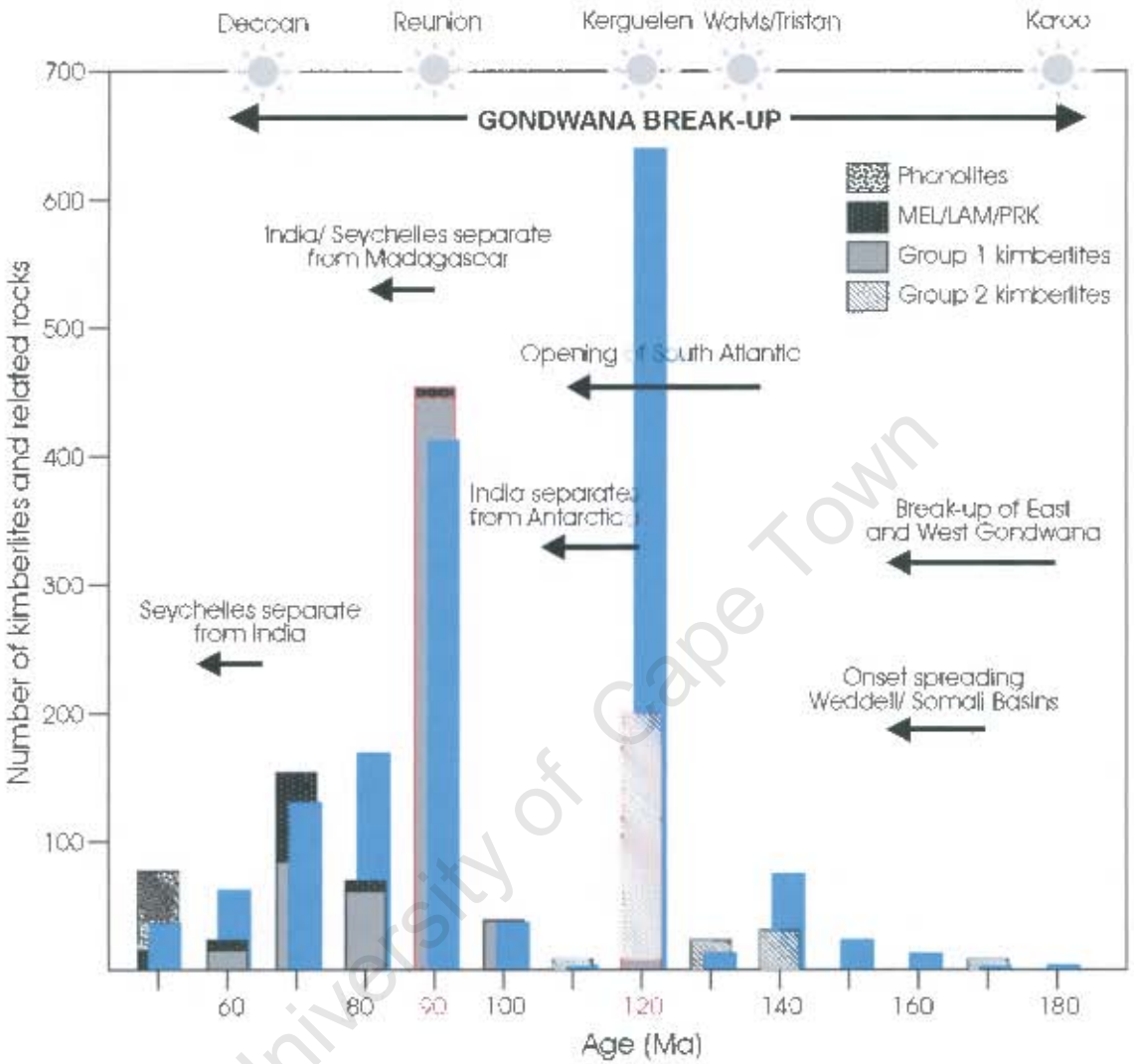

Figure 7.4: The age-frequency distribution of kimberlites and related rocks in grey (from Jelsma *et al.*, 2004) with the additional De Beers data set in blue (from Jelsma and Smith, 2004). Note the two prominent peaks of intrusion of kimberlite and related rocks at 120 Ma and 90 Ma. The discrepancy between the two data sets at 120 Ma is due to the inclusion of a large population of Angolan kimberlites in the De Beers data set.

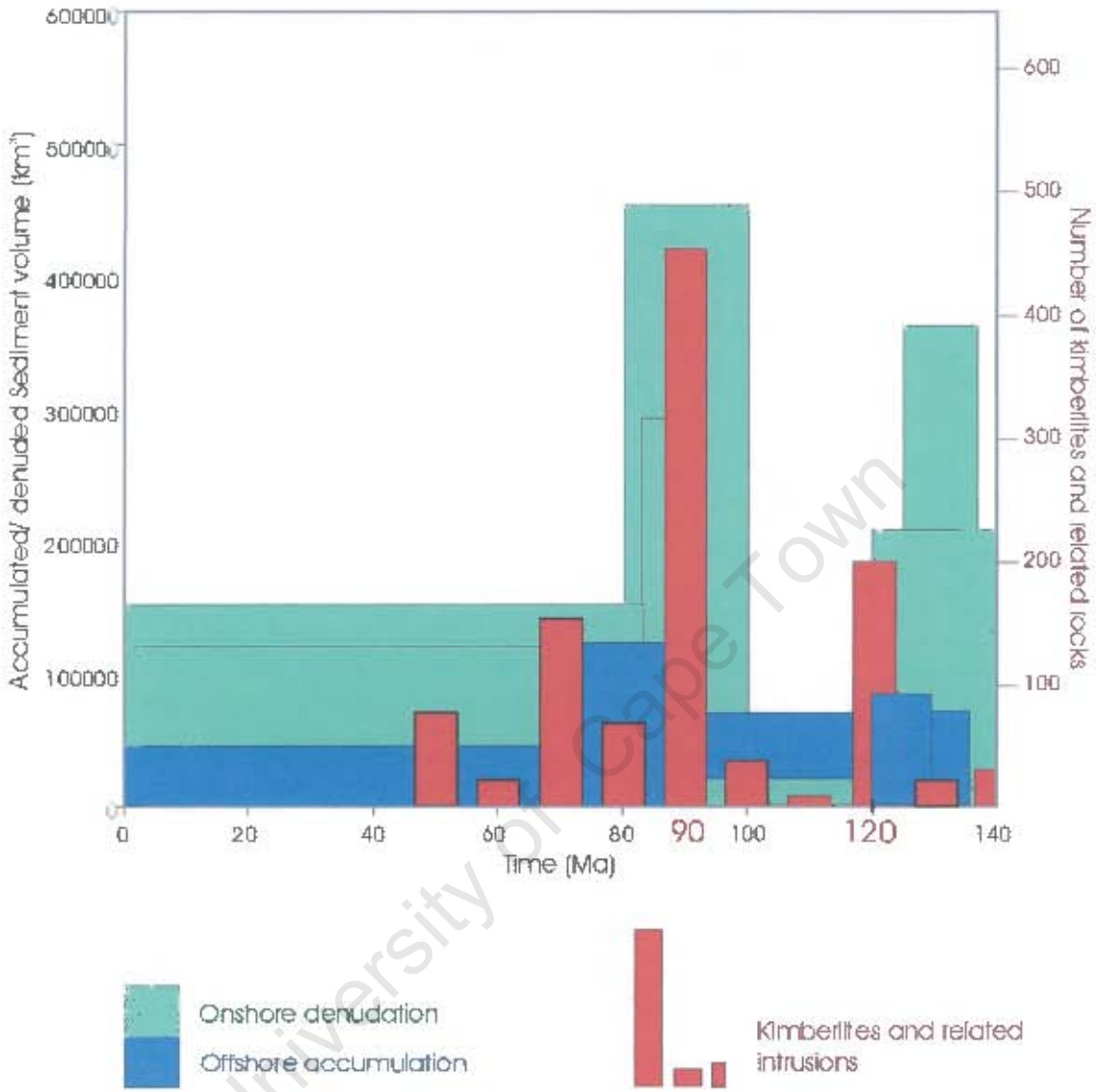

Figure 7.5: A comparison of the age-frequency distribution of kimberlite and related intrusions (right axis, from Jelsma *et al.*, 2004) to changes in denudation and accumulation since Gondwana break-up (left axis, this study). The apparent ~120 Ma peak in Group-2 kimberlite intrusions corresponds to the end of increased denudation and accumulation in the early Cretaceous as detected in this thesis. The apparent ~90 Ma peak in Group-1 kimberlite intrusions corresponds to the middle of an interval of increased denudation and accumulation in the mid Cretaceous.

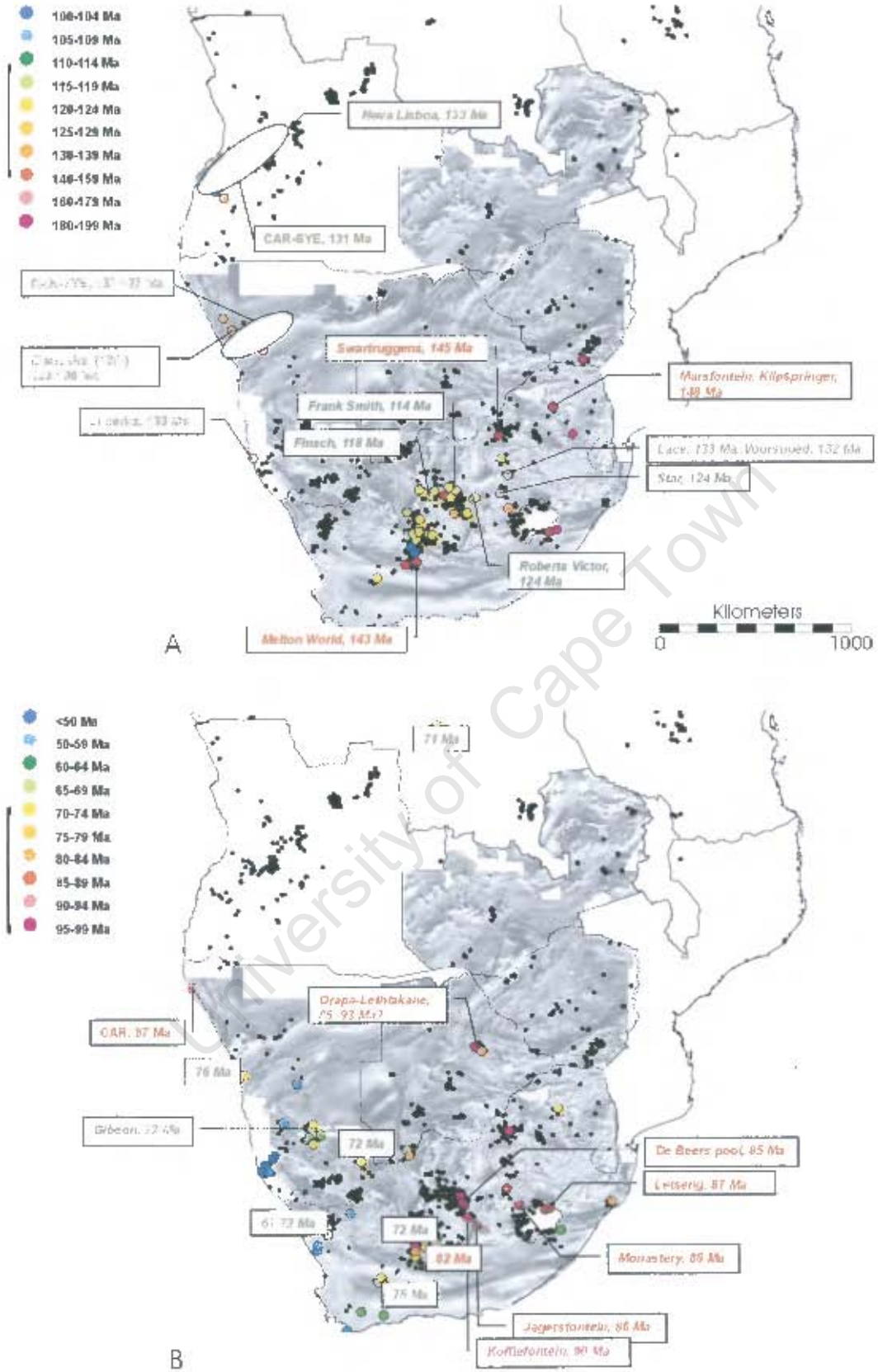

Figure 7.6: The distribution of kimberlites and related intrusions between (A) 100 and 200 Ma and (B) 0 and 100 Ma, highlighting those intrusions between ~150 and 115 Ma and ~90 and 67 Ma in A and B, respectively (from Jelsma and Smith, 2004).

7.5 Mechanisms for uplift

7.5.1 Early Cretaceous uplift (~140-120 Ma)

The apparent link between the increased frequency of kimberlite intrusions and increased denudation across the southern Cape is not as convincing in the early Cretaceous as it is in the mid Cretaceous. The peak in kimberlite intrusions occurs *at the end* of the period of increased denudation and accumulation (Figure 7.5). If the mantle processes responsible for the intrusion of ~200 kimberlites are related to early Cretaceous denudation, they must have been active for ~20 Myrs prior to peak kimberlite intrusion.

In addition to the kimberlites, there are two other products of mantle activity that may have a bearing on southern African uplift between ~140 and 120 Ma. The first of those is the Karoo volcanic province (183 ± 1 Ma, $^{40}Ar/^{39}Ar$, Duncan *et al.*, 1997), speculated to be related to the upwelling of a mantle plume beneath southern Africa and Antarctica (Encarnación *et al.*, 1996). As the upwelling of hot buoyant mantle impinges on the base of the lithosphere this may induce uplift (see Doucouré and de Wit, 2003 for overview of models). 40 Myrs separates this event from early Cretaceous uplift, therefore Karoo-aged plume activity would have to have been long-lived to account for uplift 40 Myrs later. The Paraná-Etendeka lavas dated at 132 ± 1 Ma ($^{40}Ar/^{39}Ar$, Renne *et al.*, 1996) are speculated to be related to Walvis plume activity associated with the opening of the South Atlantic. This mantle upwelling is contemporaneous with early Cretaceous uplift but occurred far to the north-west (~1700 km) to be its cause. Therefore both the Karoo and Paraná plumes are inadequate alone to explain uplift across southern Africa.

Also contemporaneous with an increase in denudation in the early Cretaceous is continental rifting that separated southern Africa from South America. Steckler (1985) proposed that rifting induces small-scale mantle convection, which adds heat to that already generated by the extension, thus adding to uplift. The relationship of continental rifting to mantle activity is debated and workers have modelled the geophysical response of the lithosphere to rifting independently of mantle processes (Chapter 3). King (1963) recognised a 'downflexing' of the lithosphere in response to rifting that then created a monocline that was subsequently eroded. Gilchrist and

Chapter 8: Concluding remarks

Offshore and onshore data support an exhumation history for the southern Cape involving erosion of 4.75 to 6.5 km since the early Cretaceous. Continental rifting and 'mantle processes' related to peak kimberlite emplacement are speculated as the driving mechanisms for the increased denudation (exhumation) in the early and mid Cretaceous, respectively. However, climate (see below), lithology (Chapter 5.2) and tectonic 'unroofing' by late-stage movements along extensional faults (e.g. the Cango Fault, Chapter 4.4.1.6) may have also influenced denudation.

The complex interplay between tectonic uplift, erosion and climate remains an intriguing puzzle (Figure 8.1). Molnar (2003) describes these competing forces as 'nature', meaning the setting of initial conditions by tectonic processes, and 'nurture', the shaping of the Earth's surface by subsequent climate related activity, including erosion by glaciers and rivers. Does erosion drive uplift or vice versa? Can the history of denudation across southern Africa proposed here (Figure 7.3) help to distinguish between competing ideas of what drives geomorphic change?

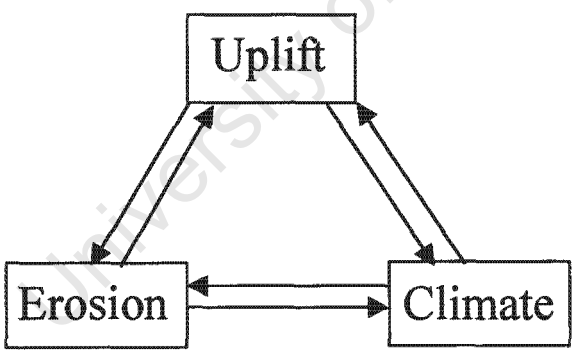

Figure 8.1: Schematic representation of the interplay and feedbacks between tectonic uplift, erosion and climate.

Molnar and England (1990) first postulated that uplift in the late Cenozoic (e.g. the Pyrenees and Alps) may be a *consequence* of climate change rather than the other way around. Wobus *et al.* (2003) similarly linked climate and uplift for the Greater Himalaya. The alternative view, championed by Raymo and Ruddiman (1992) and Burbank *et al.* (2003) amongst others, is that climate change may be a *result* of tectonic forcing.

The role of climate in erosion and uplift is indeed complex. Isostatic rebound following ice sheet retreat during interglacials is one example of climate induced uplift. Reiners *et al.* (2003) produce evidence from the Washington Cascades that supports a model where increased precipitation is the driving force for increased erosion, and in turn increased uplift. Climate-induced isostatic rebound has also been proposed for the European Alps (Cedarbom *et al.*, 2004). The connection between climate and uplift may be indirect. Lamb and Davis (2003), for example, relate Andean uplift to indirect climate forcing, through the presence or absence of trench fill during subduction. In a humid climate, fine-grained, wet sediments are deposited in the subduction trench that then, according to these authors, facilitate subduction by lubricating the subducting slab. In the absence of these sediments (in a dry environment) the lubrication is reduced, raising shear stresses that results in increased Andean uplift (Lamb and Davis, 2003).

To understand the role of climate in southern Africa's denudation, a better resolution of climate change since the Cretaceous is required. Unfortunately, denudation has resulted in the removal of almost the entire Cretaceous onshore rock record, leaving little evidence to help constrain climatic changes. Remnants of the Uitenhage Group remain, which was deposited between ~145 and 130 Ma, in a humid, oxidizing environment. The fossil assemblages found within the crater facies of Cretaceous kimberlites, where preserved, also point to a wetter climate in the late Cretaceous (Smith, 1986). One way of understanding southern African climate since the Cretaceous is by unraveling how ocean currents have shifted during the break-up of Gondwana and the opening of the South Atlantic. Ocean circulation and climate are interlinked, for example, the onset of the Benguela current at ~14 Ma (Weigelt and Uenzelmann-Neben, 2004) has been linked to cooling along southern Africa's west coast since this time. Therefore, close examination of sediment patterns and unconformities using offshore seismic data may aid our understanding of the development and shifting of ocean currents, and hence of climate.

World-wide, the Cretaceous was a hot, humid period accompanied by eustatic sea level highs (see figure 2.1) (Wilson and Norris, 2001, Poulsen, 2004, Jenkyns *et al.*, 2004). Long term global cooling in the Cenozoic Era is described by Molnar and England (1990). The Cenozoic climate in South Africa was mostly arid, as is evidenced by the

widespread development of silcretes across the southern African landscape (Partridge and Maud, 1989). Since ~55 Ma, southern Africa has also grown increasingly cooler as shown by the $\delta^{18}O$ record of Miller and Fairbanks (1985). This increase in aridity and decrease in temperature from the Cretaceous to the Cenozoic in South Africa is mirrored by a decrease in denudation across the southern Cape.

Certainly in the absence of any obvious tectonic cause of uplift, climate-driven weathering, erosion and isostatic rebound is one way of explaining increased denudation. However, in the southern Cape, tectonic uplift due to continental rifting and mantle dynamics (associated with kimberlite emplacement) is an equally likely explanation. The large amount of denudation (up to 6.5 km), and the co-incidence of maximum kimberlite emplacement and increased denudation in the mid Cretaceous, are suggestive of tectonic forcing. Molnar and England (1990) suggest that a system of positive feedbacks links climate change to weathering, erosion and isostatic rebound. An important component of this system, particularly in southern Africa, is tectonic uplift (due to mantle dynamics and/ or continental rifting). A true understanding though, of the roles of each of these elements and the feedbacks that interlink them can only come from a more detailed understanding of climate change since the Cretaceous in southern Africa and a more quantitative approach to geomorphologic evolution.

Apatite fission track analysis has proved to be a useful tool in understanding shallow crustal processes. Further work is needed to broaden its application across southern Africa, with particular emphasis on sampling all of the deep SOEKOR boreholes. Thermal modeling may be extended to higher and lower temperatures (>250°C, <60°C) by the application of zircon fission track analysis and the U-Th/He technique. Although U-Th/He analysis is a new thermochronological tool it has already proven to be a good independent check on apatite fission track analysis: U-Th/He ages on apatites must always be younger than apatite fission track ages. Absolute ages of the widespread, well documented surfaces that extend across southern Africa are needed and may be ascertained using cosmogenic isotope analysis. Relative dating and correlation of surfaces based on lithological similarities are no longer sufficient to track the details of the geomorphological evolution of southern Africa.

Boreholes off the south coast of South Africa should be sampled for apatites and

zircons and fission track analysis and modeling applied to retrieve a thermal history of the continental margin. This can be compared to the thermal history proposed here for the onshore south coast. The zircons may be used to ascertain their provenance, which would improve the link between the onshore and offshore.

Thus, an increasingly quantitative data set may help to answer some of the many geomorphological questions regarding the links between climate, erosion and tectonic uplift of southern Africa and abroad.

"Clearly, geomorphology has outgrown its early roots as a descriptive science and has become increasingly quantitative" (L.B. Leopold, 2004).

References

Allègre, C., Birck, J. L., Capmas, F., Courtillot, V., 1999. Age of the Deccan Traps using ^{187}Re-^{187}Os systematics. *Earth Planet. Sci. Lett.* **170**, 199-204.

Amstrong, R.A., de Wit, M.J., Reid, D., York, D. and Zartman, R. (1998). Cape Town: Table Mountain reveals rapid Pan-African uplift of its basement rocks. *Journal of African Earth Science*. **27** (1A), 10.

Arne, D. and Zentilli, M. (1994). Apatite Fission Track Thermochronology Integrated with Vitrinite Reflectance: A review. *American Chemical Society*. **16**. 11pp.

Barbarand, J., Hurford, T. and Carter, A. (2003a). Variation in apatite fission-track length measurement: implications for thermal history modeling. *Chemical Geology*. **198**, 77-106.

Barbarand, J., Carter, A., Wood, I. and Hurford, T. (2003b). Compositional and structural control of fission-track annealing in apatite. *Chemical Geology*. **198**, 107-137.

Barnett, W., Armstrong, R.A. and de Wit, M.J. (1997). Stratigraphy of the upper Neoproterozoic Kango and lower Paleozoic Table Mountain Group of the Cape Fold Belt revisted. *South African Journal of Geology*. **100** (3), 237-250.

Bate, K.J. and Malan, J.A. (1992). Tectonostratigraphic evolution of the Algoa, Gamtoos and Pletmos Basins, offshore South Africa. In. *Inversion tectonics of the Cape Fold Belt, Karoo and Cretaceous basins of southern Africa.* (eds.: de Wit, M.J. and Ransome, I.G.D.) *A.A. Balkema, Rotterdam*. 61-73.

Beeson, R. (1980). The relationship of siltstone geochemistry to sedimentary environments and uranium mineralisation in the Beaufort Group, Cape Province, South Africa. *Chemical Geology*. **30**, 81-107.

Ben-Avraham, Z., Hartnady, C.J.H. and Malan, J.A. (1993). Early extension between the Agulhas Bank and the Falkland Plateau due to the rotation of the Lafonia microplate. *Earth and Planetary Science Letters*. **117**, 43-58.

Birch, G.F. (1975). Continental margin off the west coast of South Africa. *PhD thesis (unpublished). University of Cape Town, South Africa.*

Bordy, E.M., Hancox, P.J., Rubidge, B.S. (2004). Provenance study of the Late Triassic-Early Jurassic Elliot Formation, main Karoo Basin, South Africa. *South African Journal of Geology*. **107**, 587-602.

Bray, R.J., Green, P.F. and Duddy, I.R. (1992). Thermal history reconstruction in sedimentary basins using Apatite Fission-Track Analysis and Vitrinite Reflectance: A case study from the East Midlands of England and the Southern North Sea. *Geological Society of London: Exploration Britain: Into the next decade. Conference Proceedings Special Publication*. 25pp.

Broquet, C.A.M. (1992). The sedimentary record of the Cape Supergroup: A review. In. *Inversion tectonics of the Cape Fold Belt, Karoo and Cretaceous basins of southern Africa.* (eds.: de Wit, M.J. and Ransome, I.G.D.) *A.A. Balkema, Rotterdam*. 159-183.

Brown, L.F. Jr., Benson, J.M., Brink, G.J., Doherty, S., Jollands, A., Jungslager, E.H.A., Keenan, J.H.G., Muntingh, A. and van Wyk, N.J.S. (1995). Sequence Stratigraphy in Offshore South African Divergent Basins: An Atlas on Exploration for Cretaceous Lowstand Traps by Soekor (Pty) Ltd. *AAPG Studies in Geology.* **41.**

Brown, R.W. (1992). A fission track thermochronology study of the tectonic and geomorphic development of the sub-aerial continental margins of southern Africa. *Ph.D. thesis, La Trobe University, Melbourne, Australia.*

Brown, R.W., Summerfield, M.A. and Gleadow, A.J.W. (2002). Denudation history along a transect across the Drakensberg Escarpment of southern Africa derived from apatite fission track thermochronology. *Journal of Geophysical Research*, **107**, (12) 18pp.

Brown, R.W., Gallagher, K., Gleadow, A.J.W. and Summerfield, M.A. (2000). Morphotectonic evolution of the South Atlantic margins of Africa and South America. In. *Geomorphology and Global Tectonics* (ed.: Summerfield, M.A.). *John Wiley and Sons Ltd.* 255-284.

Brown, R., Gallagher, K. and Duane, M. (1994). A quantitative assessment of the effects of magmatism on the thermal history of the Karoo sedimentary sequence. *Journal of African Earth Sciences*, **18** (3) 227-243.

Brown, R.W., Rust, D.J., Summerfield, M.A., Gleadow, A.J.W., and de Wit, M.C.J. (1990). An Early Cretaceous phase of accelerated erosion on the south-western margin of Africa: Evidence from apatite fission track analysis and the offshore sedimentary record. *Nuclear Tracks and Radiation Measurement*, **17**, 339-350.

Burbank, D.W., Blythe, A.E., Putkonen, J., Pratt-Sitaula, B., Gabet, E., Oskin, M., Barros, A., Ojha, T.P. (2003). Decoupling of erosion and precipitation in the Himalayas. *Nature*, **426**, 652-655.

Burbank, D.W., Leland, J., Fielding, E., Anderson, R.S., Brozovic, N., Reid, M.R. and Duncan, C. (1996). Bedrock incision, rock uplift and threshold hillslopes in the northwestern Himalayas. *Nature*, **379**, 505-510.

Burke, K. (1996). The African Plate. *South African Journal of Geology*, **99** (4) 341-409.

Carlson, D.W., Donelick, R.A. and Ketcham, R.A. (1999). Variability of apatite fission-track annealing kinetics, I. Experimental results. *American Mineralogist.* **84**, 1213-1223.

Carlson, D.W. (1990). Mechanisms and kinetics of apatite fission track annealing. *American Mineralogist.* **75**, 1120-1139.

Catuneanu, O., Hancox, P.J., Cairncross, B. and Rubidge, B.S (2002). Foredeep submarine fans and forebulge deltas: orogenic off-loading in the underfilled Karoo Basin. *Journal of African Earth Sciences*. **35**, 489-502.

Catuneanu, O., Hancox, P.J. and Rubidge, B.S. (1998). Reciprocal flexural behaviour and contrasting stratigraphies: a new basin development model for the Karoo retroarc foreland system, South Africa. *Basin Research*. **10**, 417-439.

Cedarbom, C.E., Sinclair, H.D., Schlunegger, F. and Rahn, M.K. (2004). Climate-induced rebound and exhumation of the European Alps. Geology. 32 (8), 709-712.

Clemson, J., Cartwright, J. and Booth, J. (1997). Structural segmentation and the influence of basement structure on the Namibian passive margin. *Journal of the Geological Society, London*. **154**, 477-482.

Cloetingh, S., Lankreijer, A. de Wit, M.J. and Martinez, H. (1992). Subsidence history analysis and forward modeling of the Cape and Karoo Supergroups. In. *Inversion tectonics of the Cape Fold Belt, Karoo and Cretaceous basins of southern Africa.* (eds.: de Wit, M.J. and Ransome, I.G.D.) *A.A. Balkema, Rotterdam*. 239-249.

Cockburn, H.A.P., Brown, R.W., Summerfield, M.A. and Seidl, M.A. (2000). Quantifying passive margin denudation and landscape development using a combined fission-track thermochronometry and cosmogenic isotope analysis approach. *Earth and Planetary Science Letters*, **179**, 429-435.

Cockburn, H.A.P, Seidl, M.A., and Summerfield, M.A. (1999). Quantifying denudation rates on inselbergs in the central Namib Desert using in situ-produced cosmogenic ^{10}Be and ^{26}Al. *Geology*, **27** (5), 399-402.

Cocks, L.R.M. and Fortey, R.A. (1986). New evidence on the South African Lower Paleozoic: age and fossils reviewed. *Geological Magazine*. **123** (4), 437-444.

Cole, D.I. (1992). Evolution and development of the Karoo Basin. In. *Inversion tectonics of the Cape Fold Belt, Karoo and Cretaceous basins of southern Africa.* (eds.: de Wit, M.J. and Ransome, I.G.D.) *A.A. Balkema, Rotterdam*. 87-99.

Cole, D.I and Wipplinger, P.E. (2001). Sedimentology and Molybdenum Potential of the Beaufort Group in the Main Karoo Basin, South Africa. *Council for Geoscience, Geological Survey of South Africa.* Memoir 80, 225pp.

Cox, K.G. (1992). Karoo igneous activity and the early stages of the break-up of Gondwanaland. In. *Magmatism and the Causes of Continental Break-up.* (eds.: Storey, B.C., Alabaster, T. and Pankhurst, R.J.). *Geol. Soc. Spec. Publ.*, 68, 137-148.

Crowley, K.D., Cameron, M. and Schaefer, R.L. (1991). Experimental studies of annealing of etched tracks in fluorapatite. *Geochim. Cosmochim. Acta.* **55**, 1449-1465.

Dassinnies, M.C.D., Jacobs, J., Kohn, B. and Grantham, G.H. (2004). A Combined Apatite Fission Track And Apatite (U-Th)/He Study Of The Passive Continental Margin Of Northern Mozambique. *10th International Fission Track Dating and Thermochronology. 8-13th August, 2004, Amsterdam* (abstract) pp. 72.

de Wit, M.C.J. (1999). Post-Gondwana drainage and the development of diamond placers in Western South Africa. *Economic Geology*. **94**, 721-740.

de Wit, M.J. (1992). The Cape Fold Belt: A challenge for an integrated approach to inversion tectonics. In. *Inversion tectonics of the Cape Fold Belt, Karoo and Cretaceous basins of southern Africa.* (eds.: de Wit, M.J. and Ransome, I.G.D.) *A.A. Balkema, Rotterdam*. 3-12.

de Wit, M.J. and Ransome, I.G.D. (1992). Regional inversion tectonics along the southern margin of Gondwana. In. *Inversion tectonics of the Cape Fold Belt, Karoo and Cretaceous basins of southern Africa.* (eds.: de Wit, M.J. and Ransome, I.G.D.) *A.A. Balkema, Rotterdam*. 15-21.

Dingle, R.V. and Hendey, Q.B. (1984). Late Mesozoic and Tertiary sediment supply to the Eastern Cape Basin (SE Atlantic) and paleo-drainage systems in southwestern Africa. *Marine Geology*. **56**, 13-26.

Dingle, R.V., Siesser, W.G. and Newton, A.R. (1983). *Mesozoic and Tertiary Geology of southern Africa*. A.A. Balkema, Rotterdam. 375pp.

Donelick, R., Farley, K., O'Sullivan, P. and Asimov, P. (2003). Experimental evidence concerning the pressure dependence of He diffusion and fission-track annealing kinetics in apatite. *On track*. September 2003, **13** (2) 26, 19-21.

Donelick, R., Ketcham, R.A. and Carlson, W. (1999). Variability of apatite fission-track annealing kinetics: II. Crystallographic orientation effects. *American Mineralogist*. **84**, 1224-1234.

Doucouré, C.M. and de Wit, M.J. (2003). Old inherited origin for the present near-bimodal topography of Africa. *Journal of African Earth Sciences*. **36**, 371-388.

Duane, M.J. and Brown, R.W. (1991). Tectonic brines and sedimentary basins: further applications of fission track analysis in understanding Karoo Basin evolution (South Africa). *Basin Research*. **3**, 187-195.

Duddy, I.R., Green, P.F. and Laslett, G.M. (1988). Thermal annealing of fission tracks in apatite 3. Variable temperature behaviour. *Chemical Geology Isotope Geoscience Section*. **73**, 25-38.

Duncan, A.R. and Marsh, J.R. (in press). The Karoo Igneous Province. Chapter XIIb in "Geology of South Africa" (textbook edited by R. Thomas).

Duncan, R.A., Hooper, P.R., Rehacek, J., Marsh, J.S. and Duncan, A.R (1997). The timing and duration of the Karoo igneous event, southern Gondwana. *J. Geophys. Res.* **102**, 18127-18138.

Du Toit (1954). *The Geology of South Africa, 3rd edn., Oliver and Boyd, U.K.*, 611pp.

Du Toit (1937). *Our Wandering Continents. Oliver and Boyd, U.K.*, 366pp.

Ebinger,C.J. and Sleep, N.H. (1998). Cenozoic magmatism throughout east Africa resulting from impact of a single plume, *Nature*. **395**, 788-791.

Egle, S. (1996). Paleo-hydrology of the Cape Fold Belt and the Karoo Basin, South Africa: Constraints on the Formation of the Laingsburg (DR-3) Uranium Prospecting Area. *Ph.D. Thesis. Universität Wien.*155pp.

Emery, K.O. and Uchupi, E. (1984). The Geology of the Atlantic Ocean. *Berlin, Springer,* 375pp.

Encarnación, J., Fleming, T.H., Elliot, D.H., Eales, H.V. (1996). Synchronous emplacement of Ferrar and Karoo dolerites and the early breakup of Gondwana. Geology. 24 (6), 535-538.

Fitzgerald, P. G., Muñoz, J. A., Coney, P. J. and Baldwin, S. L. (1999). Asymmetric exhumation across the Pyrenean orogen: implications for the tectonic evolution of a collisional orogen. *Earth and Planetary Science Letters.* **173** (3), 157-170.

Fleischer, R.L., Price, P.B. and Walker, R.M. (1975). Nuclear Tracks in Solids. *University of California Press, Berkeley.* 605pp.

Fleischer, R.L., Woods, R.T., Hart, H.R. Jr., Price, P.B. and Short, N.M. (1974). Short, Effect of shock on fission track dating of apatite and sphene crystals from the Hardhat and Sedan underground nuclear explosions. *Journal of Geophysical Research.* **79**, 339-342.

Fleischer, R.L., Price, P.B. and Walker, R.M. (1965a). Effects of temperature, pressure and ionization on the formation and stability of fission tracks in minerals and glasses. *Journal of Geophysical Research.* **70**, 1497-1502.

Fleischer, R.L., Price, P.B. and Walker, R.M. (1965b). Tracks of charged particles in solids. *Science.* **149**, 383-393.

Fleming, A., Summerfield, M.A., Stone, J.O.H., Fifield, L.K. and Cresswell, R.G. (1999). Denudation rates for the southern Drakensberg escarpment, SE Africa, derived from in-situ-produced cosmogenic 36Cl: initial results. *J. Geol. Soc. London.* **156**, 209-212.

Foster, D.A. and John, B.E. (1999). Quantifying tectonic exhumation in an extensional orogen with thermochronology: examples from the southern Basin and Range Province. In. *Exhumation Processes: Normal Faulting, Ductile Flow and Erosion.* (eds.: Ring, U.,

Brandon, M.T., Lister and G., Willet, S.D.). *Geological Society, London, Special Publications.* 343-364.

Fouché, J., Bate, K.J. and van der Merwe, R. (1992). Plate Tectonic setting of the Mesozoic Basins, southern offshore, South Africa: A Review. In. *Inversion tectonics of the Cape Fold Belt, Karoo and Cretaceous basins of southern Africa.* (eds.: de Wit, M.J. and Ransome, I.G.D.) *A.A. Balkema, Rotterdam.* 33-45.

Frimmel, H.E., Fölling, P.G. and Diamond, R. (2001). Metamorphism of the Permo-Triassic Cape Fold Belt and its basement, South Africa. *Mineralogy and Petrology*, **73** (4) 325-346.

Galbraith, R.F. and Laslett, G.M. (1993). Statistical models for mixed fission track ages. *Nucl. Tracks Radiat. Meas.* **21** (4), 459-470.

Galbraith, R.F. (1990). The radial plot: graphical assessment of spread in ages. *Nucl. Tracks. Radiat. Meas.* **17** (3) 207-214.

Gallagher, K. (1995). Evolving temperature histories from apatite fission-track data. *Earth and Planetary Science Letters.* **136**, 421-435.

Gallagher, K. and Brown, R. (1999a). Denudation and uplift at passive margins: the record on the Atlantic Margin of southern Africa. *Phil. Trans. R. Soc. Lond.* **357**, 835-859.

Gallagher, K. and Brown, R. (1999b). The Mesozoic denudation history of the Atlantic margins of southern Africa and southeast Brazil and the relationship to offshore sedimentation. In. *The Oil and Gas Habitats of the South Atlantic.* (eds.: Cameron, N.R., Bate, R.H. and Clure, V.S.) *Geological Society, London, Special Publications*, **153**, 41-53.

Gallagher, K., Brown, R. and Johnson, C. (1998). Fission track analysis and its applications to geological problems. *Annual Review of Earth and Planetary Science*, **26**, 519-572.

Gauffre, F.X. (1993). Biostratigraphy of the Lower Elliot Formation (Southern Africa), and preliminary results on the Maphutseng dinosaur (Saurischia: Prosauropoda) from the same formation of Lesotho. In. *The Nonmarine Triassic* (eds.: Lucas, S.G. and Morales, M.) *Bull. New Mexico Mus. Nat. Hist.*, **3**, 147-150.

Gilchrist, A.R., Henk, K. and Beaumont, C. (1994). Post-Gondwana geomorphic evolution of southwestern Africa: Implications for the controls on landscape development from observations and numerical experiments. *J. Geophys. Res.* **99** (B6). 12,211-12,228.

Gilchrist, A.R. and Summerfield, M.A. (1990). Differential denudation and flexural isostasy in formation of rifted-margin upwarps, *Nature*, **346**, 739-742.

Gleadow, A.J.W., Belton, D. X., Kohn, B.P. and Brown, R.W. (2002). Fission Track Dating of Phosphate Minerals and Thermochronology of Apatite. In. *Phosphates:*

Geochemical, Geobiological and Materials Importance, Reviews in Mineralogy and Geochemistry (eds.: Kohn, M.J., Rakovan, J. and Hughes, J.M.). **48** (16), 580-629.

Gleadow, A.J.W. and Fitzgerald, P.G. (1987). Uplift history and structure of the Transantarctic Mountains: new evidence from fission track dating of basement apatites in the Dry Valley area, southern Victoria Land. *Earth and Planetary Science Letters.* **82**, 1-14.

Gleadow, A.J.W., Duddy, I.R., Green, P.F. and Lovering, J.F. (1986). Confined fission track lengths in apatite: a diagnostic tool for thermal history analysis. *Contrib. Mineral Petrol.* **94**, 405-415.

Gleadow, A.J.W., Duddy, I.R. and Lovering, J.F. (1983). Fission track analysis: A new tool for the evaluation of thermal histories and hydrocarbon potential. *Aust. Petrol. Explor. Assoc. J.* **23**, 93-102.

Gleadow, A.J.W. and Duddy, I.R (1981). A natural long-term annealing experiment for apatite. *Nuclear Tracks.* **5**, 169-174.

Gough, D. I. (1963). Heat flow in the Southern Karoo. *Proc. Roy. Soc. London, Ser. A*, **272**, 207-230.

Gradstein, F.M., Ogg, J.G., Smith, A.G., Agterberg, F.P., Bleeker, W., Cooper, R.A., Davydov, V., Gibbard, P., Hinnov, L., House, M.R., Lourens, L., Luterbacher, H-P., McArthur, J., Melchin, M.J., Robb, L.J., Shergold, J., Villeneuve, M., Wardlaw, B.R., Ali, J., Brinkhuis, H., Hilgen, F.J., Hooker, J., Howarth, R.J., Knoll, A.H., Laskar, J., Monechi, S., Powell, J., Plumb, K.A., Raffi, I., Röhl, U., Sanfilippo, A., Schmitz, B., Shackleton, N.J., Shields, G.A., Strauss, H., Van Dam, J., Veizer, J., van Kolfschoten, Th. And Wilson, D. (2004). A Geologic Time Scale 2004. *Cambridge University Press*, ~500pp.

Gray, J., Theron, J.N. and Boucout, A.J. (1986). Age of the Cedarberg Formation, South Africa and early land plant evolution. *Geological Magazine.* **123** (4), 445-454.

Green, P.F. (2004). The importance of validating annealing models. *10th International Fission Track Dating and Thermochronology. 8-13th August, 2004, Amsterdam* (abstract). pp55.

Green, P.F. (1988). The relationship between track shortening and fission track age reduction in apatite: combined influences of inherent instability, annealing anisotropy, length bias and system calibration. *Earth and Planetary Science Letters.* **89**, 335-352.

Green, P.F. (1985). Comparison of zeta calibration baselines for fission-track dating of apatite, zircon and sphene. *Chemical Geology (Isotope Geoscience Section).* **58**, 1-22.

Green, P. F. (1981). A new look at statistics in fission track dating. *Nuclear Tracks.* **5**, 77-86.

Green, P.F. (1980). On the cause of shortening of spontaneous fission tracks in certain minerals. *Nucl. Tracks.* **4**, 91-100.

Green, P.F. Duddy, I.R. and Hegarty, K.A. (2002). Quantifying exhumation from apatite fission-track analysis and vitrinite reflectance data: precision, accuracy and latest results from the Atlantic margin of NW Europe. In. *Exhumation of the North Atlantic Margin: Timing, Mechanisms and Implications for Petroleum Exploration.* (eds.: Doré, A.G., Cartwright, J.A., Stoker, M.S., Turner, J.P. and White, N.). *Geological Society, London,* Special Publications, **196**, 331-354.

Green, P.F., Duddy, I.R., Laslett, G.M., Hegarty, K.A., Gleadow, A.J.W. and Lovering, J.F. (1989). Thermal annealing of fission tracks in apatite, 4. Quantitative modeling techniques and extension to geological timescales. *Chem. Geol. (Isot. Geosci. Sect.)* **79**, 155-182.

Green, P.F. Duddy, I.R., Gleadow, A.J.W., Tingate, P.R. and Laslett, G.M. (1986). Thermal annealing of fission tracks in apatite, 1. A qualitative description. *Chem. Geol. (Isot. Geosci. Sect.)* **59**, 237-253.

Green, P.F., Duddy, I.R., Gleadow, A.J.W. and Tingate, P.R. (1985). Fission-track annealing in apatite: track length measurements and the form of the Arrhenius plot. *Nucl. Tracks.* **10**, 323-328.

Gresse, P.G., Theron, J.N., Fitch, F.J. and Miller, J.A. (1992). Tectonic inversion and radiometric resetting of the basement in the Cape Fold Belt. In. *Inversion tectonics of the Cape Fold Belt, Karoo and Cretaceous basins of southern Africa* (eds.: de Wit, M.J. and Ransome, I.G.D.). *A.A. Balkema, Rotterdam.* 217-229.

Grist, A.M., Zentilli, M., Farley, K.A. (2004). Apatite Fission Track and (U-Th)/He thermal history modelling of the Nares Strait, Kane Basin, Smith Sound Region in eastern Arctic Canada and western Greenland. *10th International Fission Track Dating and Thermochronology. 8-13th August, 2004, Amsterdam* (abstract). pp.130.

Groenewald, G.H. and Kitching, J.W. (1995). Biostratigraphy of the *Lystrosaurus* Assemblage Zone. In. *Biostratigraphy of the Beaufort Group (Karoo Supergroup)* (ed.: Rubidge, B.S.). *SACS Biostratigraphic Series* **1**. 35-39.

Gurnis, M., Mitrovica, J.X., Ritsema, J. and van Heijst, H-J. (2000). Constraining mantle density structure using geological evidence of surface uplift rates: The cast of the African Superplume. *Geochemistry, Geophysics, Geosystems* 1.

Haddon, I.G. (2000). Kalahari Group Sediments. In. The *Cenozoic of Southern Africa.* (eds.: Partridge, T.C and Maud, R.R.) *Oxford University Press.* 173-181.

Hälbich, I.W., Fitch, F.J. and Miller, J.A. (1983). Dating the Cape orogeny. In. *Geodynamics of the Cape Fold Belt. Special Publication, Geological Society of South Africa.* (eds.: Söhnge, A.P.G and Hälbich, I.W.) **12**, 149-164.

Hammerschmidt, K., Wagner, G.A. and Wagner, M. (1984). Radiometric dating on research drill core Urach III: a contribution to its geothermal history. *Journal of Geophysics*. **54**, 97-105.

Haq, B.U., Hardenbol, J. and Vail, P.R. (1987). Chronology of fluctuating sea levels since the Triassic. *Science*. **235**, (4793), 1156-1167.

Hawkesworth, C., Kelley, S., Turner, S., le Roex, A. and Storey, B. (1999). Mantle processes during Gondwana break-up and dispersal. *Journal of African Earth Sciences*. **28** (1), 239-261.

Hawthorne, J.B. (1975). Model of a kimberlite pipe. In: *Physics and Chemistry of the Earth*. (eds.: Ahrens, L.H., Dawson, J.B., Duncan, A.R. and Erlank, A.J.). *Pergamon, Oxford*. **9**, 1-15.

Hurford, A.J. and Green, P.F. (1983). The zeta age calibration of fission-track dating: *Chemical Geology (Isotope Geoscience Section)*. **1**, 285-317.

Hurford, A.J. and Green, P.F. (1982). A users' guide to fission track dating calibration. *Earth and Planetary Science Letters*. **59**, 343-354.

Jelsma, H. and Smith, C. (2004). Geodynamic Setting of Kimberlites. AGU meeting, Montreal, May 2004.

Jelsma, H.A., de Wit, M.J., Thiart, C., Dirks, P., Viola, G., Basson, I.J. and Anckar, E. (2004). Preferential distribution along transcontinental corridors of kimberlites and related rocks of Southern Africa. *South African Journal of Geology*. **107**, (1/2) 301-324.

Jenkyns, H.C., Forster, A., Schouten, S. and Sinninghe Damste, J.S. (2004). High temperatures in the Late Cretaceous Arctic Ocean. *Nature*. **432**, 888-891.

Johnson, M.R. (1991). Sandstone petrography, provenance and plate tectonic setting in Gondwana context of the southeastern Cape-Karoo Basin. *South African Journal of Geology*. **94**, 137-154.

Johnson, M.R., van Vuuren, C.J., Visser, J.N.J., Cole, D.I., de Wickens, H., Christie, A.D.M. and Roberts, D.L. (1997). The Foreland Karoo Basin, South Africa. In. *African Basins. Sedimentary Basins of the World*. (ed. Selley, R.C.) **3**, 269-317.

Johnson, M.R. van Vuuren, C.J., Hegenberger, W.F., Rey, R. and U. Shoko (1996). Stratigraphy of the Karoo Supergroup in South Africa: an overview. *Journal of African Earth Sciences*, **23**, 3-15.

Jokat, W., Boebel, T., Koenig, M. and Meyer, U. (2003). Timing and Geometry of Early Gondwana break-up. *Journal of Geophysical Research*, **108**, (B9), 2428-2443.

Jones, M.Q.W. (2003). Thermal properties of stratified rocks from Witwatersrand gold mining areas. *J. S. Afr. Inst. Min. Met.*, **101**, 173-185.

Ketcham, R.A. (2004) HeFTy fission track software. *Unpublished.* Available from: ftp://ctlab.geo.utexas.edu/Ketcham/ft/

Ketcham, R.A., Donelick, R.A., and Donelick, M.B. (2000). AFTSolve: A program for multi-kinetic modeling of apatite fission-track data. *Geological Materials Research*, (2) 1.

Ketcham, R.A., Donelick, R.A. and Carlson, W.D. (1999). Variability of apatite fission-track annealing kinetics III: Extrapolation to geological time scales. *American Mineralogist.* **84**, 1235-1255.

King, L.C. (1963). *South African Scenery,* 3rd edn. Oliver and Boyd, U.K. 308pp.

King, L.C. (1962). *The Morphology of Earth.* Oliver and Boyd, White Plains, N.Y. 726 pp.

King, L.C. (1953). Cannons of landscape evolution. *Geol. Soc. Am. Bull.*, **64**, 721-752.

King, L.C. (1951). *South African Scenery,* 2nd edn. Oliver and Boyd, U.K. 379pp.

Kitching, J.W. (1995). Biostratigraphy of the *Cynognathus* Assemblage Zone. In. *Biostratigraphy of the Beaufort Group (Karoo Supergroup)* (ed. Rubidge, B.S.). *SACS Biostratigraphic Series*, **1**. 40-45.

Kohn, B.P., Belton, D.X., Brown, R.W., Gleadow, A.J.W., Green, P.F. and Lovering, J.F. (2003). Comment on: "Experimental evidence for the pressure dependence of fission track annealing in apatite" by A.S. Wendt et al. [Earth Planet. Sci. Lett. 201 (2002) 593-607]. *Earth and Planetary Science Letters.* **215**, 299-306.

Kooi, H. and Beaumont, C. (1994). Escarpment evolution on high-elevation rifted margins: Insights derived from a surface processes model that combines diffusion, advection, and reaction. *Journal of Geophysical Research.* **99**, B6, 12211-12228.

Kramers, J.D., Kreissig, K. and Jones, M.Q.W. (2001). Crustal heat production and style of metamorphism: a comparison between two Archean high grade provinces in the Limpopo Belt, southern Africa. *Precambrian Research.* **112**, 149-163.

LaBrecque, J.L. and Barker, P.F. (1981). The age of the Weddell basin. *Nature,* **290**, 489-492.

Lamb, S. and Davis, P. (2003). Cenozoic climate change as a possible cause for the rise of the Andes. *Nature.* **425**, 792-797.

Laslett, G.M., Green, P.F., Duddy, I.R. and Gleadow, A.J.W. (1987). Thermal annealing of fission tracks in apatite 2. A Quantitative Analysis. *Chemical Geology (Isotope Geoscience Section)*, **65**, 1-13.

Laslett, G.M., Gleadow, A.J.W. and Duddy, I.R. (1984). The relationship between fission track length and density in apatite. *Nuclear Tracks*. **9**, 29-38.

Laslett, G.M., Kendall, W.S., Gleadow, A.J.W. and Duddy, I.R. (1982). Bias in measurement of fission track length distributions. *Nuclear Tracks*. **6**, 79-85.

Lawver, L.A., Gahagan, L.M., and Dalziel, I.W.D. (1999). A Tight fit-Early Mesozoic Gondwana: A Plate Reconstruction Perspective. In. *Origin and Evolution of Continents: Proceedings of the International Symposium "Origin and Evolution of Continents," 13-14 October, 1997, Tokyo, Memoirs of National Institute of Polar Research, Special Issue.* (eds.: Motoyoshi, Y. and Shiraishi, K.). **53**, 214-229.

Leith, M.J. (1969). Well Completion Report of KW1/67. *Southern Oil Exploration Corporation (Pty) Ltd*. 51pp.

Leopold, L.B. (2004). Geomorphology: A Sliver Off the Corpus of Science. *Ann. Rev. Earth Planet. Sci.* **32**, 1-12.

Light, M.P.R., Maslanyj, M.P., Greenwood, R.J. and Banks, N.L. (1993). Seismic sequence stratigraphy and tectonics offshore Namibia. In *Tectonics and Seismic Stratigraphy.* (eds.: Williams, G.D. and Dobb, A.). *Geological Society, London, Special Publications.* **71**, 163-191.

Light, M.P.R., Maslanyj, M.P. and Banks, N.L. (1992). New geophysical evidence for extensional tectonics on the divergent margin offshore Namibia. In *Magmatism and the Causes of Continental Break-up.* (eds.: Storey, B.C., Alabaster, T. and Pankhurst, R.J.) *Geological Society, London, Special Publications.* **68**, 257-270.

Lithgow-Bertelloni, C. and Silver, P. (1998). Dynamic topography, plate driving forces and the African superswell. *Nature*. 395, 269-272.

Lorenzo, J.M. and Mutter, J.C. (1988). Seismic stratigraphy and tectonic evolution of the Falklands/ Malvinas Plateau. *Revista Brasileira de Geociências.* **18** (2) 191-200.

Martin, A.K. (1987). Comparison of sedimentation rates in the Natal Valley, south-west Indian Ocean, with modern sediment yields in east coast rivers of Southern Africa. *South African Journal of Science.* 83, 716-725.

Martin, A.K. and Hartnady, C.J.H. (1986). Plate tectonic development of the southwest Indian Ocean- a revised reconstruction of east Antarctica and Africa. *Journal of Geophysical Research.* **91**, 4767-4786.

Martin, A.K., Hartnady, C.J.H. and Goodlad, S.W. (1981). A revised fit of South America and South Central Africa. *Earth and Planetary Science Letters.* **54**, 293-305.

Martini, J.E.J., Vorster, C.J., Oosterhuis, W.R. and Wolmarans, L.G. (2001). Digital metallogenic map of South Africa and the kingdoms of Lesotho and Swaziland 2001: Scale 1: 1 000 000. *Council for Geoscience.*

Maslanyj, M.P., Light, M.P.R., Greenwood, R.J. and Banks, N.L. (1992). Extension tectonics offshore Namibia and evidence for passive rifting in the South Atlantic. *Marine and Petroleum Geology*. **9**, 590-601.

Matthews, P.E. (1978). An examination of Steenberg's Law using river-pebble measurements from the Natal Drakensberg. *Petros*. **8**, 26-33.

Maud, R.R. and Botha, G.A. (2000). Deposits of the South Eastern and Southern Coasts. In. *The Cenozoic of Southern Africa.* (Partridge, T.C. and Maud, R.R.) *Oxford University Press.* 19-31.

McCarthy, T.S., Moon, B.P. and Levin, M. (1985). Geomorphology of the western Bushmanland Plateau, Namaqualand, South Africa. *S. Afr. Geog. J.* **67** (2) 160-178.

McCourt, S. Hilliard, P. and Armstrong, R.A. (2000). SHRIMP U-Pb zircon geochronology of granitoids from the western margin of the Kaapvaal Craton: implications for crustal evolution in the Neoarchean. In. *27th Geocongress, Geol. Soc. S. Afr., Stellenbosch. J. Afr. Earth Sci.* (eds.: Kisters, A.F.M. and Thomas, R.J.), **31**, 1A, 48.

McLachlan, I.R. and McMillan, I.K. (1976). Review and stratigraphic significance of southern Cape Mesozoic paleontology. *Transactions of the Geological Society of South Africa. Special Publication.* **79**, 197-212.

McMillan, I.K. (2003). Foraminiferally defined biostratigraphic episodes and sedimentation pattern of the Cretaceous drift succession (Early Barremian to Late Maastrichtian) in seven basins on the South African and southern Namibian continental margin. *South African Journal of Science*. **99**, 537-576.

McMillan, I.K., Brink, G.J., Broad, D.S. and Maier, J.J. (1997). Late Mesozoic Sedimentary Basins Off the South Coast of South Africa. In *African Basins. Sedimentary Basins of the World,* (ed.: Selley, R.C.) *Elsevier Science B.V. Amsterdam.* **3**, 319-376.

Meyers, P.A. (2001). Miocene-Pleistocene sedimentary record of carbon burial under the Benguela Current upwelling system, southwestern margin of Africa. In. *Proceedings of the Ocean Drilling Program. Scientific Results.* (eds.: G. Wefer, W. Berger, and C. Richter). *College Station*, **175**, 1-19.

Miller, K.G. and Fairbanks, R.G. (1985). Cainozoic 18O record of climate and sea level. *South African Journal of Science*. **81**, 248-249.

Molnar, P. (2003). Nature, nurture and landscape. *Nature.* 426, 612-614.

Molnar, P. and England, P. (1990). Late Cenozoic Uplift of Mountain Ranges and Global Climate Change: Chicken or Egg? *Nature*. **346**, 2934.

Naeser, C.W. and Faul, H. (1969). Fission track annealing in apatite and sphene. *Journal of Geophysical Research*. **74**, 705-710.

Naeser, C.W. (1967). The use of apatite and sphene for fission track age determinations. *Bulletin of the Geological Society of America.* **78**, 1523-1526.

Nyblade, A.A. and Robinson, S.W. (1994). The African Superswell. *Geophysical Research Letters.* **21**, 765-768.

Partridge, T.C. (1998). Of diamonds, dinosaurs and diastrophism: 150 million years of landscape evolution in southern Africa. *South African Journal of Geology.* **101**, 167-185.

Partridge, T.C. (1997). Late Neogene Uplift in Eastern and Southern Africa and Its Paleoclimatic Implications. In. *Tectonic Uplift and Climate Change.* (ed.: Ruddiman, W.F.). *Plenum Press, New York*, 63- 86.

Partridge, T.C., and Maud, R.R. (1989). *S. Afr. J. Sci.* **85**, 428.

Partridge, T.C. and Maud, R.R. (1988). The geomorphic evolution of southern Africa: A comparative review. In. *Geomorphological Studies in Southern Africa.* (eds.: Dardis, G.F. and Moon, B.P). *A. Balkema, Rotterdam*, 5-15.

Partridge, T.C. and Maud, R.R. (1987). Geomorphic evolution of southern Africa since the Mesozoic. *S. Afr. J. Geol.*, **90**, 179-208.

Pether, J., Roberts, D.L. and Ward, J.D. (2000). Deposits of the West Coast. In. *The Cenozoic of southern Africa.* (eds.: Partridge, T.C. and Maud, R.R.). 33-54.

Petroleum Agency SA. (2000). *Petroleum Exploration Opportunities.* 24pp.

Poulsen, C.J. (2004). A balmy Arctic. *Nature.* **432**, 814-815.

Price, P.B. and Walker, R.M. (1963). Fossil tracks of charged particles in mica and the age of minerals. *Journal of Geophysical Research.* **68**, 4847-4862.

Raab, M.J., Brown, R.W., Gallagher, K., Weber, K., Gleadow, A.J.W. (2004). The post break-up denudation chronology of Namibia's passive Margin. *10th International Fission Track Dating and Thermochronology. 8-13th August, 2004, Amsterdam* (abstract). pp. 80.

Raab, M.J., Brown, R.W., Gallagher, K., Carter, A., Weber, K. (2002). Late Cretaceous reactivation of major crustal shear zones in northern Namibia: constraints from apatite fission track analysis. *Tectonophysics.* **349,** 75-92.

Raymo, M.E. and Ruddiman, W.F. (1992). Tectonic Forcing of Late Cenozoic Climate. *Nature.* **359**, 117-122.

Reeves, C. (1999). Aeromagnetic and gravity features of Gondwana and their relation to continental break-up: more pieces, less puzzle. *Journal of African Earth Sciences.* **28** (1), 263-277.

Reeves, C. and de Wit, M.J (2000). Making ends meet in Gondwana: retracing the transforms of the Indian Ocean and reconnecting continental shear zones. *Terra Nova.* **12**, 272-208.

Reeves, C. and de Wit, M.J. (1998). Gondwana re-assembly by retracing the transforms of the Indian Ocean. *Journal of African Earth Sciences.* **27**, 156-158.

Reid, D.L., Erlank, A.J. and Rex, D.C. (1991). Age and correlation of the False Bay dolerite dyke swarm, south- western Cape, Cape Province. *South African Journal Geology.* **94**, 155-158.

Reiners, P.W., Ehlers, T.A., Mitchell, S.G. and Montgomery, D.R. (2003). Coupled spatial variations in precipitation and long-term erosion rates across the Washington Cascades. *Nature.* **426**, 645-647.

Renne, P.R., Glen, J.M., Milner, S.C. and Duncan, A.R. (1996). Age of Etendeka flood volcanism and associated intrusions in southwestern Africa. *Geology.* **24**, 659-662.

Rhodehamel, E.C. (1977). Sandstone porosities. In *Geological Studies on the COST B-2 Well, U.S. Mid-Atlantic Outer Continental Shelf Area.* (P.A. Scholle, ed.), *U.S. Geol. Surv. Circ.* 750, 23.

Riley, T.R. and Knight, K.B. (2001). Review: Age of pre-break-up Gondwana magmatism. *Antarctic Science.* **13** (2) 99-110.

Robson, S. and Dingle, R.V. (1986). A GLORIA traverse over the marginal fracture zone and continental margin of SE Africa. *Marine Petroleum Geology.* **3**, 31-36.

Rogers, J. (1980). First report on the Cenozoic sediments between Cape Town and Eland's Bay. *Rep. Geol. Surv. S. Afr.*

Roux, J. (1997). Potential outlined in Southern Outeniqua Basin off S. Africa. *Oil and Gas Journal.* July 21.

Rozendaal, A., Gresse, P.G., Scheepers, R. and Le Roux, J.P. (1999). Neoproterozoic to Early Cambrian Crustal Evolution of the Pan-African Saldania Belt, South Africa. *Precambrian Research.* **97** (3-4), 303-323.

Rust, D.J. and Summerfield, M.A. (1990). Isopach and borehole data as indicators of rifted margin evolution in southwestern Africa. *Mar. Pet. Geol.* **7**, 277-287.

Smith, R.M.H. (1990). A review of stratigraphy and sedimentary environments of the Karoo Basin of South Africa. *Journal of African Earth Sciences.* **10** (1/2), 117-137.

Smith, R.M.H. (1986). Crater lakes in the age of dinosaurs. *Sagittarius, South African Museum*, 1 (1).

Stankiewicz, J. and de Wit, MJ. (2005a). The east flowing Congo River and implications for the evolution of African river basins. *Journal of African Earth Sciences* (submitted, August 2004).

Stankiewicz, J and de Wit, MJ. (2005b). Fractal river basins of southern Africa. *South African Journal of Geology* (submitted, August 2004).

Stankiewicz, J. and de Wit, MJ. (2005c). River networks of southern Africa -Scaling laws governing their geometry and deviations from scaling. *G-Cubed -Geophysics, Geochemistry and Geosystems.* (submitted January 2005).

Steckler, M.S. (1985). Uplift and extension at the Gulf of Suez: indications of induced mantle convection. *Nature.* **317**, 135-139.

Steckler, M.S. and Watts, A.B. (1978). Subsidence of the Atlantic-type continental margin off New York. *Earth and Planetary Science Letters*, **41**, 1-13.

Stephenson, J.A., Gallagher, K., Holmes, C. (2004). The influence of uncertainties in annealing algorithms on thermal history modelling. *10th International Fission Track Dating and Thermochronology. 8-13th August, 2004, Amsterdam* (abstract). pp 49.

Stern, C.R. and de Wit, M.J. (2003). Rocas Verdes ophiolites, southernmost South America: remnants of progressive stages of development of oceanic-type crust in a continental margin back-arc basin. In *Ophiolites in Earth History.* (eds.: Delik, Y. and Robinson, P.T.) *Geological Society of London, Special Publication.* **218**, 665-683.

Stevenson, I.R. and McMillan, I.K. (2004). Incised valley fill stratigraphy of the Upper Cretaceous succession, proximal Orange Basin, Atlantic margin of southern Africa. *Journal of the Geological Society of, London.* **161**, 185-208.

Streel, M. and Theron, J.N. (1999). The Devonian-Carboniferous boundary in South Africa and the age of the earliest episode of Dwyka glaciation: New palynological result. *Episodes.* **22**, 41-44.

Storey, B.C. (1995). The role of mantle plumes in continental breakup: case histories from Gondwanaland. *Nature.* **377**, 301-308.

Summerfield, M.A. (1996). Tectonics, geology, and long-term landscape development. In. *The Physical Geography of Africa.* (eds.: Adams, W.M., Goudie, A.S. and Orne, A.R.) *Oxford University Press, New York.* 1-17.

Tinker, J.H. (2001) Stratigraphic and structural interpretation of seismic reflection data across selected sections of the Kaapvaal Craton. *MSc thesis (unpubl.)* Univ. of Cape Town, South Africa.

Tinker, J.H., de Wit, M.J., Brown, R.W. and Raza, A. (2004). Apatite fission track analysis in South Africa reveals that the Cape Fold Belt was exhumed in the mid-

Cretaceous. *10th International Fission Track Dating and Thermochronology. 8-13th August, 2004, Amsterdam* (abstract). pp168.

Tinker, J.H., de Wit, M.J. and Grotzinger, J. (2002). Seismic Stratigraphic Constraints on Neoarchean- Paleoproterozoic Evolution of the Western Margin of the Kaapvaal Craton, South Africa. *South African Journal of Geology*, **105** (2), 107-134.

Tolan, T.L., Reidel, S.P., Beeson, M.H., Anderson, J.L., Fecht, K.R. and Swanson, D.A. (1989). Revisions to the estimates of the aerial extent and volume of the Columbia River Basalt Group. In. *Volcanism and Tectonism in the Columbia River Flood-Basalt Province, Special Paper 239.* (eds.: Reidel, S.P. and Hooper, P.R.), *Geological Society of America, Boulder*, 1-20.

Turner, B.R. (1999). Tectonostratigraphic development of the Upper Karoo foreland basin: orogenic unloading versus thermally-induced Gondwana rifting. *Journal of African Earth Sciences.* **28** (1) 215-238.

Turner, B.R. (1986). Tectonic and climatic controls on continental depositional facies in the Karoo Basin of northern Natal, South Africa. *Sedimentary Geology.* **46**, 231-257.

Van der Beek, P., Summerfield, M.A., Braun, J., Brown, R.W. and Fleming, A. (2002). Modeling postbreakup landscape development and denudation history across the southeast African (Drakensberg Escarpment) margin. *Journal of Geophysical Research.* **107** (B12) 1-16.

Van der Merwe, R. and Fouche, J. (1992). Inversion tectonics in the Bredasdorp Basin, offshore South Africa. In. *Inversion tectonics of the Cape Fold Belt, Karoo and Cretaceous basins of southern Africa.* (eds.: de Wit, M.J. and Ransome, I.G.D.) *A.A. Balkema, Rotterdam.* 49-59.

Van der Wateren, F.M., Dunai, T.J., 2001, Late Neogene passive margin denudation history- cosmogenic isotope measurements from the central Namib desert. *Global and Planetary Change.* **30** (3/4) 271-307.

Viljoen, J.H.A. (1992). The stratigraphy of the Heidelberg/ Riversdale Mesozoic Basin. In. *Inversion tectonics of the Cape Fold Belt, Karoo and Cretaceous basins of southern Africa.* (eds.: de Wit, M.J. and Ransome, I.G.D.) *A.A. Balkema, Rotterdam.* 77-84.

Visser, J.N.J. (1992). Basin tectonics in southwestern Gondwana during the Carboniferous and Permian. In. *Inversion tectonics of the Cape Fold Belt, Karoo and Cretaceous basins of southern Africa.* (eds.: de Wit, M.J. and Ransome, I.G.D.) *A.A. Balkema, Rotterdam.* 109-116.

Visser, J.N.J (1984). A review of the Stormberg Group and Drakensberg volcanics in Southern Africa. *Paleontologicia Africana.* **25**, 5-27.

Wagner, G.A., Coyle, D.A., Duyster, J., Henjes-Kunst, F. and Peterek, A. (1997). Post-Variscan thermal and tectonic evolution of the KTB site and its surroundings. *Journal of Geophysical Research*. **102**, 18221-18232.

Wagner, G.A. (1968). Fission track dating of apatites. *Earth and Planetary Science Letters*. **4**, 411-415.

Wefer, G., Berger, W.H., and Richter, C. *et al.* (1998). Proceedings of Ocean Drilling Program, Initial Reports **175**, College Station, Texas.

Weigelt, E. and Uenzelmann-Neben, G. (2004). Sediment deposits in the Cape Basin: Indications for shifting ocean currents? *AAPG Bulletin*. **88** (6), 765-780.

Wellington, J.H. (1955). Southern Africa: A Geographical Study. Volume 1: Physical Geography. *Cambridge University Press. Cambridge*, 528pp.

Wendt, A.S., Vidal, O., Chadderton, L.T. (2002). Experimental evidence for the pressure dependence of fission track annealing in apatite. *Earth and Planetary Science Letters*. **201**, 593-607.

White, R. and McKenzie, D. (1989). Magmatism at rift zones: The generation of volcanic continental margins and flood basalts. *J. Geophys. Res.*, **94**, 7685-7729.

Wilson, P.A. and Norris, R.D. (2001). Warm tropical ocean surface and global anoxia during the mid-Cretaceous period. *Nature*. **412**, 425-429.

Wobus, C.W., Hodges, K.V., Whipple, K.X. (2003). Has focused denudation sustained active thrusting at the Himalayan topographic front? *Geology*. **31** (10) 861-864.

Zawada, P.K. (1988). Trace elements as possible palaeosalinity indicators for the Ecca and Beaufort Group mudrocks in the southwestern Orange Free State. *South African Journal of Geology*. **91** (1), 18-26.

Appendix A: Geological legend (for figure 1.1, in chronological order, from Martini *et al.*, 2001)

Appendix B: Zeta Calibration

Table B-1: Zeta Calibration

Sample	Lu-364		Lu-564		Mu-98		Weighted Mean	
	zeta	error (±)	zeta	error (±)	zeta	error (±)	zeta	error (±)
Fish Canyon	316.99	16.87	335.05	32.0	450.29	42.57	336.37	9.762
	326.43	18.4	381.99	43.76	322.33	31.13		
	401.98	38.74	340.76	34.77	384.15	38.21		
	375.24	38.01	306.81	37.31	355.07	34.35		
	305.65	20.24						
Durango	329.11	19.07	441.35	32.63	440.27	34.3	389.56	13.35
	347.22	32.16	337.17	25.99	442.51	27.33		
	397.72	21.22	404.57	22.05	438.34	30.12		
			421.21	25.67	439.85	32.64		
			343.68	24.59				
Mount Dromedary	436.6	26.38	496.7	37.34	411.87	24.16	403.52	18.03
	496.26	39.11	414.48	27.94	352.91	22.22		
	478.03	35.94	372.6	25.51				
			344.28	23.1				
						Zeta	362.70	20.71

Table B-2: Track length Measurements

Sample	Mean Length (μm)	Error (± μm)	Std Dev. (μm)
Fish Canyon	14.95	0.13	1.27
Durango	14.37	0.11	0.98
Mt Dromedary	14.196	0.109	1.087

13 samples of unknown age were counted as well as 3 of unknown length measurements.

Appendix C: Radial plots and track length histograms

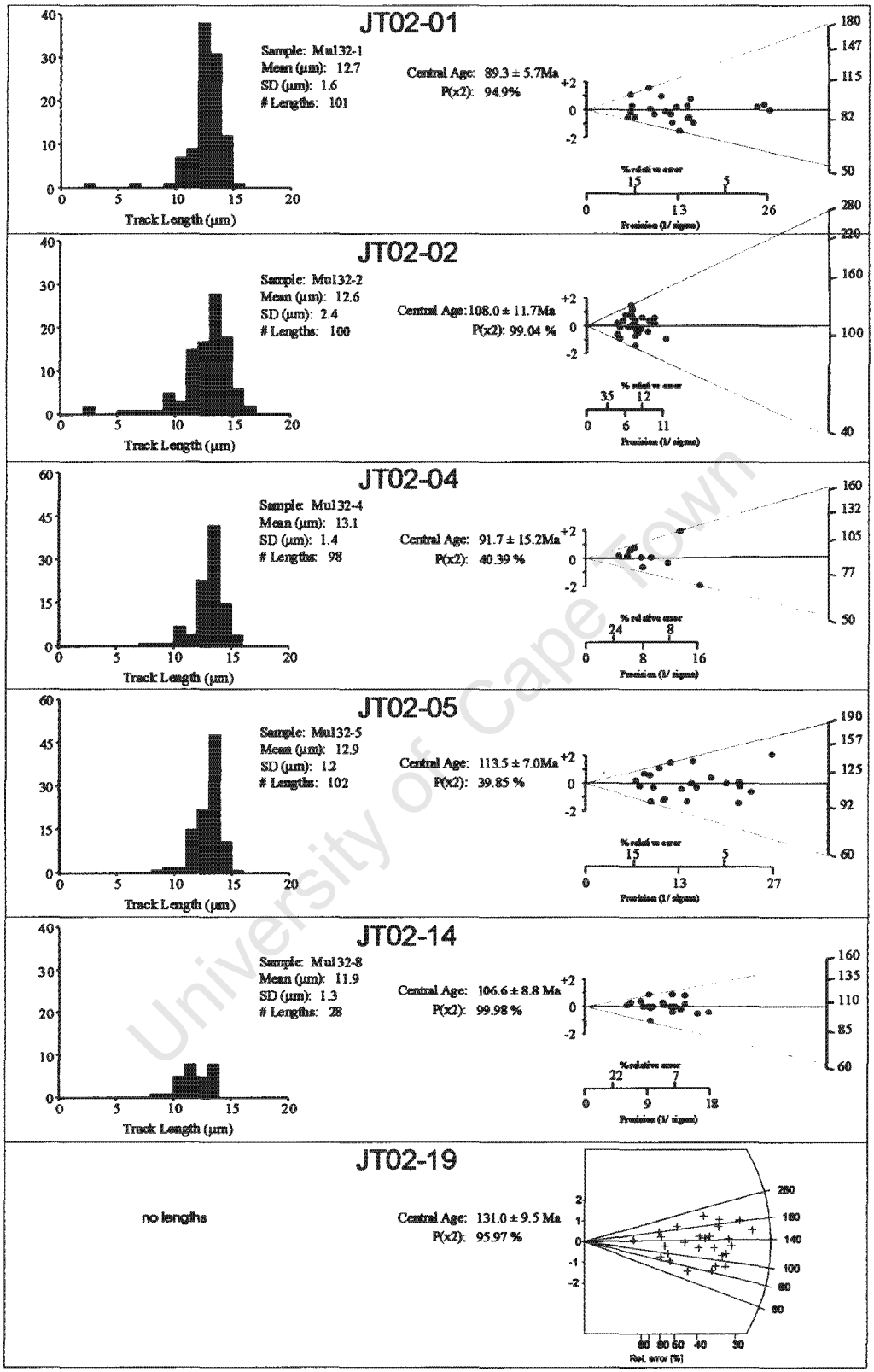

Figure C-1a to j: Radial plots of showing distribution of single grain ages, and histograms showing track length distributions of the borehole and outcrop samples. For each sample, the central age, chi^2 (%), mean track length, standard deviation on track length distribution and number of track lengths measured are given.

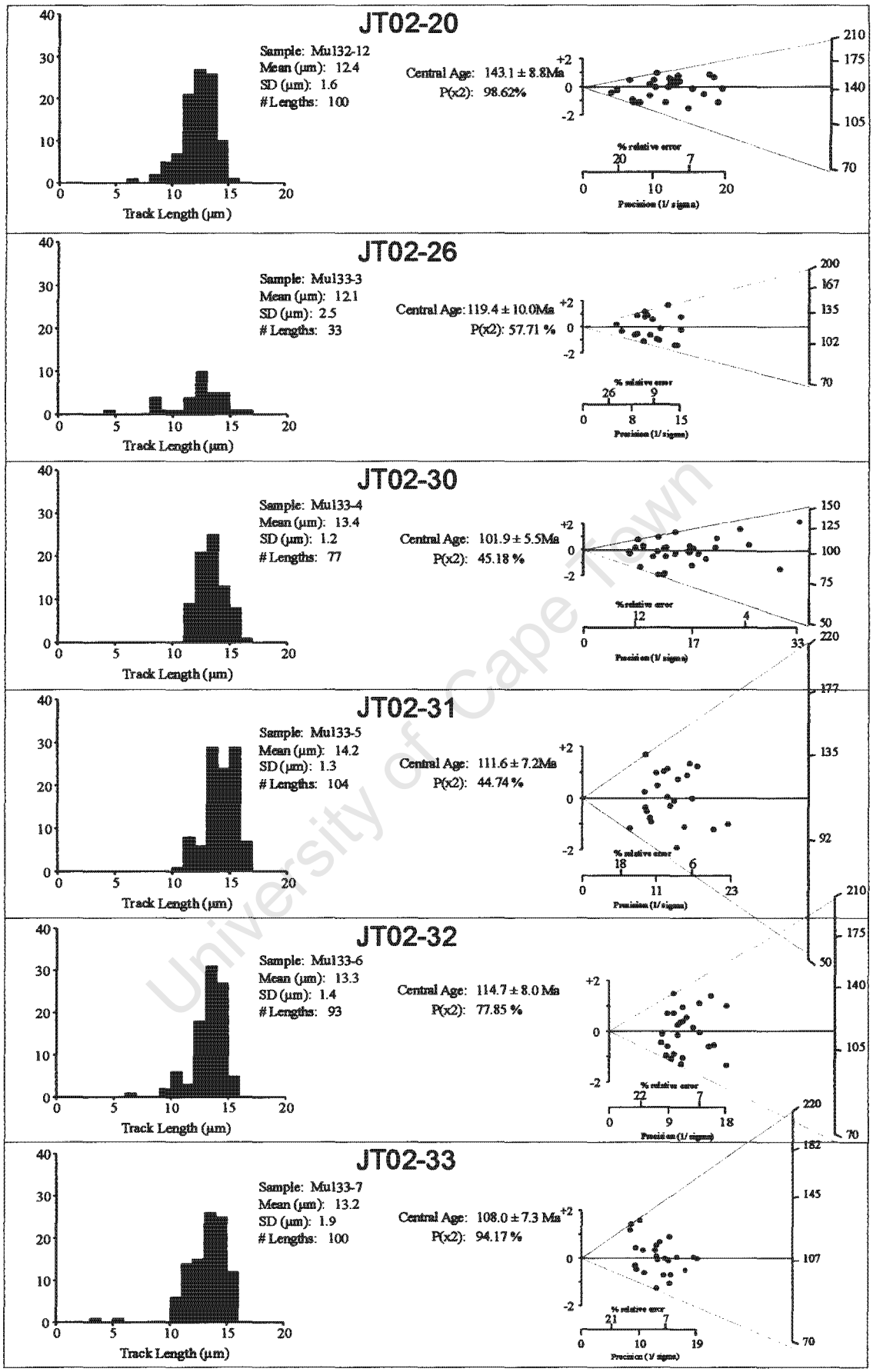

Figure C-1b: Outcrop ages and track length distributions (continued).

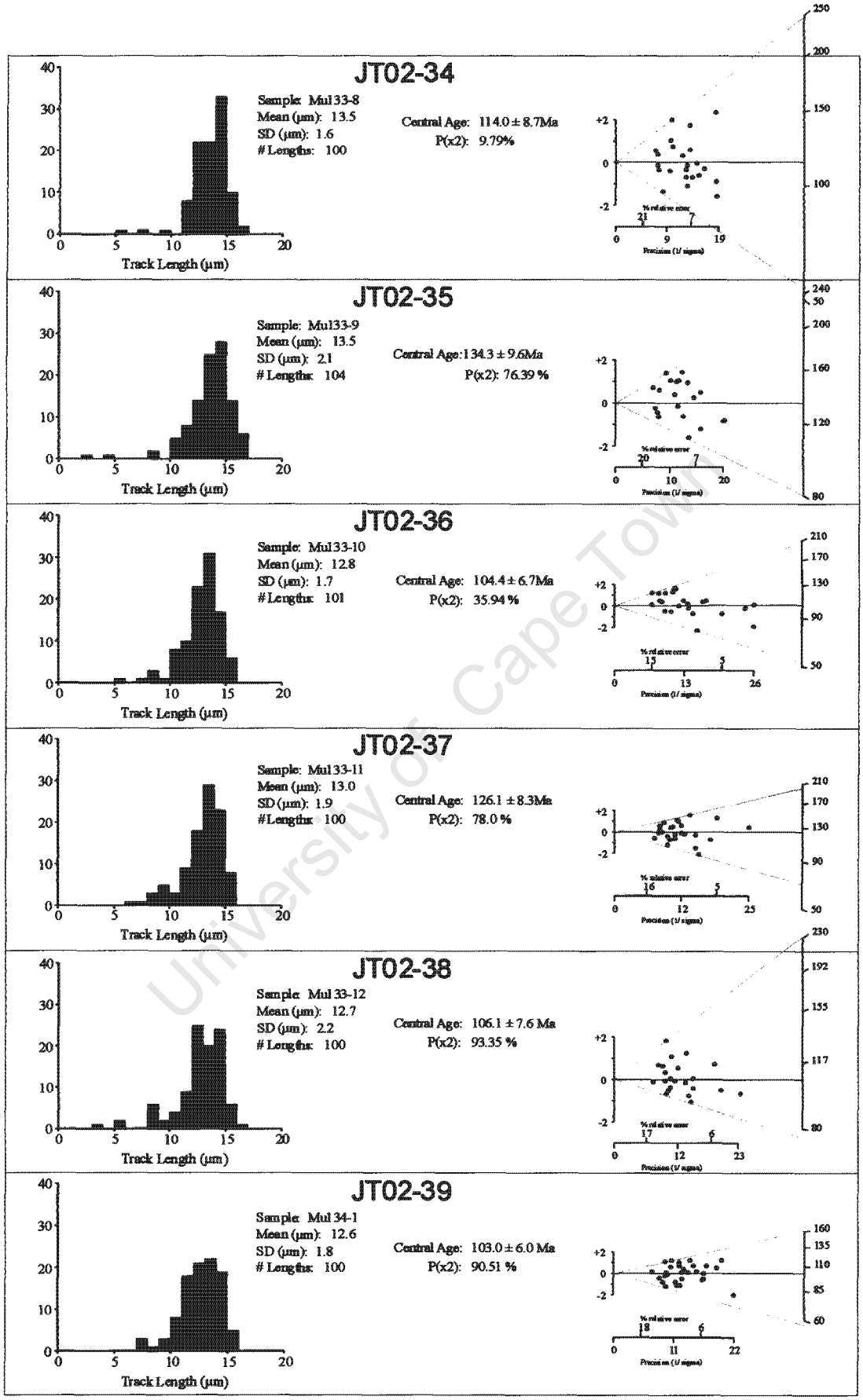

Figure C-1c: Outcrop ages and track length distributions (continued).

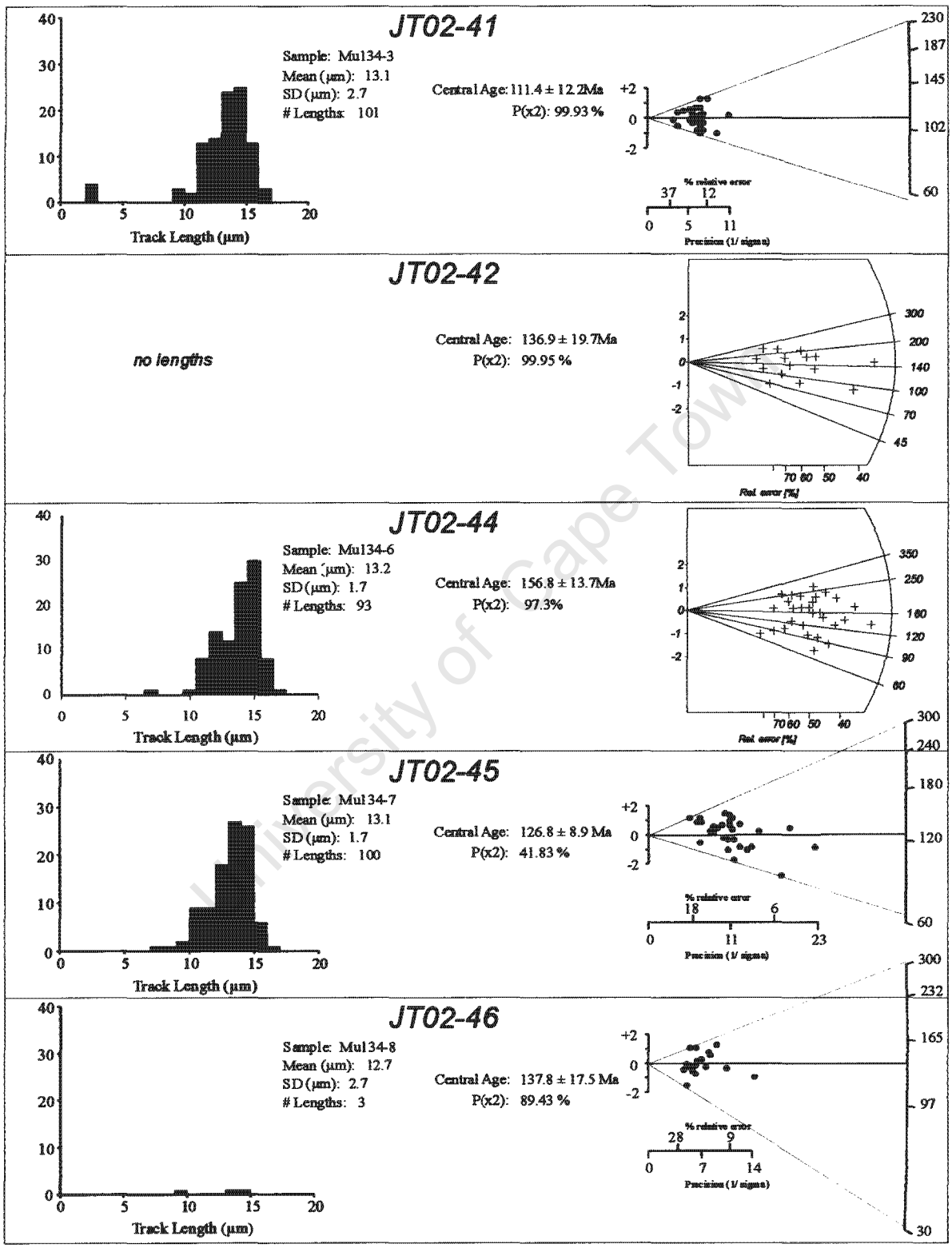

Figure C-1d: Outcrop ages and track length distributions (continued).

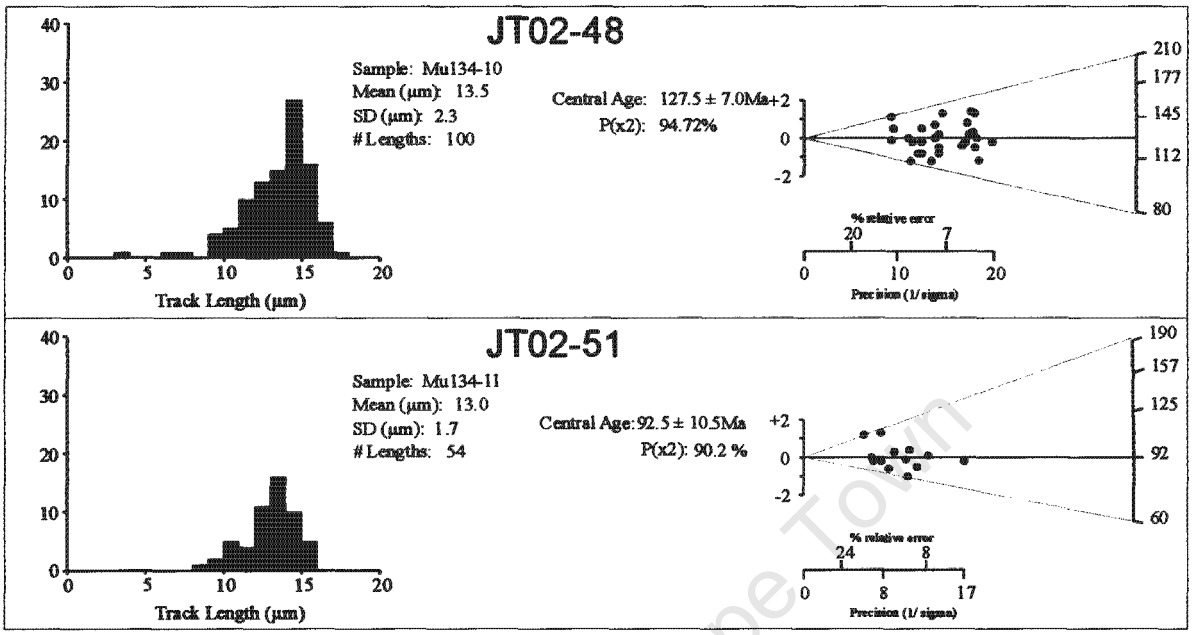

Figure C-1e: Outcrop ages and track length distributions (continued).

Borehole SA1/66 (a)

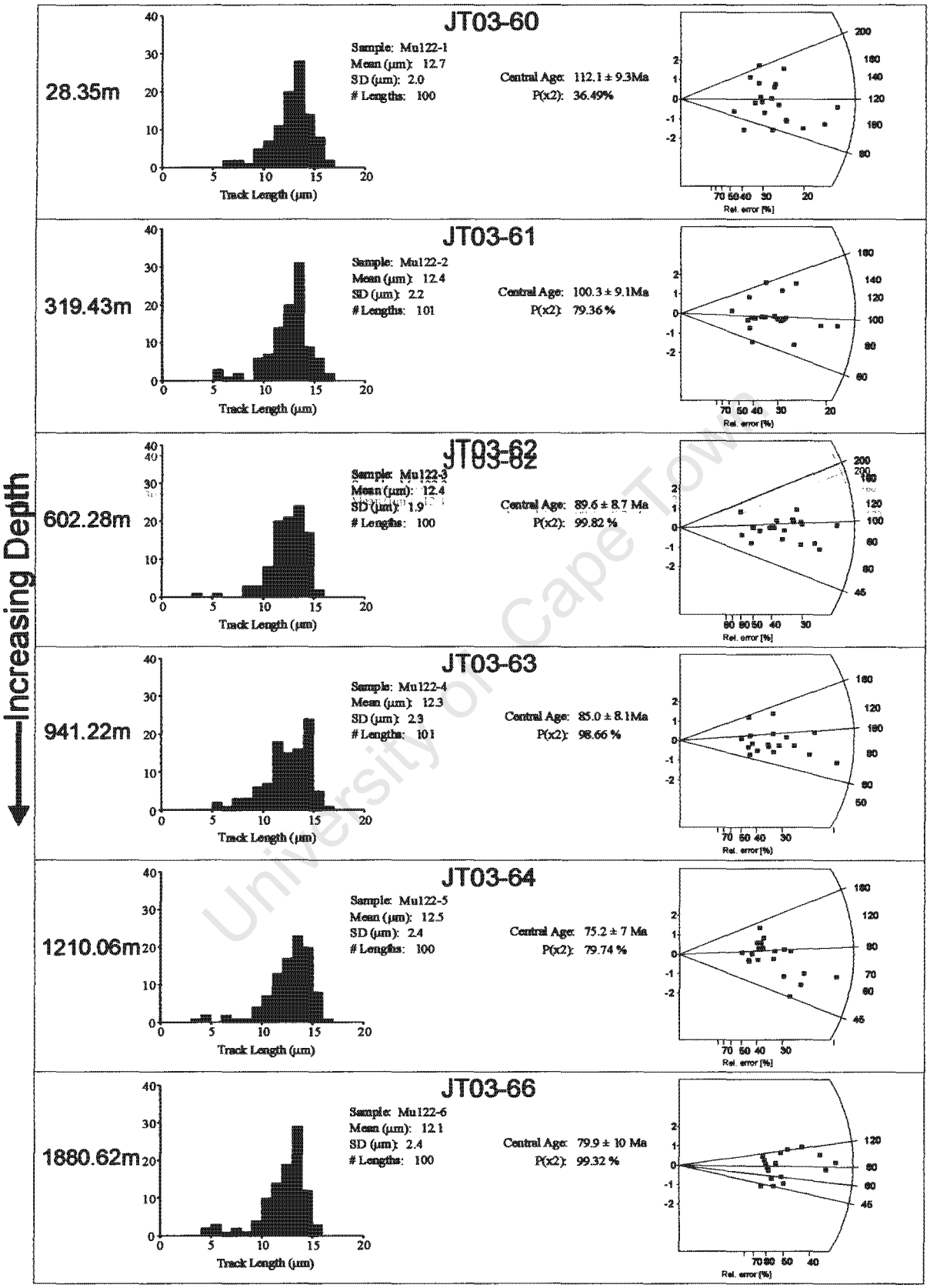

Figure C-1f: Borehole SA1/66 (upper ~1880 m)

Borehole SA1/66 (b)

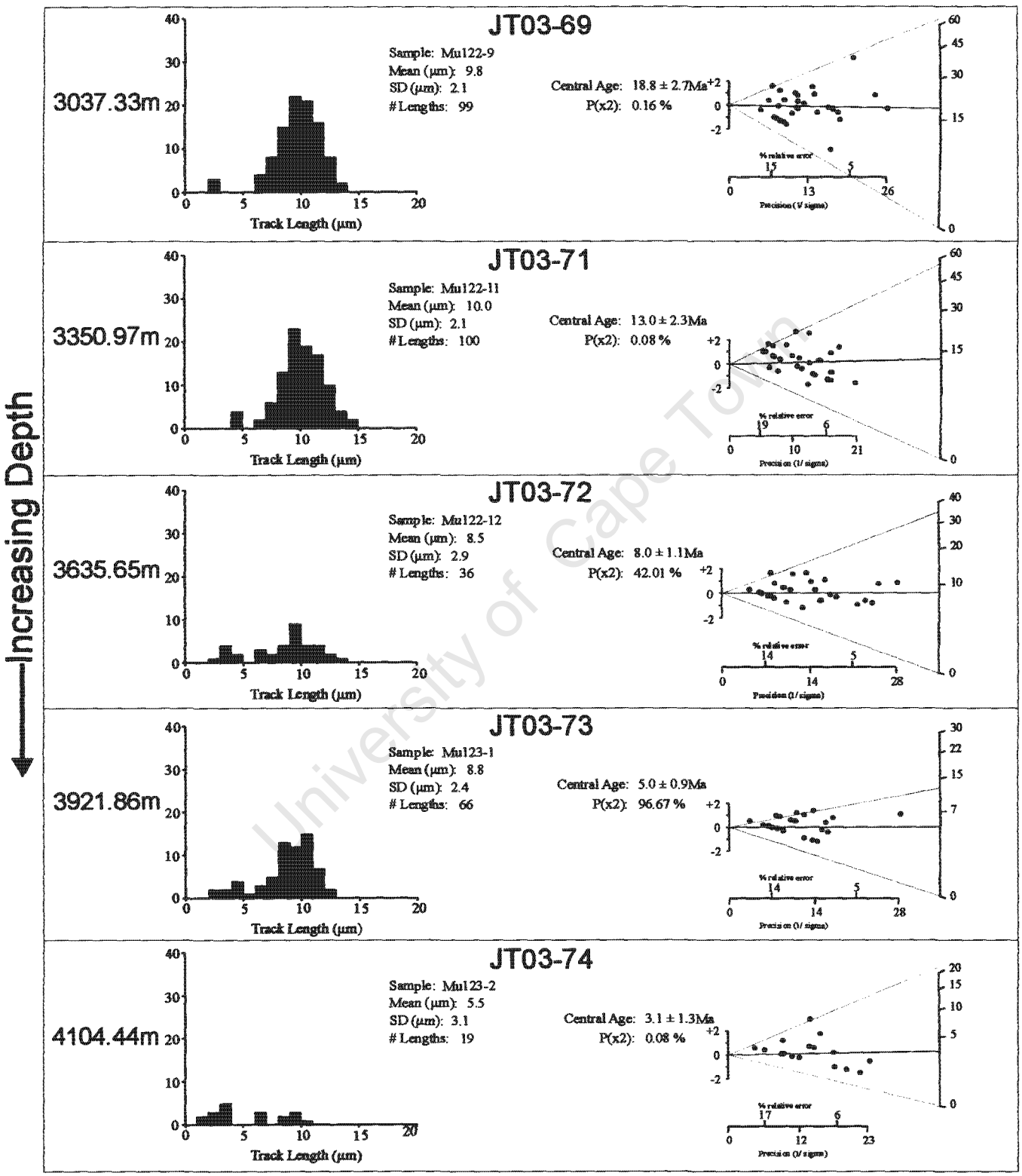

Figure C-1g: Borehole SA1/66 (to ~ 4100 m)

Borehole KW1/67 (a)

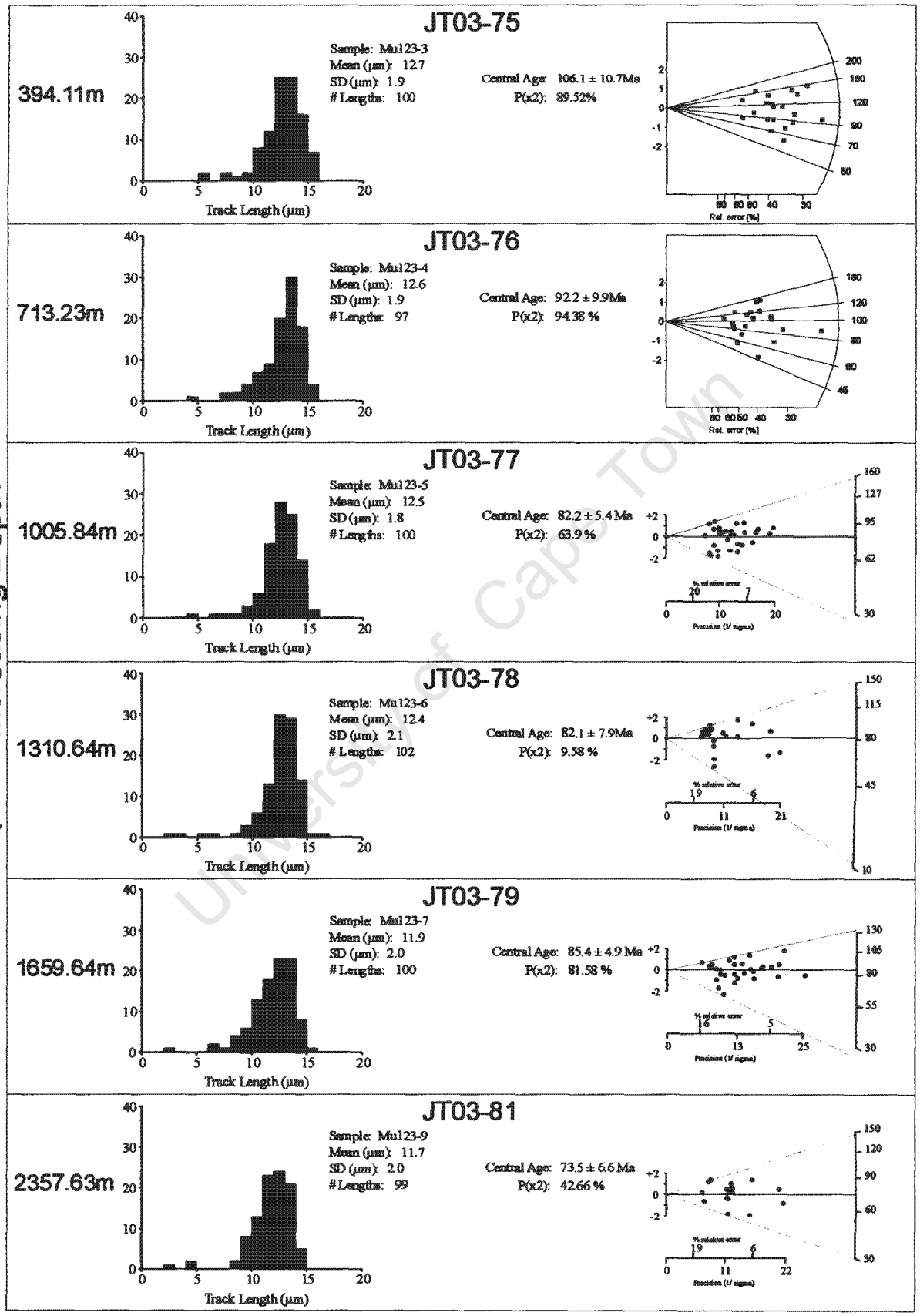

Figure C-1h: Borehole KW1/67 (upper ~2350 m).

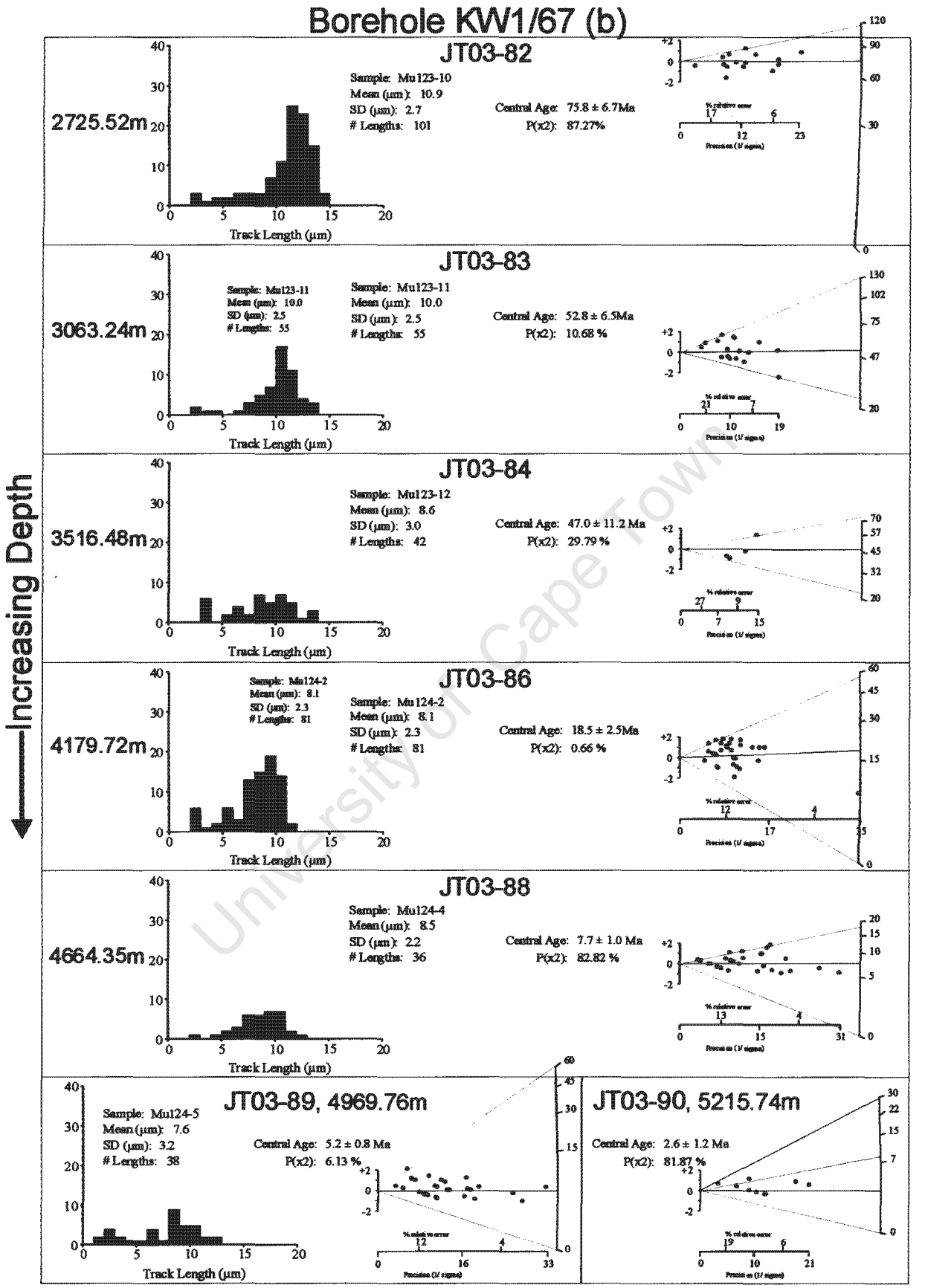

Figure C-1i: Borehole KW1/67 (to ~5210 m)

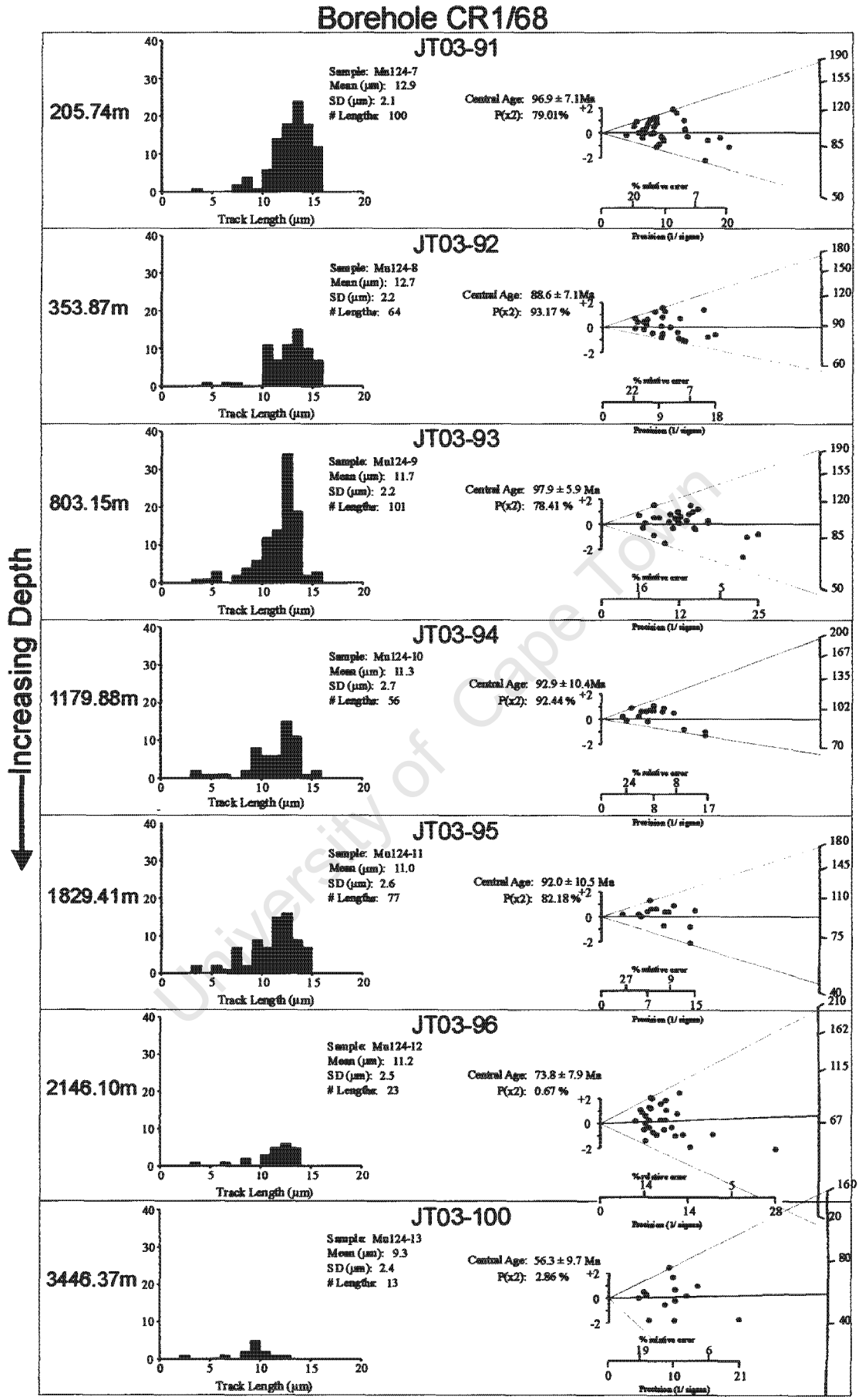

Figure C-1j: Borehole CR1/68 (to ~3440 m).

Appendix D: Sample locations

Table D-1: Locations of all outcrop samples (in degrees). *= samples from which a fission track age was measured.

Sample Number	Latitude	Longitude
JT0201 *	33.39732	22.20072
JT0202 *	33.42906	22.25193
JT0203	33.46732	22.25581
JT0204 *	33.46415	22.2539
JT0205 *	33.42154	22.24128
JT0206	33.35225	22.04571
JT0207	33.35224	22.04526
JT0208	33.34928	22.04791
JT0209	33.32847	22.04206
JT0210	33.41551	21.40336
JT0211	33.4306	21.4729
JT0212	34.18044	21.98289
JT0213	34.16196	22.09363
JT0214 *	34.00468	22.55245
JT0215	33.91889	22.40957
JT0216	33.89802	22.40224
JT0217	33.87756	22.3863
JT0218	33.83216	22.34946
JT0219 *	33.78127	22.342
JT0220 *	33.69149	22.27118
JT0221	33.65072	22.227
JT0222	33.50265	21.87827
JT0223	33.49611	21.87709
JT0224	33.48916	22.24768
JT0225	33.36323	22.06535
JT0226 *	33.34867	21.74986
JT0227	33.31903	22.03867
JT0228	33.28922	22.05236
JT0229	33.25652	22.04343
JT0230 *	33.22082	22.02561
JT0231 *	33.16909	22.03302
JT0232 *	33.11368	22.04922
JT0233 *	33.0271	22.00091
JT0234 *	32.96303	21.98609
JT0235 *	32.87557	21.96231
JT0236 *	32.76956	21.97837
JT0237 *	32.65132	22.11732
JT0238 *	32.51006	22.29901
JT0239 *	32.30865	22.57172
JT0240	32.25384	22.56944
JT0241 *	32.20749	22.55805
JT0242 *	32.18589	22.54947
JT0243	32.1483	22.47189
JT0244 *	31.6817	22.35845
JT0245 *	31.22582	22.2631
JT0246 *	30.79967	22.16619
JT0247	30.48645	22.38088
JT0248 *	30.08138	22.61431
JT0249	29.71683	22.7143
JT0250	29.58632	22.45622
JT0251 *	29.52769	22.33132
JT0252	29.46962	22.22719
JT0253	29.13756	22.04877
JT0254	28.67968	21.80472
JT0255	28.39808	21.55936

Appendix E: Sample descriptions

Table E-1: Sample descriptions.

Sample Number	Date Collected	Location			Location Description	Sample Description
		Latitude (S)	Longitude (E)	Altitude (m)		
JT0201	4.09.02	33.39732	22.20072	630	Road cut, large sst cliff ~ 7m high; Bedding fairly horizontal as shown by pebble bed (see photo); Fining upwards sequences and jointing apparent.	Very coarse grained feldspathic sst Abundant large feldspar grains, sub to anhedral up to 1.5cm in size Quartz grains up to 0.75cm Cango G.
JT0202	4.09.02	33.42906	22.25193	619	Road cut, massive uniformly coarse, grey sst; stratigraphically just above finer grained unit which is possibly associated with bedding parallel slip- fine grained unit is not continuous	Uniformly coarse grained, grey coloured sst. Cango G.
JT0204	4.09.02	33.46415	22.25390	473	Road cut just south of fault zone described in JT0203; fairly weathered outcrop with lots of lichen	Coarse grained sst with mica and possibly feldspar Cango G.
JT0205	5.09.02	33.42154	22.24128	550	Road cut just where Grobbelaar's river cuts road (usual lunch stop) interbedded coarse and finer grained sst and shale bedding near vertical, bed thickness <20cm to 1m conglomerates to north	Cango G.
JT0214	11.11.02	34.00468	22.55245	52	Just east of Victoria Bay East side of train tunnel, 2m above train tracks	Foliated, coarse grained metamorphosed granite Kaaimans G./ Formation
JT0219	11.11.02	33.78127	22.34200	526	Small road cut (only one in vicinity), highly weathered and cleaved, thinly bedded	Shale Ceres SubG. Bokkeveld G.
JT0220	11.11.02	33.69149	22.27118	472	Road cut just south of Enon Formation (~18km south of Oudtshoorn)	Heavily weathered shale Ceres SubG. Bokkeveld G.
JT0226	12.11.02	33.34867	21.74986	785	Half way up 'Die Hell' pass, just east of Gamkaskloof settlement	Highly weathered shale Ceres Subgroup, Bokkeveld G.
JT0230	13.11.02	33.22082	22.02561	633	In Prince Albert, little hill W of town	Tillite Dwyka G, Karoo SG
JT0231	13.11.02	33.16909	22.03302	550	N of Prince Albert	Adelaide SubG, Beaufort G

JT0232	13.11.02	33.11368	22.04922	660	Just N of Matjiesfontein chert marker (N of Prince Albert), half a metre road cut	Highly weathered shale Waterford, Ecca G.
JT0233	13.11.02	33.02710	22.00091	519	S of Gamka River, 2.5m road cut	Dark blue/grey medium grained Waterford, Ecca G.
JT0234	13.11.02	32.96303	21.98609	514	S of N1, 2.5m road cut	Adelaide SubG Beaufort G.
JT0235	13.11.02	32.87557	21.96231	542	Just S of N1, road cut of interbedded sst and shale, beds of undulating thickness and ~ horizontal	Adelaide SubG Beaufort G.
JT0236	13.11.02	32.76956	21.97837	547	N of Leeu-Gamka on N1	Medium grained laminated sst Adelaide SubG Beaufort G.
JT0237	13.11.02	32.65132	22.11732	623	50km SW of Beaufort West, cross bedding, jointing and shale interbeds apparent in road cut	Coarse grained massive sst unit Adelaide SubG Beaufort G.
JT0238	13.11.02	32.51006	22.29901	734	30km SW of Beaufort West	Coarse grained sst, Abrahamskraal Fmtn, Adelaide Subgroup, Beaufort G.
JT0239	14.11.02	32.30865	22.57172	903	N of Beaufort West on road to Loxton, interbedded shale and sst, ~horizontal bedding	Red brown, highly weathered Adelaide Subgroup, Beaufort G.
JT0241	14.11.02	32.20749	22.55805	1326	~16km N of B.West, Molteno pass	Dolerite sill Karoo Dolerite
JT0242	14.11.02	32.18589	22.54947	1487	Molteno pass	Cross cutting dolerite sill Karoo Dolerite
JT0244	14.11.02	31.68170	22.35845	1460	1m road cut N of Slangfontein	Weathered dolerite sill Karoo Dolerite
JT0245	14.11.02	31.22582	22.26310	1427	Interbedded sst and shale ~30km S of Carnavon	Laminated sst Adelaide Subgroup, Beaufort G.
JT0246	14.11.02	30.79967	22.16619	1158	Offroad dolerite koppie, ~15km N of Carnavon	Weathered dolerite Karoo Dolerite
JT0248	14.11.02	30.08138	22.61431	1105	Quartzite koppie ~ 20m offroad, SW of Prieska	Quartzite Uitdraai Fmtn Brulpan G.
JT0251	15.11.02	29.52769	22.33132	1059	1m highly weathered road cut, ~30km SE of Marydale	Weathered granite Skalkseput Granite

Samples JT0201-11 collected on first sample trip (coinciding with the third year field trip to Oudtshoorn, September, 2002).
Samples JT0212-55 collected on second sample trip (Mossel Bay- George- Oudtshoorn- Prince Albert- Beaufort West- Carnavon- Prieska-Upington, November, 2002).

Appendix F: Sample pictures

FIELD PHOTO

THIN SECTION

JT0201

PPL

XP

JT0201- Arkose

JT0202

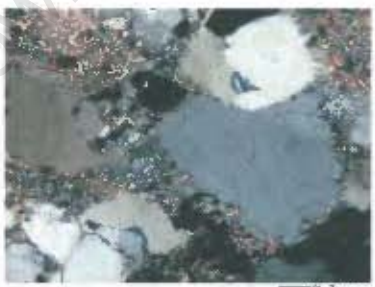

JT0202- Feldspathic greywacke

JT0204

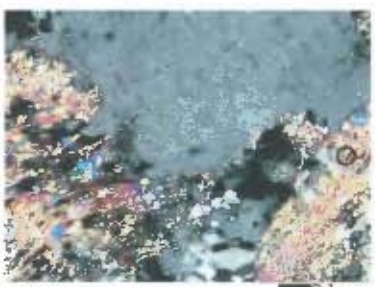

JT0204- Greywacke

JT0205

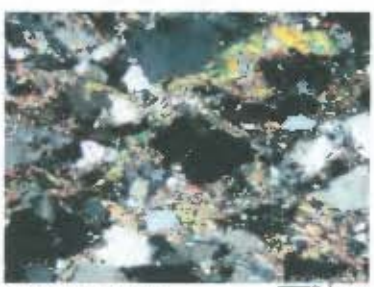

JT0205- Feldspathic Greywacke

FIELD PHOTO

THIN SECTION

JT0214

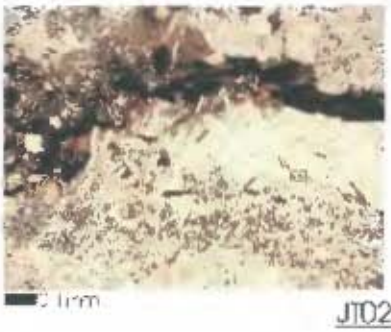

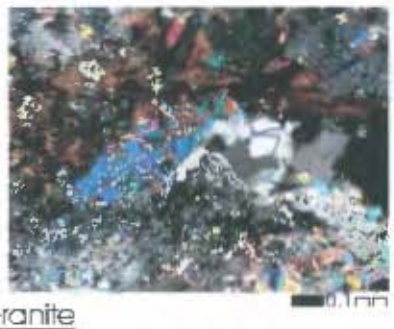

JT0214- Granite

JT0219

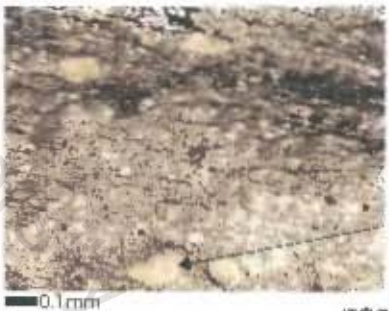

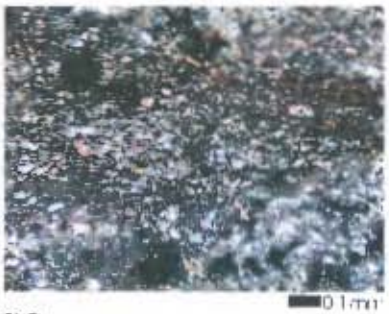

JT0219- Shale

JT0220

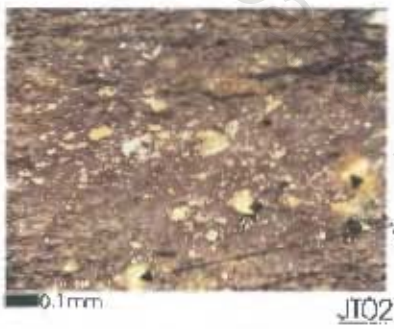

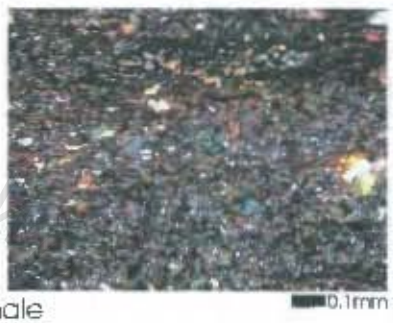

JT0220- Shale

JT0226

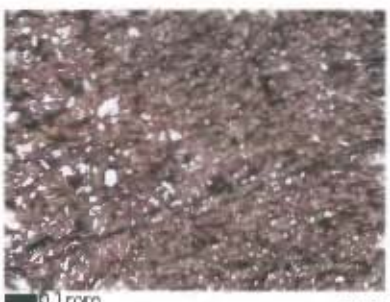

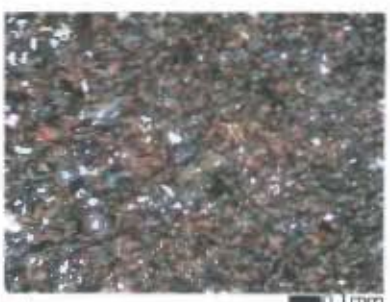

JT0226- Shale

FIELD PHOTO

THIN SECTION

JTC23C

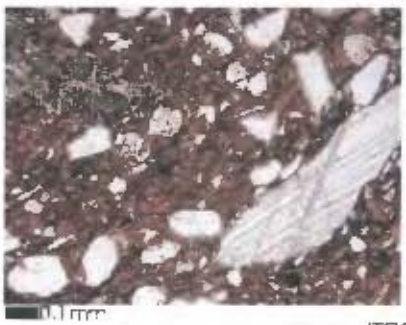

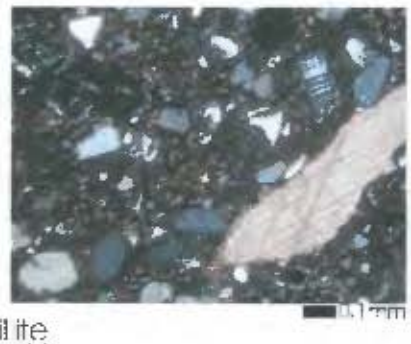

JT0230- Tillite

JT0231

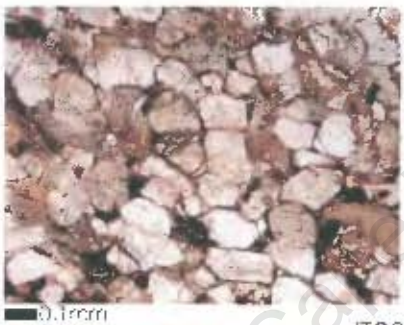

JT0231 - Arkose

JT0232

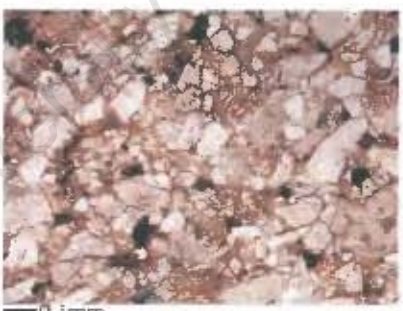

JT0232- Arkose

JT0233

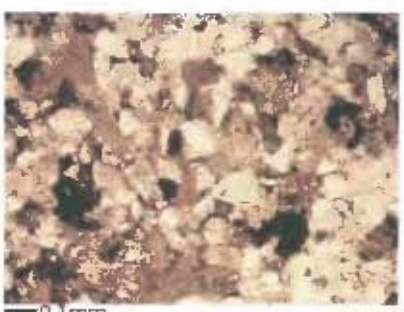

JT0233- Arkose

FIELD PHOTO

THIN SECTION

JT0234

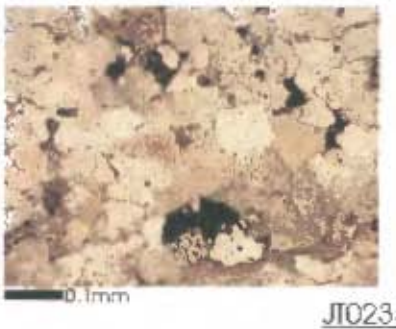

no picture available

JT0234- Arkose

JT0235

no picture available

no picture available

JT0235- Arkose

JT0236

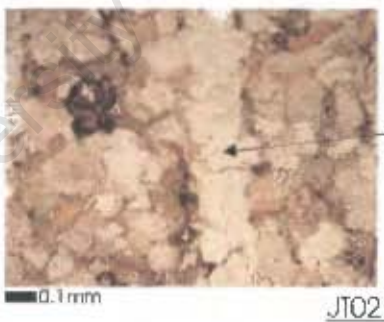

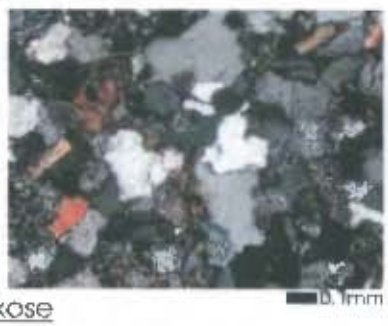

JT0236- Arkose

JT0237

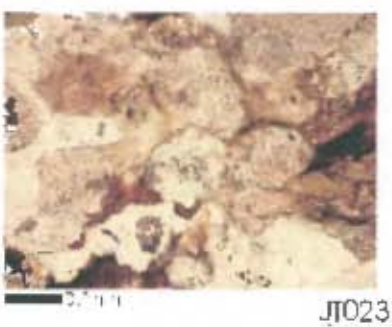

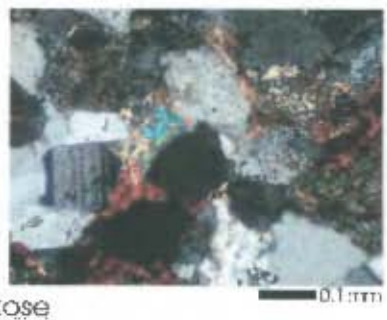

JT0237- Arkose

FIELD PHOTO

THIN SECTION

JT0238

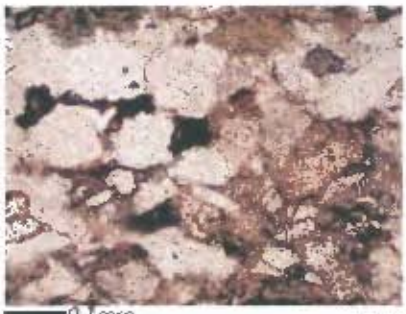

0.1mm

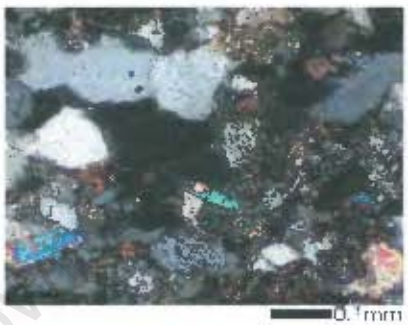

0.1mm

JT0238- Arkose

JT0239

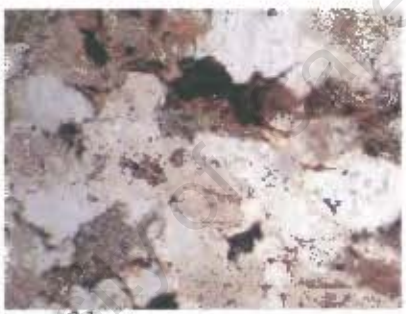

0.1mm

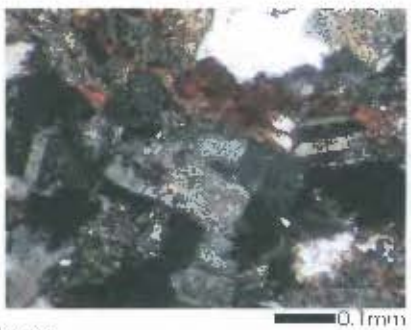

0.1mm

JT0239- Arkose

JT0241

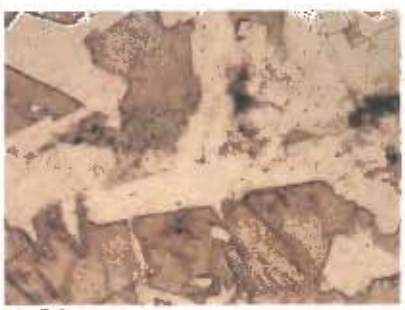

0.1mm

0.1mm

JT0241 - Dolerite

FIELD PHOTO

THIN SECTION

JT0242

0.1mm

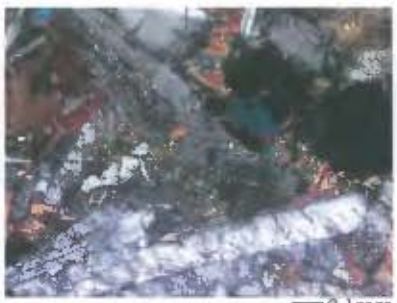

0.1mm

JT0242- Dolerite

JT0244

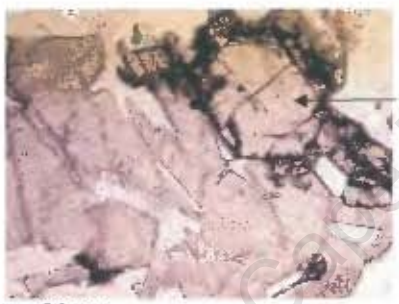

0.1mm

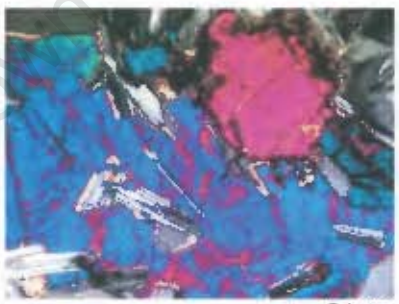

0.1mm

JT0244- Dolerite

JT0245

0.1mm

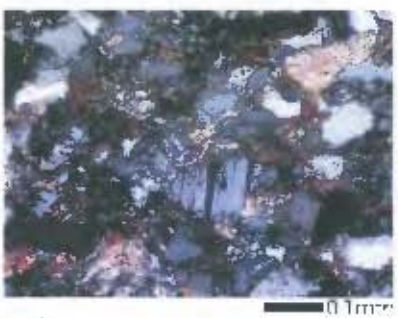

0.1mm

JT0245- Arkose

FIELD PHOTO

THIN SECTION

JT0246

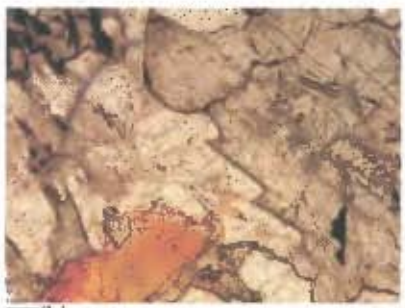

0.1mm

0.1mm

JI0246- Dolerite

JI0248

0.1mm

0.1mm

0.1mm

0.1mm

JI0248- Quartzite

JI0251

biotite showing radiation damage

0.1mm zircon

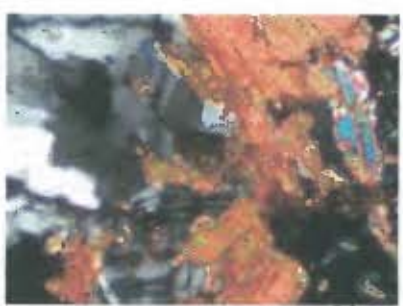

0.1mm

JT0251 Granite

Appendix G: Calculation of sediment volumes offshore

Accumulated sediment volumes were calculated in the Outeniqua Basin (Bredasdorp, Pletmos, Gamtoos and Algoa Basins) and the Southern Outeniqua Basin using two different methods due to differences in the extent of data coverage.

Outeniqua Basin

The calculations of sediment volume offshore use data from an internal well compilation report of the Southern Oil Exploration Corp. (Pty.) Ltd. (Soekor) that lists the depths below seafloor to several regional unconformities for 173 boreholes. These boreholes are distributed unevenly offshore of the south coast, in less than 200 m water depth (Figure G.1).

Sediment volume for each of the 5 time intervals (~136-130 Ma, ~130-120 Ma, ~120-93 Ma, ~93-67 Ma and ~67-0 Ma) is estimated for an area over which deposition occurred (Figure G.1). The area was bounded by the shoreline in the north, the 200 m isobath (south), the Agulhas- Columbine Arch (west) and the Port Alfred Arch (east). Thickness of accumulated sediment for each time interval is calculated at each borehole location by subtracting the true depth of each unconformity from the unconformity stratigraphically below (schematically shown in Figure G.2). (The true depth is equal to the depth read from the well report minus the water depth (estimated from a map of water depth and minus the Kelly Bushing (~25 m- depth from water surface to top of drill rig)). The results of these calculations are given in section 6.3.

The point values of accumulated sediment thickness at each borehole are transformed into sediment volume over the specified area by gridding the data using Oasis Montaj 6.0 (Geosoft Inc.). The minimum curvature method was used which fits the smoothest possible surface to the given data values. This method was chosen as it is best suited to randomly distributed data points. In minimum curvature gridding the grid values for the nodes of a coarse grid are estimated from the nearest actual data points. The grid is then iteratively adjusted to improve its fit to the data. The projection of the gridded data was changed from geographic latitude/ longitude in degrees to x and y in metres (Projection method: UTM zone 35S, Datum: Cape) so that grid volume (sediment accumulation) could be measured in section 6.3.

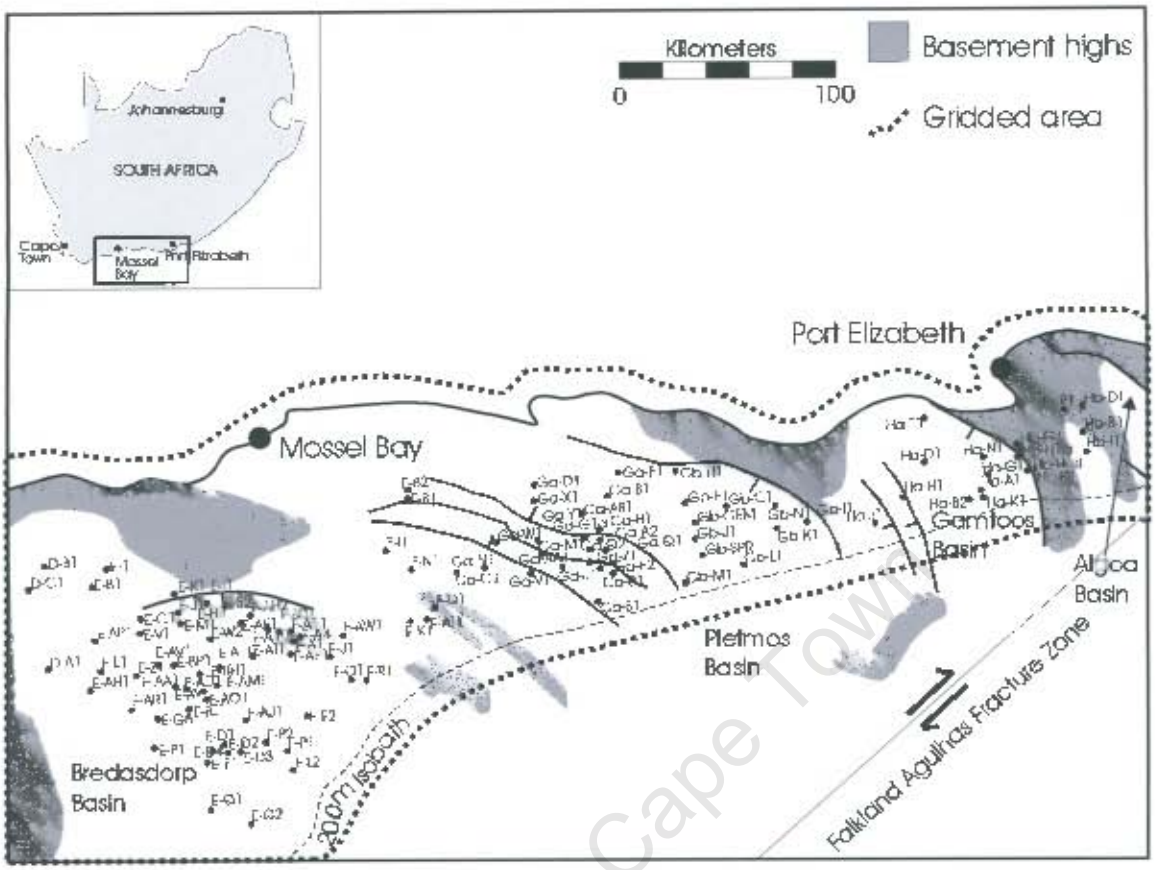

Figure G.1: Distribution of a selection of the 173 boreholes offshore. Dashed line indicates the gridded area.

10 contour maps were generated for the Outeniqua Basin: 5 detailing depths to each unconformity and 5 showing sediment thickness for each time interval. These maps are composed of two types of data, the gridded contour map of the depth of an unconformity below the seafloor and the extra information which places the contour map in its geographic context (towns, faults, shoreline, 200 m isobath and FAFZ).

Vector data (including the shoreline, faults, 200 m isobath and Falkland-Agulhas Fracture Zone) were digitized using a GIS package, ILWIS, (Integrated Land and Water Information Systems) and then converted into Arcview GIS 3.2© shape file format. Point data (for example towns) were digitized in the same way. Vector and point data were then imported into the Oasis Montaj project and added to the gridded data to produce 10 maps. The superposition of the 5 contour maps to produce figure A.2 used the Oasis Montaj 3D tool.

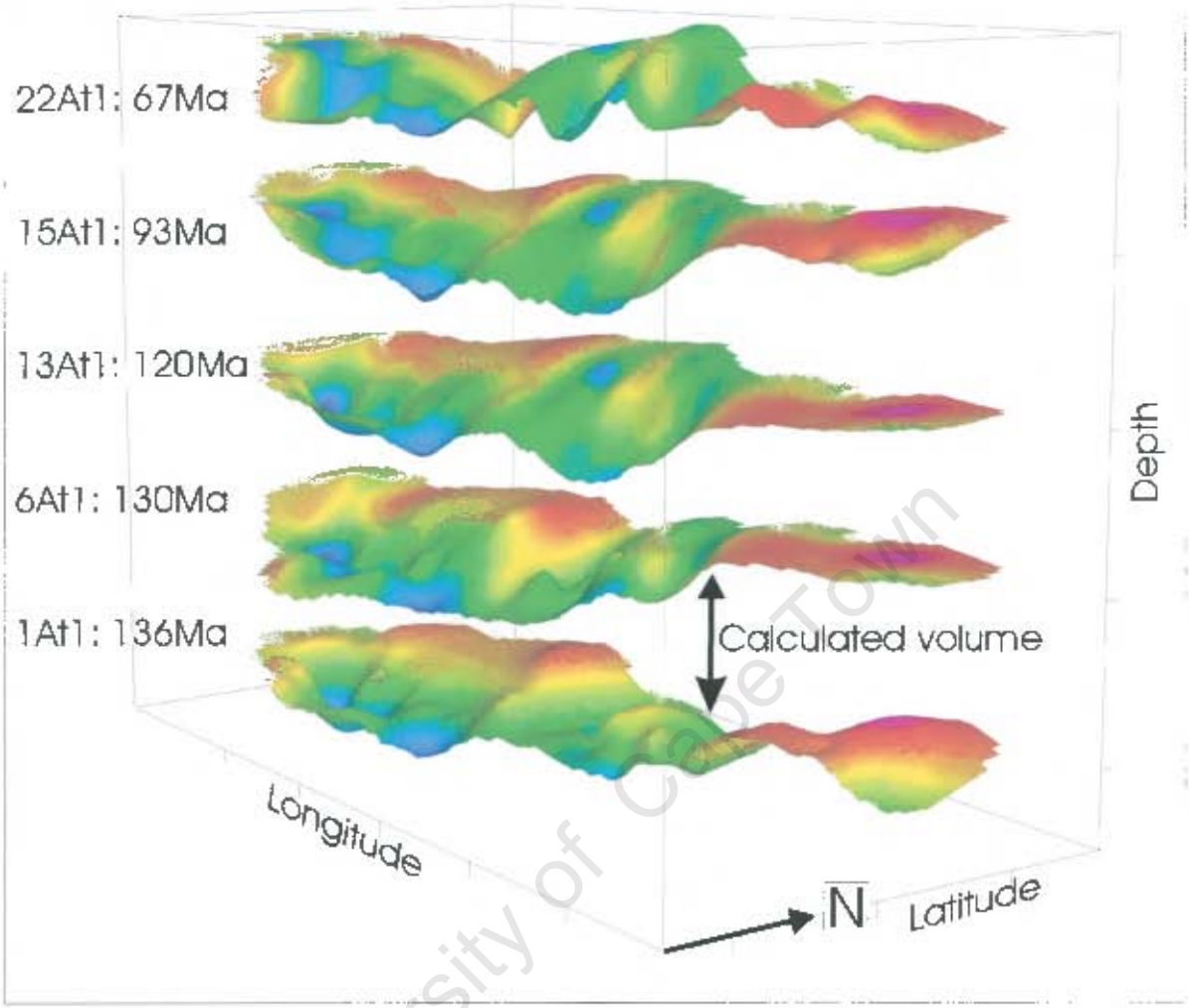

Figure G.2: The thickness of accumulated sediment is calculated between regional unconformities.

Southern Outeniqua Basin

The lack of boreholes through the Southern Outeniqua Basin makes estimating accumulated sediment volume difficult. Roux (1997) used seismic coverage of this basin to produce a schematic section across the southern Bredasdorp Basin, Southern Outeniqua Basin and marginal fracture ridge (Figure G.3). From this schematic section thicknesses of each time interval (~136-130 Ma etc.) were measured at locations 1 to 5 (Figure G.3). An average thickness across this section was calculated for each time interval. This average thickness was multiplied by the aerial extent of the basin, 20 000 km^2 (Roux, 1997), to obtain accumulated sediment volumes for each time interval (listed in Table 6.3, Chapter 6.3).

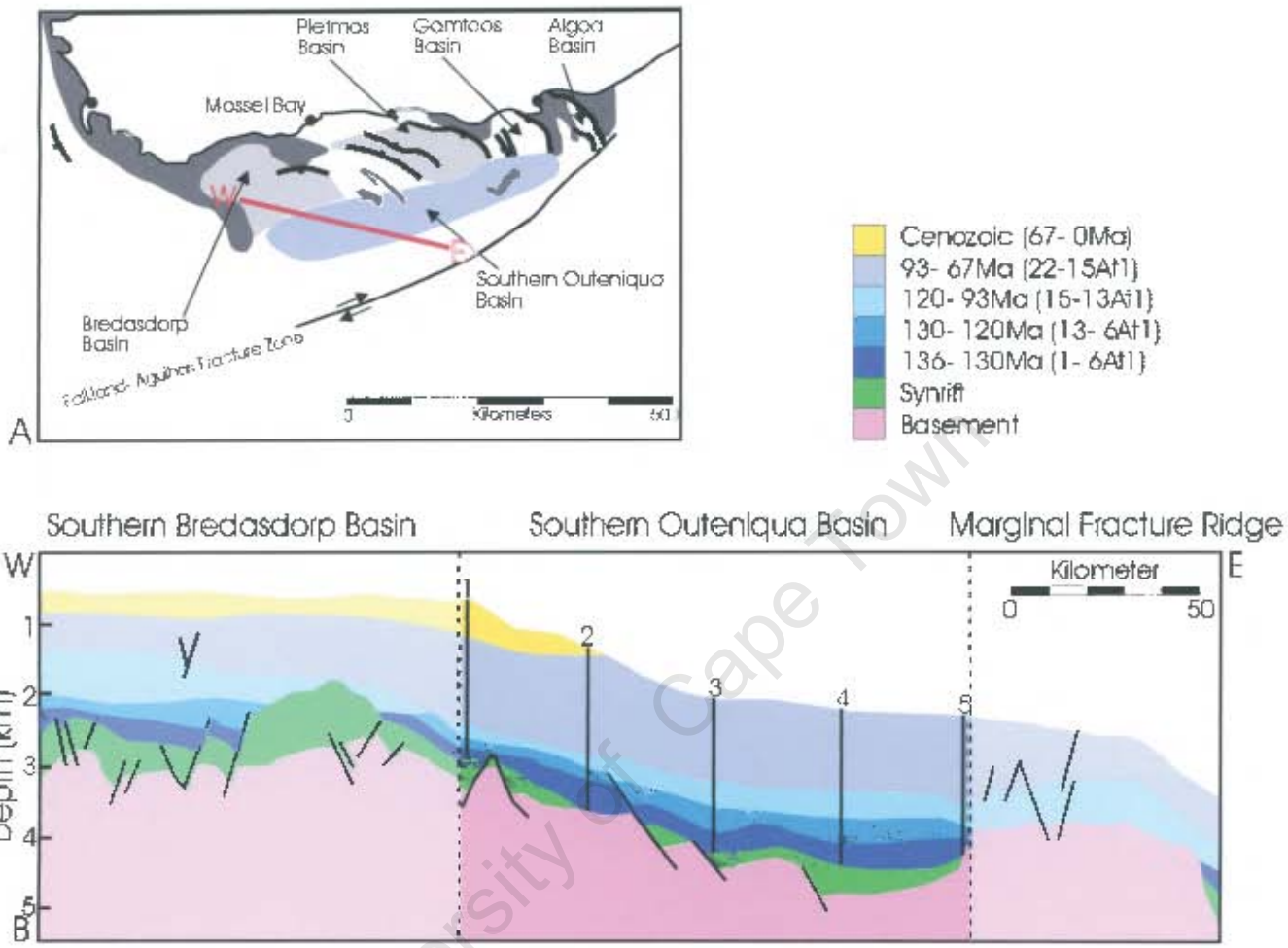

Figure G.3: (A) The location of (B), a schematic section across the Southern Outeniqua Basin (adapted from Roux, 1997). Sediment thicknesses measured at points 1 to 5.